

:: csem

SCIENTIFIC AND
TECHNICAL REPORT
2016



IMPRINT

Full report title CSEM Scientific and Technical Report 2016

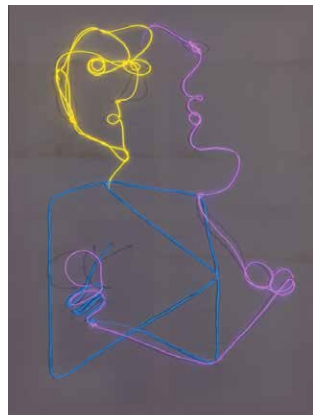
Editor and publisher
CSEM SA
info@csem.ch
T +41 32 720 5111

Design
CSEM Communications
media@csem.ch
T +41 32 720 5111

Publication
Frequency yearly
Media printed and electronic
Website www.csem.ch/str2016

Printing Imprimerie Baillod SA, Bevaix (Switzerland)

Cover page
Projection of artwork by coherent illumination of
designed optical nanostructures.



The project creates a connection between nanotechnology and art by using designed nanostructures to project artwork in single and full color. Once the optical nanostructures have been designed and a physical master created, an infinite number of low-cost copies can be reproduced.

The original artwork, from the artist Véronique Lecomte, known as Velec, is made of neon light tubes.
Courtesy: VELEC www.velec.ch

CSEM SA

CSEM is a private, non-profit research and technology organization (RTO) and a Swiss innovation accelerator—a catalyst for the transfer of technologies and know-how from fundamental research to industry.

CSEM's extraordinary success in the field of innovation and its diffusion stems from its promotion of technology-based activities that address the next generation of trends—the future of energy, the Internet of Things revolution, the advent of wearable technologies for wellness and medical applications, or the rendering widespread of machine-to-machine (M2M) communications required by Industry 4.0.

CSEM's research strategy is built around five strategic programs:

Microsystems technology—Design, integration, and packaging of devices that sense and monitor our environment and aspects of our daily lives, exploring new frontiers at the interface of nanotechnologies, materials science, and biotechnologies and delivering enhanced performance, miniaturization, and new properties.

Systems engineering—An application-oriented interdisciplinary program with a special emphasis on system integration, systems engineering aggregates different components and subsystems designed to collaborate and deliver targeted functionality, taking into consideration resource limitations (in terms of processing and power consumption), reliability, production cost, maintenance, and environmental conditions.

Ultra-low-power integrated systems—A strong focus on analog and mixed IC design as well as wireless communication and vision technologies, the key technologies required to build very-low-power, wirelessly interconnected, embedded smart systems or remote sensing nodes.

Surface engineering—Focuses both on the novel properties of engineered surfaces and interfaces, to deliver breakthrough surface effects, and on their “up compatible” manufacturing processes, to bridge the gap to industrial applications.

Photovoltaics & energy management—Development, covering the full chain from prospective PV cell and module technologies through fully integrated energy systems, where energy efficiency and management is delivered by intelligent hardware and algorithms.

CONTENTS

PREFACE

MULTIDISCIPLINARY INTEGRATED PROJECTS—MIPS

- MiniNOB—Cooperative Sensor SoC for ECG and EIT
Wear-a-Watt—Energy Autonomy for the Wearables
ALS—MEMS Scanner for Assisted Laser Surgery
GWAPO—Generic Wireless Autonomous Conformable Patch with Display
MS-MET—Integrated Inductive Charge Detection Sensor and Analyzer for Mass Spectrometry
ECAM—Image Sensor with Stacked a-Si:H Photodiodes
SMAC3P—Assembly and Functional Tests of a Flat Form Factor Miniature Atomic Clock
muTish—Tools to Monitor and Handle Medium Sized Biological Entities
HybSi—High-precision Mechanisms at the Centimeter Scale based on Silicon Hybridization
TeraXplore—Single Detector for Multi-color Terahertz (THz) Imaging

MICROSYSTEMS

- A MEMS-based Gas Chromatograph Front-end for a Miniature Spectrometer
A MEMS UV Laser Pointing Mirror for Atmosphere Monitoring
3D Printing for Advanced Manufacturing
Novel Microfabricated Infrared Optical Filters
How Robust are MEMS for Space Applications?
MAMOS—Metal-based Additive Manufacturing on Silicon
Low-temperature Reactive Nanofoil Die-attach Bonding for MEMS
Low-temperature Laser-assisted Sealing of Glass Lid on Silicon
ACTION—Technologies for Cochlear Implants
ACTION—Hermetic Packages and Flexible Substrates for Implants
Improved Lifetime of Miniaturized Vapor Cells in Atomic Clocks
Nanofoil Bonding of Laser Micromachined Components

SURFACE ENGINEERING

- A Photolinker Polymer with High Density Functional Groups for more Sensitive Bioassays
Online Monitoring of Water Contaminants with an Optical Biosensor
Detecting and Measuring Nanoparticles in Complex Matrices: the SMART-NANO Platform

7	Fluorescence Lifetime Imaging (FLIM) made easy Cell-based Microfluidic Chip to Study Bone Healing Mechanisms	42 43
9	Microfluidic in-vitro Model of Bladder Cancer for Drug Profiling Wearable Sensors for Ion Monitoring	44 45
11	Rapid and Cost-effective Detection of Tuberculosis (TB)	46
12	Glucose Sensors on Demand	47
13	Controlled, Pressure-driven, Sequential Actuation of Fluids for a Food Quality Monitoring System	48
14	RASECAN—Parallel AFM for Rapid Cancer Diagnosis System for Airborne Nanofibers Exposure Monitoring	49 50
15	Asymmetric Color Appearance with Aluminum Plasmonic Substrates	51
16	Four Color Filters in One using Large Area Plasmonic Substrates	52
17	Micro- and Nanostructuring of Steel Inserts for Aesthetics and Security in High Volume Industrial Injection Molding	53
18	Table-top Classification and Sorting System for Small Model Organisms	54
19	Development of Electrochemical Flow-cell for Advanced <i>in situ</i> X-ray Investigations	55
20	Slot Die Deposition of Functional Films	56
21	Large Area Nanoreplication on Flexible Substrate Integration of New Sol-gel Films into Miniaturized Optical CO ₂ Sensors for Air Quality Monitoring	57 58
24	Advanced Microlenses Fabrication Techniques	59
25	Ultra-thin Direct-lit LED Modules with Beam-shaping Thin-film optics	60
26	Printed Sun Sensors for Satellites	61
27	Inkjet Printing Structural Colors based on Plasmonics	62
28	Aerosol-jet Printing, an enabling Technology for printing Electrodes, Interconnects, Sensors or Antennas on 2-or 3-D Parts	63
30	PV-CENTER & ENERGY MANAGEMENT	65
31	Platform for High-efficiency Silicon Heterojunction Solar Cells	68
32	Back-contacted Silicon Heterojunction Solar Cells with a Simplified Photolithography-free Processing	69
33	Direct Interconnection of plated Silicon Heterojunction Solar Cells	70
34	Multiple Metallization Schemes enabled by Multi-wire Interconnection.	71
35	Above 30% Efficiency Tandem Solar Cells using Silicon Heterojunction Bottom Cell	72
39	Development of Indium-free TCOs for Silicon Heterojunction Solar Cells	73
40	Upscaling of Perovskite-based PV Devices within Project CHEOPS	74
41		

Silicon Photovoltaics for Hydrogen Production	75	ULTRA-LOW-POWER INTEGRATED SYSTEMS	103
Plastics Compounding Platform for Reliable and Dedicated Packaging Materials for PV Modules	76	Illumination for a Laser Profilometry System Targeting Fast Moving Objects	105
Solarstratos—a Solar Airplane to the Edge of Space	77	Real-time Face Detection and Recognition on the Vision-In-Package System	106
Embedded Light Management Films for All-season Energy-harvesting in Printed Photovoltaics	78	A Contactless Vision-based Technology for Heart and Respiration Rates Estimation	107
Results from Non-intrusive Load Monitoring	79	Compact and Flexible Tracking System for Total Knee Replacement Surgery	108
TRIBUTE—Automatic Building Simulation Model Calibration and Diagnostics	80	An Integrated Circuit for Future X-ray Imaging Detectors based on a Ge Pillars Absorption Layer	109
Electrical Energy Storage Optimization based on Predictive Control	81	Vision-based Monitoring of Manual Assembly Processes	110
Battery Performance Evaluation and Modelling for Stationary Applications	82	Hyperspectral Imaging using a Commercial Light-field Camera	111
Set-up and Operation of a Low-voltage DC Micro-grid Demonstrator	83	RF Sensing of Human Physical Condition in the mm-Wave / THz Frequency Range	112
Towards High Efficiency Flexible Printed Tandem Solar Modules	84	3D Printed Antennas for mmW / Sub-THz (100GHz–500GHz) Applications	113
SYSTEMS	85	WiseSkin for the Restoration of Natural Sense of Touch	114
A Wearable Dietary Monitor using a PPG-based Chewing Sensor	87	REP—Making Self-healing Wireless Networks Efficient	115
Wrist-located Optical Monitoring Device for Atrial Fibrillation Screening	88	Publish-Subscribe Communication for Swarms of Unmanned Vehicles	116
Novel Ambient Light Rejection System for PPG-based Measurement Devices	89	Autonomous Sensor Network for Smart Street Lighting	117
Cuffless Blood Pressure Monitoring: CSEM's catalog of applications	90	Secure Wireless Link for Ultra-low Power Wireless Sensor Networks	118
WELCOME—Wearable Sensors for Patients Suffering from Cardiopulmonary Diseases	91	Long Range Low-power Localization	119
Autonomous Medical Monitoring and Diagnostics	92	IoT Objects Localization based on Time Difference of Arrival Measurements	120
Light Management for Treatment of Chronic Wounds	93	Reactive Low-power Software Stack for BTLE Implementation	121
X-ray Phase Contrast Imaging: from High Resolution to High Speed	94	Indoor Localization using IR-UWB	122
VISARD—Vision Automation Robotics Designer	95	Implementing Bluetooth Low-Energy 5 in icyTRX	123
Visualization Tool to Understand the Learning of a Deep Network	96	Asynchronous Digital Design for Sub-threshold Regime Operation	124
Novel System for Pressure Measurements on Yacht Sails	97	Sub-threshold Latch-based icyflex2 32-bit Processor with Wide Supply Range Operation	125
Ultra-low Phase Noise Microwave Generated with Photonics	98	Physical Unclonable Function (PUF) based on 0.18 um Sub-threshold SRAM	126
A Vision-based LiDAR Sensor Technology for Space Debris Removal	99	Library Design in a DDC Technology Optimized for Sub-threshold Regime	127
Efficient Femtosecond Laser Stabilization via Stimulated Emission	100	Sensor Interface for a Resonator-type Mass Spectrometer	128
Additive Manufactured Metallic Compliant Mechanisms and Flexible Structures	101	A Fully Integrated Adaptive Energy Harvesting System for Ultra-low Power Applications	129
Qualification Test Program for CCM and Prototype Flight Model	102	CMOS Embedded NEMS Resonator with Acoustic Confinement	130

ANNEXES

	131	
Publications	131	European Space Agency (ESA), Swiss Space Office, Austrian Space Applications Programme (ASAP), and CNES Projects
Proceedings	133	146
Conferences and Workshops	137	Industrial Property
Publicly Funded Projects	138	147
Swiss Commission for Technology and Innovation (CTI)	140	Collaboration with Research Institutes and Universities
European Commission Projects	144	147
		Teaching
		151
		Theses
		152
		Commissions and Committees
		153
		Prizes and Awards
		156

Market segmentation synopsis



AERONAUTICS & TRANSPORTATION

13; 14; 17; 24–25; 29–31; 35; 55–56; 61; 63; 82; 92; 94; 95–96; 97; 105–107; 111; 116; 118; 122



PHARMA, BIOTECHNOLOGY & LIFE SCIENCES

15–16; 18; 24; 26; 29–31; 35; 39–44; 46–50; 54; 56–58; 63; 87–88; 92; 94–97; 106–109; 111; 128



INFORMATION & COMMUNICATION TECHNOLOGIES

14; 17; 29–31; 34; 57; 59; 61; 63; 113–114; 116–123



ENERGY & BUILDING SOLUTIONS

30–31; 55–56; 63; 68–84; 97; 117; 121; 125



ENVIRONMENT

15; 24; 27; 29; 39–42; 50; 55–58; 63; 69–72; 75; 111; 116–119



FOOD & AGRICULTURE

14; 20; 24; 29–30; 39–42; 55–58; 63; 94–96; 111



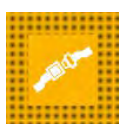
HEALTHCARE, WELLNESS & SPORT

11–15; 17; 20; 26; 29; 31–33; 35; 39–40; 45–48; 50; 58; 63; 87–97; 106–109; 111–114; 119–120; 122–123; 129



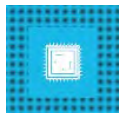
HOME & INDUSTRIAL AUTOMATION

16; 20; 24; 27; 29–31; 35; 58; 60–61; 63; 94–97; 105–106; 108; 110–111; 117; 119–123; 125–126; 129–130



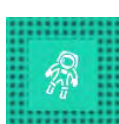
SECURITY & SURVEILLANCE

15–16; 24; 27; 29; 42; 51–53; 56; 59; 62–63; 96; 105–107; 109–111; 116–122; 125–126; 129



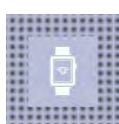
SEMICONDUCTOR INDUSTRY

16; 24; 26; 29–31; 33; 35; 50; 55; 63; 69; 73; 94; 96; 113–114; 123–125; 127; 129–130



SPACE & ASTROPHYSICS

15; 17; 24; 28–31; 34–35; 59; 61; 63; 92; 94; 98–102



WATCHMAKING

12; 17; 19; 29–31; 34–35; 50; 57; 63; 88; 94; 96; 106–107; 124–127; 129–130

PREFACE

Dear Reader,

New technologies and innovations are constantly changing and evolving, improving the way we do things, the way we think, the way we work and live.

This year, as always, I'm pleased to share with you the latest news about the work we've done and the successes we've enjoyed over the last twelve months. You'll discover numerous examples of how we're continuing to expand as a preeminent research and technology organization, providing new solutions to a number of challenges. These include technologies for a greener and more sustainable planet; the deployment of precise, dedicated sensors contributing to human well-being or environmental sensing; the rethinking of advanced manufacturing for the industry of the future; and the leveraging of synergies across our different technologies platforms, to name just a few.

In everything we do, we recognize that success is founded on partnership. Together, day after day, we help industry and society prepare for the future. That's why I would like to take this opportunity to thank personally our partners, our clients, and my colleagues for their efforts and dedication to this joint endeavor.

Mario El-Khoury
CEO, CSEM SA

MULTIDISCIPLINARY INTEGRATED PROJECTS—MIPS

Harry Heinzelmann

CSEM's Multidisciplinary Integrated Projects (MIPs) complement the center's programmatic research activities, which are carried out within the framework of its five research programs: **Microsystems, Surface Engineering, Integrated Systems, Ultra-Low Power Integrated Systems, and PV-center & Energy Management**. These programs are constantly advanced, reviewed, and adapted to emerging trends and anticipated future demand from industry. They are presented in detail in the following chapters.

The MIP program has been established to drive innovation through a multidisciplinary effort that combines the strengths of our five thematic research programs. For many years CSEM has dedicated an important part of its resources to these highly interdisciplinary projects, targeting demonstrators with a high level of maturity (high technology readiness level (TRL)) for novel applications with high market potential in relatively short development times. Starting in 2016, two new categories were introduced into the MIP program, allowing us to rapidly explore new concepts (Feasibility MIPs) and pursue long-term joint technology development (Technology MIPs). All the projects of the MIP program remain strictly multidisciplinary.

The MIP program is re-evaluated annually, and consists of ongoing projects and new proposals in a healthy balance, making possible quick response times to newly emerging market needs. In this way, the MIPs complement CSEM's five topical research programs in an ideal way. The MIP program enables CSEM to offer its industrial clients an even richer portfolio of technologies beyond the possibilities of its thematic research programs.

CLASSICAL MIPs

MiniNOB—Miniaturized, wearable system for blood pressure measurement

MiniNOB targets the development of a TRL-5 medical, miniaturized, wearable system for the continuous recording of non-occlusive mean blood pressure (NOBP) and ECG. The state of the art for non-invasive blood pressure (NIBP) monitoring is based on an inflatable cuff, which can provide only intermittent measurements (typically every half an hour). Such a technology is bulky and uncomfortable. MININOB will develop a solution based on CSEM's technologies—namely, NOBP based on cooperative sensors (button sensors). A further goal is the reduction of the size of the individual sensors. The final demonstrator and its validation are foreseen for 2017.

Wear-a-Watt 2—Energy harvesting in wristbands

The objective of Wear-a-Watt 2 is to create an integrated energy harvesting solution for wristbands and watchcases. The final result will be the acquisition of wearing test data, which will be used to demonstrate the potential of this solution to new customers. The project targets applications mainly in the watch market. More generally, it benefits from the broad market trend in wearable technologies. Wear-a-Watt 2 will focus on successful component integration, while improving—with regard to the preceding project (Wear-a-Watt)—in a number of aspects, including increased PV performance. The

demonstrator will allow the energy generated to be monitored, making possible a wearing test that will deliver user data that helps us to assess the potential of energy harvesting in real-life conditions, and to understand certain key performance parameters of the wristband.

ALS—MEMS scanner for assisted laser surgery

The goal of the ALP project is the development of a laser microsurgery tool that can be integrated into an exploratory vision system like an endoscope. The targeted application is integrated endoscopic surgery, but the technology can be applied to other kinds of surgery that necessitate very fine and controlled cuts, including—for example—eye surgery. The laser surgery tool will be based on an integrated MEMS scanner and allow the steering of a high-power laser beam that will be provided through an optical fiber. Interactive control by the surgeon, or automated operation following special, pre-defined patterns, will be possible. In the future, an optical coherence tomography (OCT) system might be integrated for complementary depth measurements.

GWAPo—Generic, wireless, autonomous, conformable patch with display

The project GWAPo aims at creating a platform for thin, miniature, flexible, and rechargeable wireless interactive sensors and actuators. The GWAPo patch combines sources of energy—including, for example, from photovoltaics—with sensors, electronics, displays, interactive components, and antennas. The result will look like a sticking bandage that can be attached to the skin or other non-flat surfaces, with potential applications that cannot be addressed using classical sensor nodes. For this, a number of flexible technologies have to be combined. The envisaged prototype will be able to be worn on the body and operate autonomously for weeks, remotely transmitting selected physiological parameters.

MS-MET—Mass-spectrometer for metabolomics based on CSEM's MicroMS Technology

The goal of the project MS-MET is to develop a mass spectrometer demonstrator specific to metabolomics, thus addressing a key emerging global market. CSEM's resonator and pickups, both developed in the MIP MicroMS (2014–15), will be at the core of the MS-MET system. The focus of this project is the introduction of adequate sample preparation, as well as the development of separation and ionization units for the specific market of metabolomics. The envisaged demonstrator is a versatile, high-resolution, tabletop mass spectrometer able to analyze complex molecule mixtures and to detect low-concentration metabolites rapidly and reproducibly.

TECHNOLOGY MIPs

ECAM—Enhanced CAMera

The project ECAM aims at demonstrating an image sensor module for low light imaging with high photomultiplication gain. Traditional image intensifier systems based on multiple conversion stages introduce noise and are limited in terms of speed and spatial resolution. The proposed system consists of a photocathode and a silicon sensor in a vacuum envelope with a transparent front

window. This approach is simple, and offers a good signal-to-noise ratio, high spatial resolution, and a fast response time.

SMAC3P—Swiss miniature atomic clock

SMAC3P continues the building of the first miniature atomic clock (MAC) with a functional, flat-form-factor physics package (PP). The targeted application is the integration of an atomic clock into a wristwatch for the Swiss watchmaking industry. Other potential applications include any that require an ultra-stable time base or frequency reference in a compact and power efficient package. The flat-form-factor physics package PP will be realized by combining low-temperature co-fired ceramics (LTCC), smart integration, and MEMS atomic vapor cell and planar waveguide technologies. The envisaged SMAC3P demonstrator consists of an evaluation kit demonstrating the performance of the flat-form-factor miniature atomic clock, with a frequency stability better than 10^{-9} sec and an overall power consumption of less than 50 mW.

muTish—Manipulation and characterization of micro-tissue

Fast manipulation of cell clusters and micro-tissues, including classification, sorting, analysis, and monitoring, are of increasing importance in the pharmaceutical industry. The project muTish continues developments that began in 2015 and has the goals of pushing CSEM's CellFactor technology toward smaller object sizes (100–500 μm) and of equipping it with a low-cost, fluorescence-based monitoring system. The envisaged demonstrator features high-speed image analysis for object classification and sorting; low-cost fluorescence analysis for high-speed quantification; and smart, multiwell plates with integrated biosensors—plates that enable the long-term monitoring of pH and lactate or glucose concentration at the location of the sorted objects. muTish's technology addresses the important 3R policy (replacement, reduction, and refinement of animal testing), as this and similar *ex vivo* technologies will lead to the replacement of animal tests for toxicology screens in the pharmaceutical and chemical industries.

HybSi—Integration and hybridization of silicon for “macroMEMS”

HybSi 2016 aims at developing technologies for the hybrid integration of silicon-based components in high-precision micromechanisms at the macroscopic scale (macroMEMS). Given the importance of the watch industry in Switzerland and the current trend of integrating silicon components into high-end mechanical watches, the project focuses on the hybridization challenges typical of this industry. Further applications for macroMEMS technology are expected to emerge in the medical industry. In 2016, HybSi will mainly address wafer-level assembly techniques, additive manufacturing on silicon, and the molding of macroMEMS parts.

FEASIBILITY MIPS

TeraXplore—Exploring terahertz imaging technologies

The main objective of TeraXplore is to investigate the possibilities of active, multicolor terahertz imaging in the 100 GHz to 500 GHz band for the inspection of composite materials and solar cells, and to study possible implementations of the THz detectors required. As penetration depth and resolution depend on the frequency of the THz radiation used, the use of multiple frequencies will give richer information (“multicolor”). This can be achieved either by sweeping a single monochromatic source, or by using several sources in parallel. The THz detector to be developed will be based on the “direct detection method”; that is, it consists of an antenna and an RF receiver. Different composite materials and photovoltaic cells will be measured in order to evaluate the possibilities of multicolor and 3-D imaging.

MiniNOB—Cooperative Sensor SoC for ECG and EIT

A. Bischof, M. K. Augustyniak, Y. Zha, B. Schaffer, P. Persechini, P. Heim, C. Monneron, O. Chételat, E. Haenni

A system-on-chip (SoC) has been developed in a $0.18\text{ }\mu\text{m}$ CMOS process. This SoC is at the heart of a miniaturized wearable system for the continuous measurement of several multi-dimensional physiological signals such as multi-lead ECG (electrocardiogram) and EIT (electrical-impedance tomography). The integrated functions are: communication and synchronization of cooperative sensors, voltage measurement and current injection for EIT, as well as multi-lead ECG measurement.

Cooperative sensing is a patented CSEM's approach for wearables measuring physiological signals, such as bio-potential or bio-impedance. The advantage to the state-of-the-art technology (where a set of passive electrodes is connected to a single measurement unit) is that a high quality signal can be measured with dry electrodes by using only one non-shielded (and possibly even non-insulated) conductive electrical connection. In addition, each sensor is running autonomously and on its own battery, which makes easy the sensing of additional signals, such as optical or acoustic signals. Moreover, adding more cooperative sensors to the system is easy and makes therefore the approach scalable and configurable.

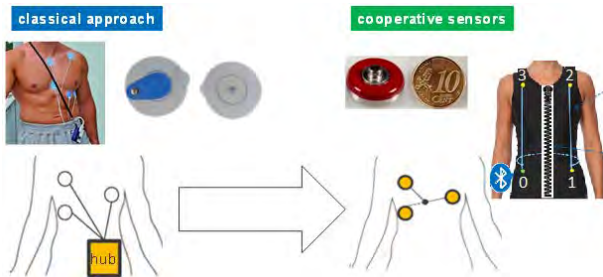


Figure 1: Classical approach and cooperative sensors (MiniNOB).

In the MiniNOB system, which is designed to measure ECG and NOBP (non-occlusive blood pressure), four cooperative sensors are used (see Figure 1, far right). Sensor 0 acts as master and collects the data from all other sensors prior to transmission through BTLE (Bluetooth low energy). Furthermore a current is injected in order to control the reference node (sensor 1) to ground potential. Sensors 1 and 2 measure the body surface potential (BSP) and impedance (IMP) signal, and send the data to the master through the communication channel. Sensor 3 injects a current and also sends digitized BSP measurement data to the master. The entire system is running on a single wire. The body is used as the return path. This is possible as the BSP, IMP and communication signals are located in different frequency bands (see Figure 2).

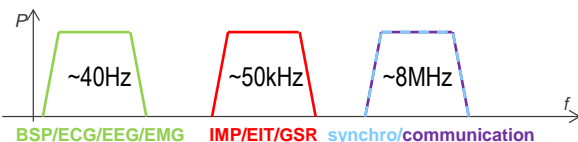


Figure 2: Frequency band for BSP, IMP and communication.

A system-on-chip (SoC) was integrated such that it can be configured as any of the four sensors. It contains two main blocks: communication and sensing. The communication block (see Figure 3) can be configured as either master or slave. In the latter case, a dual-loop clock and data recovery (CDR) block extracts the sampling clock from the incoming data pulses. Otherwise an internal reference clock is used. Note that since the communication pulses share the channel with the 50 kHz

signal used for impedance measurement, a 3rd order high-pass filter was needed before any communication pulses can be detected. In the digital TX part, data whitening is applied prior to Manchester encoding. For every 1000th bit, the start of a new frame is indicated by a violation in the Manchester code ("code break"). Finally the data is pulse-modulated, i.e. data '1' is transformed into a positive pulse followed by a negative pulse. Data '0' is transformed into a negative pulse followed by a positive pulse.

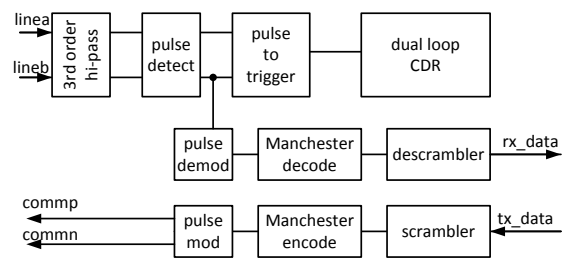


Figure 3: Block diagram communication part.

In the digital RX part, the detected pulses are demodulated, Manchester-decoded and finally descrambled. Code breaks are used to synchronize to the data frame.

The sensing part of the SoC is shown in Figure 4. The BSP measurement chain consists of a pre-amplifier, a passive low-pass filter, an instrumentation amplifier, and an ADC. The closed-loop gain (26 dB to 40 dB) and hi/low pass cutoff frequency (0.67 Hz resp. 40 Hz) of the pre-amplifier are set by external components.

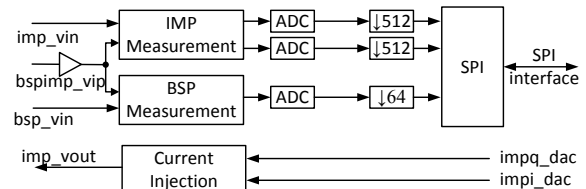


Figure 4: Block diagram sensing part.

The IMP measurement chain consists of a pre-amplifier with filter, a de-modulator, a passive filter, and an ADC. First the in-band signal (49 kHz to 51 kHz) is amplified and out-of-band signals are suppressed. The purpose of the current injection block is to deliver a modulated current in the 50 kHz band. It consists of a modulator, a filter and a voltage-to-current converter by means of an external resistor.

The SoC has been implemented in a $0.18\text{ }\mu\text{m}$ CMOS technology. Samples are expected to be evaluated in the fall of 2016.

Wear-a-Watt—Energy Autonomy for the Wearables

J. Bailat, D. Dominé, M. Crettaz, P. Häfliger, P. Kohler, L. Löfgren, N. Badel, A. Bionaz, L. Zhou, R. Gentsch, P. Liechti, R. Rusconi, N. Blondiaux, G. Cattaneo, L. Sansonnens, L.-E. Perret-Aebi, P.-F. Rüedi, J. Deng, P. Heinstein, S. Nicolay, R. Pugin, M. Dadras, A. Luu-Dinh, R. Ferrini, M. Fretz, J. Kaufmann, M. Correvon, A.-S. Porret, J. Krauss, C. Bosshard, C. Ballif

CSEM is developing ultra-low power solutions and flexible thin-film silicon photovoltaic cells to prepare for tomorrow's autonomous watches and other wearables. The Wear-a-Watt project demonstrator consists of a wristwatch which can measure the instant power produced by the flexible solar cells in the wristband. The evaluation platform and harvested data will be used to develop autonomous applications for the wearables.

No chargers and no wires anymore: The multidisciplinary project Wear-a-Watt builds on the strengths of CSEM in its five research programs to create ultra-low power wearable systems which can live off the energy harvested from their environment without requiring recharging or wiring. The programs involved in this project cover (i) the nano-textured flexible substrate used for the PV cells, (ii) the production and characterization of the PV cells and their optimization for low-illumination conditions, (iii) the development of an ultra-low-power chip for power management and (iv) the engineering of the complete system.

In the first part of the project, lab prototypes were realized to assess the amount of energy available under different illumination conditions (Figure 1). A first watch prototype was then realized (Figure 2). The project's prototype is equipped with a wristband with custom-made flexible solar cells covering a total area of 9 cm² on the watchband. The cells are connected to the measurement circuit through the watchcase. The red hand shows on the dial how much power is harvested by the PV cells in units of milliwatt on a logarithmic scale. Since this harvested energy depends indeed on the habits and the environment of the watch bearers, real life tests 'au porté' are best suited to help estimate the energy that can be collected.

The PV cells are produced onto nano-imprinted flexible polymer foils. These transparent substrates were developed in-house and up-scaled to an area of 300 mm × 300 mm. The thin-film solar cells used in this project are deposited by plasma-enhanced chemical vapour deposition for the active silicon layers and by sputtering for the front and back contacts in CSEM's new cleanroom facilities using processes developed in-house. Shadow masks are used to pattern these flexible solar cells to the required dimensions.

An integration concept for the PV into the wristband has been developed which gives mechanical stability and robustness to the wristband and cell assembly and ensures a good electrical contact of the cells to the contacting lines. The contacting lines transport the current through the watchcase by a watertight feedthrough. Ultra-low power system for energy management and wireless communication has also been designed using in the current stage leading edge commercial off-the-shelf components. The watch can send via the low power communication protocol 'bluetooth low energy' the amount of energy harvested to a smartphone or a tablet for further data analysis.

The resulting PV cells show excellent performance even at low illumination levels. With the first demonstrator, indoor measurements showed that a power of a few tens to hundreds of microwatts is produced. This value can reach to 10 to 15 milliwatts in the sun (indirect exposure). This is considerably more than what can be obtained with mechanical energy harvesting opening therefore new functions.

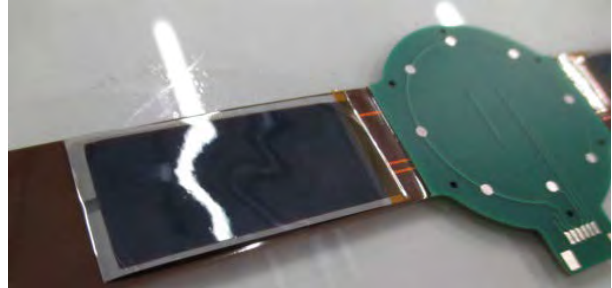


Figure 2: Lab prototype (2015).



Figure 2: Wearable prototype with thin-film PV cells integrated in the wristband (2016). The cells are put on both parts of the plastic wristband and cover an area of 2.0 × 4.5 cm². From indoor to outdoor the light intensity typically varies typically by 3 orders of magnitude which is why the milliwatt units are represented on a logarithmic scale on the watch dial (white and red tick marks) instead of the usual hour ticks.

In parallel, CSEM's IP blocks such as the IcyTRX ultra-low-power RF transceiver, subthreshold microcontroller and a power management unit are developed and integrated.

This wearable test device for the Wear-a-Watt project can accommodate PV cells issued from other PV technologies provided they can fit the required dimensions and tolerances. It can therefore be used to evaluate PV cells from different technologies in real life conditions. Based on the first steps presented here, autonomous systems will further be developed. The applications will target different fields: med-tech, advanced watches, sports watches, and the broader field of the endpoints of the 'internet of things'.

ALS-MEMS Scanner for Assisted Laser Surgery

S. Lani, D. Bayat, Y. Petremand, P.-A. Clerc, M. Amine, S. Ischer, J. Pierer, S. Grossmann, J. Kaufmann, Y.-J. Regamey, E. Onillon, R. Gentsch, P. Heck, S. Pernecker, P.-A. Beuchat

CSEM has developed a new surgical tool prototype based on a high power laser for cutting tissues and/or coagulating, a MEMS deflecting unit and its associated electronics to position the laser spot; and a user interface for controlled trajectory generation.

One way to reduce surgery costs is to reduce surgery time. It can be achieved by different ways: improved preparation, experience or new tools. In this development, a new surgical tool was developed. It relies on a high power laser capable of cutting tissues or bones, as well as performing coagulation of bleeds or local optical treatment. Using laser in surgery presents many advantages like scars size reduction and fast recovery. The main limitation to the application of laser surgery inside the human body is the accuracy of the positioning of the laser beam. So far it is only used in contact mode, hence touching the tissues to be removed. This enables very precise and fine cuts, as seen in the eye surgery.

To achieve laser surgery in non-contact mode, it is necessary to control the position of the laser beam, shined by a fiber tip of a typical size smaller than 1 mm. It is then mandatory to integrate an actuation mechanism and an accurate controller.

The solution proposed in this project aims at realizing an endoscope integrating a high-power laser, a millimeter-scale camera for target observation and positioning control, and a MEMS based steering unit (Figure 1).

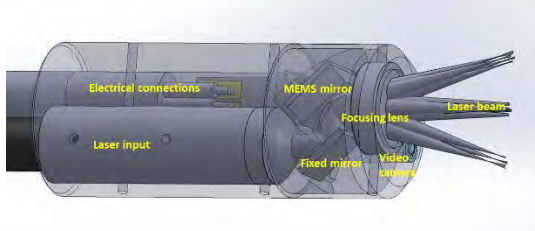


Figure 1: Endoscope head design.

The high power laser has a $3\text{ }\mu\text{m}$ wavelength to ensure a very high absorption by water, the most present molecule in the human body. A second laser at low power and visible wavelength (green), is mounted in parallel for the position control of the invisible high power laser. The associated optics are integrated to obtain a laser spot size on the target of 0.3 mm or 0.8 mm (two optical designs), depending of the field of work of the system, respectively of 2.5 mm or 7 mm. So far, only two low power lasers have been used, as the optics for $3\text{ }\mu\text{m}$ wavelength do not exist and shall be custom made, which is too expensive for this prototyping phase.

The MEMS scanner is used for the fine positioning of the laser beam. It consists of a 2 mm diameter mirror attached to a compliant membrane and based on silicon micro machining (Figure 2). The electromagnetic actuation is achieved by fixing a SmCo micromagnet on the compliant membrane (moving magnet design), while mounting the device on a ceramic PCB containing micro coils. The device is capable of +/-15° 2D mechanical tilting and a z motion of at least 50 μm . The final chip size is $2.5 \times 3 \times 1.8\text{ mm}$. In addition, a second MEMS scanner (Figure 3) was fabricated to evaluate the possibility of adding a focusing system, integrated in the MEMS and based

on microchannel and pneumatic actuation. Theoretically, a focus distance down to 2 mm could be achieved.

The position of the laser beam is controlled using a state-space control algorithm running on a dSpace platform. The position of the main laser is evaluated by measuring the position of the visible laser with a camera (FISBA FISCam™, 2 mm diameter). The algorithm calculates the requested trajectory from the actual position of the laser, and converts it into an output signal feeding the micro coils and hence driving the micromirror.

A prototype of the endoscope head was fabricated (Figure 4) using 3D printing. The optical design was performed with Zemax® software.

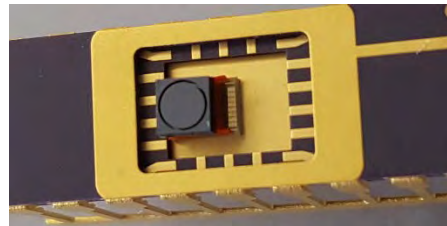


Figure 2: Fabricated MEMS scanner on a ceramic package for performances evaluation.



Figure 3: MEMS scanner with integrated focus.



Figure 4: Endoscope head prototype.

At the current stage, all components have been developed and fabricated. Preliminary results confirm the simulated behavior. The endoscope head is currently under assembly (Figure 4) and tests will follow shortly.

This strategic activity is performed in the frame of a multidivisional research program and CSEM would like to thank the Swiss Confederation for financial support.

GWAPo—Generic Wireless Autonomous Conformable Patch with Display

C. Hennemann, J.-D. Decotignie, B. Perrin, P.-A. Beuchat, Y. Liechti, S. Gray, S. Generelli, D. Migliorelli, J. Disser, N. Glaser, F. Zanella, T. Offermans, N. Marjanović

With the GWAPo platform, CSEM is offering a thin, miniature, flexible, and rechargeable wireless interactive sensor system, i.e. a smart patch. It combines energy sources (e.g. PV/OPV), with pressure and temperature sensors, electronics, displays, interactive components and antennas.

Wearable technologies are proliferating, from smartwatches and activity trackers to hearing aids, virtual reality devices and implantable sensors. While the first wave of wearables borrowed technologies from the mobile industry and was consequently limited to rigid devices such as headsets and smartwatches, the second wave is more focused on technologies for sensors that may be worn almost anywhere on the body [1]. Current technologies are limited, in particular with regards to their wearability and ease of use. Moreover, most of the current products use bulky disposable batteries offering limited autonomy.

To address these challenges, CSEM has developed the generic wireless autonomous conformable patch with display (GWAPo), which consists of an autonomous, flexible and wearable platform with embedded sensors, electronics for computation, display, rechargeable battery and renewable power source (photovoltaic), and wireless connectivity, including the antenna. The main goals of the project are to optimally combine the building blocks, to develop the necessary interconnection techniques and to integrate all components into a single thin "patch". The resulting solution is a disruptive platform for thin, miniature, flexible and rechargeable wireless interactive sensors and actuators that can be placed on body, as well as, on everyday objects or sports equipment.

The current GWAPo prototype patch (Figure 1) is comprised of 3 layers: The electronic layer, incl. pressure and temperature sensors, energy management, processing and communication; the PV cell and display layer; and the flexible battery layer. The electronic layer is optimized for 3D flexibility using flexible PCB technology on which the integrated circuits are placed on "rigidified" tiles in order to reduce the chance of breakage. Several concepts for electrical interconnection have been studied, from conventional to hybrid integration techniques, where sensors and energy harvesters are printed and integrated into the GWAPo thin patch.



Figure 1: Generic and autonomous wireless patch.

[1] IDTechEx 2016

The energy source of the GWAPo prototype can be either a thin film silicon-based PV cell or an organic solar cell (both developed by CSEM). Both energy sources are able to provide typically 150 µW with an active area of 2.5 cm² and under 1000 lux. An ultra-low power processor provides the necessary processing capability for sensor acquisition including user interaction, wireless communication using the CSEM icyTRx radio chip, and display on the low power thin, flexible display.

A thin-film pressure sensor was made with an ultra-soft PDMS layer which was structured by imprinting on Ag-electrode PET-foil using an inkjet printer. Static pressures from 1 mN/cm² up to 400 mN/cm² were recorded. This corresponds to pressures from 0.15 mmHg to about 30 mmHg. The response of the sensor to physiologic pressure levels is linear in the range. A glucose sensor was also adapted with an expanded concentration range from 0.1 mmol to 30 mmol.

The antenna and the pressure sensors were printed on a flexible substrate and integrated with the patch. Figure 2 provides a 3D view of the GWAPo patch before packaging. Then, a specific waterproof coating, extremely robust against tearing and bending, is applied.

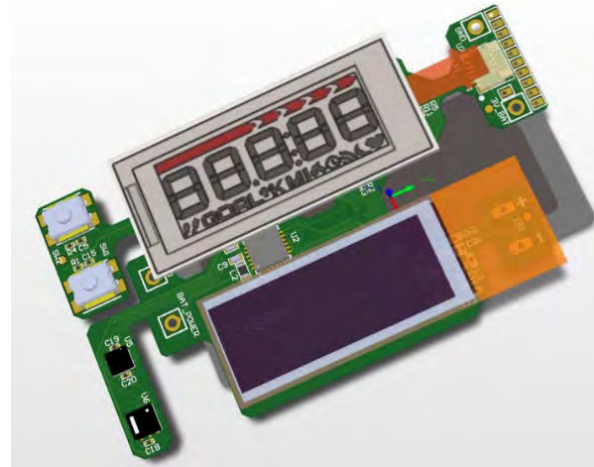


Figure 2: 3D view of the assembled patch.

Flexible and wearable solutions such as GWAPo can support a wide range of applications such as the monitoring of wounds, the direct display of vital signs, and more generally, applications requiring embedded sensing and display. Additionally, the GWAPo platform can actually provide "real-time feedback loops capable of influencing our life style in terms of physical and mental activity, nutrition, hydration, promoting healthy habits and, in general" [2], enabling long-term multi-parameter sensing systems expected by physicians and patients.

[2] A. M. Ionescu, "Smart wearable technology: enabling future prevention-based healthcare", ASA/SVV Medinfo 2(2014) 30

MS-MET—Integrated Inductive Charge Detection Sensor and Analyzer for Mass Spectrometry

D. Schmid, L. Hofer, M. K. Augustyniak, D. Z. Bayat, S. Bitterli, S. Grossmann, A. Hoogerwerf, I. Kjelberg, V. Revol, P.-F. Rüedi, G. Spinola Durante, S. Widmer

Mass spectrometry (MS) is a powerful analytical tool and the market is growing steadily. New components are needed to further push MS towards small, affordable but still powerful instruments. The MicroMS technology developed at CSEM provides nondestructive charge detection means (patent pending) together with a miniaturized standalone setup based on a linear electrostatic ion trap. Small, robust and high resolution instruments could profit from these elements in applications such as space, large molecules and nanoparticle identification, and ion mobility spectrometry.

Today's MS instruments are either powerful (high sensitivity, high resolution), but complex and delicate or small and robust, but lacking high resolution and versatility. Having a small and truly robust analyzer and detectors could be a game changer.

Existing commercial sensors fail to detect charges nondestructively, which would allow for higher mass resolution^[1] or coupled further analysis of the ions, i.e. in sequential tandem-MS and they only work in ultra-low vacuum.

CSEM's MicroMS technology features a nondestructive low-noise charge detection sensor^[2] (patent pending) and a test setup including a miniaturized 8-cm linear electrostatic ion trap^[3], an electron impact storage ion source from Bern University's Space group, a 30 cm vacuum system with turbomolecular pump for fast evacuation (down to 10^{-9} mbar) as well as external data acquisition system (NI PXI) and custom developed data analysis algorithms.

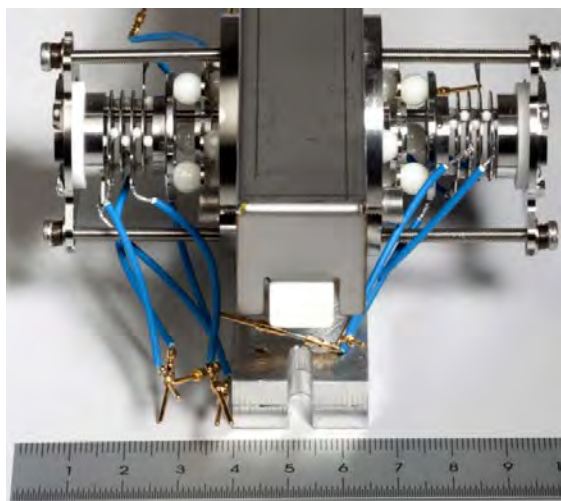


Figure 1: MicroMS linear electrostatic resonator, featuring the charge detection unit in the middle, covered by an electric shield.

The charge detection sensor features multiple independent inductive charge pick-up rings that can sense the mirror charge generated by ions flying through them. Thanks to CSEM's expertise in ultra-low noise charge detection technology, a new integrated sensor could be developed that does not suffer from noise limitations and with a limit of detection as low as 117 e^- , compared to a LoD 3'100 e $^-$ for state-of-the-art solutions^[4].

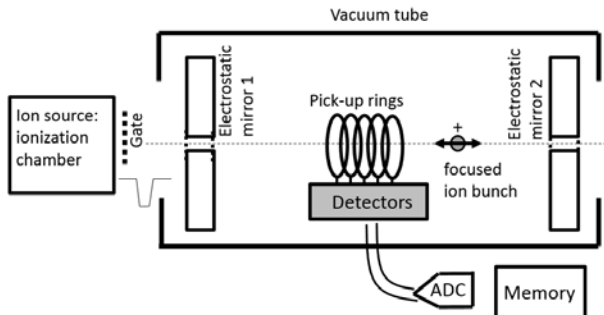


Figure 2: MicroMS linear electrostatic resonator, featuring the charge detection unit in the middle, covered by an electric shield.

Furthermore, the detectors don't need cooling and even work at atmospheric pressure, thus application in ion mobility spectrometers or for large molecules detection with high background gas pressure is possible. The analyzer on the other hand is intrinsically robust and of low complexity and predestined for applications in harsh environment or space.

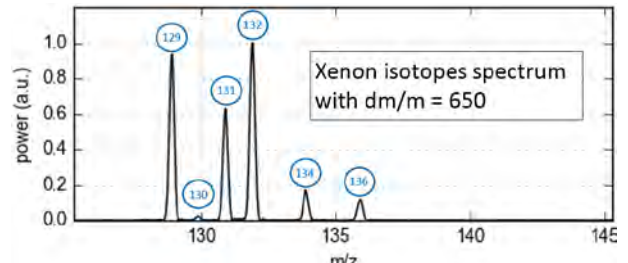


Figure 3: Measurement of Xenon, displaying the natural isotopes.

Feasibility was confirmed with this setup. Current results:

- Characterized with noble gas mixture (Ar, Xe), isotopes resolved
- Mass resolving power: 10^3 m/dm , expected to reach 10^4
- Limit of detection (10^3 extractions): 20 e^-
- Dynamic range: 10^4 , potential to reach 10^6
- Mass range: not restricted (limited only by ion source)

As a next step, the MicroMS technology will be further developed to reach higher sensitivity, and will be characterized with various test environments (different ion sources, combination with GC and/or LC).

[1] D. Zajfman, et al., "High resolution MS using a linear electrostatic ion beam trap", Int. J. Mass. Spec. 229 (2003) 55.
[2] M. K. Augustyniak, et al., "Sensor Interface for a Resonator-type Mass Spectrometer", in this report, page 128.

[3] M. Dahan, et al., "A new type of electrostatic ion trap for storage of fast ion beams", Rev. Sci. Instrum. 69, 1998.
[4] J. D. Alexander, et al., "Determination of absolute ion yields from a MALDI source through calibration of an image-charge detector", Meas. Sci. Technol. 21 (2010).

ECAM—Image Sensor with Stacked a-Si:H Photodiodes

P.-F. Rüedi, P. Heim, J. W. Schüttauf, J. Bailat, G. Spinola Durante, K. Vaideeswaran, M. Dadras

We developed an image sensor with a-Si:H photodiodes stacked over the pixels. It will be used in conjunction with a photocathode in a second phase for ultra-low light imaging. Applications include scientific imaging and night-vision systems.

Image intensifiers are useful for a wide range of applications and markets, including surveillance, medical imaging and scientific imaging such as the rapidly growing field of fluorescence imaging. They are also used in night-vision instruments.

Traditional image intensifier systems combine a photocathode, a micro-channel plate, a phosphorous screen, a light guide and an image sensor. These multiple conversion stages introduce noise and a limited speed and spatial resolution due to the phosphorous screen.

The goal of this project is the development of a vision system for ultra-low light imaging with high photomultiplication gain which is much simpler than the above mentioned approach. The system, illustrated in Figure 1, consists of a vacuum envelope with a transparent front window. A photocathode which is deposited on the inner side of the window converts photons into electrons. These electrons are emitted by the photocathode and accelerated by a potential difference of a few kV directly onto the silicon sensor, which is kept at ground potential. Each electron impinging on the image sensor will generate a large number of electron-hole pairs, leading to a photomultiplier effect. Charges can then be collected by the individual pixels of the image sensor. The photocathode and the image sensor need to be encapsulated in a high vacuum.

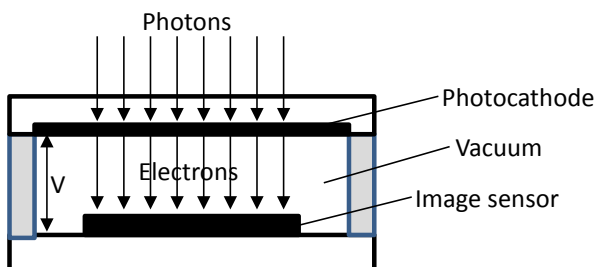


Figure 1: Image sensor module principle.

Whereas passivation and the several micrometer thick oxide are transparent for photons, they would stop electrons, thus preventing them from generating electron-hole pairs. To circumvent this problem, we have deposited on top of unpassivated pixels a layer of amorphous silicon (a-Si:H). In each pixel, the a-Si:H layer is connected to the pixel circuitry through the top metal layer, as illustrated on Figure 2. A layer of ITO (Indium Tin Oxide) deposited on top of the a-Si:H forms a transparent counter electrode.

An existing CSEM image sensor [1] with a pixels pitch of 14 μm has been modified to accommodate the a-Si:H layer. It contains

pixels with Nwell to p substrate photodiodes with a fill factor of 20% and pixels with a-Si:H photodiodes with different metal contacting areas on the same chip for comparison purpose. Two types of junctions have been deposited: i-p and n-i-p.

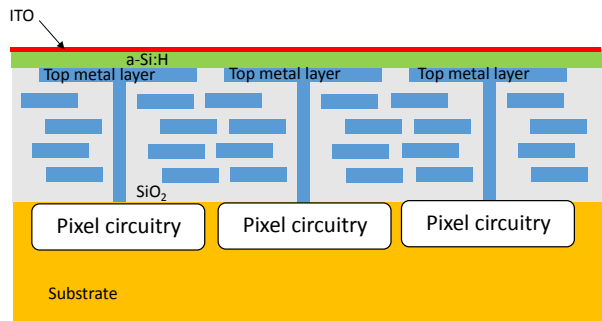


Figure 2: Image sensor module principle.

Figure 3 shows a microphotograph of the chip covered with a-Si:H and ITO. The areas with different metal contacting areas are clearly visible (right part of the pixel array with 3×3 rectangles), as well as the area with photodiodes (left part of the pixel array).

The characterization of the chip should be available in early 2017.

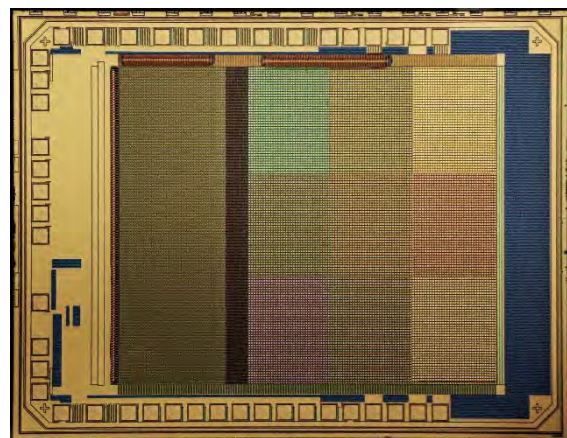


Figure 3: Microphotograph of the chip.

In addition to image intensifiers, the proposed approach can also be used for electron imaging, such as vacuum imaging of particles, electron microscopy, beam imaging and X-ray applications. It also offers benefits for standard visible light imaging. Depositing photodiodes on top of the read-out ASIC enables close to a 100% fill factor, while freeing space in the pixel for more electronics as there is no photodiode any more in the pixel.

[1] P. Heim, F. Kaess, P.-F. Rüedi, "High dynamic range versatile front-end for vision systems", CSEM Scientific and Technical Report (2007) 25.

SMAC3P—Assembly and Functional Tests of a Flat Form Factor Miniature Atomic Clock

L. Balet, J. Haesler, S. Karlen, S. Dasen, J.-A. Porchet, S. Lopera, T. Overstolz, B. Gallinet, D. Ruffieux, M. Lützelschwab, S. Lecomte

The preliminary building blocks of a miniature atomic clock (MAC) physics package (PP) with a height of less than 5 mm were presented in the past years. CSEM presents in this paper the manufacturing and functional testing of the main MAC constituents.

It has been shown previously that a height of less than 5 mm for the physics package is requested in order to integrate a MAC in portable devices. Such a flat packaging is made possible by a planar arrangement of the individual components (cell, laser, and detector) with an optical connection by a planar multimode waveguide (patent pending).

The atomic vapor cell (Figure 1) is the core component of the MAC. Loading it with rubidium is obtained by a proprietary process based on RbN_3 solution dispensing and UV-decomposition. The cell lifetime and intrinsic frequency drift could be drastically improved thanks to protective coatings.

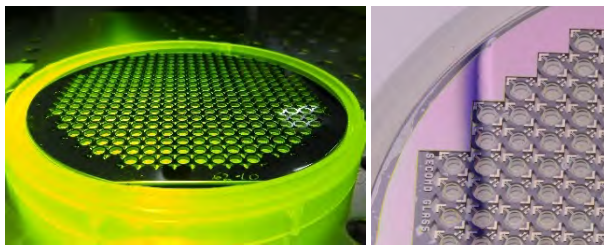


Figure 1: Wafer of 332 cavities (left) and functionalized cells (right).

Light coupling from the laser to the atomic cell and to the photodetector is realized by a planar waveguide ($11 \times 14 \text{ mm}$) with three in- and out-coupling diffraction gratings (Figure 2). The fabrication process has been optimized in order to fulfill the requested yield and overall light transmission efficiency.



Figure 2: Planar waveguides with three diffractive gratings each.

The different MAC components are packaged thanks to low temperature co-fired ceramics (LTCC) fabricated at CSEM Brazil, offering smart assembly solutions, 3D electrical routing, low thermal conductivity and vacuum compatibility. The LTCC cavity is obtained by co-firing more than 20 LTCC tapes with a final top waviness lower than $20 \mu\text{m}$ (Figure 3).



Figure 3: (Left) LTCC cavity (blue) and thermal holder (white); (right) Bottom of LTCC cavity with ball grid array (BGA) pads.

Vacuum encapsulation of the physics package remains one of the biggest challenges to be solved for the MAC to meet the low-power (minimal thermal losses) requirements. Different sealing approaches have been evaluated and preliminary vacuum encapsulation tests are ongoing (Figure 4).

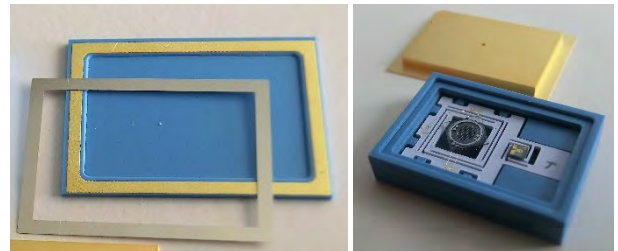


Figure 4: Sealing test samples (left); LTCC cavity and cap (right).

Driving the atomic clock is realized by a newly designed ASIC (Figure 5), offering highly improved frequency lock-in and temperature sensing capabilities, which are currently being tested and validated with representative MAC prototypes.

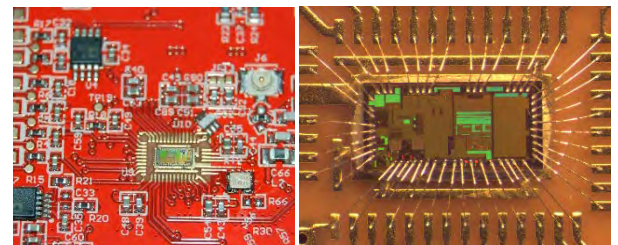


Figure 5: Test PCB (left) and ASIC micrograph (right).

Functional testing of the MAC will be made on a test PCB platform equipped with a dedicated MAC PP socket (Figure 6). Driving the PCB and the ASIC is realized by a micro-controller with a LabVIEW® interface.

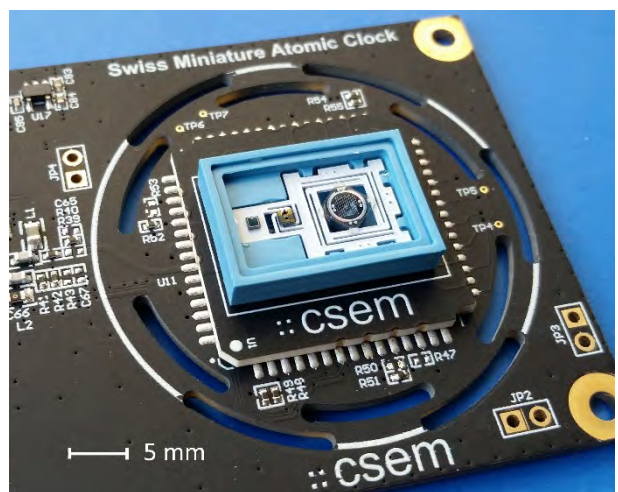


Figure 6: Test PCB platform with a dedicated socket for the MAC PP.

Parallel and complementary developments for a ceramic based MAC prototype are being conducted in collaboration with the European Space Agency (ESA) and VTT in Finland.

muTish—Tools to Monitor and Handle Medium Sized Biological Entities

S. F. Graf, N. Schmid, R. Limacher, C. Beyer, I. Kastanis, D. Bösel, C. Hofer, S. Cattaneo, S. Generelli, L. Barbe, D. Migliorelli, D. Caminada, N. Glaser, F. Schleiss, M. Schnieper, H. F. Knapp, P. Steiert, M. Krieger, H. Heinzelmann

A cell sorter and SmartPlate are being developed to monitor and handle medium sized biological entities, such as 3D human tissue models or cell clusters to fill gaps in high throughput screening for drug development and toxicity testing. The spheroid entities in a size range of 50 to 800 μm can be characterized on-the-fly by real-time imaging, fluorescence detection and multi-frequency impedance analysis and be dispensed into multi-well plates, such as the SmartPlate where the solution in which the biological entities are dispensed is monitored for pH, glucose and lactate levels as indicator for the ongoing metabolism.

Artificial microtissues or 3D cell clusters can be used as models for replacing, reducing and refining animal testings in drug development and toxicology. However, tools for reproducible and automated handling of such biological samples are hardly available, or are very expensive. Thus, CSEM combined its expertise in fluidics, optics, sensor systems, machine learning, printed electronics, and electro chemistry, to develop new tools to monitor and handle medium sized biological samples under the umbrella of the CSEM CellFactor-technology^[1]. A cell sorter is being developed which analyzes unlabeled samples using imaging or impedance analysis while tagged entities can be observed by fluorescence. Samples of interest can be individually dispensed into a multi-well plate. Furthermore, printed electrochemical sensor are being integrated into a multi-well plate creating the SmartPlate. The SmartPlate records pH, glucose and lactate levels in solution in order to monitor the metabolism of the samples over a long period of time for quality control.

Within the cell sorter, samples with a size range of 50 to 800 μm are moved by a pressurized sample container. An additional sheath flow is used to center and align the samples for the detectors, where samples of interested can be dispensed into a multi-well plate by a short cross flow. Remaining samples are moved towards a second sample container.



Figure 1: Detection/sorting unit of the cell sorter where fluorescence detection and imaging take place.

The built-in detectors are aligned along the sample path within the flow cell (see Figure 1) and use

- High-speed image analysis processed on a GPU (graphical processing unit)
- Fluorescence detection in combination with a lock-in amplifier (see Figure 2)
- Dual-frequency impedance analysis in combination with a lock-in amplifier



Figure 2: Fluorescence module with optical setup and electronic board with integrated digital lock-in amplifier.

The SmartPlate (see Figure 3) uses printed electrodes with conductive vias to monitor the samples in the well and read out the signals. The electrodes are biochemically modified with stable functional layers sensitive to pH, glucose and lactate.



Figure 3: 24-well SmartPlate with printed and biochemically modified electrodes on the inside of the well contacted through conductive vias towards the outside to measure pH, glucose and lactate levels.

The technologies described were designed in close contact with our lead users hepia and fGen which work with neurospheres and alginate beads, respectively.

CSEM would like to thank the Swiss Federation and the M CCS Micro Center Central Switzerland for their financial support and hepia as well as fGen for their technical inputs.

^[1] S. F. Graf, et al., "Table-top classification and sorting system for small model organisms", in this report, page 54.

HybSi—High-precision Mechanisms at the Centimeter Scale based on Silicon Hybridization

F. Barrot, F. Cosandier, G. Musy, J. Kruis, S. Droz, L. Giriens, W. Glettig, S. Lani, M. Liley, Y. Petremand, A. Bionaz, P.-A. Clerc, M. Amine, S. Ischer, R. Smajda, G. Voirin, E. Scolan, P. Niedermann, M. Despont, M. Dadras, G. Andreatta

High-precision mechanisms at the centimeter scale can greatly benefit from the high-precision micro-structuration of silicon and its good mechanical properties. This approach opens up new opportunities for key Swiss industries such as the watch and scientific instrumentation industry. However, the handling and assembly of silicon is a challenge due to its brittleness. Combining its expertise in the domains of precision mechanisms and micro-manufacturing techniques, CSEM is taking up the challenge to become the Swiss competence center for the design, manufacturing, assembly and characterization processes of hybrid silicon-based mechanisms.

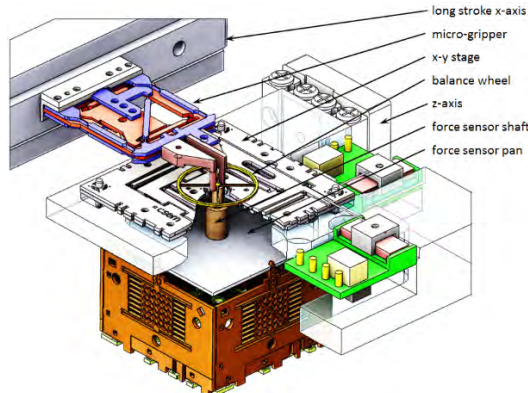


Figure 1: Silicon-based micro-platform targeted for the assembly and characterization of MacroMEMS.

Inherited from the micro-electronics sector, the batch micro-structuring of silicon enables the design and production of mechanical parts with a micrometric precision at the centimeter scale. At a scale between MEMS and classical mechatronics, this approach, referred to as MacroMEMS, can be used for the design of precision mechanisms targeted for different industrial fields such as the watch industry (new watch mechanisms) or scientific instrumentation (micro-gripper, precision XY tables, precision force sensor). Figure 1 shows a silicon-based platform that can be used for micro-assembly and characterization of such systems; the platform itself is a combination of three different silicon based mechanisms designed and produced at CSEM^[1].

To enhance the functionalities of MacroMEMS parts, overcome the 2D structuring limitations of silicon processing and propose a cost effective alternative to wafer level assembly (Si/Si, Si/metal), CSEM believes that precise 3D printing on silicon is a promising approach (Figure 2) that can open up novel business opportunities. Following this approach mechanical, electrical, optical and fluidic interfaces can be designed and added to silicon parts; these functionalities can even be mixed together, offering a high level of integration.

Some tests have been conducted with different materials and adhesion promoters. A microfluidic demonstrator combining 3D printed microfluidic channels, 3D printed seals and 3D printed mechanical interfaces (including precise positioning and assembly functions) with a high-precision silicon-based micro-

filter^[2] and the use of a micro-pump^[3] has been designed and produced (Figures 3 and 4).

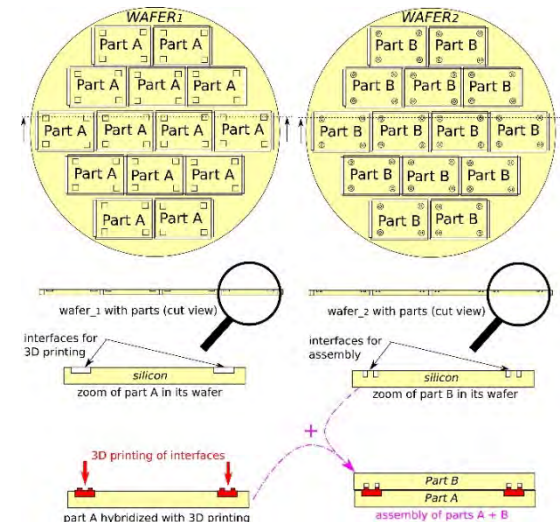


Figure 2: Interfacing and assembly of two silicon parts using precise 3D printing on silicon.

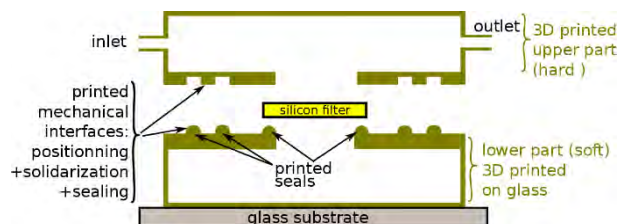


Figure 3: Precisely 3D printed parts comprising mechanical, fluidic and sealing functions, combined with a high-precision silicon filter.

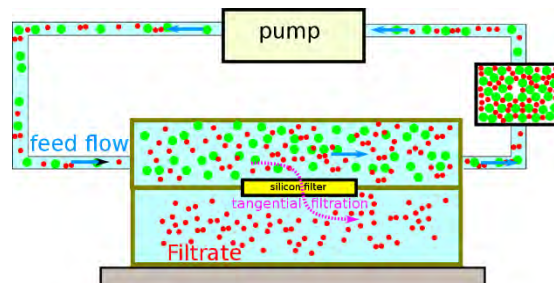


Figure 4: Working principle of the micro-fluidic filtering system.

[1] F. Cosandier, et al., "A three device silicon based platform for micro-assembly and characterization", EUSPEN 2016.

[2] R. Pugin, et al., "IPoSiM – Integrated Porous Silicon Membranes", CSEM Scientific and Technical Report (2013), 20.

[3] J. Goldowsky, et al., "Turbisc Pump with an Integrated Flowsensor for Closed-loop Operation", CSEM Scientific and Technical Report (2014), 112.

TeraXplore—Single Detector for Multi-color Terahertz (THz) Imaging

E. Le Roux, O. Vorobyov, C. Beyer, V. Revol, G. Voyrin, J. Levrat, A. Bischof

Active multi-color Terahertz (THz) imaging technology has a very large potential for inspection of composite materials. In this project the possibilities of the THz technology were explored on a test setup using off-the-shelf THz source and detectors. Furthermore, a single pixel detector was implemented in 0.18 μm CMOS technology.

THz imaging technology is becoming more and more important in non-destructive material inspection and quality control as it has advantages over other technologies like microwave, infrared, or x-ray. It provides good sensitivity, penetrates electrically non-conductive materials, is safe to use and at the same time can provide spectral information. Multispectral THz imaging can reveal features that are not present in a monochromatic image. This technology has the potential to cover a wide range of applications:

- Analysis of chemicals in powder and tablet form
- Investigation of moisture distributions
- Distinguishing crystalline and amorphous structures
- Determining the layer thicknesses of multi-layer systems
- Detection of food contaminants or foul products
- Medical diagnosis (e.g. detection of skin cancer)
- Identifying flaws and cavities in non-conductive components

Although THz imaging has demonstrated its potential for non-destructive inspection in previous academic work [1], the application is limited due to the lack of multi-color pixel array detector. In the course of the MIP project TeraXplore, a single THz detector was developed based on the “direct detection method”, i.e. the detector consist of an antenna and a (CMOS based) RF receiver (see Figure 1). The antenna and rectifier were integrated in a test chip, the readout was implemented with discrete components.

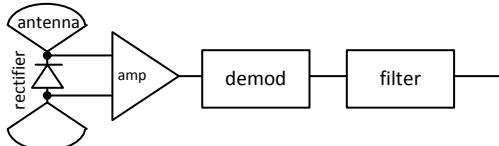


Figure 1: Detector architecture.

Due to the lack of devices for operation up to 500 GHz, dedicated rectifiers have been developed. The following options were considered: Shallow-Trench-Separated (STS) Schottky diode, Poly-Gate-Separated (PGS) Schottky diode and diode-connected MOS transistor of different sizes. The only way to verify the performance is through measurements, thus all these options were implemented on the test chip.

Two different types of antennas were designed (see Figure 2). The patch antenna can be integrated directly using the chip’s metallization layers, which leads to a very short connection to the rectifier. However as the maximum thickness of the dielectric is limited to 6 μm , it results in a very narrow band antenna. In order to be able to support multi-spectral imaging a dedicated antenna tuned to each center frequency is needed. In the current implementation, the supported frequencies are 375 GHz, 425 GHz and 475 GHz. The test chip has been implemented in a 0.18 μm CMOS technology. Samples are expected to be evaluated in the fall of 2016.

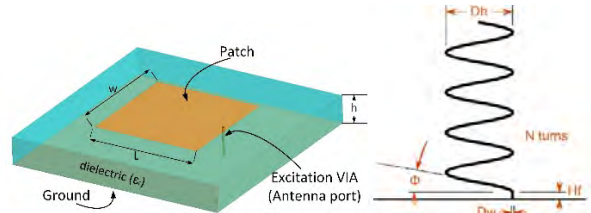


Figure 2: Patch antenna (left) and helix antenna (right).

In addition, an off-chip helix antenna was designed, which can support the entire frequency range from 300 GHz to 500 GHz. Prototyping was done using 3D printing technology. This can be done by either metal printing directly on the outside of a cylinder, or by wrapping a 70 μm wire around a 3D-printed cylinder (see Figure 3)

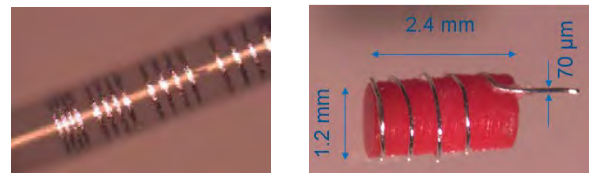


Figure 3: 3D printed antennas.

For the connection of the antenna, the best option found is to deposit gold directly on the chip using aerosol jet, place the helix antenna and then cure it at 200°C. In addition the helix plastic part of the helix antenna is fixed with glue.

In parallel to the detector development, a test setup was built based on off-the-shelf components, which allowed to evaluate the potential of multi-color THz imaging technology for inspection of composite materials and photovoltaic cells. Detailed results are expected this fall.

[1] C. Stoik, "Non-destructive evaluation of aircraft composites using terahertz time domain spectroscopy", PhD thesis, Air Force Institute of Technology (2008).

MICROSYSTEMS

Michel Despont

Today, MEMS technology is used almost everywhere in devices that sense and monitor our environment and help us in many aspects of our daily lives. It is used to fabricate a large variety of devices, and has attained a market size of USD 10 billion. As an example of how MEMS technology has penetrated our daily activities, today's cars can make use of over 30 different devices based on MEMS-related technology for monitoring and controlling engine functions, safety, navigation, and passenger comfort. Similar trends can be seen in portable devices such as smartphones, the most recent models containing a dozen MEMS-based sensors. Global technology trends like the Internet of Things (IoT) require the more and more massive use of connected sensors and promise large new markets for MEMS technologies, including in building automation, healthcare and the life sciences, consumer goods and home automation, transportation, industrial and environmental monitoring, security, and retail and logistics. All of these applications are looking for autonomous, low-power, small-form-factor, low-cost sensor and actuator devices and thus find MEMS technology very attractive.

MEMS processes are often derived from those used in the fabrication of microelectronic circuits, so one could be forgiven for thinking that MEMS-based devices can be manufactured using low-cost, high-volume fabrication techniques similar to those achieved for CMOS technology thanks to process standardization. However, in reality, the development and fabrication of different types of MEMS often requires a broad spectrum of processes that is much more diverse than that used in microelectronics. On one hand, this is due to the extreme variety of physical effects used in MEMS devices, which means that a specific set of processes and materials is required for each type of device. On the other, the market is highly fragmented, with large differences in requirements regarding cost, time to market, form factor, operating environment, and performance. It is therefore extremely difficult to have a common technology platform for all types of MEMS devices, and customized MEMS and related packaging technologies are often developed for each specific application. Moreover, as MEMS devices can have mechanically or chemically functional structures and are exposed to their environment—which is often harsh—reliability and lifetime need particular care.

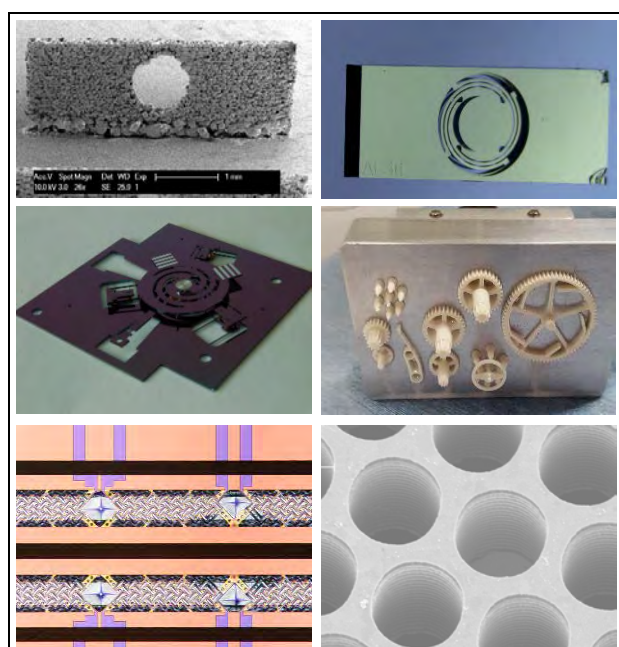
Swiss industry—in particular SMEs—has recognized the potential of integrating MEMS into its products, as such integration acts as a strong differentiator, and many SMEs are global leaders in niche markets. For these companies, it is crucial to fill the pipeline of innovation from fundamental research to the industrialization of new technologies so that they are able to continue to offer innovative products based on MEMS technology. CSEM has a track record in bringing MEMS and packaging technologies to market and is uniquely positioned to be an essential partner in the drive to bring ideas to market for many Swiss high-tech SMEs active in MEMS. Moreover, CSEM is intensifying its pursuit of cross-disciplinary solutions, using the demand from the fields of nanotechnology,

bioscience, and materials science to drive innovation in MEMS and to make new devices and microsystems possible.

Looking back a few years, the MEMS program was concentrating mainly on the elaboration of micro-parts for mechanical watches and integrated optoelectronic devices. Although these topics are of great importance to Swiss industry, the spectrum of technologies being developed within the program must address a broader field of applications. Over the last few years the program has thus taken several new initiatives in order to diversify into new application fields, including instrumentation, aerospace, and medical devices, all of which reflect the strength of the Swiss industrial ecosystem.

MEMS at CSEM is focused on:

- 1) Innovating for mechanical watches at the cross-over between high-performance materials, advanced manufacturing, and innovative design.
- 2) Excelling in microsystem technology for harsh environments, for a broad range of applications ranging from medical to aerospace.
- 3) Developing key technologies in the field of infrared sensing and imaging.
- 4) Enhancing the technology portfolio in optical MEMS and optoelectronic device assembly.
- 5) Integrating soft materials into microsystems, thus employing a better interface for applications in medtech and biology.



A selection of developments pursued at CSEM in the Design & Process activity. From upper-left to lower-right: metal-based additive manufacturing on silicon, a 2-D micro-mirror for endoscopic applications (laser surgery), a MEMS UV laser pointing mirror for atmosphere monitoring, 3-D printed ceramic composite mechanical microcomponents, a TCD device for MEMS-based gas chromatography, and a plasmonic structure for an IR filter.

Long-term objectives

The global objective of the MEMS program is to establish MEMS device microfabrication and packaging technologies for CSEM's partners and to offer to Swiss and international industries a full product-development platform from feasibility demonstration of new device ideas to industrialized, qualified fabrication processes including the production of mature devices in small volumes. Therefore, the activities of this program are aimed at continuing to excel and to build up new competences in MEMS technology—in particular for application fields such as watch technologies, scientific instrumentation, optoelectronics, and medical device technology—with a strong focus on packaging, reliability, and cost reduction for demanding applications.

To address the demand for MEMS technology, the program comprises two main activities: (1) *Design & Process* and (2) *Integration & Packaging*.

The *Design & Process* activity deals with the development and industrialization of specific MEMS in a wide spectrum of applications. The global objective of this activity is to maintain a state-of-the-art platform capable of developing and fabricating reliable MEMS products, from prototypes to small volume production or technology transfer. This platform, at the service of Swiss SMEs and industries, consists of a fully equipped MEMS fabrication clean room, a reliability laboratory, and an R&D infrastructure focusing on the pursuit of advanced and novel MEMS-based devices. Today, development is underway in the fields of watches and timekeeping, instrumentation and aerospace, and health, biotech, and lifestyle. These are domains in which Swiss industry is highly successful at a global level and which have a large impact on the Swiss economy.

For industrial applications, reliability is of the utmost importance and CSEM's reliability and microstructure characterization capabilities are a powerful tool for supporting process development aiming at eliminating defect- and stress-generated failure modes and performance limitations. The continuous improvement and systematic documentation of development and production process flows within ISO-9001 ensures the successful exploitation of the technology platforms developed. This enables a systematic approach to MEMS development from feasibility demonstration, via prototyping, to industrialization.

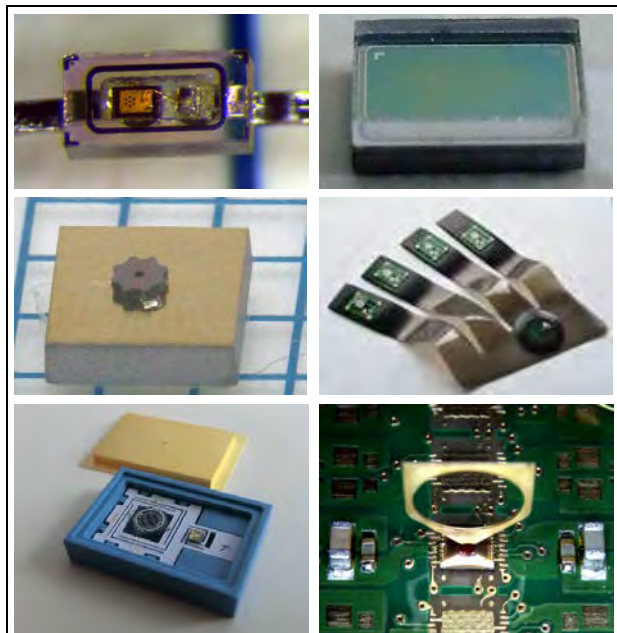
The *Integration & Packaging* activity focuses on (i) the development of new integration platforms for CSEM's customers, and (ii) the realization of new products based on these platforms. The chosen approach allows CSEM to serve a large number of customers in different application fields and markets. Its primary objectives are the integration of active MEMS dies, sensors, and actuators into prototype systems and products for different applications and markets. The activity addresses today's global packaging challenges in sensor platforms for medical and environmental monitoring, integration of measurement solutions for harsh environments, and optoelectronics. The integration of microsystems continues to be a key element of many future high technology application areas. Hybrid integration technologies—from embedded silicon in polymer to M(O)EMS—find broad uses in markets such as healthcare and energy. Combined with hermetic sealing and

embedded self-testing, they open up additional applications for sensors in harsh environments, such as in the medical field. In addition, miniaturization in optoelectronics continues to be an innovation driver, from devices to architecture.

The valorization of the MEMS program is leveraged through CSEM's multidisciplinary capabilities and system approach and is naturally strongly linked to the research programs Systems (novel mechanical watch mechanisms, precision mechanics, or miniature atomic clocks), Ultra-Low-Power Integrated Systems (ASICs), and Surface Engineering (chemical and biosensors). This adds unique value as all aspects of a system can be included early in its development.

Highlights

Today's *infrared (IR) filters* are Bragg lattices of dielectric materials. These devices have proved to be expensive and have several drawbacks, such as angular dependence, bulkiness, and incompatibility with array arrangement. An array arrangement is a key requirement for hyperspectral imaging. At CSEM, we have developed a new type of Fabry-Pérot IR filter using MEMS technology. Mirrors are made of metal films integrated onto a silicon microporous membrane. Our characterization has shown superior optical fineness and improved transmission as compared to commercially available filters. Moreover, the technology has the potential to significantly reduce costs, to be less angle dependent, and to be suitable for array configuration. The last of these is achieved by the fact that the wavelength to be filtered is defined by the geometrical design of the membrane's micro-porosity, enabling each membrane to have a different geometry resulting in each filter having a different absorption spectrum.



A selection of developments pursued at CSEM in the *Integration & Packaging* activity. From upper-left to lower-right: long-term-implantable laser source for a cochlear implant, low-temperature hermetic sealing ($<100^{\circ}\text{C}$) of glass to silicon, nano-foils-based microjoining, integration of a tactile module on a "soft-skin", LTCC-based package of a miniaturized atomic clock, and microassembly of MEMS-based ion pickup electrodes on CMOS.

Miniature atomic clocks providing high accuracy at small size ($<1 \text{ cm}^3$) and low-power consumption ($<100 \text{ mW}$) have generated increased interest for applications in handheld communication and navigation devices. At CSEM, we developed a MEMS-based rubidium vapor cell for atomic clock applications that is suitable for low-cost batch fabrication. The stability and lifetime of such a device depends inherently on the control of the gas mixture inside the cell. Hence, hermeticity and the absence of gas diffusion through the material that forms the cell are both key. We have developed a sealing technology and a thin film serving as a chemical diffusion barrier that improves the stability and the lifetime of the cells by orders of magnitude. With this development we achieve a lifetime expected to be in the range of 10 to 20 years (@ 100°C) and a frequency drift $\leq 10^{-11}/\text{day}$. This is the first time that a MEMS-based atomic clock matches industrial specifications.

Helping to create economic value through the creation of start-ups is also part of CSEM's mission. Recently, the *start-up SIMPLInext was founded* to commercialize novel, thin, microporous, silicon nitride membrane, multi-well inserts as cell culture supports for in vitro cell biology, pharmacology, and toxicology. SIMPLInext is positioning its products for in vitro testing, which is a fast-growing field given the implementation of more and more stringent government regulations in the field of animal testing. The development of this MEMS-based disruptive technology and the preliminary validations—which are the very foundation of the start-up—took place at CSEM.

A MEMS-based Gas Chromatograph Front-end for a Miniature Spectrometer

A. Hoogerwerf, G. Spinola Durante, E. Scolan

We have made all the key components of a miniature gas chromatograph: the pre-concentrators, different gas separation columns and detectors. All components have been designed for low temperature die-to-die assembly and connections to conventional GC tubing have also been included. The development is one step forwards to truly portable gas analysis instruments.

The miniaturization of gas chromatographs (GC) has many advantages, amongst which the reduction of power needed to heat the system and the reduction of the carrier gas consumption. We have developed a GC that will function as a front end for a mass spectrometer for space applications. The results of the project can also be used towards the portable gas analysis systems.

The schematic diagram of the GC is shown in Figure 1. The dashed structures in this figure are the MEMS components, the blue lines below a device indicate that it can be cooled, and the red ones, heated. The sample gas is drawn into the cooled pre-concentrator by a vacuum where it is adsorbed. Once sufficient material has been adsorbed, the sample gas and vacuum valves are closed and a carrier gas is led to the pre-concentrator and into the column. The temperature in the pre-concentrator is abruptly increased to obtain a sharp desorption peak of the sample material into the column, where it is separated. The separated sample is then analyzed by a Thermal Conductivity Detector (TCD) that compares its conductivity with that of a reference gas. The reference gas is the carrier gas whose flow has been reduced by a flow restrictor to the same level as the gas that elutes from the long gas column.

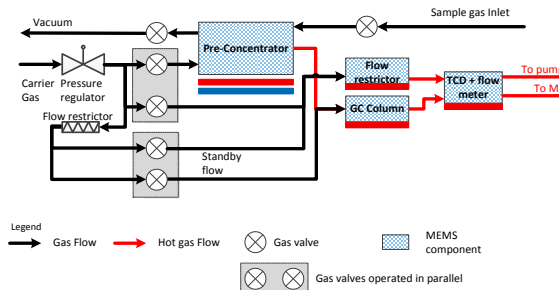


Figure 1: Schematic diagram of a gas chromatograph.

The pre-concentrator is a small cavity made of silicon and glass with metallic feedthroughs. The metallic feedthroughs connect to silicon pillars in the cavity which can be heated resistively to create a sharp desorption peak. The entire pre-concentrator will be mounted on a thermo-electric cooler to lower its temperature during the adsorption phase. The cavity of the pre-concentrator is filled with a commercial Tenax® absorbent.

The column consists of a silicon-glass sandwich, with a long serpentine channel dry etched into the silicon. The dimensions of the channel are 100 µm width, 250 µm depth and up to 4 m length, which is similar to the smallest commercial columns. The cross-section of the channel is rectangular, which presents a challenge for the deposition of the stationary phase. The thickness of stationary phase must be uniform, since thickness variations of the stationary phase result in variations of the time substances are retained. This retention time variation results in peak broadening, making it more difficult to separate different species passing through the column. Recently developed techniques like Atomic Layer Deposition (ALD) and Molecular

Vapor Deposition (MVD) are very suitable for the deposition of uniform layers in structures with extreme aspect ratios and have been used to deposit both aluminum oxide and a silane monolayer on the surfaces of column channels.

The TCD consists of a total of ten resistors, suspended over two independent flow channels. This allows the TCD to measure differentially between a reference flow and a separated sample flow. Two resistors in each channel allow the connection of the resistors in a Wheatstone bridge. The three additional resistors in each channel allow the measurement of the flow using a differential heat measurement. Each resistor is defined in a platinum layer sandwiched between two isolating LPCVD silicon nitride layers.

An especially challenging task of the project has been the development of fluidic connections to the external world and between the different devices of the GC. The column can be heated up to 330°C, a temperature that the fluidic connections must be able to handle. At the same time, some of the column coatings cannot withstand temperatures over 250°C, limiting the bonding temperatures. The selected method has been the Au-Sn liquid phase soldering of miniature tubes to specially made gold coated silicon structures. Once this solder has molten at approximately 280°C, it absorbs the gold on the silicon structures, increasing its melting temperature to over 350°C. All silicon structures are gold coated and are connected using thermocompression bonding at temperatures under 250°C. The bonded gold is a noble metal that will not interact with the sample gases and the thermocompression bond yields a hermetically sealed connection between the two wafers.

All GC components have been successfully fabricated and are now being tested for their chemical performances prior to a complete assembly.

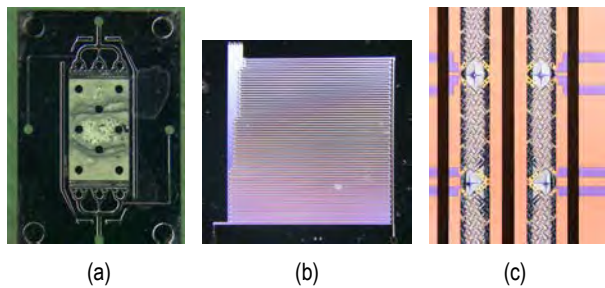


Figure 2: Pictures of the different components of the GC: (a) the pre-concentrator, (b) the column, and (c) the TCD.

This work has been funded by ESA contract AO/1-7381/NR-01.

A MEMS UV Laser Pointing Mirror for Atmosphere Monitoring

A. Hoogerwerf, D. Z. Bayat, B. Timotijevic, V. Revol, T. Burch

A MEMS mechanism is being developed that allows a tip-tilt, large angle (+/- 15° optical), actuation of a ultra-violet laser mirror. The aim of the development is a scientific space mission, but the design can be used for other applications that need a steerable mirror for the pointing of a high energy laser beam.

The goal of the Extreme Universe Space Observatory (EUSO), to be installed on the International Space Station (ISS), is to detect about 10^3 Ultra-High Energy Cosmic Ray (UHECR) "events" and produce, for the first time, a large signal statistical all-sky map of the distribution of the arrival directions of the highest energy cosmic rays with angular resolution close to 1 degree. EUSO^[1] will use the Earth's atmosphere as a calorimeter particle physics detector, measuring the ultraviolet fluorescence produced by the air molecules excited by the UHECR induced extensive air shower (EAS). The EUSO ultraviolet telescope has an aperture of 2.5 m, a field of view of 60°, and will be operating in the 300-400 nm wavelength range.

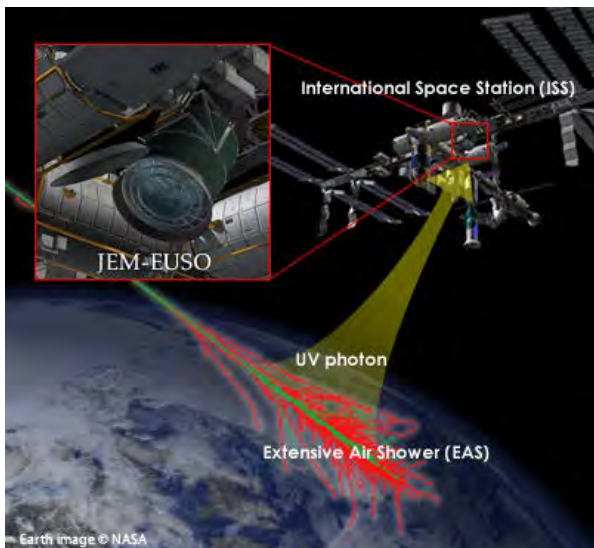


Figure 1: The EUSO concept.

EUSO will be equipped with a dedicated Atmospheric Monitoring (AM) system consisting of an infrared camera and a Light Detection And Ranging (LIDAR) device, since the intensity of the UV light is strongly affected by the transmittance and scattering characteristics of the atmosphere around the shower. The LIDAR is composed of a transmitting and a receiving system. The transmission system comprises a Nd:YAG laser, whose the third harmonic wavelength at 355 nm is used and a pointing system to steer the laser beam in the direction of the triggered EAS events. The receiver of the laser backscattered signal will be the EUSO telescope.

The pointing system of the LIDAR consists of a 3.5 mm diameter quartz UV mirror with an optical aperture of 3 mm, sandwiched between two silicon MEMS structures. The minimum size of the mirror is determined by its ability to withstand the high energy pulses of the UV laser. The silicon structures, consisting of planar springs, form together with the

mirror a steering mechanism. Actuating the mechanism in the X- and Y directions by two voice coils generates a tip-tilt movement of the mirror. The mirror can be oriented in two directions with a +/- 15 degree angle. The angle will be measured for a precise closed loop control feedback.

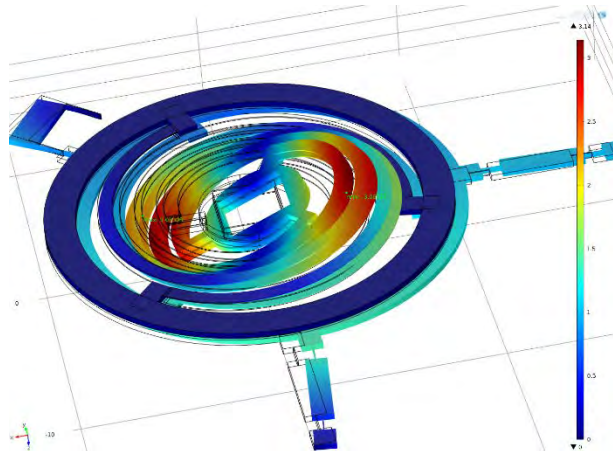


Figure 2: The deformation of the silicon mechanism that converts a linear actuation in a tilting movement of the mirror.

A full-scale functional model of the mechanism has been fabricated and assembled, with the primary goal to verify the functional parameters of the device to compare them with the simulation results. The manufacturability of the device could be demonstrated and a first model could be assembled with glue. The current focus of the fabrication is on the assembly of the device with pressure fittings for space requirements compatibility.

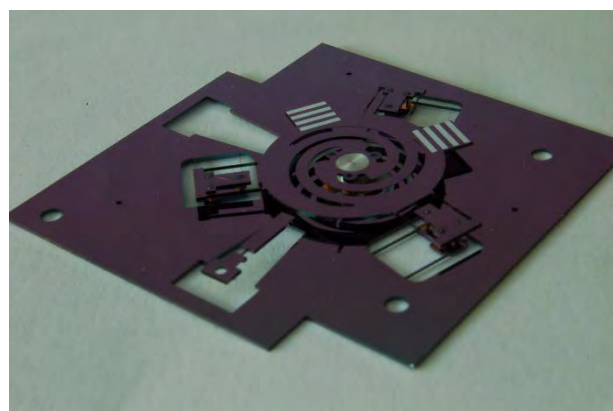


Figure 3: Functional model assembled from precision silicon mechanical parts.

The work has been funded by the Swiss Space Office under the PRODEX programme.

[1] J. H. Adams.,et al., "The JEM-EUSO mission: An introduction", <http://adsabs.harvard.edu/abs/2015ExA....40....3A>.

3D Printing for Advanced Manufacturing

S. Lani, A. Bionaz

The 3D printing technology called UV stereo-lithography (SLA) has been evaluated for the realization of high precision prototypes and for the hybridization of material and fabrication technology. The aim is to form unique components with a high level of complexity and create new opportunities of development. This technology offers a new methodology of product development by enabling a rapid assessment of the feasibility of a design.

Additive manufacturing, also known as 3D printing, is the method of fabricating an object by adding only the material needed, without using a mold or a mask. Several countries are currently massively investigating the development of the different 3D printing techniques, estimated to a total higher than 30. In 2013, President Obama said that "3D printing [...] has the potential to revolutionize the way we make almost everything". It is certainly very optimistic to say that it will replace any fabrication technology so far, but 3D printing is already changing the way we do R&D and prototyping. And it will move forward to the way we develop products. Even if CSEM cannot compete on the development of 3D printing systems with centers receiving funding of several tens of millions dollars, it can still be very efficient in niche markets with high added value components.

For several years, CSEM has been investigating the application of 3D printing to silicon based microfabrication. The objective is not only the hybridization of material but also the combination of fabrication technologies like semiconductor or MEMS microfabrication, glass structuring, electro or electroless plating, surface engineering and 3D printing to obtain components with improved performances or new functionalities.

In an early step, several techniques like UV stereolithography (SLA), fused deposition modelling (FDM) and selective laser sintering (SLS) were evaluated. SLA appearing as the most promising of these technologies, it has been thoroughly investigated in 2016.

The 3D printing system available at CSEM is based on a DLP videoprojector with the UV filter removed in order to achieve the selective cross linking of a UV sensitive resin. A 3D CAD design is sliced in layers of 0.01 to 0.1 mm. Each layer is then projected on the build plate or a substrate to fabricate the components layer by layer and without any mold.

The used material is a photo crosslinkable polymer, which can be mixed with an inorganic material like ceramic (Figure 1). Some of the material parameters are given in the table below.

Polymer	Hardness	Max. operating temperature
High resolution	75 shore D	<100°C
Soft	Shore A 65 Shore D 19	<100°C
Hard	75 shore D	<225°C
Ceramic composite	-	>1000°C if fired

This technology is capable of producing prototype or functional parts, depending of the material used, with an accuracy up to 10-20 µm and a minimum detail size down to 50 µm. It can for

example be used to fabricate lattice structures that form lightweight but resistant components. Two examples are presented in Figure 1 and Figure 2 which are respectively a sphere with a 0.4 mm lattice made of a polymer-ceramic composite, and a C letter made of polymer with 0.15 mm tetrahedral lattice. To achieve the realization of hybrid components, a substrate or an object that have received a surface treatment for adhesion promotion, can be loaded on the build plate. A fine alignment system is currently under investigation.



Figure 1: Different ceramic composite mechanical components (left); ceramic composite sphere with a 0.4 mm lattice (right).

Different hybrid components can be achieved with this technique, but a very promising one is a microfluidic device composed of different materials. Here, we are proposing the fabrication of compact and highly integrated fluidic systems made by 3D printing directly on a silicon or glass substrate already processed. In Figure 3, a first demonstrator is shown which consists of a 3D-printed microfluidic system with connectors built on a glass substrate. The channel diameter is 0.25, 0.5, 0.75 or 1 mm.

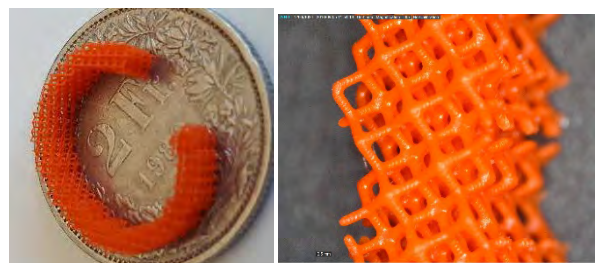


Figure 2: C-shape lattice structure.

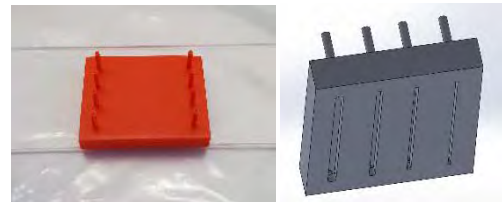


Figure 3: 3D-printed fluidic system on glass substrate (left); CAD design of the 3D-printed part (right).

Novel Microfabricated Infrared Optical Filters

R. P. Stanley, B. Timotijevic, L. A. Dunbar

We have designed and fabricated narrow-band, optical filters using a simple silicon technology. The advantage of these filters is that (a) they can be made in a matrix with different central wavelengths and (b) their central wavelength can be tuned post-processing. Some of the key applications include environmental monitoring, security cameras, medical analyzers.

The simplest narrowband optical filter that can be fabricated consists of two metal layers separated by a spacer. This Fabry-Perot (FP) structure is straightforward to fabricate and low cost, but they have a few important limitations. Firstly, the maximum transmission is limited by the intrinsic absorption in the metal layers. This limits the combination of transmission and linewidth *i.e.* narrow linewidth filter has a poor transmission and vice versa. Secondly, after fabrication the position of the center wavelength cannot be tuned, creating yield problems if the spacer layer is not homogeneous. Thirdly, it is difficult to create a matrix of filters with different central wavelengths without varying the thickness of the spacer layer which in practice prohibits their fabrication due to the added complexity. Finally, in the infrared, metal filters are unpractical because a metal layer thin enough to transmit some light, would be so thin that metal could not be deposited as a continuous film.

It is possible to overcome these drawbacks by using small apertures in metal and spacer layers as shown in Figure 1. The apertures allow for simultaneously high reflectivity and good ratio between transmission and absorption. This increases the figure of merit for metal FP filters, particularly at infrared wavelengths. In addition, when a porous layer has features much smaller than the wavelength then its effective refractive index varies with the porosity. If the porosity is two dimensional, then it is rather easy to vary the porosity in-plane though processing (mask design).

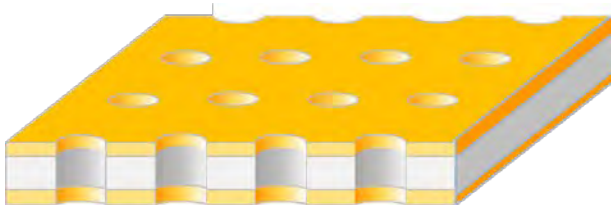


Figure 1: Basic filter consists of continuous metal membranes with apertures and a solid optically transparent spacer layer with holes.

There are few simple design rules which should be met when engineering these optical filters. The metal layer should be continuous to allow a high reflectivity. The spacer layer should be transparent in the IR and porous such that its effective index can be tailored by varying the porosity. Silicon and gold are well known microfabrication materials that can be easily processed to meet all these requirements.

Microfabrication follows a straight forward process consisting of a photolithography, dry etching and HF release. Figure 2 shows a close-up SEM of a filter made of 5 μm Si spacer layer metalized on both sides with 50 nm of Au.

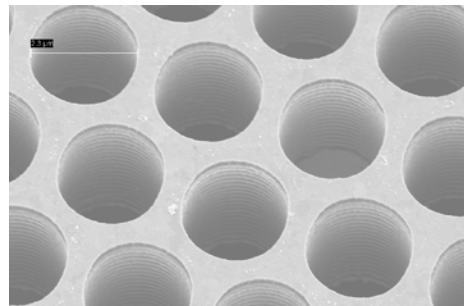


Figure 2: Fabricated optical filter with 50 nm of Au as a metal layer and 5 μm of crystalline Si as a spacer layer. Hole diameter is 2.2 μm and the period is 2.5 μm .

The filters were measured in transmission using a MCT detector in a Fourier transform infrared spectrometer microscope (Bruker-Hyperion). The FP filter measured has a central silicon spacer of 5 μm . There is a 50 nm Au layer on both sides. The hole diameters are 2 μm and arranged in a hexagonal lattice with a period of 3.6 μm . Figure 3 shows a typical example of the transmission properties of the filter. The two FP peaks have approximately 10% transmission and a 1.5% linewidth. Ideally a metal / silicon / metal FP in this configuration having a similar linewidth would have a transmission of only 0.2%! Thus showing that we have a factor of 50 improvement.

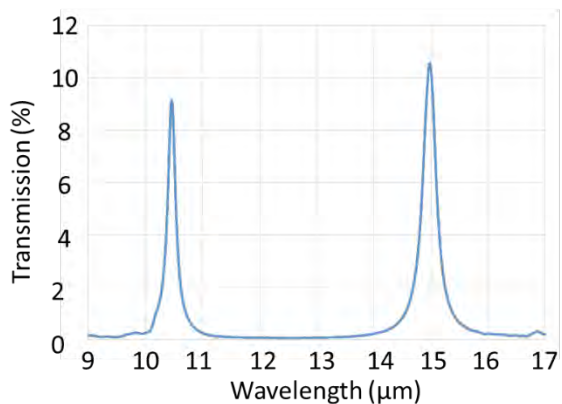


Figure 3: Measured transmission of the FP optical filter made from a 3.6 μm period hexagonal array with a 2 μm diameter hole size.

We have designed, fabricated and tested FP optical filters using gold porous mirrors and a silicon spacer layer. Traditional metal / spacer / metal FPs without apertures could achieve the same linewidth but this would come at the cost of 50 times lower transmission. In addition, these filters have a great potential in possibility of the post-process engineering of the central wavelength and in making the filter matrix with different central wavelengths.

How Robust are MEMS for Space Applications?

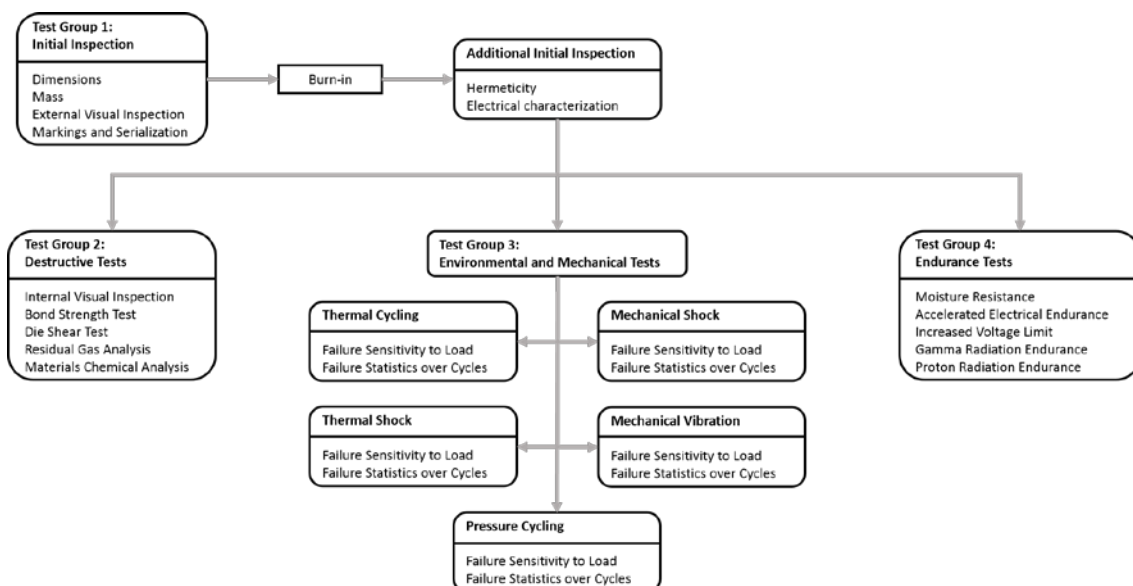
I. Marozau, M. Lahti •, D. Vogel ••, F. Souchon *, O. Sereda

Micro Electro Mechanical Systems (MEMS) have proven themselves in Earth-based applications such as automotive, medical, displays by showing outstanding performance and reliability figures. In space, MEMS have a large potential in applications like communication, navigation, Earth observation and scientific mission. In particular, MEMS can be utilized for fostering new types of scientific missions and instruments; reducing size, mass, cost, and time from mission conception to launch; increasing performances, reliability and redundancy of certain components. An approach for MEMS reliability assessment is being developed by a consortium of European characterization centres led by CSEM with an aim to develop a standardization methodology and Technical Memorandum for the reliability assessment of MEMS products for space applications.

The dramatically lower mass, the lower-power consumption, the smaller volume, and the possibility of tight integration with electronics, the field of MEMS offers new functionality and performance advantages, but also brings new challenges, particularly in the fields of testing and qualification. Today, only a few MEMS components have been or are planned to be used in space applications. Despite the growing interest for this new technology for space and the great reliability figures shown by earth-based sensors for application, specific space MEMS components have a low technology readiness level. One important reason for this low technology readiness level is the lack of possibility to assess the reliability of MEMS component in a standardized fashion and the lack of appropriate standards for qualification of MEMS components on which the industry could base themselves for future development and space usage.

The main aim of the present activity is to establish a Technical Memorandum for the standardization methodology for reliability assessment of MEMS products. The methodology is to be followed in evaluation of the product's capabilities as required for space applications and thereby to anticipate, as far as possible, component behaviour during reliability testing. Therefore, the aim of such testing is to overstress specific characteristics of the component concerned with a view to the detection of possible failure modes. A detailed destructive physical analysis is performed to facilitate failure analysis.

The developed methodology includes four groups of tests to address reliability of MEMS devices regarding packaging,



* VTT Technical Research Centre of Finland, Finland

•• Fraunhofer-ENAS, Germany

* CEA-LETI, MINATEC Campus, France

[1] MIL-STD-883 Test method standard microcircuits, DLA Land and Maritime - VA, P.O. Box 3990, Columbus, OH 43218-3990.

MAMOS—Metal-based Additive Manufacturing on Silicon

A. Hoogerwerf, J. Jhabvala •, E. Boillat •, M. Despont

We have developed an additive manufacturing method to write metal structures directly onto silicon. The method will enable us to extend our traditional MEMS offering with new and innovative devices manufactured with a combined technology.

Additive manufacturing (AM) has recently become a very popular method to fabricate a wide variety of devices. Its popularity stems from its quick turnaround time, which is especially attractive for rapid prototyping. But it has also become more and more interesting for small volume production, for its freedom to create intricate 3D structures and for its potential of material saving.

CSEM recognized the potential of AM and pursues developments in particular for microsystems applications. Hence our main focuses are:

- Optimize processes for micro-size dimensions
- Add functionalities such as flexible mechanical structure and electrically active components
- Combine additive manufacturing with other micro and nano technologies (i.e. MEMS, 3D micro-moulded parts, ...)

In this work we have explored the AM-based fabrication on top of silicon substrates, as a starting point for integration with MEMS technology.

The combination of additive manufacturing with silicon MEMS requires a good adhesion of the parts additively manufactured to the silicon base material. We therefore executed an exploratory project with EPFL aiming to analyze how the adhesion could be controlled. As a test vehicle, we took the manufacturing of metal pickup rings on a silicon platform. The rings are intended as pickup rings for a Time-Of-Flight Mass Spectrometer. For this application, we need multiple rings that are relatively closely spaced and that will operate under vacuum. They, therefore, present a nice test case for the technology.

The process that was used to define the metal rings is Selective Laser Melting (SLM) [1]. This method, depicted in Figure 1, deposits a thin layer of a metal pre-cursor powder on a workpiece. The powder is then heated locally with a laser, melting the metal locally. A next metal powder layer is deposited and again locally heated. After the entire piece has been defined layer-by-layer, the un-sintered metal powder is removed, leaving behind the piece defined.

The SLM process has been executed with aluminum and silver particles of different sizes. It was found that the SLM locally heats the metal to very high temperatures, causing a metal line written directly on silicon to tear off a part of the silicon. The fracture stress of untreated silicon is more than 1 GPa, attesting to the stress induced by the process. This difficulty could be overcome by reducing the sintering energy and optimizing the writing strategy. With these optimized parameters, the

structures shown in Figures 2 and 3 could be fabricated. The electrode wall thickness is about 100 µm and the electrode hole is 800 µm.

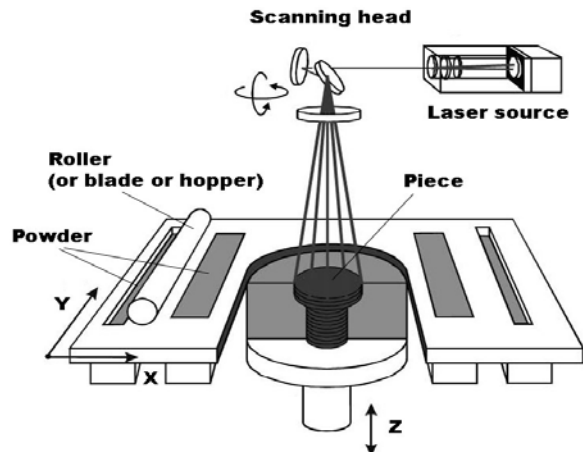


Figure 1: The selective laser melting additive manufacturing principle [1].

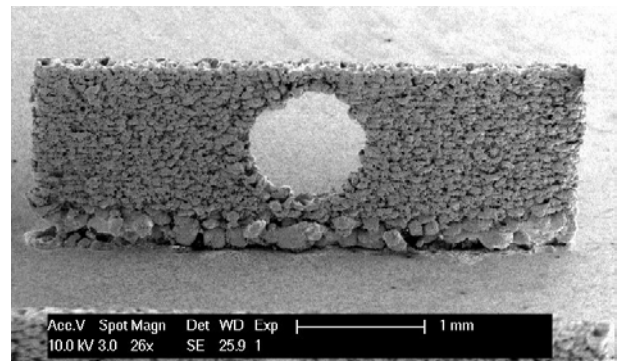


Figure 2: Side view of the Ag-electrode structures written on patterned silicon.

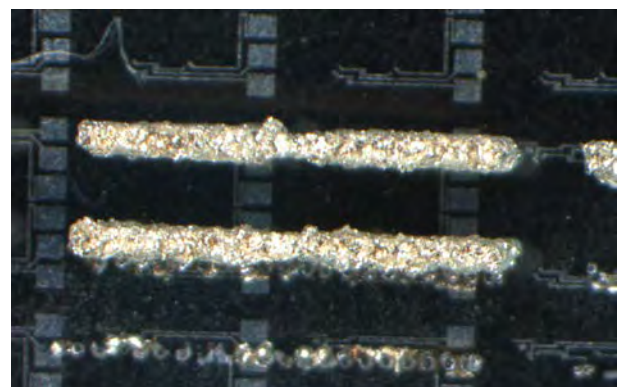


Figure 3: Top view of the structure of Figure 2 on aluminum patterned oxidized silicon (mockup of an interconnect base).

• Ecole Polytechnique Fédérale de Lausanne, EPFL

[1] J. Jhabvala, "Study of the consolidation process under macro- and microscopic thermal effects in Selective Laser Sintering and Selective Laser Melting", PhD. thesis, EPFL. 4609, 2010.

Low-temperature Reactive Nanofoil Die-attach Bonding for MEMS

G. Spinola Durante, R. Jose James, K. Krasnopolksi, S. Mohrdiek, U. Lang*

This new furnace-free^[1] sealing technology enables a MEMS die-attach solder process onto a generic substrate material. As opposed to laser bonding, this additional low-temperature approach is viable also for non-transparent MEMS components and substrates. In this paper a technology demonstrator is shown with silicon chips mounted on coated stainless steel, achieving shear strength values above 10 MPa. Direct bonding on stainless steel and on other hard-to-bond materials is also evaluated.

MEMS components have reached a very high penetration in the consumer market, largely covered by bulky sensor solutions. Miniaturized and robust solutions for MEMS-based sensors is in growing demand to address higher performance requirements specifically for use in harsh environments. These sensors have usually critical parts and the housing is made of stainless-steel, since this material has proven to survive many chemically aggressive environments. "Packaging for harsh environments" is considered an enabling technology being part of the global "Internet of Things" (IoT) trend.

The Nanofoil technology fits quite well to this requirement of industrial sensors to keep stainless steel as a base manufacturing material. The Nanofoil is a commercially available metal based on reactive foils that enables the die-attach soldering of a silicon chip onto a small or even bulky stainless steel part. The assembly of a MEMS chip cannot be done directly onto stainless steel substrates due to its surface inertness, but requires a solderable coating on both sides of the solder joint. In Figure 1 are shown the assembled chip on coated stainless steel and the different solder & Nanofoil preforms. The stainless substrate and the silicon chip are also shown.

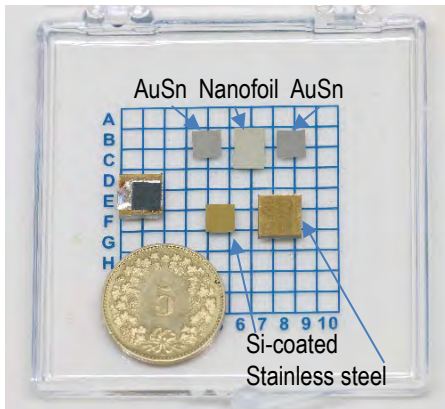


Figure 1: Solder and Nanofoil preforms are shown on the top. The gold-coated chip and stainless steel are also shown below. The mounted chip is shown on the left side above the coin.

The main advantage of the Nanofoil-based reflow process is the inherently low temperature and therefore low stress at the bulk level of components. The heat generated by the triggered exothermic process with the Nanofoil will only melt the thin solder preforms layers. Moreover, the process does not need a dedicated reflow oven like in the case for soldering and is therefore furnace-free.

This coating strategy can also be implemented with different silicon to generic substrate combinations and with any solder

having melting point <300°C. The solder will melt when the Nanofoil is ignited. This bonding configuration can be used with non-transparent substrates, as opposed to low-temperature laser bonding, provided there is access to ignite the Nanofoil.

A key to the success of this technology is the customization towards different solder melting points, different chip dimensions, and substrate sizes and materials. CSEM has developed a solderable coating strategy consistent with the AuSn solder choice, exploiting results from previous projects. Both solder and Nanofoil are cut into preform shape to ease the assembly procedure, providing the exact match to the solderable metallization layout (Figure 2). A cutting process has been developed which does not trigger the exothermic reaction using picosecond laser micromachining done in-house at CSEM.

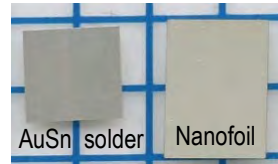


Figure 2: AuSn solder preform 4×4 mm², Nanofoil preform 4×6 mm².

The Nanofoil preform (Figure 2 on the right side) is larger than the solder preform size to enable the ignition. This protrusion could be made much smaller or even laser-cut to ensure a proper clean bonding edge. Laser cutting after ignition is also an option.

The Nanofoil-based solder joints have been tested for shearforce, according to tests performed at the HSLU* Laboratories^[1]. The resulting shear stress according to standardized measurements^[2] are in the order of 10-15 MPa for silicon chips in the range of 4-16 mm² of bonded surface. While these values are lower compared to typical solder values of 30-50 MPa and more similar to adhesive bonding shear values, the throughput of the Nanofoil bonding is quite high. Reflow process usually take between 10-30 minutes depending on solder melting point and component size. Nanofoil bonding in comparison takes around 1 ms for 1 mm-scale parts.

There is a push for technology enabling direct integration of sensors into high-end sensing systems. Implementation of Nanofoil technology to a production environment requires activation of hard-to-bond substrates in a viable and cost-effective manner. This strategic research is ongoing at CSEM with the collaboration of HSLU, to enable direct soldering on stainless steel and highly corrosion resistant alloys, targeting highly demanding industrial MEMS-based applications.

[2] MIL-STD-883 method 2019.9 Die shear strength.

* Hochschule Luzern Technik & Architektur (HSLU)

^[1] G. Spinola Durante, R. Jose James, K. Krasnopolksi, "Furnace-free micro-joining with reactive Nanofoils", CSEM Scientific and Technical Report (2015), 34.

Low-temperature Laser-assisted Sealing of Glass Lid on Silicon

S. Berchtold, R. Jose James, S. Mohrdiek, G. Spinola Durante

This new low-temperature sealing technology enables hermetic packages of environmentally sensitive components like VCSEL, CCD eventually combined with ASICs. The advantage of a high shear strength (~ 150 MPa) and fast laser-assisted sealing makes this technology suitable for a wide range of applications.

The low temperature bonding and hermetic sealing of different materials like glass, ceramics, and single crystals is still challenging. Many applications use high temperature sealing techniques (e.g. soft soldering and thermo-compression bonding at $>250^\circ\text{C}$) to realize a robust hermetic seal. Many electronic components are not compatible to such high temperatures.

Developments in MOEMS and optoelectronics technology during recent years for smaller integrated low-power sensors and optical components opened up new fields of applications. In domains where exposure to harsh environments or long term stability is required (e.g. implants) or where electrical components (e.g. VCSEL) prone to degradation with moisture are used, hermetic sealing into a package is needed using materials with very low water permeability. Moreover temperature sensitive components like VCSEL, CCD eventually combined with ASICs would need to be encapsulated at a temperature of less than 150°C to ensure proper functionality without any degradation.

A novel laser based hermetic sealing method was developed (Figure 1). This hermetic sealing technology which was proven for sapphire in earlier developments [1] and has been extended to bonding of silicon onto glass. The sealing process is very fast and takes only a few seconds to provide a strong bond. The temperature inside the sealed chamber will be less than 150°C [1]. The sealed packages were also tested to be helium leak tight to better than 10^{-10} mbar·L/s, which is the detection limit of the measurement method.

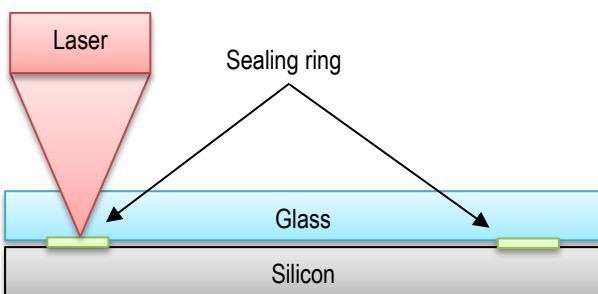


Figure 1: Laser-assisted sealing of glass lid on silicon with sealing ring.

In Figure 2, a hermetically sealed and perfectly aligned package is displayed. The color (red, green) of the interference fringes implies the flatness of the sealed package.

Accelerated tests were carried out to verify that the bonded chip can withstand harsh environmental conditions. Therefore two tests methods based on MIL-STD-750 where used to ensure

that the right test condition is used. The tests used were moisture resistance test based on "Method 1021.3 moisture resistance" and thermal cycling tests based on "Method 1051.7 temperature cycling (air to air)" [2].



Figure 2: Hermetically sealed glass on silicon package.

To test the bond strength of the sealed chip a shear tester was used. It could be shown, that the shear strength did not change significantly after environmental stress testing. A comparison of the shear test values between reference samples (which were not submitted to accelerated testing) and samples which went through accelerated tests is given in Figure 3. On average very good shear strength values of about 150 MPa were achieved. After environmental testing 94% of the packages were still helium leak tight to better than 10^{-10} mbar·L/s.

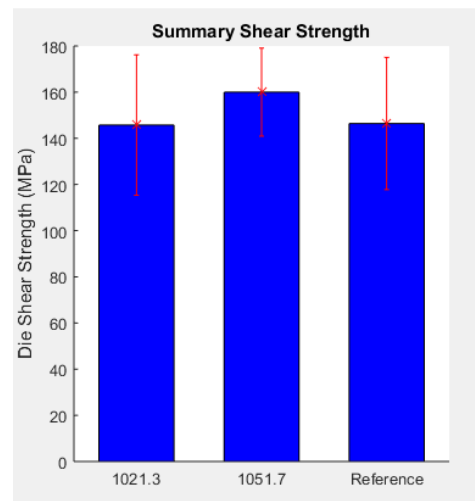


Figure 3: Summary of shear strength, with reference without MIL-STD-750 tests.

Further process development will be elaborated to explore new material combinations for chip material and sealing ring. This allows even more technology applications to be covered with this unique laser sealing technology taking advantage of low temperature hermetic sealing concept with high throughput.

[1] R. Jose James, et al., "Low Temperature Hermetic Sealing of Sapphire Substrates", CSEM Scientific and Technical Report (2014), 41.

[2] Test Method Standard, Environmental Test Methods for Semiconductor Devices Part1: Test Methods 1000 through 1999, Department of Defense, MIL-STD-750 (2012).

ACTION—Technologies for Cochlear Implants

M. Fretz, R. Jose James, G. Spinola Durante, S. Bitterli, T. Burch

The aim of the project is to develop a novel type of cochlear implant. This is a medical device used to restore auditory sensations for hearing-impaired listeners. We use tiny laser diodes to generate soundwaves inside the fluids of the cochlea. Hair cells register these vibrations and send electric signal to the brain.

ACTION is a European Project combining the knowledge and experience of seven companies and research institutions in the fields of lasers, optics, electronics, medicine, biology, chemistry, implant technology and packaging. Such a wide spread of expertise is required to address all the challenges in developing long-term implantable devices. For example, lasers are delicate semiconductor devices. Exposing the lasers to the aggressive fluids of the body would destroy them long before the anticipated end of life of a cochlear implant (CI). Vice versa, the laser contains substances toxic to the human body. A biocompatible package is therefore mandatory. But, as every foreign body is slowly being encapsulated by fibrous tissue, the surface of the package has to be modified to slow down and minimize tissue encapsulation. Otherwise, the laser light will be absorbed by the encapsulation, reducing the efficiency of the implant over the course of several weeks, potentially to a level where the device becomes insufficient to generate hearing.

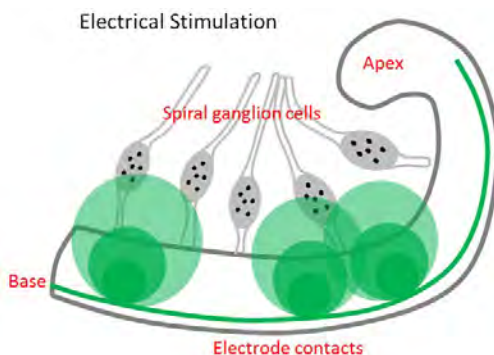


Figure 1: Schematic representation of a cochlear implant. The generated electric fields are depicted with green discs. The spreading of the fields leads to excitation of unwanted sound or tones.

Understanding the principles involved in optoacoustic stimulation helps appreciate the challenges involved. State-of-the-art cochlear implants use small electrodes placed inside the cochlea to electrically stimulate the (spiral ganglion) nerve cells, bypassing the hair cells (Figure 2). Patients suffering from severe hearing loss might not have these hair cells, but electrical stimulation might restore some hearing. Optoacoustic stimulation, on the other hand, relies on 'mechanically' stimulating the hair cells, which need to be present and functional. A focused burst of light from a laser was previously proven to generate sound waves in the cochlea fluids [1]. The sound wave, eventually, causes the hair cells to move, which sets in motion the process of generating and propagating

electric signals to the brain (also referred to as Compound Action Potentials, or CAP). This sequence of events is identical to normal hearing. The condition, as above mentioned, is the presence of healthy hair cells. Consequently, a cochlear implant based on the optoacoustic effect cannot be a replacement for current cochlear implants. But they might be used in combination: Some CI users retain hearing in the low frequency region and can use a special speech processor including a hearing aid. However, this requires an earmould to be used, which is not always acceptable to the recipient. Use of the implantable laser developed in this project will allow sound transmission without an earmould.



Figure 2: Conventional cochlear implant. Courtesy of MED-EL GmbH.

Optoacoustically generating CAPS depends on the system's ability to create soundwaves powerful enough to move the hair cells sufficiently. The amplitude of the sound wave is expected to increase monotonously with the laser intensity. Unfortunately, the current cannot be ramped up arbitrarily. The laser and the electric wires might heat, damaging neighbouring tissue. The laser might also get damaged by overheating. Combining the right materials and stimulation patterns, we recently managed to produce a CAP generated by specially designed VCSELs and microlenses [2].

This project helped CSEM to further its expertise in medical packaging with a focus on miniaturized devices. The technology is not limited to the cochlea, but can be used in all applications requiring minuscule biocompatible packages.

The research leading to these results has received funding from the European Union Seventh Framework Programme FP7/2007-2013 under grant agreement FP-ICT-611230. The cantons of Central Switzerland support the project as well.

[1] ACTION consortium, "Periodic Report Year 2" (website: www.action-project.eu).

[2] ACTION consortium, "First oaCAP Measurements" (website: www.action-project.eu).

ACTION—Hermetic Packages and Flexible Substrates for Implants

M. Fretz, R. Jose James, G. Spinola Durante

In the frame of the European Project ACTION, CSEM and its consortium partners developed a prototype implantable laser to explore the optoacoustic effect. This effect is used to stimulate hearing nerves in the cochlea through the generation of a sound wave in the cochlea fluid. The sound wave is created by laser light absorbed in the fluid.

One of the core activities of CSEM in this project was the development of a package (i.e. housing) for the laser. It has to be kept in mind that the human body reacts aggressively to foreign bodies and that certain materials used in the semiconductor industries may be toxic or even carcinogenic. Therefore, the package has to be hermetically sealed in order to prevent leaching of toxic substances and ingress of moisture, which might damage the internal electronics. Material choice for the package is for the same reasons limited to a small selection of metals, ceramics and polymers. Latter are, however, not suitable to protect the laser and internal electronics over a period of several years. A proprietary laser assisted bonding process allowed us to hermetically seal a miniature sapphire package with cavity dimensions as small as $0.6 \times 0.6 \times 1.2 \text{ mm}^3$ (Figure 1). Sapphire has all the properties required for this application. It is a strong material, chemically stable and non-toxic to the body. In fact alumina, which is the amorphous version of sapphire, has a long track record in long-term medical implants. Furthermore, sapphire is highly transparent in the wavelength range of the emitted laser light.

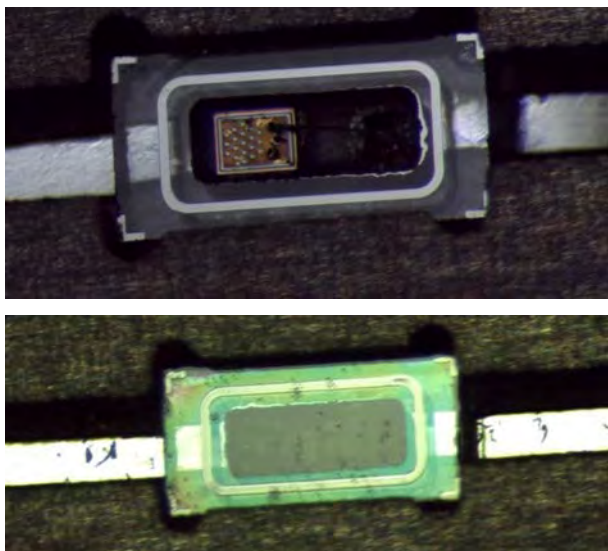


Figure 1: Sapphire micropackage. Before sealing (top). The VCSEL is visible in the pocket. After sealing (bottom). The uniform green colour indicates a successful bond of constant bondline thickness.

A further feature of the miniature package are two hermetic feedthroughs, exclusively made of biocompatible materials. The feedthroughs are integrated in the bottom of the package. The electric connections extend horizontally beyond the side walls. These easily accessible platinum ribbons may then be laser, spot or resistance welded to a platinum wire.

We also developed a flexible substrate (i.e. flex print, Figure 2) for the VCSEL. It provides mechanical support and electric connection. It is made of the biocompatible materials silicone and platinum.

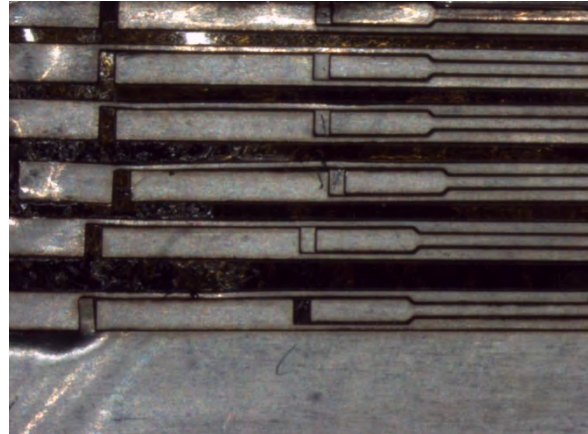


Figure 2: (top) Laser milled platinum foil. The structure of the flex print is repeated several times; (bottom) three packages welded to the flex prints. Separation of the devices is the last step in the manufacturing process.

The development of a package and further key technologies at CSEM and its project partners opens the door for implantable light sources. The ongoing miniaturization of the components – essential for cochlear implants – has two further advantages: On one hand, it will allow new medical treatments due to the fact that smaller implants may be placed in parts of the body which are inaccessible to current size implants. On the other hand, surgical procedures will be less invasive. The patient benefits too because, for example, only local anesthetics will be required. Recovery will be much quicker and the procedure cheaper.

The competences that CSEM builds within the frame of this EU-project are not restricted to medical applications. Packaging solutions for microsystems in harsh environments are door openers for many industrial applications. CSEM is willing and prepared to support industrial partners in Switzerland.

The research leading to these results has received funding from the European Union Seventh Framework Programme FP7/2007-2013 under grant agreement FP-ICT-611230. The cantons of Central Switzerland support the project as well.

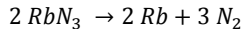
Improved Lifetime of Miniaturized Vapor Cells in Atomic Clocks

T. Overstolz, J. Gobet, S. Karlen, J. Haesler, L. Balet, A. Bionaz, T. Volden

CSEM has successfully solved lifetime issues of MEMS-based rubidium vapor cells and has demonstrated lifetime estimations of 10-20 years.

CSEM has developed and improved over the past years the technology for miniaturized atomic clocks. One of the key components of an atomic clock is the vapor cell which contains minute amounts of an alkali metal, in our case rubidium (Rb).

We have developed a method to batch-fabricate vapor cells on a wafer scale with a very high yield (Figure 1). The fabrication comprises pipetting of dissolved rubidium azide (RbN_3) into cavities etched into a silicon wafer and closed on one side with a glass wafer, and sealing the cavities by anodic bonding under Ar atmosphere with a second glass wafer. Irradiation under UV light results in decomposition of the inert RbN_3 according to



One of the characteristics of this fabrication method is that the quantity of metallic Rb inside the vapor cell is directly related to the N_2 partial pressure. Since the latter one must be limited, we have below 1 μg of metallic Rb inside a vapor cell which is much less than in the vapor cells of most competitors. As a result we have very quickly encountered lifetime issues with our vapor cells. The spectroscopic absorption signal of the Rb atoms disappeared after operation times of some days or even after only a few hours at a working cell temperature of 100°C.

In-situ and non-destructive Raman spectroscopy was developed [1] in order to evaluate the residual partial pressures of nitrogen, oxygen, and hydrogen inside the cells at different states of accelerated thermal aging. Careful observation of condensed metallic Rb droplets inside the vapor cell and software-based monitoring of the droplet size allowed us to estimate the evolution of metallic Rb quantity. Hence we could show that the aforementioned partial gas pressures did not change during accelerated aging, but the quantity of metallic Rb decreased. This let us to the conclusion that the vapor cells are leak tight, and that the mechanism of diminishing Rb quantity must be related to Rb diffusion into the borofloat glass. To support this hypothesis we developed different types of molecular vapor deposition (MVD) diffusion barrier coatings.



Figure 1: Rubidium vapor cell of $4 \times 4 \text{ mm}^2$ and 1.6 mm thickness including Pt resistive heaters on both cell windows.

Figure 2 shows that an appropriate diffusion barrier stops the diffusion of Rb into glass very efficiently. The rate of diffusion of the Rb in the glass is expected to follow Arrhenius' law describing the temperature dependence of reaction rates. According to Arrhenius' law the reaction rate depends on the thermal activation energy of the process, a parameter that can be considered as an energetic barrier to be overcome for a reaction to proceed. Accelerated aging tests at several high temperatures are ongoing to estimate the activation energy of the rubidium consumption process. At this stage only a preliminary estimation is possible due to the excessively long test times involved. The estimation yields an Rb consumption of $\leq 0.01 \mu\text{g}$ Rb per year at the working cell temperature of 100°C (see Figure 3). Hence lifetime of CSEM's vapor cells exceeds 10-20 years, matching thus industrial standards.

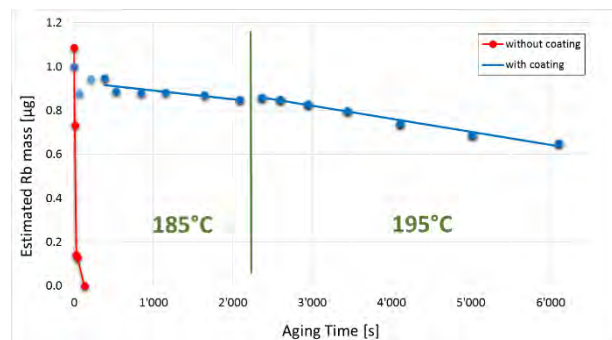


Figure 2: Rb consumption in vapor cells without (red graph) and with (blue graph) protective coating.

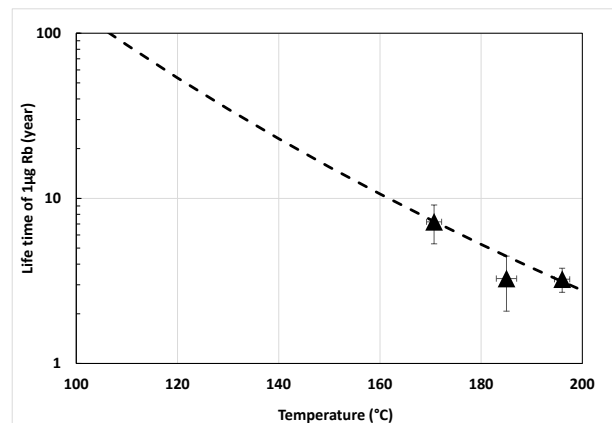


Figure 3: Arrhenius plot for the Rb consumption rate, preliminary estimate of the activation energy 50-60 kJ/mole.

This research activity is performed in the frame of a multidivisional research program and CSEM would like to thank the Swiss Confederation and the Canton of Neuchâtel for their financial support.

[1] J. Gobet, et al., "Nondestructive Raman Spectroscopy for Hermetic Package Reliability Analysis", CSEM Scientific and Technical Report (2015), 30.

Nanofoil Bonding of Laser Micromachined Components

G. Spinola Durante, J. Kaufmann, A. Steinecker

This paper describes a bonding technology using Nanofoils, which enables furnace-free, low-temperature soldering of transparent or non-transparent laser micro-machined components, without reaching the bonding temperatures for solder reflow processes. Nanofoils can be patterned with ps-laser into exact preform shapes. An example is given of a silicon gear mounted onto gold-coated stainless steel with a shear force above 10 MPa.

Manufacturing of small and complex laser micro-machined parts in silicon with high quality is a complex task which is becoming more and more popular due to the availability of laser equipment and corresponding processing software (Figure 1) looking back to at least 10 years developments in the field.



Figure 1: ps-Laser facility in Center Alpnach.

Assembly of a laser-machined MEMS with high precision onto a substrate is a complementary technology to laser manufacturing of micro-machined parts. In this respect both bonding process and pick & place automation strategy play a significant role. The Nanofoil technology enables to be independent of the solder material choice and of its melting temperature, and moreover, is a furnace-free bonding process [1]. It requires for its ignition a very small access point where an electric current or a laser beam can start the fast exothermic reaction. The Nanofoil bonding is much faster than any soldering or adhesive snap-cure process, since no heating ramp is required and it takes only a few milliseconds to perform the assembly.

The advantage of using Nanofoils for bonding are manifold: a significant advantage comes in view of the temperature budget since the Nanofoil reaction is very fast, i.e. below 1 ms for a 1 mm size part. Therefore the parts do not overheat and very little stress is embedded into the solder joint. This enables to provide a bond close to surfaces which are sensitive to temperature and otherwise cannot withstand more than e.g. 150°C. The Nanofoil is also adapted for non-transparent components [2] or substrates if compared to low-temperature laser bonding, providing a significant improvement. The solder schematic including additional preforms and coatings is shown in Figure 2. The pre-forms are part of the solder joint, being placed both above and below the Nanofoil preform itself to achieve the mechanical interconnection.

An example is hereafter discussed to underline the key aspects of the assembly process, according to the bonding scheme in Figure 2. The demonstrator is made by laser micro-machining of a gold-coated silicon gear and a Nanofoil preform, laser-cut into the exact preform shape (Figure 3).

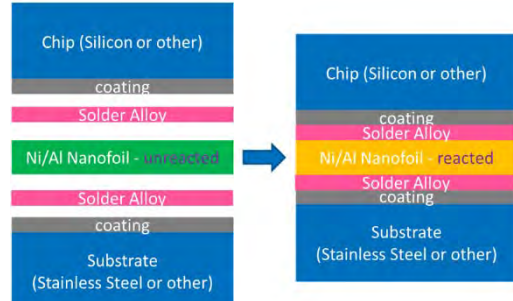


Figure 2: Nanofoil-based solder joint configuration.



Figure 3: Laser micro-machining of coated silicon wafer and of Nanofoil metal sheet into small shape preforms.

The final assembly can be seen in Figure 4a where the small Nanofoil foil is protruding where the exothermic process is triggered. This enables the ignition by electrical contact with a 9V battery electrodes directly shorted onto this foil tip. The laser-milled Nanofoil is shown zoomed in Figure 4b and the small hole for an eventual pin or gear axis insertion can be exactly manufactured without triggering any exothermic reaction. The joint interconnection was tested for shear force and yielded average shear values above 10 MPa [3].

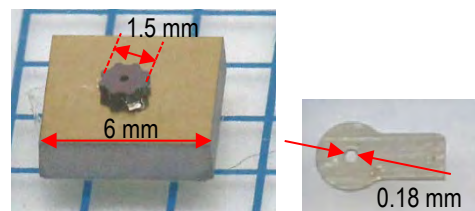


Figure 4: a) Hermetically sealed glass on silicon package; b) Nanofoil laser micro-machined showing a small feature of 180 um diameter.

CSEM is further investigating the Nanofoil technology to achieve cost effective bonding solutions, taking advantage of the flexibility and speed of the bonding process. Process adaptations are required to use the Nanofoil approach to customer specific bonding applications, respectively substrate materials, ensuring optimal coating and assembly strategy with higher shear test values, if compared to standard adhesive solutions.

¹ G. Spinola Durante, et al., "Furnace-free micro-joining with reactive Nanofoils", CSEM Scientific and Technical Report (2015), 34.

² G. Spinola Durante, et al., "Low-temperature reactive NanoFoil die-attach bonding for MEMS ", in this report, 30.

³ Test MIL-STD-883 method 2019.9 Die shear strength.

SURFACE ENGINEERING

Harry Heinzelmann

With advancing miniaturization, surfaces become increasingly important for the properties of components. Surfaces' topographical and chemical properties determine a wide range of effects, such as surface adhesion and friction, optical reflectivity and color, electrical conductivity, and (bio-) chemical affinity. The determination, understanding, and controlled modification of surface topography and chemistry are therefore of great importance for the development of small components and devices, and the ability to fabricate nano-engineered surfaces on large scales and at a competitive cost is a key competence that supports industrial applications.

CSEM's Surface Engineering program addresses some of the most important areas with regard to controlling surface properties (both topographical and chemical) and developing manufacturing technologies. The *Nanosurface Engineering* activity concentrates on the development and fabrication of nano-structured surfaces and nanoporous films with added functionality, as well as on the design and realization of nano-optical components based on nano-engineered surfaces. The *Biosurface Engineering* activity addresses the biochemical functionalization of surfaces that are developed for use in (affinity) sensors and as cell and tissue support substrates, and includes microfluidics and sample-handling instrumentation. Finally, the *Printable Electronics* activity deals with printing processes for both organic and inorganic electrical circuits, the design and testing of electronic components, and the higher level integration of printed electronics components for flexible solutions.

All three activities of the Surface Engineering program not only address questions at the material and process levels; they also aim to develop manufacturing methods and higher level integration pathways that enable CSEM to offer attractive solutions to industry. The program hence develops scientific knowledge in the design, modelling, generation, and understanding of functional surfaces, alongside technological expertise in the development and stabilization of up-scalable fabrication methods, characterization, and integration.

The vision of the program can therefore be summarized as follows: to "research and develop engineered surfaces and interfaces by controlling their (nano-) structured topography and their surface material composition using processes compatible with large-scale manufacturing, in order to design and optimize predominantly their (bio-) chemical, optical, and electrical properties, and to improve the performance of the respective components".

Long-term objectives

The global, long-term objectives of the Surface Engineering program are twofold. On the one hand, it is important to strengthen CSEM's technology position in those areas where CSEM can offer unique and valuable solutions to industry. These include the development of well-designed surfaces with novel optical and chemical properties and corresponding fabrication methods that allow competitively priced manufacturing, the conception of lab automation equipment for use in cell sorting and tissue preparation environments, and the

further development of printed electronics solutions on flexible substrates, for example for the fabrication of printed electrochemical sensors that are biochemically functionalized for their specific applications. On the other hand, it is a long-term objective of the program to continue to provide both the state-of-the-art understanding of optimizing surfaces and the corresponding methods that are necessary to leverage key CSEM technologies originating in other technological programs. Examples of this supporting role include the increase of amorphous silicon PV cell conversion efficiencies by the optimization of the surface roughness of intermediate adsorption layers, the improvement of the sealing properties of atomic clock cavities by the adsorption of conformal surface layers, and the design of novel optical filters and masks that can be directly fabricated onto vision sensors.

More specifically, the long-term objectives in *Nanosurface Engineering* are the development of state-of-the-art methods of originating nanoscale surface structures—such as by means of molecular self-assembly, nanoparticle assembly, and sol-gel processes; the development of appropriate fabrication methods that allow us to structure larger than lab-scale surfaces at a competitive cost; and the exploitation of those surfaces, in particular for sensing applications and for their optical functionalities, with an emphasis on light management and plasmonics.

In *Biosurface Engineering*, the long-term objectives are to develop novel tools that address current needs in life sciences, clinical diagnostics, and food and environmental sensing and monitoring, ranging from single components to integrated solutions. This includes work on biochemical surface functionalization in order to generate suitable substrates for molecules and cells as well as specific sensor affinities, the development of appropriate cell support carriers for 2- and 3-D cell culturing, and the integration of microfluidics and optical monitoring for cell handling and biological tissue preparation.

The long-term objectives in *Printable Electronics* are to provide the key elements for maintaining a flexible technology platform in the field, including the identification and characterization of suitable materials and the optimization of processes. Thin-film encapsulation of functional layers and the packaging of functional organic devices will be added to the technology portfolio. Design capabilities need to be maintained and their applicability extended to organic materials; the regulatory requirements of materials used and entering potentially in contact with the human body will be increasingly important for the acceptance of printed electronics solutions for health applications (on-skin sensors, implants, etc.).

The research carried out in this program is concentrated on the following activities:

- *Nanosurface Engineering*, specifically addressing micro-/nano-manufacturing technologies, functional nanocoatings, and nanophotonics engineering.
- *Biosurface Engineering*, specifically addressing cell handling, sensors, and sample handling.

- *Printable Electronics*, specifically addressing printable electronic processes and components; design, modelling, and testing; and application and hybrid integration.

The *Nanosurface Engineering* activity concentrates on the development and fabrication of nano-structured surfaces and nanoporous films with added functionality, as well as on the design and realization of nano-optical components based on nano-engineered surfaces. This includes novel methods of nano-structure origination; replication methods for nano-scale structures; tooling (e.g., for embossing and injection molding); coatings from sol-gel films with tunable nano-porosity and their application-specific functionalization (e.g., by introducing guest materials for sensing or optical amplification); the modelling of the optical properties of, for example, nanoporous metal films showing anomalous transmission; and the design and realization of related optical components and devices.



Figure 1: Optical microstructure for decoration and security (left); airplane model covered with pressure sensitive paint (right).

The *Biosurface Engineering* activity addresses the biochemical functionalization of surfaces that are developed for use in (affinity) sensors and as cell and tissue support substrates, as well as microfluidics and sample handling instrumentation. This includes surface grafting with specific biomolecules showing the desired affinities, for electrochemical sensing and for cell cultures; the design of novel cell supports such as beads and bioreactors, for 3-D cell cultures; the development of cell platforms with integrated sensors, for cell-based (ex vivo) toxicology studies; and the development of compact microfluidic modules with integrated sensors, for the handling of (biological) samples.

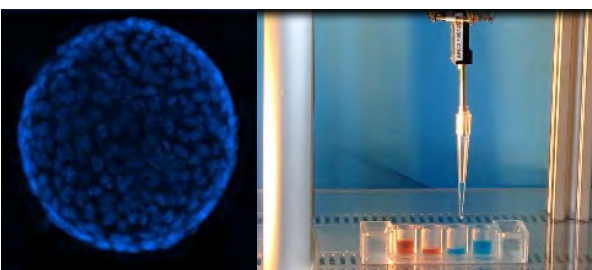


Figure 2: Microbead carrier for cell growth (left); novel pipetting solution with passive flow control (right).

The *Printable Electronics* activity deals with printing processes for both organic and inorganic electrical circuits, the design and testing of electronic components, and the higher level integration of printed electronics components for flexible solutions. This includes high-resolution, large-area printing processes (such as Aerosol Jet Printing (AJP)), for electronic components (both inorganic and organic) and circuits on flexible substrates, encapsulation, and packaging; the modelling of higher integrated components such as light management solutions for organic light-emitting diodes and

organic photo-detectors; and printing processes for large arrays of electrochemical sensors.

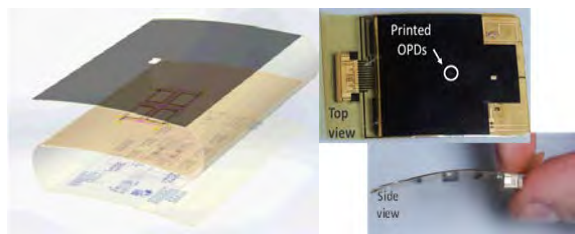


Figure 3: Scheme and realization of hybrid integration (left); lightweight and flexible sun sensor for ESA applications (right).

The three activities of the program have strong mutual synergies, for example in the development of printed electrochemical sensors that are specifically functionalized for applications in environmental or biochemical sensing, in the development of cell culture supports with optimized surface topography and chemistry and integrated electrochemical sensors for monitoring, or in plasmonic sensing for high-sensitivity, label-free analytics.

Highlights

Successful development and transfer projects include award winning collaborations with Onera (France) on the development of pressure-sensitive paints with increased performance for airflow modelling in wind tunnel testing for airplane development (recognized by the Innovation Prize, awarded by the Franco-Swiss Chamber of Commerce) and the fabrication of first- and second-level security features in plastic molded pieces (recognized by the Innovation Prize in holography technology, awarded by the International Hologram Manufacturers Association). Further examples are the transfer of CSEM's proprietary air restriction control to SIAS/Tecan, thus introducing a new and disruptive pipetting technology, and the collaboration with EAWAG and the Helmholtz-Zentrum für Umweltforschung to establish CSEM's CellFactor platform as a tool for the classification and sorting of small model organisms for toxicological screening.

Several other technologies developed in this program were recognized by Swiss innovation prizes. These include the Swiss Technology Award (category "inventors"), given for our development of wound pads with integrated biosensors, and VentureKick for the start-up SiMPLEnext, which aims to develop ultra-thin support membranes for cell cultures.

The Surface Engineering program is well integrated into CSEM's global research program and has numerous synergies with the four other thematic research programs. It thus supports the further development of a range of core technologies as well as their transfer to industry.

A Photolinker Polymer with High Density Functional Groups for more Sensitive Bioassays

H. Gao, D. Caminada

CSEM's proprietary photolinker polymers are applied to develop covalently modified surfaces that can have additional (bio-)functionalities. Two developments enlarge the family of these photolinker polymers and extend their use for applications such as coatings for woundpads and catheters. First, the number of secondary functional groups to bind biomolecules has been increased and results in more sensitive bioassays. Next, a non-biodegradable organic photolinker (OptoBOD) has been developed to offer covalent coatings of increased stability and hydrophilicity.

The OptoDex technology is a versatile platform for covalent surface bioengineering and has been applied in diagnostics applications such as functionalization of biochips and microarrays. The degradable nature of the polysaccharide chains limited or even prevented its use for long-term stable coatings such as coatings for catheters and woundpads. We have developed a non-degradable organic polymer-based photolinker branded OptoBOD by replacing the dextran-backbone by a polyethylenimine-backbone. It maintains the advantages of OptoDex and increases the stability and hydrophilicity of the coating. OptoBOD addresses the needs for long-term and non-biodegradable coatings. The organic composition of OptoBOD makes it highly dissolvable in organic solvents, thereby allowing a more efficient coating process.

Biomolecules can be immobilized in two ways with our photolinker polymers: 1) by a dry-state photobonding process and 2) by secondary functional groups (e.g. -NH₂, -COOH, -SH, -Biotin, -Alkanes). Some biomolecules cannot stand a dry-state and only the latter approach can be applied. We have increased the numbers of available functional groups two- and four-fold compared to the first generation of OptoDex. The higher surface density of biomolecules on these two photolinkers results in a higher bioactivity.

The characterization of OptoBOD® included the determination of photoreactivity, binding efficiency, biocompatibility, surface property and stability. The UV spectra of OptoBOD® are recorded before and after irradiation to detect the photoreactivity. The decrease of specific adsorption at 365 nm indicates that the polymer labelled with photoreactive groups were activated by UV light, thereby generating carbene radicals for covalent crosslinking (Figure 1).

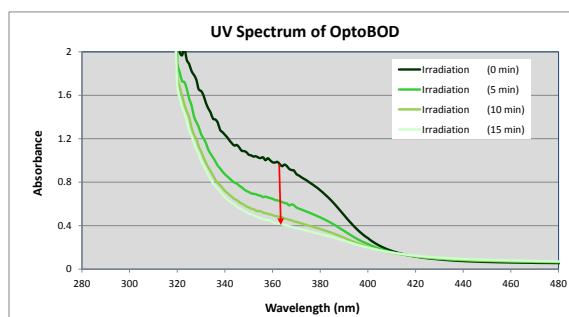


Figure 1: The UV spectra of OptoBOD® before and after irradiation, decreasing the adsorption at 365 nm, i.e. the specific wavelength of the photoreactive groups.

The binding efficiency of the photolinker polymers and the bioactivity of bound biomolecules were characterized by:

- i) Photoimmobilization of peroxidase on polystyrene (microtiter plate) and determination of enzymatic activity.
- ii) Photoimmobilization of monoclonal Anti-Peroxidase antibody onto polystyrene (microtiter plate), formation of immuno-complex by binding of peroxidase, and determination of

enzymatic activity. The results of both tests (Figure 2) demonstrate an efficient light-dependent covalent binding of biomolecules and that the immobilized biomolecules maintain their bioactivity. However, the background signal increased with increasing numbers of functional amino groups available on the polymer. This is caused by the enriched positive charges on the surfaces (Figure 2).

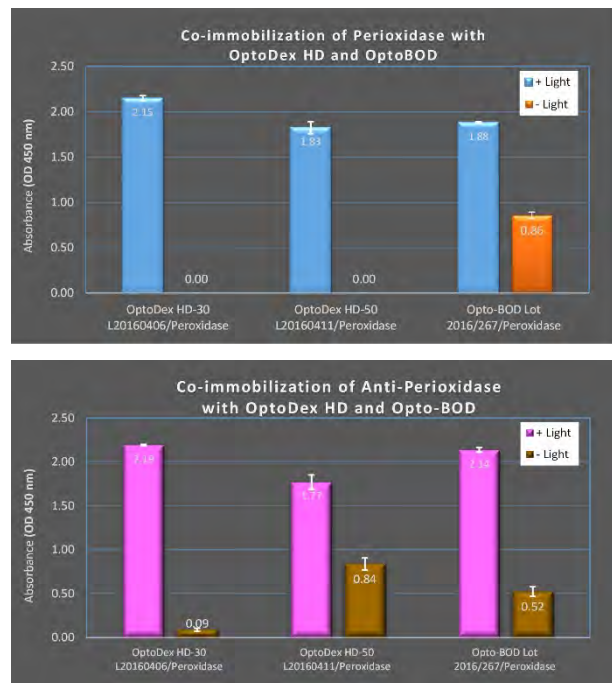


Figure 2: Photoimmobilization of peroxidase (top) or Anti-Peroxidase (bottom) on polystyrene (microtiter plate) and determination of remained enzymatic activity directly or after immuno-complex formation. Non-irradiated samples were used as controls.

The changes of material surface properties have been measured before and after coating with the photolinker polymers by contact angle measurement. All newly developed photolinker polymers (OptoBOD, OptoDex with high density functional groups) improve the wetting properties of materials (data not shown), i.e. the functionalized surfaces were more hydrophilic than the bare surfaces.

The two developments described here enlarge the CSEM family of photolinker polymers. They will allow to develop surfaces of more potent bioactivity, of higher stability, and of increased hydrophilicity.

Online Monitoring of Water Contaminants with an Optical Biosensor

H. Gao, D. Caminada

Water contaminants are an emerging challenge in the water management. Devices that can continuously monitor on or at site and are needed in order to guarantee a fast reaction time to incidents. CSEM's WIOS (Wavelength Interrogated Optical Sensing) system is a label-free optical biosensor and has been applied for the analysis of biologic samples. This project aims at demonstrating that it can be adopted for measuring relevant water contaminants such as atrazine in a robust, fast and reliable way. The monitoring workflow comply with automated sampling of different water matrices (e.g. lake water, seawater, treated sewage water, drinking water). The biochip can be regenerated repeatedly and forms the basis of the robust and competitive WIOS monitoring system.

There are several well-established methods to detect and quantitate contaminants (e.g. pesticides, drugs) in drinking and surface water by bioanalytical means. Most of them require a laboratory environment with a dedicated and usually bulky instrumentation as well as specifically trained personnel (e.g. mass-spectrometry, ELISA). The aim of the presented project is the development of a bioassay platform with the following characteristics:

- Reliable detection of several water contaminants, with sensitivities within the regulatory scope, and a time to result of less than 1 hour.
- A user-friendly detection platform, featuring a high degree of automation allowing robust operation and autonomy. The detection platform has to be operated by personnel not specially trained in performing bioassays.
- Cost efficiency concerning instrumentation as well as consumables.

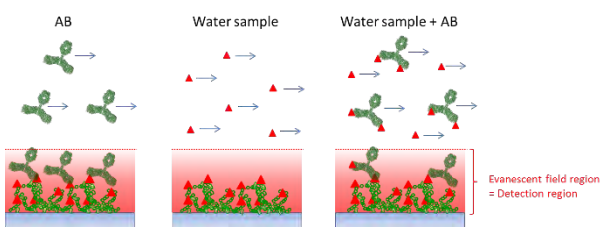


Figure 1: Schematic of the competitive ImmunoAssay on a label-free biosensor applied in this work.

The biosensing surface plays a crucial role in terms of stability, robustness and reproducibility of the system. Capture molecules (in particular small molecules) coupled to a dextran polymer (e.g. AtraDex) have been covalently bounded to the biochip surface using the OptoDex™ surface functionalization technology. The advantages are, (i) robust immobilization via multiple photobonding sites (mesh-like linking), (ii) well designable surface properties (e.g. density of capture molecules) and, (iii) suppression of non-specific binding due to the dextran basis of both, capture and cross-linker (OptoDex™) molecules.

In addition, AtraDex surfaces are very stable and a regeneration of more than 80 times is possible. These surfaces can be stored in buffer for at least 2 months and in dry state for at least one year without losing their properties. The synthesis of small molecules linked to dextran polymers seems therefore the method of choice also for other pesticides (or drugs) and water contaminants.

A competitive immunoassay (Figure 1) for the detection of atrazine has been developed and performed with the WIOS system (Figure 2). Figure 3 shows a calibration curve for the pesticide atrazine performed on the system. The sensitivity of

the instrument was shown to be below 10^{-6} refractive index units for bulk refractometry and the limit of detection for the adsorption of small molecules corresponded to a surface coverage of 0.3 pg/mm^2 . On the system, eight channels are available and can be measured simultaneously allowing the analyses of several contaminants including controls in parallel.



Figure 2: Schematic view of the WIOS system (right) and the automatic fluidic and sample preparation system (left).

In summary, the system allows to monitor online water contaminants with the following properties:

- Label-free sensing with WIOS
- Competitive immunoassay (antigen linked to surface)
- Multiple sensing surfaces (different characteristics)
- In-assay calibration/normalization
- Regenerative biochip (>80 times)
- Low detection limit of analyte ($0.02 \mu\text{g/L}$)
- Compensation of interfering effects

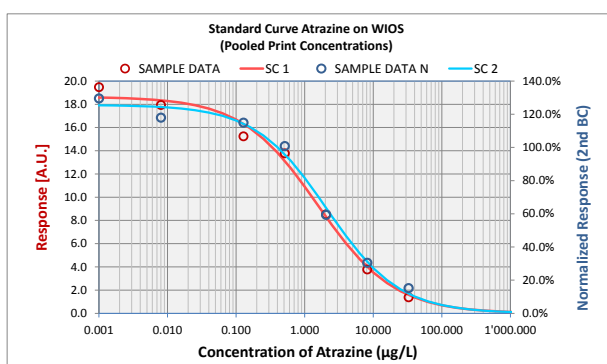


Figure 3: Fitted standard curve of atrazine measured on the WIOS system. Red fit: curve corresponds to response values without built-in calibration (in arbitrary WIOS units, left y-axis). Blue fit: calibrated with built-in calibration (in %, right y-axis) using a second response curve in the assay.

Detecting and Measuring Nanoparticles in Complex Matrices: the SMART-NANO Platform

D. Müller, C. Hofer, S. Cattaneo, L. Calzolai[•], H. Every^{••}, R. Welz^{•••}, K. Cunningham *, M. Portugal-Cohen **, D. Lyons***, S. Todeschi[•]

We report on the final integration of the complete SMART-NANO technology platform, which was developed to detect and characterize nanoparticles in various complex matrices, such as cosmetic products. The platform was shown to fulfill the performance requirements in four key application fields, while reducing cost, ecological impact and time required for the analysis of complex nanoparticle-containing samples

The current European regulations on cosmetic products and food require all ingredients present in the form of nanomaterials to be clearly indicated as such. Such a clear statement implies the need for comprehensive analytical procedures to thoroughly check the compliance of any manufacturer with these regulations. The analysis of nanoparticles in complex multicomponent media, such as emulsion-based cosmetic products, is however a complex process requiring several steps, including sample pre-treatment, the separation of the engineered nanoparticles (ENPs) from their matrix, and so on. The most pressing research needs hereby are the development of new analytical techniques for nanoparticle extraction, cleanup and separation, which should ideally improve the speed, sensitivity and specificity of the downstream analytical methods.

The project SMART-NANO tackled this complex needs by developing an innovative, cost-effective technology platform providing a total solution “from sample-to-result” for the detection, identification, and characterization of engineered nanoparticles (ENPs) in a wide range of matrices. The technology platform is based on a modular and scalable approach, which gives the flexibility to adapt towards new applications with minimal optimization. Four key application fields (Consumer Products, Food, Environment and Biota) were targeted through the development of specific ENP-containing model kits. Parallel to the development of the technology platform, a range of miniaturized, ready-to-use, cost-effective cartridges were developed, together with corresponding analytical protocols.

Previously, we reported on the development of a novel sample preparation method, the miniaturization of the employed particle separation cartridge, as well as the implementation of new UV absorption and Multi-Angle Light Scattering (MALS) prototype systems (see CSEM Scientific Reports 2012 – 2015). In the last year, all of those components were combined into the SMART-NANO technology platform (shown in Figure 1) and the new setup was extensively tested using ENP-containing kits specifically developed for the four application fields. These tests proved the efficacy of the SMART-NANO platform in detecting and characterizing ENPs in complex matrices, demonstrating significant advantages over currently used techniques. Key innovations introduced by SMART-

NANO include the use of inverse supercritical fluid extraction for the treatment of ENP-containing samples, as well as miniaturized, disposable cartridges for flow-field-flow fractionation. Overall, the benchmarking of the SMART-NANO platform confirmed that the platform fulfils the requirements of the application fields in terms of all analyzed parameters (accuracy, reliability, size, sensitivity, repeatability, linearity, LoD and LoQ), while reducing cost, ecological impact and time required for the analysis of complex ENP-containing samples. Most importantly, the presence of nanoparticles in complex samples could be unequivocally demonstrated, and accurate size distribution could be obtained in the vast majority of samples, including the highly relevant case of cosmetic creams.

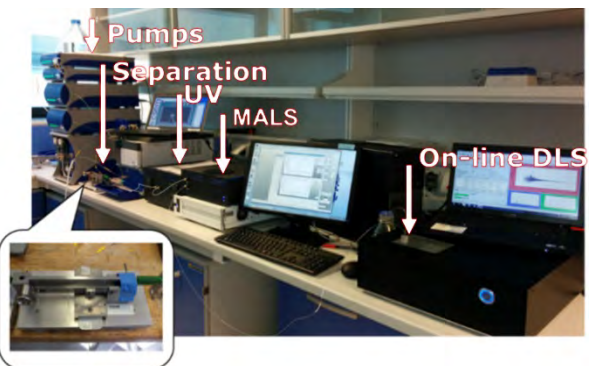


Figure 1: The complete SMART-NANO technology platform, incorporating all the newly developed sample treatment and analysis modules.

The SMART-NANO consortium was formed by 8 partners (3 academia and 5 SME's) from 8 different countries and led by CSEM as the project coordinator. The balance between industrial and academic partners was one of the key strengths of the project, ensuring the alignment between research efforts and industrial requirements. The results of the SMART-NANO project led to several publications in leading scientific journals and conference presentations. The commercial exploitation of the results has already started with the commercialization of key components of the platform, and will continue with the development of a fully integrated system in the following years.

This work was supported by the European Commission 7th Framework Programme (project SMART-NANO, NMP4-SE-2012-280779). CSEM thanks them for their support.

* Joint Research Center (JRC), Ispra, Italy

** Feyecon Carbon Dioxide Technologies, Weesp, The Netherlands

*** Postnova Analytics GmbH, Landsberg am Lech, Germany

* AvidNano Inc., London, United Kingdom

** AHAVA Dead Sea Laboratories, Lod, Israel

*** Ruđer Bošković Institute, Rovinj, Croatia

• Abich S.r.l., Verbania, Italy

Fluorescence Lifetime Imaging (FLIM) made easy

S. Cattaneo, C. Hofer, H.-R. Graf, A. Bischof, B. Schaffer, S. Emery

We report on the development of a compact, stand-alone prototype for real-time, wide-field fluorescence lifetime imaging (FLIM) in the frequency domain. The prototype yields a 2D map of fluorescent lifetimes in the nano- to microsecond range without the need for scanning. Its portable size, low cost and ease of use show potential for a variety of applications based on monitoring fluorescence lifetime.

Fluorescence signals are characterized by three main parameters: intensity, wavelength and lifetime^[1]. The fluorescence intensity depends on the concentration of the fluorophore and its quantum efficiency. Fluorescence intensity images therefore yield the spatial distribution of a fluorophore. The emission spectrum is a characteristic of the fluorophore. Images containing spectral information thus allow different fluorophores to be identified. The third property, the fluorescence lifetime, depends on the type of the fluorophore and on the molecular environment surrounding it. It is influenced by the presence of fluorescence quenchers, by binding of the fluorophore to different biological targets, or by the presence of other optical absorbers to which it may interact. Fluorescence lifetime imaging (FLIM) can therefore be used to obtain information on the molecular environment of the fluorophore molecules, or to identify fluorophores based on their fluorescent lifetime^[2]. Unfortunately, fluorescence lifetime imaging has traditionally been associated with complex and expensive equipment, and has therefore found limited applications outside of research laboratories.

To demonstrate the potential of FLIM and open the door to novel applications, we developed a compact, stand-alone prototype incorporating all the necessary hardware components for wide-field frequency-domain FLIM (Figure 1).

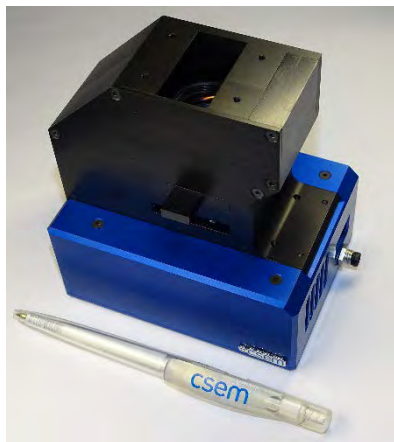


Figure 1: Compact stand-alone prototype for real-time, wide-field fluorescence lifetime imaging (FLIM) in the nano- to microsecond range.

The prototype includes a modulated light source (LED), a CMOS Time-of-Flight imager (256×256 pixels), dedicated FPGA-based electronics, and optical components for illuminating the probe and collecting the fluorescence emission.

^[1] J. R. Lakowicz (Ed.), "Principles of fluorescence spectroscopy", Springer Science & Business Media (2013).

The camera electronics is based on a stacked PCB approach, including a base board, a FPGA processing module and a sensor head PCB. A MATLAB GUI running on a separate PC is used to set the measurement parameters (such as modulation frequency, illumination intensity and integration time) and display the results. The optical modulation frequency can be varied between 3 kHz and 20 MHz, allowing the measurement of fluorescence lifetimes from hundreds of microseconds down to a few nanoseconds.

The FLIM prototype yields a 2D map of fluorescent lifetimes in a single shot (Figure 2), without the need for scanning. With the current optics an area of 6×6 mm is imaged. The emission wavelength can be selected by exchangeable spectral filters.

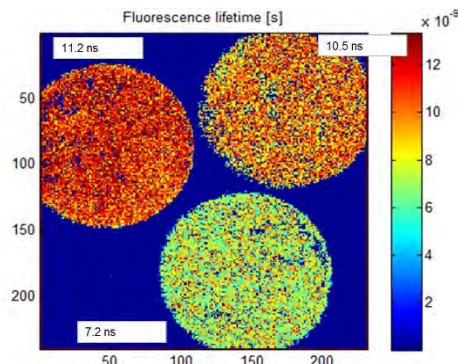


Figure 2: 2D map of fluorescence lifetime obtained with the FLIM prototype, showing lifetime differences on the order of a few nanoseconds.

The FLIM prototype was benchmarked against several high-end commercial FLIM systems on a wide range of fluorescent probes. In general a good agreement was found, although in some cases deviations between instruments (even commercial ones) were observed. The performance of the CSEM prototype was essentially on par with high-end systems, despite a considerably reduced size and cost.

Current applications of the FLIM system are in the field of wound monitoring and chemical sensing (oxygen, pH), but other applications in the nondestructive analysis of probes, either based on fluorescence tags (anti-counterfeiting, forensics, etc.) or on auto-fluorescence (food analysis, medical diagnostics, etc.) can be envisaged.

The work was supported by Nano-Tera (RTD project FlusiTEx) and by the CTI (project SecureFLIM). CSEM would like to thank them for their financial support.

^[2] M. Y. Berezin, S. Achilefu, "Fluorescence lifetime measurements and biological imaging", Chemical reviews, 110 (2010) 2641.

Cell-based Microfluidic Chip to Study Bone Healing Mechanisms

M. Herrmann •, Z. Wang, M. Alini •, S. Verrier •, L. Barbe

Microfluidic technologies permit the replication in vitro of geometrical features essential for the homeostasis of all vascularized tissues in vivo. These in vitro models aim at reducing animal testing for drug development and at bringing a modular tool for mechanistic studies.

A functional microvasculature is critical for the homeostasis of all vascularized tissues. Accordingly, several diseases are associated with alterations in the microvasculature, like for instance in tumor angiogenesis. Furthermore, the formation of new vessels by angiogenesis is critical in the restoration of tissue function. In tissue engineering, sufficient neovascularization is thought to be a prerequisite for the integration of the implant. These conditions have been extensively studied in animal models. However, in vivo studies have several limitations, including species differences and limited possibilities for imaging and tracking cells in the living animal. They also do not permit high-throughput and multiplexing applications. The development of microfluidic models of microvasculature and the endothelial barrier could help to overcome these problems, and most importantly, would replace a significant amount of animal experimentation^[1].

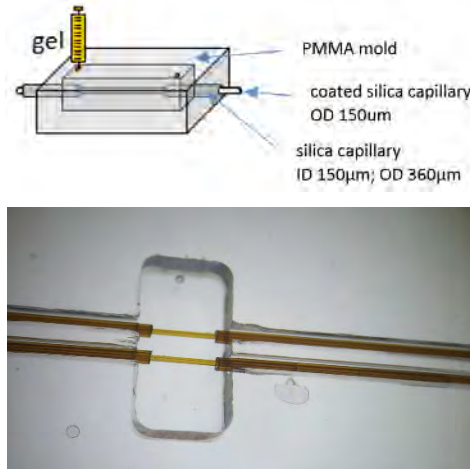


Figure 1: Drawing of the microfluidic device (top); microscopic picture of the chamber containing thin capillaries used as molds (bottom).

CSEM and the AO Research Institute in Davos (Switzerland) addressed this problem by developing a microfluidic device mimicking microvessels (diameter between 100 and 200 µm).

- AO Research Institute, Davos, Switzerland

This tool allows to study the interactions of various factors with the endothelium over the course of several days.

In order to create a perfusable microvessel, micromolding in a biocompatible hydrogel has been used, as shown in Figure 1. A cavity micro-machined in a thermoplastic layer is crossed by a microcapillary. A gel is injected and after polymerization, the capillary removed, thus leaving a cylindrical void (Figure 1, bottom and Figure 2A). The wall of the microchannel is subsequently covered by different cell types (Figure 2B). In order to bring nutrients to the cells, a perfusion system, comprising of piezo-electric pumps, reservoirs and bubble trap, was developed.

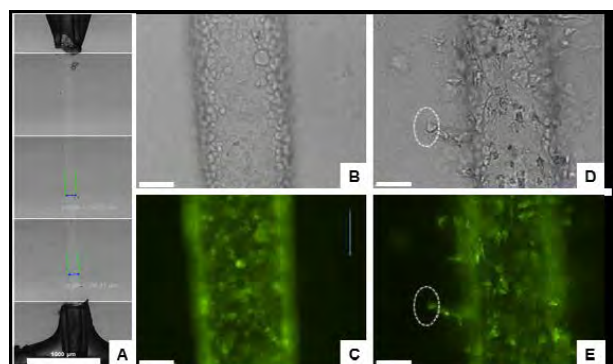


Figure 2: A) Microchannel within collagen gel. B-E. High magnification images of the microchannel seeded with GFP-HUVECs after 1 h (B, C) or 28 h (D, E) of perfusion. Dotted circles indicate areas of sprouting. Scale bars 1000 µm (A); 100 µm (B-E).

This system allowed to observe endothelial cells up to 100 hours under physiological conditions, using time-lapse microscopy and fluorescence imaging.

The next iteration of this platform will bring more complexity to the in-vitro model, as well as increasing the throughput.

CSEM would like to thank the 3R foundation for their financial support.

^[1] L. Barbe, M. Alini, S. Verrier, M. Herrmann, "In vitro models to mimic the endothelial barrier", ATLA, 43 (2015) 34.

Microfluidic in-vitro Model of Bladder Cancer for Drug Profiling

Z. Wang, C. Oehler •, R. Strelbel •, D. Zwahlen •, L. Barbe

Physiologically relevant in-vitro models are required tools to precisely study cancer progression and to develop efficient therapies. Combining microfluidics and 3D cell culture, this simple platform aims at providing an insightful tool for drug screening.

Bladder cancer is the fifth most common cancer in Western society, with the global burden predicted to increase significantly in the foreseeable future (383'000 cases worldwide in 2008^[1]). Three quarters of all cases are diagnosed as superficial disease. Whilst half of these cases are cured by simple surgical treatment, about half will develop recurrences. 20-25% of patients develop more aggressive tumors requiring stronger therapies and carrying significantly worse survival rates. Therefore, there is a need to better understand the mechanisms involved in tumor progression and recurrence. The recently identified bladder cancer stem cells are considered to be mediators of resistance to current therapies and therefore represent strong candidates of biological targets for next generation therapies.

The goal of this project is to develop an easy and relevant 3D in-vitro assay in order to evaluate therapies targeting cancer stem cells, thus providing a better diagnostic tool towards personalized medicine.

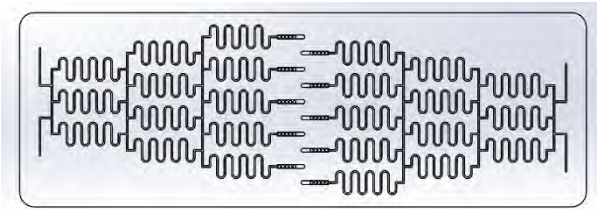


Figure 1: CAD drawing of the microfluidic chip with a gradient generator and spheroid traps in the center. Dimensions of the chip are 75 × 25 mm.

Anticancer drug discovery has been hampered by the poor prediction of the preclinical models, leading to a large attrition rate and high costs. In the last 15 years three-dimensional (3D) cell culture systems have shown to provide more accurate physiologically relevant environments compared to their 2D counterparts. However, most studies are using cell aggregates (spheroids) in static conditions, not reflecting physiological conditions where tumors are vascularized.

In this project, CSEM developed a microfluidic chip for drug efficacy screening, combining perfusion and 3D cell culture. The design shown in Figure 1 comprises of a microfluidic gradient generator to facilitate the handling and testing a multiple conditions on the same chip. The chip, made of a thermoplastic, can be connected to a portable pressure-driven perfusion system. At this stage, spheroids were prepared in a

different device using the hanging drop technique, and subsequently loaded into the microfluidic chip. In the next iteration of the chip design, spheroids will be formed in the same chip.

Perfusion allows to bring nutrients to the spheroids as well as chemotherapeutic agents to be tested, and reagents to assess their efficacy. Figure 2 (left side) shows a part of the microfluidic chip where spheroids are loaded and perfused.

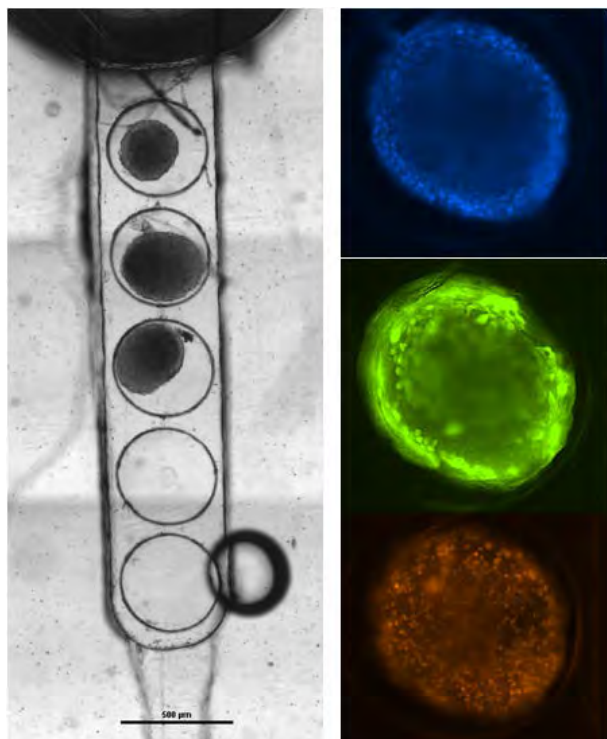


Figure 2: Microscopic image of the microfluidic chip. Microcavities containing 3 tumor spheroids (left); fluorescence imaging of the spheroid (right), labeled with fluorophores for the cell nuclei (blue), live cells (green) and dead cells (red).

The right inset of Figure 2 depicts fluorescent staining of a spheroid, providing quantifiable data on the potency of the tested anti-cancer drugs.

The next step will be to use cells extracted from patient biopsy, to eventually allow tailored therapies.

CSEM would like to thank Graubünden Krebsliga for their financial support.

• Graubünden Kantonsspital, Chur, Switzerland

[1] G. B. Boustead, S. Fowler, R. Swamy, R. Kocklebergh, L. Hounsome, "Stage, grade and pathological characteristics of bladder cancer in the UK", BJU International, 113 (2014), 924.

Wearable Sensors for Ion Monitoring

M. Viviani, T. Parkel, R. Junuzovic, D. Migliorelli, F. Pereira, S. Generelli

Fitness trackers, and more in general wearable wellness monitoring devices have become in the last years a common tool, sold in millions of pieces. The integration of additional markers for the evaluation of the metabolic status of the body is the natural evolution of them, and would open the way for the application of wearables in healthcare and at-home patient tracking.

The last years have seen the rapid and widespread adoption of fitness trackers going to nearly zero in 2010 to several million users in 2016 [1]. The latest developments in the wearable world are going mostly in the direction of combining the vital signs sensors as heart rate, temperature, etc. with sensors for metabolic markers. In order to provide an affordable solution for the professional and non-professional athletes market, CSEM is developing solutions for disposable, flexible sensors for potassium ion, sodium ion, glucose, lactate, pH, sweat rate and impedance that can be eventually integrated in wearable solutions.

The first sweat monitoring device developed at CSEM focusses on pH, potassium ion and sodium ion, parameters related to the hydration state of the body. The pH sensors cover a range of pH 3-9, potassium and sodium ion sensors with a linear range of 0.1 mM to 100 mM, and 0.1 mM to 200 mM, respectively (characterization in artificial sweat). All these disposable sensors can be used with minimal preconditioning and are stable for 2 hours, the time of a typical workout session.

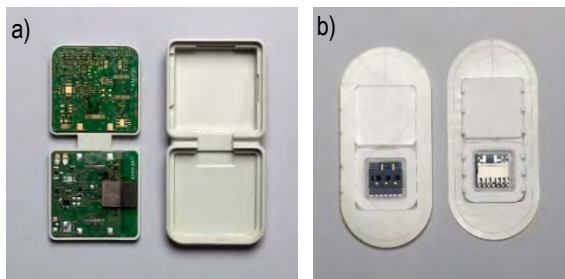


Figure 1: The wearable sweat monitoring device comprises of two parts: a) Flexible data acquisition and transmission electronics; b) Disposable sweat monitoring patch.



Figure 2: The sweat monitoring device is placed on the back of a test subject.

The wearable device comprises a re-usable part, including data collection and transmission electronics, connected by Bluetooth to a portable device and sending data in real-time. The sweat monitoring sensors are printed on a disposable patch, which is used to fix the system on the athlete's body (Figures 1 and 2).

The device was used for on-body measurements during a session of ergometer cycling. The parameters measured after 15 minutes warm up from the ergometer, as well as an example of the real-time data for temperature, heart rate, pH, K⁺ and Na⁺ are shown in Figure 3.

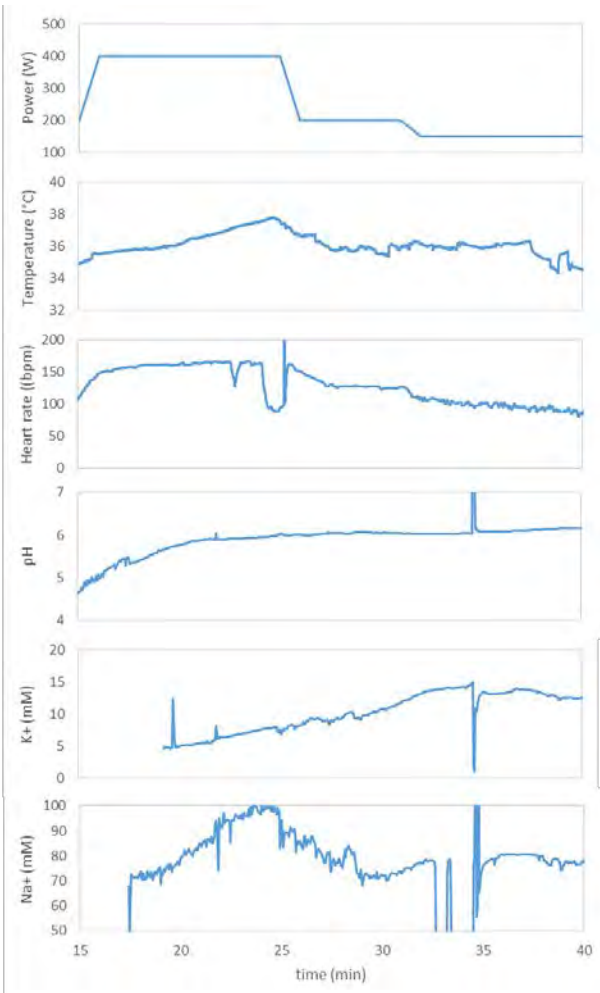


Figure 3: Real-time data collected during an ergometer session. From top to bottom: power set on the ergometer, temperature measured at the forearm and heart rate monitored at the fingertip, both measured with a BioRadio wireless physiology monitor, pH, K⁺ concentration and Na⁺ concentration, measured with the wearable sweat monitoring device, placed on the back of the test subject.

[1] www.statista.com

Rapid and Cost-effective Detection of Tuberculosis (TB)

S. Generelli, D. Migliorelli, H. Chai-Gao, S. Paoletti, T. Broger •

High costs are often among the major limitations to a widespread use of diagnostics tools at scale, especially in resource-limited regions. A simple, rapid, sensitive, biomarker-based, point-of-care TB diagnostic that makes use of an easily accessible sample like urine is considered to be one of the most urgently needed test by expert stakeholder groups. In collaboration with FIND^[1] we are working on addressing this unmet need through the development of an assay for the rapid and highly-sensitive detection of Lipoarabinomannan (LAM) in urine using a combination of bead-based analyte concentration technology and detection with Screen Printed Electrodes (SPEs).

Two weeks of cough is a widely used symptomatic indicator to identify individuals with presumed active pulmonary tuberculosis (TB) who require diagnostic testing. Since most individuals with suspected TB do not have TB, a triage test can help narrow down the population that needs the more costly confirmatory testing^[1]. A triage test is a simple, low-cost test for use by community health workers to rule out TB and direct individuals who require further evaluation (i.e. triage test positive) via a confirmatory test. Triage testing could take place at the same level of care as confirmatory testing especially in settings with a large influx of patients (e.g. crowded outpatient clinics), but typically would be done at lower levels of care (e.g. microscopy centre, primary care clinics, etc.). If the test turns out to be specific enough, it could even be used to diagnose TB and immediate treatment initiation (without confirmatory testing).

Commercially available point of care tests, based on lateral flow immunoassays have a too high detection limit, estimated to 500 pg/ml, not adapted for sensitive detection in patients suspected of having TB.

In order to respond to this unmet need, an improved LAM detection assay was developed in our labs based on antibodies provided by FIND. The target detection limit stated by FIND of 50 pg/ml was achieved, with a potential for further improvement to an estimated detection limit of less than 10 pg/ml (background +3 standard deviations) (Figure 1).

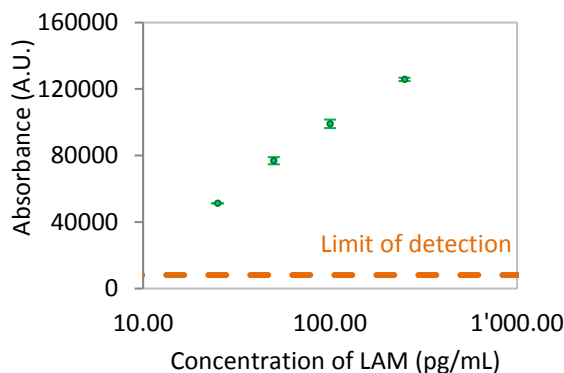


Figure 1: Calibration curve of LAM in PBS buffer.

- FIND Switzerland

The improved assay is being used as the basis for the development of a simple to use, cost-effective and rapid assay, compatible with the large-scale deployment in health care institutions.

CSEM has developed a process for diagnostics using Screen Printed Electrodes (SPEs) in combination with functionalized magnetic particles. This system was used in the past for the detection of TB biomarker ESAT-6 in a saliva matrix.

The process consists mainly of:

- Pre-concentration step: in order to collect the biomarkers of interest in a simple preparation procedure, functionalized magnetic particles were used. In addition the use of the chosen sample pre-concentration strategy allows the subsequent detection and quantification to be more sensitive and reach lower detection limits
- Detection step: Screen Printed Electrodes (SPEs) are cost effective, disposable devices that can be miniaturized and integrated in disposable microfluidic cartridges, if necessary, to work with sample volumes in the microliter range. SPEs will be used as the matrix to perform and quantify sandwich-type immunoassay.

The two pre-concentration and detection steps can be used in concomitance with each other, or used separately. For example, the pre-concentration step may be used as a pre-purification and pre-concentration step for the subsequent detection using commercially available ELISA detection kits or lateral flow immuno-chromatographic assays. This approach is applicable and adaptable for diagnostics on various body fluids as for example saliva, sputum, urine and of course blood.

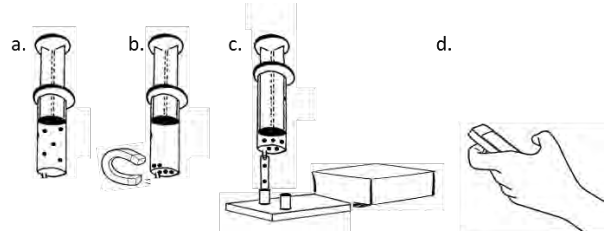


Figure 2: Schematic of the diagnostic assay. a) Sample collection and incubation; b) Pre-concentration; c) Injection in automated sensing device and further incubations; d) Data are sent to the user interface.

[1] www.finddx.org

Glucose Sensors on Demand

D. Migliorelli, R. Junuzovic, L. Mühlebach, M. Dias Figueiredo Nogueira, S. Generelli

Since several years there is a clear trend towards disposable sensing technology for different applications. Especially in the medical field there is an extraordinary need and demand from the diabetic community, since blood glucose measurement for the management of diabetes comprises approximately 85% of the world market for biosensors. The same trend can be observed in biotech applications: with the increasing adoption of disposable bioreactors the demand for components for on-line control of such disposable bioreactors increased as well.

Despite the many technological advances in biosensor research and development and the introduction of many different products, glucose biosensors still account for approximately 85% of the current world market for biosensors [1]. The reasons why the glucose market was particularly receptive to the introduction of biosensors are numerous, but the single greatest factor was the prevalence of diabetes in developed nations. Electrochemical biosensors (Figure 1), with their ability to give a rapid, accurate answer using a disposable strip, with no possibility of instrument contamination, have dominated the market in the last years.



Figure 1: Glucose sensor strip [1].

The same type of sensors found more recently an application in the field of bioprocess optimization and control. A clear trend towards disposable technology in this field (Figure 2) lead to the increasing demand of on-line measuring devices, for measuring not only pH and dissolved oxygen (DO_2) but also glucose, lactate, CO_2 and other parameters. The relative lack of single-use sensors in the market is limiting the adoption of this single-use technologies.



Figure 2: Biosensor integrated in a single use bioreactor [2].

In order to be in line with the very different specifications these applications require, it is necessary to have a technology for the fabrication of glucose sensors with a linear range that can be modulated depending on the target application. Indeed, blood glucose analysis, both point of care and implanted, need a linear range between 1 mM–30 mM, whereas a much more sensitive range is required for the bioreactor monitoring, which can be between 1 μM –5 mM.

In order to respond to this request, our laboratory developed a method, using the screen printed technology, based on the

modification of the polymeric enzymatic membrane, in order to manipulate the linear range of the glucose sensors.

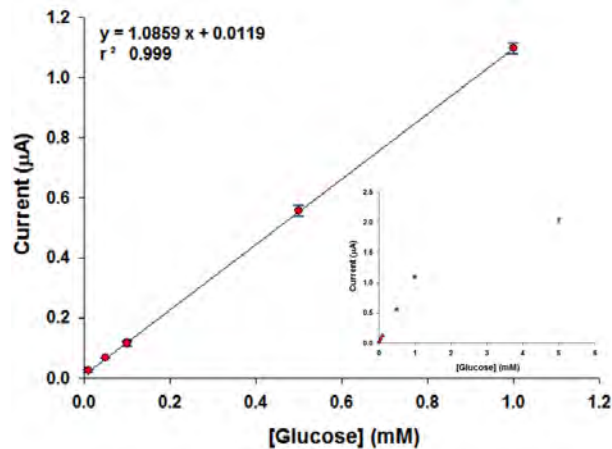


Figure 3: An example of glucose sensor calibration presenting a linear response in the lower concentration range 5 μM –1 mM. Glucose calibration curve in phosphate buffer 0.05 M + KCl 0.1 M pH 7.4.

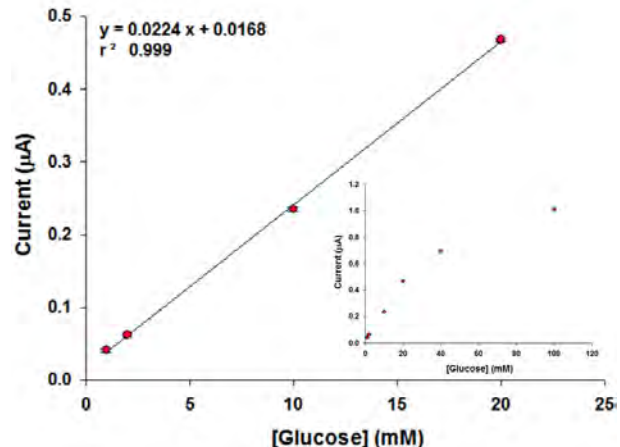


Figure 4: An example of glucose sensor calibration presenting a linear range in the higher concentration range 1 mM–20 mM. Glucose calibration curve in phosphate buffer 0.05 M + KCl 0.1 M pH 7.4

As it is showed in the graphics above (Figures 3 and 4), it is possible to obtain either a high sensitive glucose sensors with a linear range between 5 μM –1 mM (Figure 3), suitable for applications where low detection limit for glucose is required, or less sensitive glucose sensor, but able to recognize glucose concentrations up to 100 mM, with a linear range between 1 mM–20 mM (Figure 4), applicable for blood glucose analysis.

[1] A. P.F. Turner, Chem. Soc. Rev., 2013, 42, 3184.

[2] www.tvc.utah.edu/2015annualreport/applied_biosensors.php

Controlled, Pressure-driven, Sequential Actuation of Fluids for a Food Quality Monitoring System

J. Goldowsky, S. F. Graf, T. Volden, H. F. Knapp

Numerous dispensing and dosing solutions for a broad range of applications such as life sciences are available, all with their individual advantages. However, when working with aggressive solvents, most of these solutions are not suitable due to material incompatibility of tubing or inline sensors. Some of these solutions also fail for mobile applications due to their weight and size. For a mobile food quality monitoring system, we have implemented our controlled pressure driven dispensing system which precisely and contact-less measures the volume dispensed out of a bottle. It only requires one valve located in fluid communication, which is available for high chemical resistance. One lightweight control unit can be used to dispense from multiple bottles filled with different solvents. Further the system offers the capability to dispense gases with the same precision as for liquids. In our specific application, water, acetonitrile, and air are dispensed in volumes of $100 \mu\text{l}$ up to 10 ml with accuracies of about 3%. The resulting continuous and pulsation-free flow is advantageous for many microfluidic applications.

Based on the fundamental principles of the ideal gas law, a low-cost, small outline control unit has been developed which enables the precise dispensing of critical liquids such as acetonitrile, hexane and other solvents as much as gases (air) and water from containments that can be pressurized. While pressurizing the containment, the pressure trend is evaluated and the encapsulated gas volume is calculated. For known containment volumes this gives direct feedback of its fill-level and enables automatic refilling or messaging to the user to request refilling where appropriate. Once the gas volume is detected this information is used for calculating target pressure points when dispensing (see Figure 1). For more details refer to Graf, et al. [1]

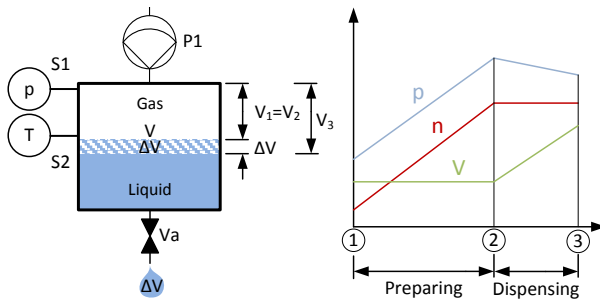


Figure 1: (left) Schematics of the device; (right) Gas parameter change during containment compression and liquid dosing.

This dispensing method combines the benefits of time pressure dispensing (TPD) with additional direct sensing of the dispensed amount of liquid. Hence differences in viscosity of the medium or flow resistance of the system (filter, SPE, etc.) are not important. Due to the working principle compressing the gas volume needs a few seconds, so that first dosing cannot be performed instantaneously. After performing this initial procedure, fast dispensing is possible.

As the system operates only with a pressure sensor - in fluid communication with the gas volume - one control unit can be used to sequentially dispense from a multitude of containments. This can be done by actively selecting the containment to be dispensed from, without recompressing the containment [2]. By

that system outline and weight are reduced, when compared to getting the same functionality with multiple syringe pumps even drastically. Additionally various types of containments can be used within one system setup. The system for food quality monitoring uses standard 80 ml and 150 ml laboratory bottles. Compared to syringe pumps this allows the dispensing of high amounts of liquids without additional effort of refilling the syringe for dispensing.



Figure 2: Food quality monitoring system integrating a controlled, pressure driven dispensing subsystem (all five bottles are controlled).

The control automatically detects clogging of the downstream fluidic system as well as leakage of the gas volumes and enables therefore an advanced system monitoring when incorporated in automated systems.

Two versions of the system (bottle cap and multi-bottle actuation Figure 2) have been tested for volumes between a few ml and $100 \mu\text{l}$. However, due to the underlying physical principles the system is scalable, both, to higher and smaller volumes and one can expect comparable dispensing deviations.

This work was supported by the Swiss federation, MCCS Micro Center Central Switzerland, and the European Commission (FP7-611528 BIOFOS). CSEM thanks them for their support.

[1] S. F. Graf, J. Goldowsky, H. F. Knapp, "Compact, Pressure-based Flow System for Sequential Actuation of Fluids with Integrated Flow Monitoring", CSEM Scientific and Technical Report (2014), 114.

[2] S. F. Graf, J. Goldowsky, T. Volden, H. F. Knapp, "Automation of Traditional Sample Preparation for Oil, Milk, and Nuts", CSEM Scientific and Technical Report (2015), 50.

RASECAN—Parallel AFM for Rapid Cancer Diagnosis

G. Weder, R. Ischer, M. Favre, M. Liley, H. Heinzelmann, M. Despont

Changes in cell stiffness (and extracellular matrix) are characteristic of breast cancer cells and affect disease prognosis. Indentation atomic force microscope (AFM) on biopsy samples of living breast tissues shows different stiffness profiles for benign and malignant tissues. CSEM is developing a new parallel AFM diagnostic tool using parallelized mechanical sensors to analyze breast tissues within fifteen minutes, for hospital use.

Cancer initiation and progression are accompanied at the molecular level by complex structural changes in both cells and extracellular matrix^[1]. The histological analysis of breast cancer biopsies is currently a slow and qualitative process taking several days and requiring an expert visual evaluation of the samples. However, recent scientific work has demonstrated an alternative approach to histological analysis: the use of atomic force microscopy (AFM) to measure the local mechanical properties of the breast biopsy samples. Typical stiffness profiles have been correlated to histopathological analysis of healthy and malignant human breast tissues (Figure 1) demonstrating a correspondence of the two approaches. These distinct nanomechanical signatures of breast cancer can be used as a diagnostic tool.

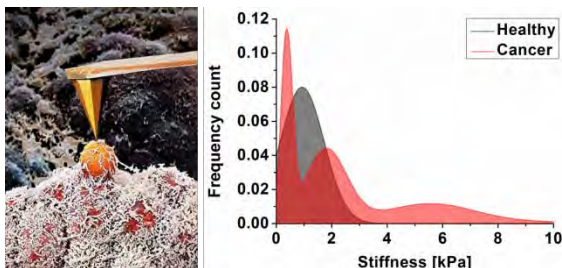


Figure 1: Nanometer-scale palpation of breast tissue (left) and (right) typical mechanical profiles of healthy (single peak in grey) and cancerous (multiple peaks in red) tissues.

AFM is the ideal tool to reliably and quantitatively investigate the mechanical properties of breast biopsies. However, it is slow. AFM analysis of a single biopsy sample requires the acquisition of around 15'000 individual force displacement curves since a large number of measurements are required for a statistically meaningful set of data. This is a significant limitation because one of the major obstacles for a routine use of AFM analysis in hospitals is the diagnostic time which currently takes several hours.

CSEM is addressing the need for reduced analysis time by developing a new AFM diagnostic tool using parallelized mechanical sensors. The objective is to reduce data acquisition time from hours to minutes. This new instrument is based on an existing commercial AFM-based diagnostic tool called ARTIDIS® (Automated and Reliable Tissue DiagnosticS) from Nuomedis/Nanosurf that performs highly automated but serial measurements. The standard procedure starts with a breast biopsy of the suspicious lesion under ultrasound imaging guidance. Multiple stiffness maps are then acquired across the entire biopsy using one AFM cantilever. The replacement of this single cantilever by a 1D array of cantilevers - eight cantilevers operating in parallel – involves an innovative parallel read-out

of the probes. Compared to the current state of the art where only one probe is used, these arrays will reduce the data acquisition time by a factor of eight.

The strategy consists of reading the 1D cantilever array by eight semiconductor lasers (VCSELs, Vertical Cavity Surface Emitting Laser). Each laser beam is focused on the end of one of the cantilevers (Figure 2), with the reflection monitored by a position sensitive photodetector. A major technical challenge of the project is the implementation of a simple system for the alignment of VCSELs, optical systems, cantilevers and sample.

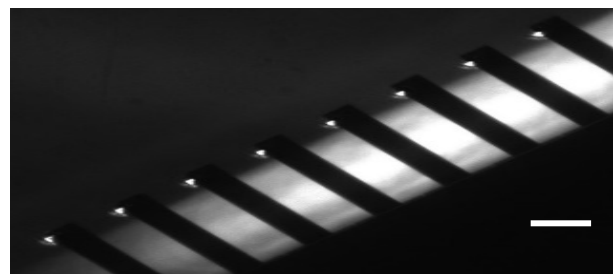


Figure 2: Optical image of a 1D array probe composed of eight cantilevers and their lasers during alignment (scale bar 250 μm).

The first phase of the project yielded the proof-of-principle with ultrafast readout of a 1D cantilever array and parallel force spectroscopy demonstrated on hydrogels of similar stiffness to living tissues. Currently, the second phase is approaching a working prototype (Figure 3). An easy-to-use alignment system has been miniaturized and integrated in the ARTIDIS instrument, while packaging and drivers for the VCSEL arrays have been implemented. The first force displacement curves have been acquired in parallel on hydrogels. Throughout testing and validation of the prototype, it was observed that reduction of biopsy roughness might be required to facilitate the parallel measurements.

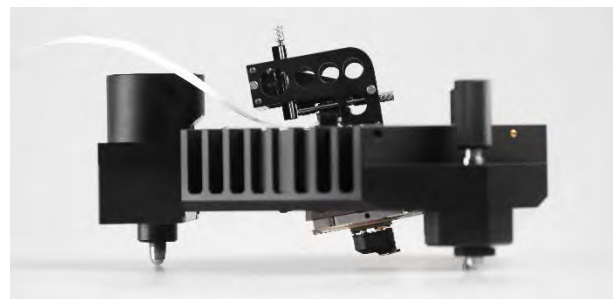


Figure 3: The parallel AFM prototype, with the mechanical laser alignment (top) and the probe array holder (bottom).

This work is partially funded by the Swiss research program Nano-Tera.

^[1] M. Plodinec, et al., "The nanomechanical signature of breast cancer", *Nature Nanotechnology*, 7, 2012, 757-765.

System for Airborne Nanofibers Exposure Monitoring

D. Schmid, G. Andreatta, D. Bayat, S. Bitterli, S. Cattaneo, P.-A. Clerc, O. Dubochet, K. Krasnopski, P. Niedermann, G. Orawez, R. Pugin, I. Dolamic[•], T. Bürgi[•], R. Bieri^{••}, J. Borek-Donten^{••}, B. Zijlstra^{••}

Today's advances in man-made nanomaterials bring new and unprecedented risks to employees along the whole value chain. Airborne, inhalable nanofibers pose asbestos-like health risks when inhaled. CSEM developed with Stat Peel AG and the University of Geneva a compact dosimeter for the selective detection of airborne nanofibers, e.g. carbon nanotubes (CNTs), in workplaces.

Asbestos fibers have undisputable technical qualities. However, history taught us a painful lesson: prolonged inhalation caused fatal illness (lung cancer, mesothelioma), leading to more than 2 million deaths worldwide. Today, asbestos fibers are banned, but new, highly promising materials, such as carbon nanofibers (CNTs), emerged and are praised for their exceptional properties: Are we about to make the same mistake again?

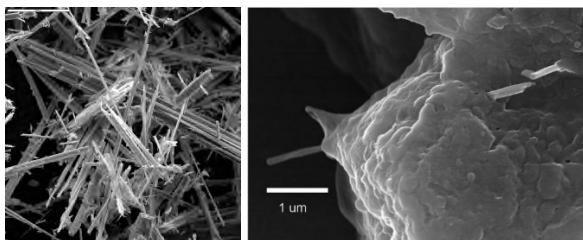


Figure 1: Left: Asbestos fibers^[1] (left); MWCNT penetrating alveolar epithelial cells of the lung^[2] (right).

As the use of nanomaterials grows, so do the dangers. Nanofibers can pose health risks^[3] and existing devices cannot detect CNTs reliably and discern them from less harmful particles like pollen, dust or carbon black from diesel exhaust. Both, SUVA and NIOSH (US institute for occupational safety and health) proclaim that all types of CNTs should be considered an occupational respiratory hazard.



Figure 2: Airborne nanofibers detection system.

Stat Peel has developed together with CSEM and University of Geneva a system, based on a wearable unit and a desktop reader that will protect both employees' health and employers' liability. The high-tech but easy to use detection system can monitor an individual's long-term exposure to nanotubes in

workplaces. It allows university labs, R&D departments, start-ups, fiber producers and any company using material containing CNTs to monitor every individual employee – a must-do in any occupational environment.

Health effects resulting from deposition of an aerosol in the respiratory tract depend on the dose received and the body's response to the particles. Continuous monitoring is therefore needed with a wearable dosimeter, worn by employees in risk of exposure, close to the personal breathing zone, reflecting the inhaled dose, which can differentiate between inhalable, thoracic and respirable fractions.

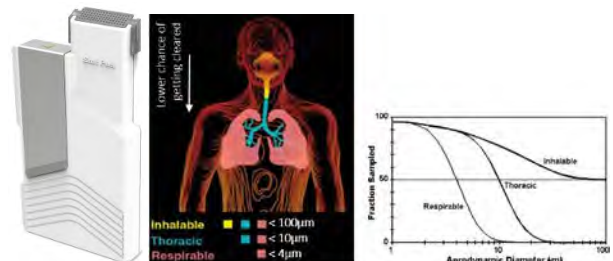


Figure 3: Wearable sampling unit for airborne nanofibers, enabling a differentiation between different size fractions.

The features of the developed system include:

- unprecedented selectivity, distinguishing CNTs from dust and carbon black, even different CNT types
- 10⁴ times lower limit of detection (absolute 0.2 ng) than the recommended exposure limit by NIOSH
- more than 10³ times lower limit of detection than state of the art thermal optical analysis for elemental carbon^[4]

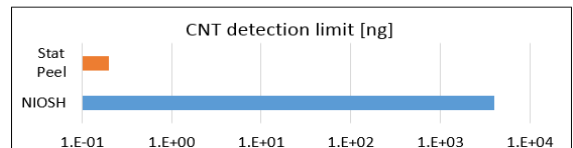


Figure 4: Stat Peel 10'000 lower limit of detection compared with NIOSH recommended exposure limit.

The monitoring technology is based CSEM's expertise in nanotechnology, microfabrication, microfluidics, low-power electronics for wearables and system integration. The system can be adapted to detect different types of airborne nanofibers.

- University of Geneva, Department of Chemical Physics
- Stat Peel AG, Glarus, Switzerland, statpeel.com
- <http://usgsprobe.cr.usgs.gov/picts2.html>
- R. Mercer et al. Distribution and persistence of pleural penetrations by MWCNT. Particle Fibre Toxicology 7:28.

[3] K. Yamashita et al. CNTs elicit DNA damage and inflammatory response relative to size and shape. Inflammation 33: 276-280.

[4] NIOSH. Occupational Exposure to Carbon Nanotubes and Nanofibers. Current Intelligence Bulletin 65.

Asymmetric Color Appearance with Aluminum Plasmonic Substrates

L. Duempelmann, B. Gallinet, D. Casari, A. Luu-Dinh, G. Basset, M. Schnieper

We demonstrate tilted nanostructured aluminum lamellas showing asymmetric optical appearance [1]. In particular they show a switch from colorless to colorful transmission. Such an effect is very valuable for applications in optical security. The fabrication of the structure utilizes the earth abundant aluminum and is compatible to roll-to-roll processes thus allowing cost-efficient large-scale production.

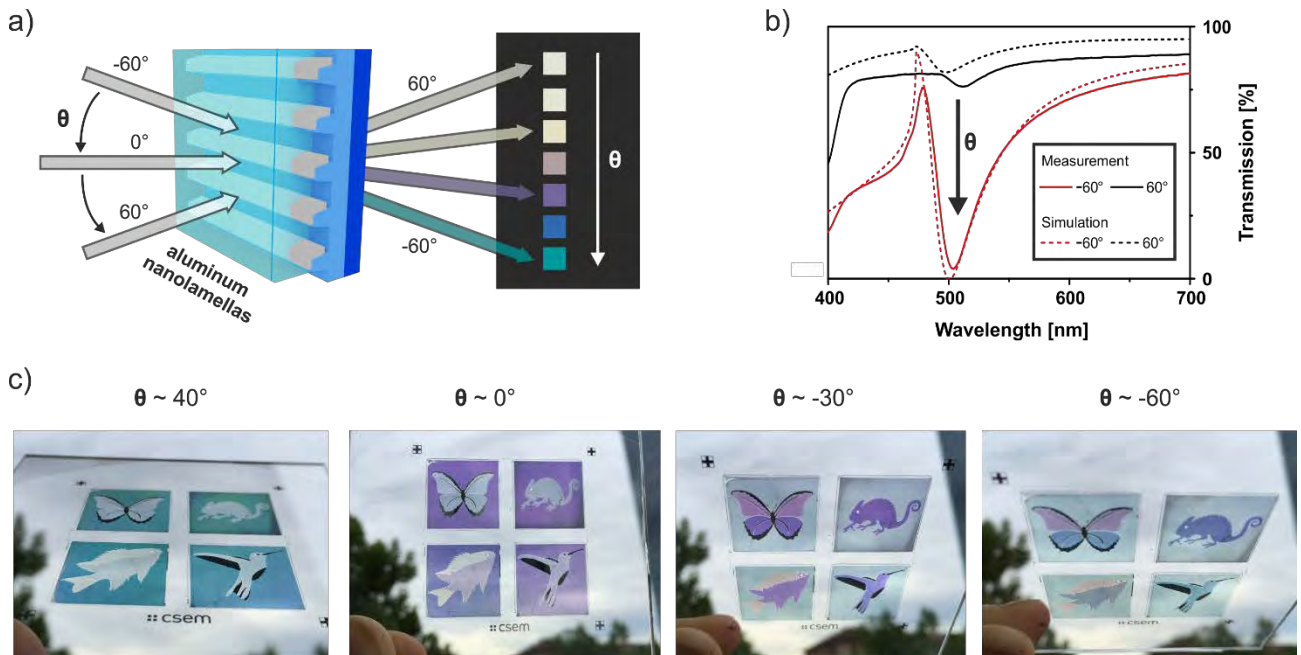


Figure 1: (a) Scheme of the plasmonic structure rendering distinct colors at varying incident angles θ of the light. The patches show the measured colors upon polarized light of different substrates. (b) Measured and simulated transmission spectra at $+60^\circ$ and -60° tilt angle. (c) Photo of a sample at different tilt angles in unpolarized daylight. The sample contains animals with structural colors in nature. The different optical appearance is achieved by variation of the evaporation angle.

In recent years, the interest in plasmonics and especially their potential applications has strongly increased. Plasmonics describes the collective oscillation of electrons on metal structures interacting with incident light. This can cause absorption or reflection in specific spectral ranges of the incident light, leading to colorful transmissions or reflections. Such so-called structural colors can be used for various applications such as optical security devices or active tunable filters.

We demonstrate plasmonic substrates with asymmetric optical appearance based on geometrical tilted aluminum nanostructures (see Figure 1a). Upon certain viewing angles we observe a strong color filtering property, which changes with variation of the angle (e.g. blue at -40° , green at -60°). In contrast observing the structure from the other tilting direction does not show any colored transmission. The great difference in transmission is shown in Figure 1b, where the red curve shows a very narrow resonance dip at about 500 nm for negative angles. This is caused by strong coupling of a plasmon resonance and a propagating resonance, depending on the shape of the aluminum and the period of the structures respectively.

The color filtering properties of the structure can be tuned with the nanostructure's geometrical parameters. We fabricate such structures by transferring a pattern of periodic nanostructures into polymers or sol-gel, by evaporating aluminum at a specific angle and finally by embedding the structure with a polymer or a sol-gel. Variation of the evaporation angle leads to distinct geometry of the aluminum nanolamellas directly influencing the color filtering properties. The final embedding step is crucial for anti-counterfeiting applications since it prevents direct copy of the structure and protects the structure from scratches and dirt enabling use at ambient conditions (Figure 1c). The fabrication method is compatible for roll-to-roll processes and high-throughput fabrication.

Figure 1c shows a demonstration of such a plasmonic device designed for optical security [2]. The sample was made at different evaporation angles for each sample areas (e.g. butterfly). Thus different colors appear at distinct tilt angles of the design. A complete switch between colored background and animal structure is observed within less than 10° tilt angle. The proposed effect is not based on diffractive effects. Therefore it is clearly visible in unpolarized and diffused light (challenging with classical holograms based on diffraction).

[1] L. Duempelmann, D. Casari, A. Luu-Dinh, B. Gallinet and L. Novotny, ACS Nano 9 (12) (2015) 12383–12391.

[2] G. Basset, et al., patent pending, (2015).

Four Color Filters in One using Large Area Plasmonic Substrates

L. Duempelmann, B. Gallinet, A. Luu-Dinh, M. Schnieper

Nanostructured silver nanowires can lead to polarization-dependent color effects in transmission. This effect is based on the collective and resonant oscillation of electrons in the metal, referred to the field of plasmonics. Overall this can lead to four distinct transmitted colors and their intermediate gradations. The proposed active tunable color filters are nearly incidence angle-independent and have great potential for several applications including optical security or tunable filters. They can be fabricated by roll-to-roll processes, potentially enabling cost-effective manufacturing^[1].

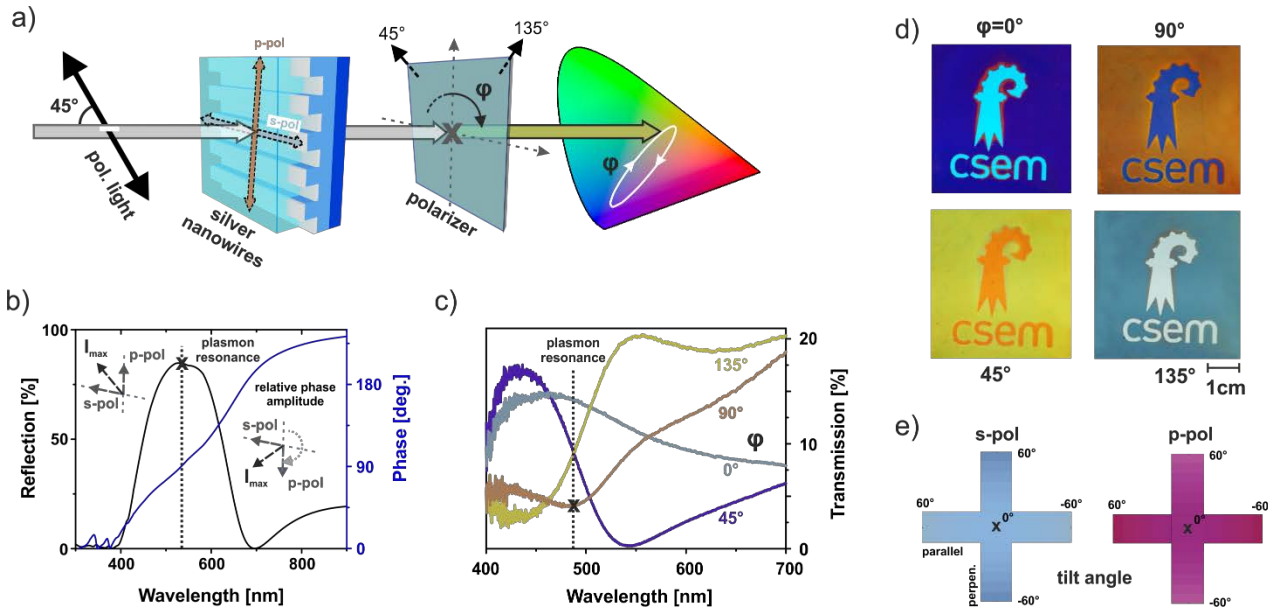


Figure 1: (a) Diagonal polarized light passes the plasmonic structure as s- and p-polarized light and is analyzed by rotation of a subsequent polarizer (angles in bold). (b) Graph of the reflection and phase shift present at the plasmonic resonance; inset displays the relative phase amplitude of the polarized states (before and after the resonance). (c) Measurement of the four main transmission spectra showing a cross-over of the two diagonal states (45° and 135°) at the plasmon resonance (lines are colored as measured) (d) Photos of a sample made at different rotation angles of the polarizer (bold). The sample (4.7×4.7 cm) was fabricated with 20 nm (logo) and 30 nm (background) silver thickness. (e) Simulated colors of the s- and p-pol of the filter upon different tilt angles (parallel and perpendicular to the nanowires).

Active tunability of filters can be essential for applications where varying spectral filtering properties are required, e.g. for visual effects or display applications. Compared to conventional color filters based on chemical dyes, the color filters based on plasmonics allow such active color tunability. Plasmonic resonances, responsible for the filtering property, are sensitive to the polarization and the tilt angle of the incident light.

Here we present a plasmonic filter based on periodic silver nanowires. It is designed to vary actively the color filtering properties via change of the polarization. The filter is also designed such that the optical properties are preserved at different tilt angles, which is essential for applications where a high field-of-view is required. The thickness of the proposed filter can be within few micrometers, making it highly attractive for miniaturized systems. Fabrication is done by replication of periodic nanostructures, evaporation of a thin layer of silver and embedding of the full structure. This protects it against oxidation, scratches, etc. and enables use in ambient condition.

The scheme of the plasmonic filter is shown in Figure 1a. Polarized light at 45° incidence excites the two polarization axes (arrows) of the periodic nanostructure. The polarization perpendicular to the nanowires (p-pol) excites a plasmon

resonance, causing a wavelength-dependent phase shift of this polarization state around the resonance. The simulated reflection, phase shift, and the relative phase amplitude wavelength-dependent of this state is shown in Figure 1b. Rotation of an analyzing polarizer with angle φ leads to a four fold transmission, as a crossing of two states is observed at the plasmon resonance (see Figure 1c), which specifically creates high contrast filters. Using the polarizer at smaller angular steps increases the number of filters far beyond the four basic ones.

Figure 1d shows photos of a sample taken at different polarization angles, leading to a completely different optical appearance. By changing the thickness of the silver nanostructures the plasmon resonance and therefore the color appearance can be altered. For many applications it is essential that these filtering properties are stable upon different tilt angles. The proposed plasmonic filter is designed to be stable in both tilt directions (perpendicular and parallel to the nanowires). Figure 1e shows such simulated colors (top-bottom and left-right respectively) for s-pol and p-pol of the filter.

The proposed active tunable plasmonic filters are compatible with large-scale fabrication processes, can be tuned spectrally via the geometry and are protected for ambient use.

^[1] L. Duempelmann, A. Luu-Dinh, B. Gallinet and L. Novotny, ACS Photonics 3 (2) (2016) 190-196.

Micro- and Nanostructuring of Steel Inserts for Aesthetics and Security in High Volume Industrial Injection Molding

D. Kallweit, C. Schneider, M. Schnieper

In 2016, CSEM continued the development of its steel technology. For the first time, CSEM not only supplied the nanostructuring of steel inserts itself, but also supplied a brand new set of steel mold inserts "Made in Switzerland" – all from one source. All inserts were fabricated in Switzerland according to the client's specifications, and finally delivered with two different holographic designs within only 3 months; injection molding tests and optimization phase with on-site support in South-Korea included.

Since many years CSEM has gained experience and continuously advanced its steel nanostructuring technology. That technology allows to fit steel surfaces with custom designed optical nanostructures for either security or aesthetic purposes, or both.

Most commonly CSEM's steel nanotechnology is used to structure steel inserts for the use in high volume injection molding, since these steel inserts show significantly less wear compared to nickel shims and even can be made with curved surfaces and with cavities. The range of possible structures is wide and goes from static and dynamic color effects, microtext / microimages over hidden laser readable images to 3D effects like visual depth, lens effects or bas-relief.

Figures 1 and 2 show one of the latest deliveries of CSEM to an industrial client in South Korea. In this case the fabrication of a set of mold inserts as well as writing of the different designs into the steel was supplied by CSEM as a one-stop service.

Figure 1 shows a photograph of the first of the two designs. Shown is a mold insert with a 40 mm diameter top surface. The hologram consists of two images, which are shown in a) and b).

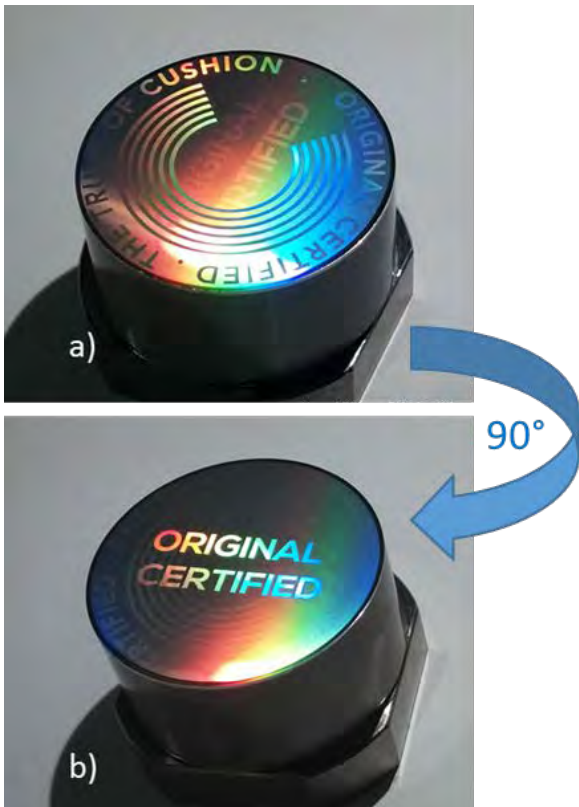


Figure 1: Hologram with switching effect on a 40 mm steel insert for injection molding. a) First main image is shown. b) In-plane turning by 90° the second image.

The first image showing the "C" logo disappears and the second image "Original Certified" is revealed if the sample is

turned in-plane by 90°. The other non-visible security features must be kept confidential.

Figure 2a shows a mold insert with the second design. It consists of logo with the lettering "HERA" which is filled with a specially designed diffractive nanostructure. The insert has the same dimensions as the one in Figure 1.

If a part of the HERA lettering is illuminated with laser light at the correct angle the custom designed image "The truth of cushion" is revealed. Figure 2b shows a picture of the projected image on a piece of paper at a distance of roundabout 15 cm.

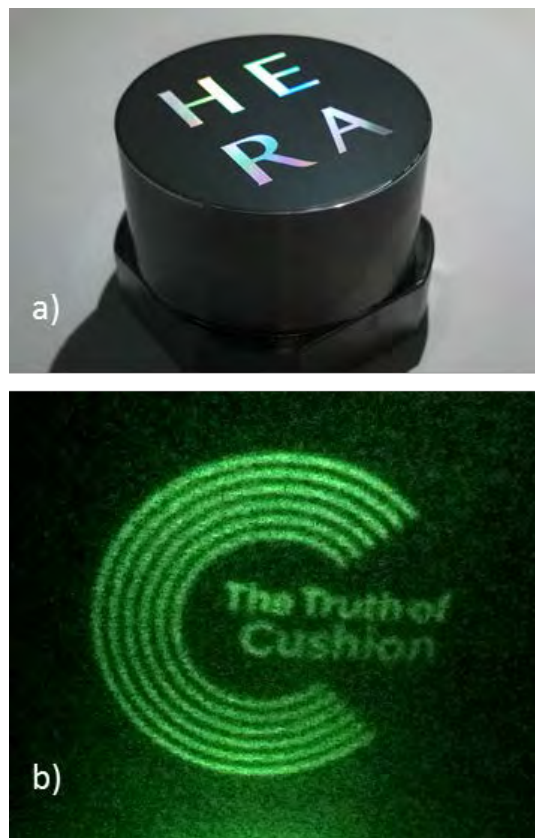


Figure 2: a) HERA logo with diffractive nanostructures on the steel insert. b) Photograph of the hidden image that is projected if the logo is illuminated by green laser light.

All pictures shown have been horizontally mirrored in order to allow a more comfortable reading of the lettering. Actually all holograms on the steel inserts are wrong reading in order to form right reading images on the molded plastic pieces.

This industrial project was conducted in collaboration with Sergio Lizzola and his company LK Forensic Competencies LLC, Chemin des Cerisiers 15, 1860 Aigle, Switzerland.

Table-top Classification and Sorting System for Small Model Organisms

S. F. Graf, D. F. Bösel, I. Kastanis, H. F. Knapp

CSEM's CellFactor platform is used for automated sorting of small model organisms, such as Zebrafish larvae, into multi-well plates for toxicology screens in the pharma and chemical industry. In the newest design, the system is now encased, has a real-time speed measurement implemented and additional sensors/actuators installed. Real-time measurement at frame rates of >60 Hz increases the ejection success while the sensors and actuators reduce user involvement during filling and emptying the system. This allows highly qualified personnel to focus on data interpretation instead of tedious and repetitive work like identification, sorting, and dispensing.

Over the past years, CSEM has developed its CellFactor-technology, which automates the handling of small model organisms to reduce animal testing. The CellFactor technology contains solutions for keeping organisms in a homogenous suspension. To analyze the organisms either fluorescence detection, impedance analysis or imaging in combination with machine learning algorithms for detection and classification can be used. Finally, the analyzed organisms can be sorted into flasks or be dispensed into multi-well plates for further processing. Currently, two applications of the CellFactor technology are being developed. The muTish demonstrator [1] works with small model organisms in the size range of 50 to 800 µm while the CellFactor (shown in Figure 1) is optimized for the Zebrafish model with a size range of 500 to 2000 µm. The transport mechanism for the Zebrafish larvae is based on viscous drag forces for which the patent recently has been granted [2].

Latest improvements of the CellFactor are the encasing of the sorting and dispensing module into a housing which also contains the mechanics, optics, electronics as well as the buffer and waste bottle (see Figure 1 and Figure 2). Easy access to the bottles and the sample supply port are given and the multi-well plate can now be moved to a suitable position for manual or automated exchange.

Furthermore, bubble detectors and automated pinch valves were integrated to allow the automatic filling and emptying of the system.

The improved imaging system can now additionally be used for real-time measurement of the speed of the passing larvae. More than 60 frames per second (frame size 688 × 164 pixel) are analyzed. A tracker tags each larvae and calculates its speed. Using the real-time speed of the larvae, improved the ejection success rate and reduced the time to fill a multi-well plate to about 4 minutes.

Currently, the built-in machine-learning classifier is being trained with early stages of fertilized Zebrafish eggs with the goal to automatically differentiate between fertilized eggs in the 2- and 4-cell state (which corresponds to the first hour past

fertilization) and to dispense the latter into a multi-well plate for further processing. This greatly improves the efficiency of post treatment procedures of the fertilized eggs, as required by end-users that CSEM is in contact with.



Figure 1: CellFactor in its newest form for analysis and sorting of small model organisms.

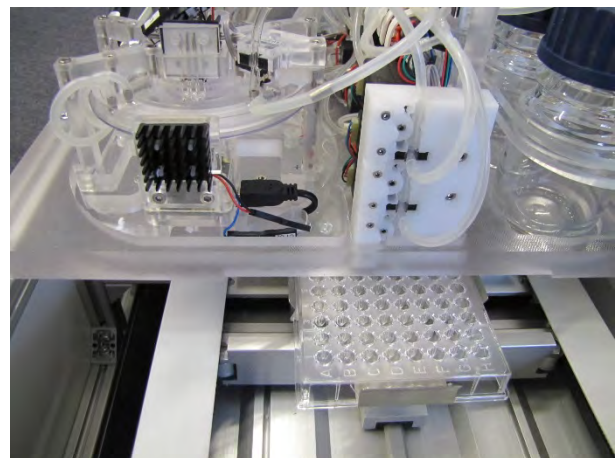


Figure 2: CellFactor interior. (top left) sorting module, (bottom) well-plate handler, (top right, white) dispensing module.

CSEM would like to thank the Swiss Federation and the MCCS Micro Center Central Switzerland for their financial support.

[1] S. F. Graf, et al., "muTish—Tools to monitor and handle medium sized biological entities", in this report, page 18.

[2] S. F. Graf, N. Schmid, H. F. Knapp, "Device, System and Method for Storing and Sorting Cellular Samples". U.S. Patent 8,940,541, issued Jan 27, 2015.

Development of Electrochemical Flow-cell for Advanced in situ X-ray Investigations

J. Tillier, T. Binninger •, T. J. Schmidt •, O. Sereda

There is a clear need for high-efficiency and non-polluting energy conversion technologies for the automotive application. Therefore, an increasing interest to the Polymer Electrolyte Fuel Cells (PEFCs) has been seen over last 5 years. One critical issue facing the commercialization of PEFCs is the gradual decline in performance during operation, mainly caused by the loss of the Electro-Chemical Surface Area (ECSA) of the supported Platinum NanoParticles (Pt-NPs) at the cathode^[1]. The ECSA decrease of the cathodic catalyst can arise from different degradation mechanisms which take place simultaneously, especially during potential cycling. Only thanks to the *in-situ* analytical investigations the understanding of this phenomenon can be addressed in a proper way.

Electrochemical *in situ* Small Angle X-ray Scattering (*in situ* SAXS) offers the unique opportunity not only to observe the evolution of the Pt-NPs size distribution during an electrochemical degradation experiment, but also to simultaneously monitor the evolution of the absolute platinum mass content of the electrode. *In situ* SAXS experiments can be conveniently performed at synchrotron X-ray sources. The high photon flux from these radiation sources yields a very good scattering signal-to-noise ratio in a short acquisition time despite the strong X-ray absorption of the electrolyte layer in transmission geometry. Despite these advantages, *in situ* SAXS experiments at synchrotron facilities face the major drawback of highly restricted availability of beam time. Therefore, the laboratory equipment can play a key role in this regard. The multi-purpose laboratory X-ray diffractometers represent an attractive alternative to perform electrochemical *in situ* SAXS experiments due to their widespread availability. However, both the drastically reduced photon flux (10^{-9} of a typical synchrotron X-ray source) and the reduced flexibility at the sample stage of such systems impose major challenges to the engineering of a respective electrochemical *in situ* cell.

Here, we present the new designed electrochemical three-electrode flow-cell and the results obtained by *in situ* SAXS experiments on a laboratory diffractometer. The design was based on the same principles as the SAXS/XAS flow-cell for synchrotron facilities presented in Part I^[2]. However, the cell was adapted to the strong geometrical constraints defined by the sample holder and special configuration of the diffractometer (see Figure 1). An elongated electrode geometry was required in order to fully utilize the line-shaped X-ray beam of the device. Furthermore, the constant electrolyte flow prevented X-ray induced electrolyte degradation and heating. In this way, the system guaranteed constant experimental conditions even during long-term experiments.

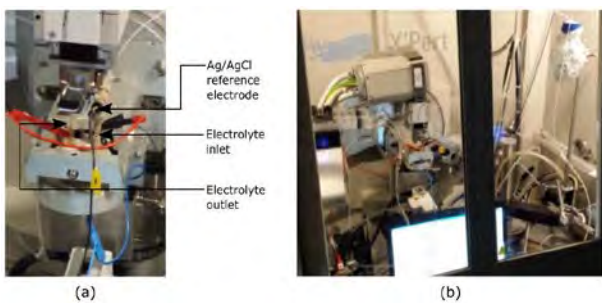


Figure 1: Pictures of the running *in situ* SAXS setup.

The raw SAXS curves $I_{\text{scat}}^{\text{meas}}(q)$ recorded during the *in situ* start/stop degradation study of the Pt-Vc 2 electrode are shown

in Figure 2 (left side). The Pt-NP-related scattering bumps shift to lower q-values with increasing number of degradation cycles. This behaviour is a clear signature of the growth of Pt-NPs due to Pt dissolution/re-deposition cycles (electrochemical Ostwald ripening) during potential cycling between 0.5 and 1.5 V_{RHE}.

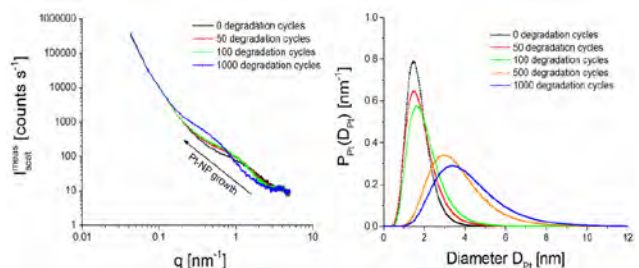


Figure 2: *In situ* degradation results of the Pt-Vc 2 electrode: raw data (left) and log-normal distributions for the diameter of Pt-NPs (right).

The Pt-NPs size distributions at different stages of the electrochemical protocol are depicted in Figure 2 (right side). As qualitatively already found from the analysis of the SAXS scattering curves, the size distributions demonstrate a particle growth with increasing number of degradation cycles. The distributions become broader and shift to larger particle sizes and the average diameter of the Pt-NPs increases from 1.8 nm in the initial state up to 4.2 nm after 1000 degradation cycles.

By performing the *in situ* investigations, the electrochemical degradation protocol has been established, which mimicked the corrosive conditions during PEFC start/stop events by potential cycles up to 1.5 V_{RHE}. An absolute normalization procedure for the SAXS data yielded net Pt differential scattering cross sections at various stages during the degradation cycling that could be analyzed not only for the Pt-NP size distribution, but also for the absolute number of Pt-NPs and the absolute Pt mass content of the nanoparticle phase. In this way, different degradation mechanisms could be distinguished. Carbon corrosion of the Vulcan support was qualitatively established in a separate experiment for a Pt-free Vulcan carbon electrode. The quantitative analysis of the Pt nanoparticle degradation revealed electrochemical Ostwald ripening as the dominant degradation mechanism for the Pt surface area. Thus, reducing Pt dissolution is the most important factor to prevent the degradation of catalyst performance under the start/stop potential cycling conditions.

Acknowledgments: this work was supported by CCEM Switzerland and Umicore AG & Co KG within the DuraCat project.

• Paul Scherrer Institut, CH-5232 Villigen PSI, Switzerland

^[1] Polymer Electrolyte Fuel Cell Durability, Springer (2009).

^[2] Journal of the Electrochemical Society, 163 (10) H906-H912 (2016).

Slot Die Deposition of Functional Films

N. Blondiaux, A. Grivel, E. Scolan, R. Pugin

We report on the development of functional thin films using slot-die coating. Challenging aspects approached here are coating porous and pre-structured substrates. Two case studies are considered. In the first, a mesoporous sol gel layer is coated with a CO₂ responsive film for the fabrication of a highly sensitive sensor. In the second, a microlenses-covered wafer is coated with standard photoresist in order to implement multilevel photolithography.

There is increasing interest in new coating techniques for functional thin film. During the last decade, the development of advanced wet coating techniques has been underpinned by the flat panel display industry. Critical issues such as accuracy, cost, and scalability have been addressed. Materials have also been developed and optimized for specific deposition techniques^[1]. Equipment and processes are now available and have been integrated in manufacturing chains in combination with vacuum deposition techniques.



Figure 1: photograph of a slot die deposition head.

Among the wet deposition techniques used in production, slot die coating has been employed in a wide range of domains for the fabrication of flat-panel displays, batteries, photovoltaics, OLEDs, and paper media to name a few. The liquid to be coated is delivered with an accurate flow rate using a coating head (slot die) and the sample is moved at a predefined speed. The final "wet thickness" depends only on the flow rate, the coating width and the speed, thus defining slot die coating as a pre-metered technique. In contrast to self-metered coating techniques such as dip-, spin- or blade-coating, the physical properties of the chosen liquid do not affect the final thickness of the coating. Other significant advantages of slot die coating is its very high throughput and very low material waste (<10%). Although this technique has been used in some applications to produce thick coatings (tens of micrometers), the emergence of new markets (TFT LCDs) led to the development of advanced slot die coaters for the fabrication of ultra-thin films (down to tens of nanometers).

In this project, slot die coating has been tested for coating various resins and formulations on porous and pre-structured substrates. More specifically, we have chosen to investigate two case studies representative of specific applications. In the first case, slot-die coating was applied to the fabrication of a CO₂ sensitive patch. The starting substrate was an A4 sheet coated with a mesoporous layer. A formulation based on CO₂

responsive molecules has been developed. Our objective was to apply uniformly a thin coating of this formulation on the mesoporous matrix. The very large surface area of the mesoporous matrix leads to an enhanced sensitivity of the patch. The major advantages of slot die coating in this case study were the absence of mechanical contact on the mesoporous layer, the low material waste and the very low volume needed for the deposition. A slot die coated sample is presented in Figure 2a.

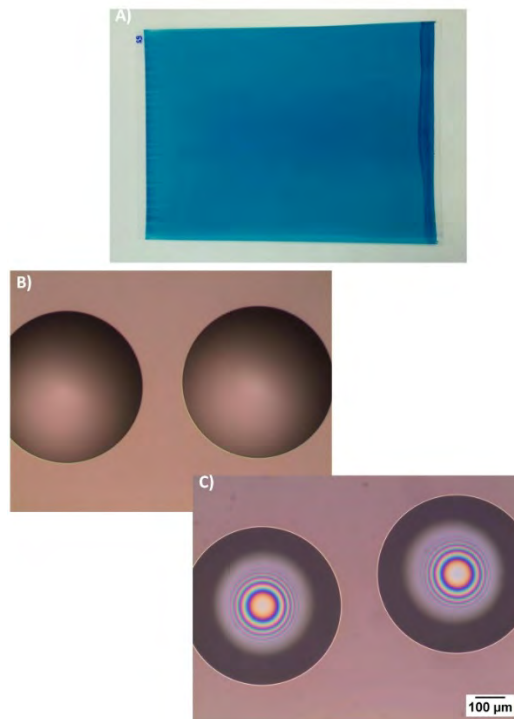


Figure 2: a) Mesoporous film coated with CO₂ sensitive layer. Optical images of microlenses before (b) and after photoresist coating (c).

In our second case study, the main objective was to coat a silicon wafer presenting an array of microlenses with a layer of photo resist. In contrast to spin-coating which is not well adapted to pre-structured substrates, slot die coating showed very promising results. A homogeneous coating over 150 mm wafers was obtained and its uniformity was not affected by the presence of the microlenses. An optical image of the coated microlenses is presented in Figures 2b and 2c. Further investigations will use slot die coating for other types of substrates presenting higher aspect ratio structure and will identify coating windows depending on the type of photoresist.

Wafers with microlenses were kindly supplied by SUSS MicroOptics. We would like to thank them for their support.

[1] www.ixsenic.com

Large Area Nanoreplication on Flexible Substrate

N. Blondiaux, A. Bionaz, D. Dominé, P. Häfliger, R. Pugin

We report on the development of a replication process for the production of nanotextured substrates. The targeted application is the fabrication of thin, flexible photovoltaic cells. The selection of materials, which had to withstand the cell deposition process, the control of surfaces and interfaces and the upscale of our replication process up to samples sizes of 300×300 square millimeters proved to be critical. Samples produced have then been used for the fabrication of flexible thin film solar cells.

CSEM has developed within the multi-interdisciplinary project Wear-a-Watt an ultra-low power watch operating only off the solar energy harvested from its environment [1]. One of the main achievements is the fabrication of thin, flexible solar cells and their integration in the wristbands of the watch. The development of these custom solar cells required specific substrates with a high transparency and an optimized surface texture to enhance light trapping.

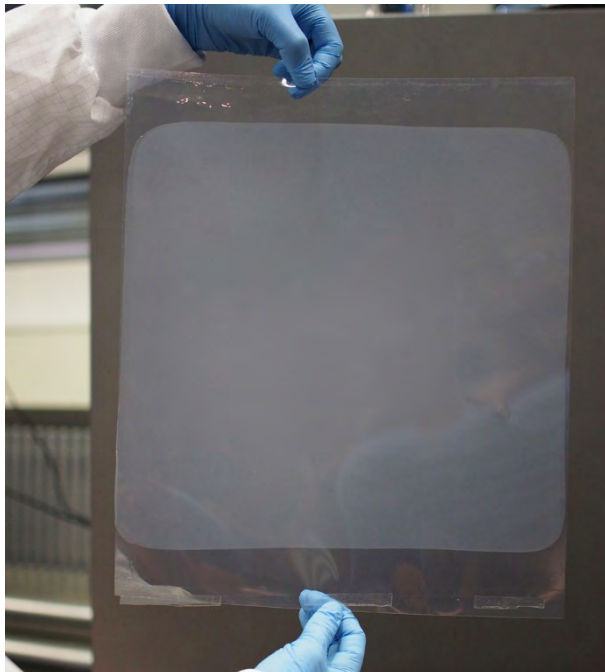


Figure 1: Photograph of a 300×300 mm 2 sample. The nanoimprinted structures give a milky aspect to the substrate. The final thickness of the textured foil is 130 micrometers.

In this work, our standard nanoimprint process has been up-scaled for the production of flexible, textured substrates with a maximal size of 300×300 mm 2 . This size was deemed to be a good compromise between lab scale samples and substrates produced using high throughput techniques such as roll to roll replication. Several conditions had to be met such as transparency and heat resistance during the solar cell deposition process.

Many high temperature substrates (withstanding temperatures above 200°C) were benchmarked and ranked according to their compatibility with the different process steps, their mechanical properties (rigidity) and the performance of the final solar cells. The nanoimprint process involved first a coating of the substrate with a UV curable resin followed by the imprinting

step using a textured mold. We identified a robust surface preparation of the substrates to ensure good adhesion of the coating at temperatures up to 200°C. Good results were obtained using a hybrid primer directly deposited on the substrate.

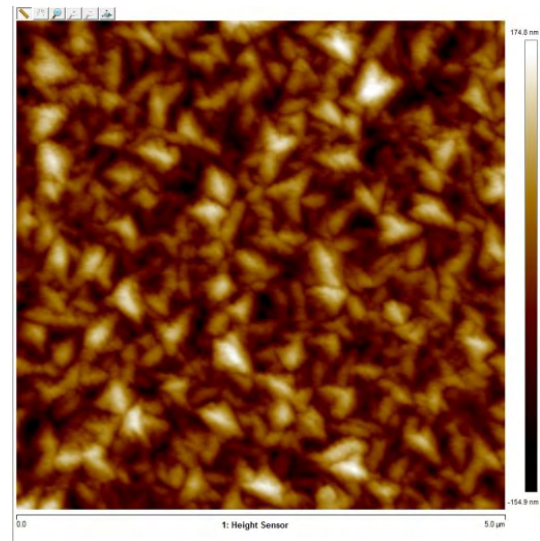


Figure 2: AFM image of the surface of a nanoimprinted replica with light trapping structures.

Cross cut tests (ISO 2409) have been performed to characterize the adhesion of the UV-curable coating on the primed substrate. The results were similar to those obtained using our standard plasma activation. However, the deposition of the primer was easily up-scaled to the targeted sample-size. Concerning the nanoimprint step itself, specific equipment was designed and fabricated for the processing of 300×300 mm 2 samples.

As shown in Figure 1, large nanoimprinted samples have been produced. The fabrication of such samples leads to an increase in throughput of one order of magnitude in comparison with the lab-scale fabrication of textured substrates done until now. Figure 2 presents an AFM image of the textures obtained on the nanoimprinted substrates. The patterning process is homogeneous over the 300×300 mm 2 area and faithfully replicates the original structure of the master.

Ongoing work focuses on the validation of these textured substrates for the fabrication of thin flexible solar cells and their integration in low-power wearable devices. Further investigations will ensure a complete evaluation of their mechanical performances.

[1] J. Bailat, et al., “Wear-a-Watt—Energy Autonomy for the Wearables”, CSEM Scientific and Technical Report (2015), 12.

Integration of New Sol-gel Films into Miniaturized Optical CO₂ Sensors for Air Quality Monitoring

E. Scolan, R. Smajda, A. Bionaz, G. Voirin, R. Pugin, N. Thronicke •, A. Winzer •, A. Albrecht •

We present the development of a new CO₂ sensor, combining groundbreaking sol-gel thin films nanotechnologies with state-of-the-art optical detection. These smart gas sensors provide the necessary data for an energy-saving ventilation and air-conditioning in industrial and public buildings.

Carbon dioxide is a natural part of air. It is also the most important indicator of indoor air quality. A person working in an office exhales about 20 liters per hour of this odorless and tasteless gas. In the current regulation on air quality DIN EN 1946-2, a CO₂ limit of 1500 ppm is specified as the maximum permissible value. High CO₂ concentrations affect the performances of people and can lead to fatigue and headaches.

Sensors play a vital role in establishing the state of our environment and monitoring changes due to human activities. Conventional CO₂ analysis is usually carried out using infrared spectroscopy, using the strong absorbance of CO₂ at 4.26 μm. Unfortunately, this method presents significant drawbacks, such as the bulky and expensive nature of the equipment used and its susceptibility to humidity. In addition, the miniaturization of sensors into wearable devices entails sensors being small, cost-effective, reliable, and with a low energy consumption. Sensors based on change of luminescence in the presence of a specific molecule are promising candidates complying with these specifications since the change of luminescence can be measured by compact optical readers.

In this frame, the technology on which optical CO₂ sensors are based corresponds typically to the encapsulation of a pH indicator dye in an inert nanoporous sol-gel matrix. The sensing mechanism is based on a local change in pH upon reaction with a quaternary ammonium base selective for CO₂. This event is monitored with a pH indicator dye that can be luminescent or colored.

CSEM has developed innovative sol-gel based sensitive layers enabling the optical detection of volatile or dissolved analytes with enhanced performances [1]. To overcome the disadvantages of optical sensors based either on microporous or meso-, and macroporous sensitive layers embedding photosensitive dyes, the host film is made of a double matrix, a microporous sol-gel network encapsulating the active species, which is embedded into a mesoporous coating. These hierarchically nanostructured films are deposited on various substrates such as steel, glass, and flexible plastic sheets. The hierarchical nanostructure enhances the performances of the sensitive layers, e.g. higher optical signal, improved sensitivity, robustness, mechanical resistance, transparency, and selectivity, and a faster response.

Several pH indicator dyes, matrix chemistries, and printing process parameters have been screened to limit the impact of humidity and temperature, and to extend the lifetime of the probed patches (Figure 1).

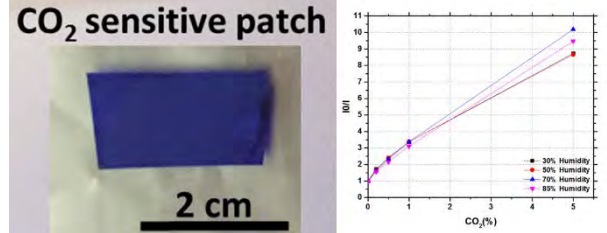


Figure 1: (Left) Picture of CO₂ sensing patches; (Right) Stern-Volmer curves of CO₂ sensitivity showing the low impact of humidity.

A miniaturized optical device for the detection of CO₂ is currently under development for air quality monitoring in buildings (Figure 2). A disposable and low cost sensitive patch is interrogated in a closed module containing LEDs, lenses, and photodetectors. Data processing based on artificial neural networks has been designed to limit the signal deviation (<0.05%). Once integrated into a system comprising humidity and temperature sensors, the device has a low detection limit (yet down to 1 ppm) enabling the monitoring of air quality. Moreover, it can also be used in combination with conductimetric sensors to ensure accurate calibration at 0 ppm.

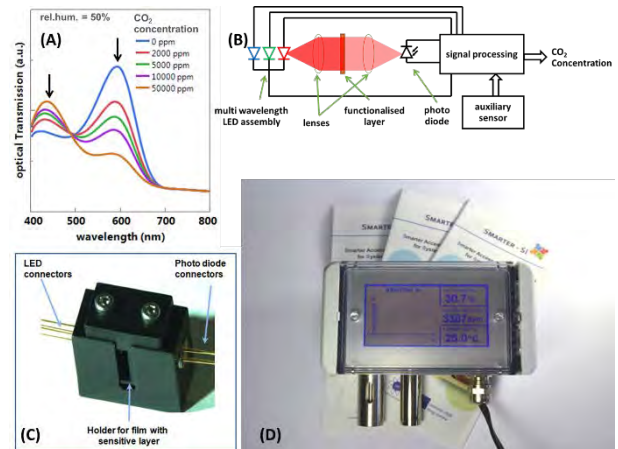


Figure 2: (A) Absorbance spectra of m-cresol purple dye functionalized sensitive patches at different CO₂ concentrations; (B) Working scheme of the optical reader; (C) picture of the reading module; (D) Picture of the sensor demonstrator for indoor air quality monitoring.

The consortium (CSEM, CiS, ConSens, IL Metronic) gratefully thanks the European Commission Program H2020 (SMARTER-SI project, GA No. 644596) and the Swiss State Secretariat for Education, Research, and Innovation (SERI) (contract No. 15.0085) for their financial support.

• Partners from CiS Forschungsinstitut für Mikrosensorik GmbH

[1] E. Scolan, B. Wenger, R. Pugin (2015), "Optical Sensor for detecting a chemical species", EP patent application EP15201731.5.

Advanced Microlenses Fabrication Techniques

G. Basset, A. Luu-Dinh, C. Schneider, F. Herzog, F. Zanella, A. Mustaccio

A way to increase the quantum efficiency of image sensors is by adding a microlens array. The microlenses located on top of each pixel direct light preferentially into the active pixel volume, to offset the limited fill factor in front illuminated CMOS image sensors. Such microlens arrays are commonly produced using CMOS processes, which are best suitable for pixel pitches below 5 μm . At the opposite, larger microlens arrays, with pitches of a few tens of microns to several hundred microns in diameters are fabricated by the thermal reflow of photoresists.

This fabrication method gives excellent optical performance and much affordable fabrication for large microlenses. These dimensions matches the pixel pitches of some specialized image sensors such as Single-Photon Avalanche Photodiode (SPAD) arrays^[1], scientific and space observation cameras. Additionally, several applications, such as 3D displays, digital optical processors, optical communication or optical security make use of high quality microlens arrays. CSEM has improved its capabilities to fabricate microlenses based on thermal reflow processes, opening the possibility for new shapes and flexibility.

Microlenses produced by reflow are made of a photoresist patterned by photolithography and thermal melting. They are limited to relatively low aspect ratio (sag to diameter) shapes. Arrays of high aspect ratio microlenses are unstable because of a risk of merging of adjacent microlenses during reflow that can result in the collapse of the array. By using a surface functionalization self-aligned to the photoresist, it is possible to control accurately the shape of the microlenses during the reflow to circumvent this limitation. This opens the possibility to produce very high aspect ratio microlenses as shown in Figure 1.

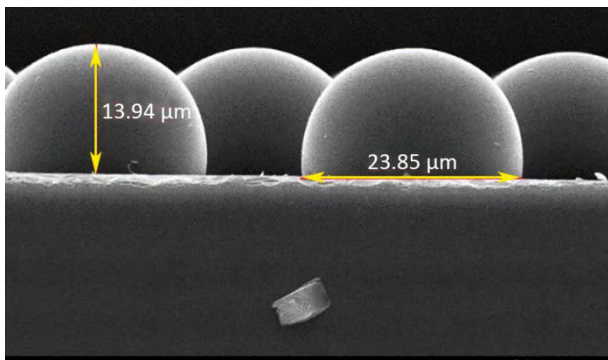


Figure 1: SEM image of more than hemispherical microlenses produced by reflow—cross-section view.

As other examples, this method allows the fabrication of high quality microlenses on heavily patterned surfaces such as optical diffuser as shown in Figure 2 and of arrays of high aspect ratio microlenses with inter-lens gaps well below 2 μm , as shown in Figure 3.

Finally we also demonstrate the possibility to directly inkjet print microlenses with high optical quality polymers on standard substrates as a digital and additive manufacturing approach as shown in Figure 4.

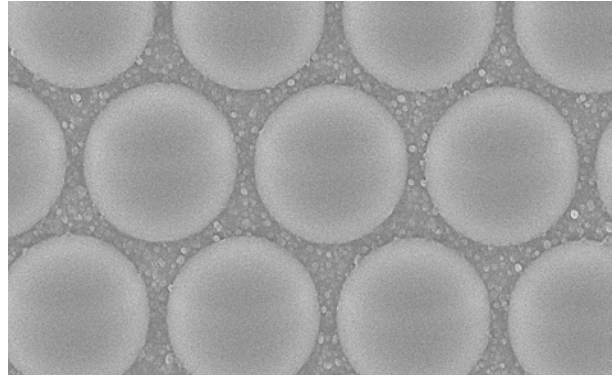


Figure 2: SEM image of a microlens array produced by reflow on a diffusive structure—top view.

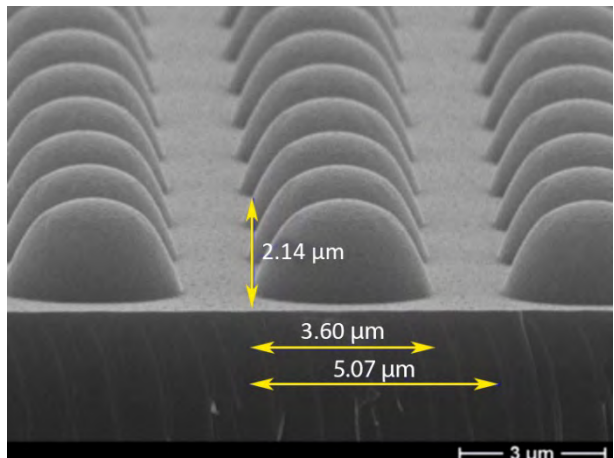


Figure 3: SEM image of an array of very small microlenses with high aspect ratio produced by reflow—oblique view. Diameter: 3.6 μm , height: 2.1 μm .

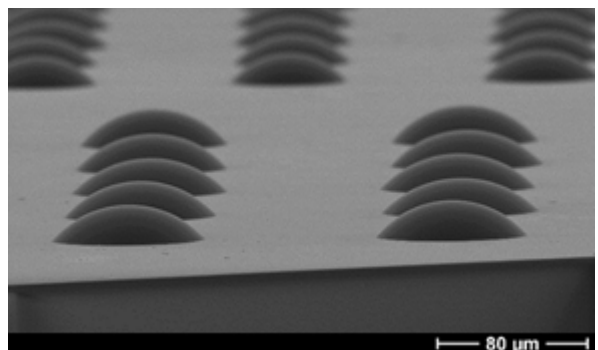


Figure 4: SEM image of directly inkjet printed microlenses on a glass substrate.

[1] J. M. Pavia, M. Wolf, E. Charbon (2014), “Measurement and modeling of microlenses fabricated on single-photon avalanche diode arrays for fill factor recovery”, Optics express, 22(4), 4202–4213.

Ultra-thin Direct-lit LED Modules with Beam-shaping Thin-film optics

O. Fernández

Large-area panels based on LED arrays are widely used, for example in offices and shops due to their appropriate illumination characteristics. Direct-lit LED modules offer several advantages over edge-lit both cost and performance-wise. However, large light-mixing air gaps are required to provide aesthetically appealing and glare-free uniform luminance over the entire emitting area of the panel. Consequently these LED modules are significantly bulky. The air gap can be substantially reduced by beam-shaping the typical Lambertian emission pattern of the LEDs into a batwing shape without compromising the luminance uniformity (LU) value. CSEM has envisioned a thin-film solution based on pixelated periodic microstructures which have theoretically demonstrated effective batwing beam-shaping and over 60% panel thickness reduction compared to unshaped lambertian LEDs.

White LEDs have become mainstream in lighting products. Although extremely bright, the small emitting area results in optical output levels insufficient for professional or residential applications. Consequently, LED-based lighting modules very often use LED arrays.

The light emitted by the LEDs in the array needs to be properly handled to prevent undesired effects such as glare, multi-shadows and non-uniformly lit areas, common causes of visual discomfort and eye fatigue.

A common and effective solution is to distribute the emitted light over a large area. In the so-called edge-lit approach, the LED light is edge-coupled into a few millimeters thick light mixing transparent plate whereas in the direct-lit approach, a diffusive plate/foil is directly illuminated by the LED array, located several centimeters below.

The direct-lit design offers interesting benefits over the edge-lit one, including lower weight, higher efficiency and higher luminance uniformity. Unfortunately, the Lambertian emission, typical of LEDs (black curve in Figure 1; top), requires air gaps larger than the LED pitch.

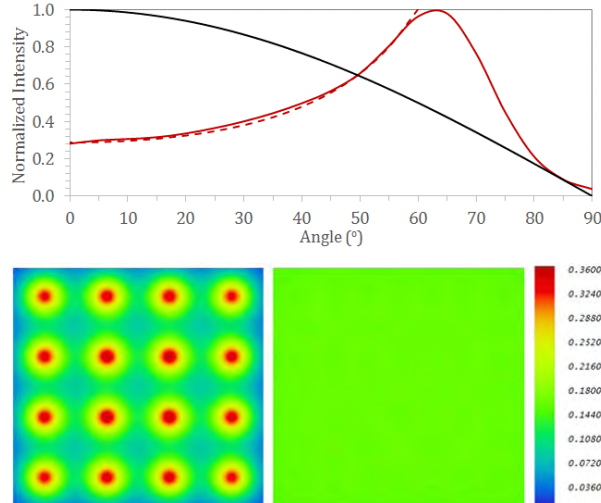


Figure 1: (Top) Lambertian (red), cosine-cubed (dotted red) and optimum batwing (solid red) normalized intensity distributions. (Bottom) Irradiance produced by a 4×4 LED array over a plane target situated 15 mm above the array for lambertian (left) and batwing-shaped (right) LEDs.

Beam-shaping offers a way to reduce the air gap thickness. Indeed, the illuminance produced by a Lambert emitter over a planar target decreases as $1/\cos^3\theta$; being θ the incident angle referenced to the target normal. Therefore, the so-called inverse cosine-cubed distribution (dotted red line in Figure 1; top) produces more uniform illumination (see Figure 1; bottom).

Beam-shaping can be achieved attaching lenses to the LEDs. Such "one lens per LED" approach, currently exploited by Samsung, OSRAM, and LG is nonetheless costly.

Alternatively, complex free-form optical microstructures can be used with their profiles at every point specifically tailored to the incident angle of the incoming light at this point. However, the microscopic profiles needed might be rather complex and not compatible with standard fabrication techniques such as diamond milling.

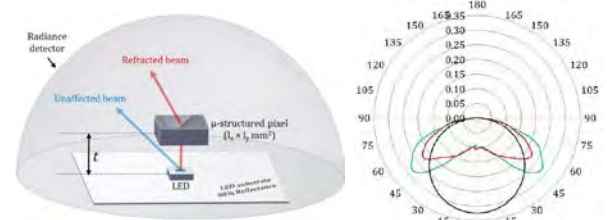


Figure 2: (Left) Conceptual representation of the proposed beam shaping thin-film solution. (Right) Theoretical angular emission pattern of an LED without (black) and with (green: C0-180 and C90-270 planes; red: C45-225 plane) CSEM thin-film solution.

A much simpler solution is provided by periodic microstructures (prismatic, lenticular) replicated in the form of small pixels. The final shape of the beam is then determined by the profile of the microstructures as well as by the pixel aperture, i.e. by the pixel area and its distance to the LEDs as sketched in Figure 2; left.

With the selected microstructures and optimized pixel size (l_x , l_y) and distance (t) values a batwing emission pattern is predicted (Figure 2; right). In an array, this translates into a 60% reduction in the number of LEDs (for 80% LU; see Figure 3). Alternatively, for the same number of LEDs, a twofold thickness reduction of the modules can be realized.

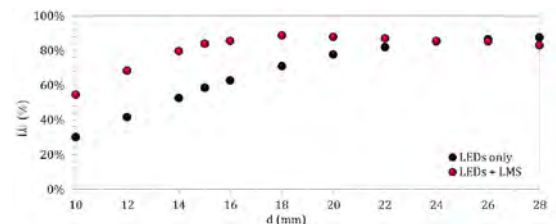


Figure 3: Luminance uniformity of a 15 mm thick 600×600 mm 2 area lighting module as a function of the air gap thickness. t : 1 mm, LED pitch: 30 mm.

The research leading to these results has received funding from the European Union Seventh Framework Programme [FP7/2007-2013] under grant agreement n°619556, project LASSIE-FP7.

Printed Sun Sensors for Satellites

N. Marjanović, J. Disser, F. Zanella, J. Schleuniger, A. Mustaccio, R. Ferrini, M. Schnieper

The developed sun sensor comprises inkjet printed organic photodiodes, printed resistors and capacitors, high-end Si-based SMDs and operational amplifiers on a flexible circuit board. The fabricated flexible sun sensor is suitable for pico / nano satellites since it is extremely thin (~2 mm) light weight (<2 g) and cost-effective (potentially one order of magnitude cheaper than state-of-the-art products). The sun sensor demonstrates i) the potential of hybrid technology by offering a new way of system integration (coupling printed and Si-based electronics), ii) a new possibility for system designers (smart PCBs), iii) using electronically functional materials (e.g. printable Ag-inks), and iv) extends the current range of products where flexibility counts (e.g. wearable, bendable electronics).

This paper describes an innovative electronic system assembly approach, namely hybrid integration which combines printed electronic components with/on flexible circuit boards (FCBs) equipped with conventional Surface-Mounted components (SMDs). Technology-wise, a clear benefit was derived from the combination of the advantages of both large area printed electronics based on solution processes (e.g. flexibility, light weight, cost effectiveness, etc.) and SMDs with high-end functionalities and robustness.

The sun sensor described here consists of four single organic photo diodes (OPDs)^[1] with common bottom contact (thin Al-layer), printed active polymer-based layer and individual top contacts (a semi-transparent thin Au-layer). Other stand-alone components such as resistors, capacitors, thermistors, and OPDs were designed, printed and characterized by CSEM on HIGHTEC's pre-patterned polyimide (PI) substrates (Figure 1).

The selected printed stand-alone components were used to size the preliminary front-end circuit on standard printed circuit board (PCB).

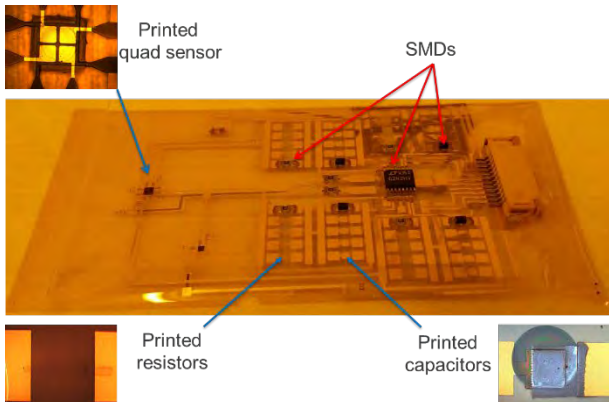


Figure 1: Components printed on FCB with embedded SMDs – first step towards demonstrator.

The flexible circuit board (FCB) design relies on the connection-on-demand approach which consists in putting stand-alone printed and SMD components side-by-side. The connection of the selected printed/SMD component to the whole system is done after characterization of the printed component through

inkjet printed conductive ink. This approach allows enhancing the production yield and minimizing the system integration risks.

Purchased stiffeners and spacers ensure a fixed illumination configuration while the illumination aperture was opened by laser drilling. In order to easily fold the PI foil, pre-perforation was also performed by laser drilling. In order to operate the sun sensor demonstrator CSEM realized a computer interface with a data acquisition card from National Instruments.

Finally, CSEM and HIGHTEC AG fabricated and folded the sun sensor demonstrator addressing the unique properties of the hybrid technology (Figure 2) in terms of volume, flexibility and weight.

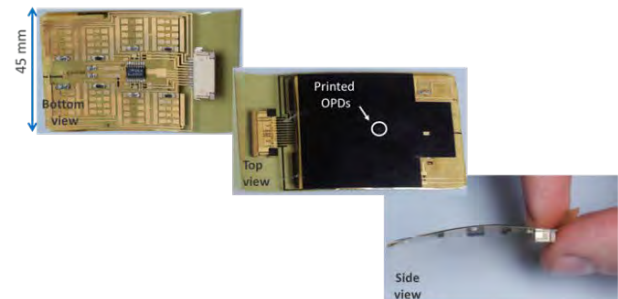


Figure 2: Assembled and folded flexible sun sensor demonstrator.

The validation was performed with a green laser manually aimed at each of the 4 cells while the light spot position and light incident angle are calculated by a custom-made software. The calculated position follows well the illuminated pattern and the sun sensor is validated for incident angles comprised between -80° to 80°.

The resulting hybrid sun sensor is

- extremely thin (thickness of the embedded SMD)
- extremely light weight (<2 g)
- cost-effective (projected cost significantly lower than current solution)

This example of hybrid technology offers new possibilities to the system designers (towards smart PCBs), material providers (printable functional inks) and extends the current range of products (e.g. wearable, flexible electronics).

^[1] G. Maiellaro, et al., IEEE Trans. on Circuits and Systems — I: Regular Papers, Vol. 61, No. 4, pp.1036-1043, April 2014.

Inkjet Printing Structural Colors based on Plasmonics

F. Lütolf, J. Müller, L. Duempelmann, B. Gallinet, A. Luu-Dinh, G. Bassett, R. Ferrini

Inkjet printing is a wide-spread coloration technique for home applications, but also for high-end graphics and security elements. This work demonstrates novel color effects based on inkjet printing that circumvent some of the drawbacks of the typically used chemical dyes, such as photobleaching and smearing. Utilizing a plasmonic foil as a substrate and applying transparent inks of varying refractive indices allows the creation and control of structural colors with conventional equipment like desktop inkjet printers and any drawing program. Apart from private users, this technology could be attractive for advertisement, security and brand protection due to the simple, digital serialization of pictures or numbers.

Inkjet printing is one of the most common processes in the graphic industry. Nowadays, such techniques are by far not limited to classical dyes though; research on metallic and dielectric nanoparticle inks are for example on a steep rise. Inkjet print-heads are still constantly evolving, as higher accuracy, faster printing speed or lower material consumption are highly sought-after. Furthermore, novel concepts such as 3D printing have been implemented in the past decades.

Coloration using inkjet is typically based on chemical dyes or pigments, which are prone to photobleaching and smearing when coming into contact with water or grease. Further, the color space available is limited and no metallic gloss, matte finish or actively tunable coloration can be achieved with classical inks. In contrast, structural colors as found in nature on various butterflies or beetles for example do not have these drawbacks. Unfortunately, they are much more difficult to realize and control on an industrial level. Typically, pictures have to be defined lithographically on a nanoscopically patterned master and cannot be adapted in a simple fashion. Combining inks of varying refractive indices and plasmonic nanostructures sensitive thereto might solve this problem.

In the present experiments, a plasmonic substrate consisting of U-shaped aluminum nanowires was chosen. The resonances found in such structures are very sensitive to the refractive index of the surrounding media; it is therefore possible to change the resonant wavelength by adapting the coating material. In other words, by dispensing inks of different refractive indices, it is possible to locally control the color of the plasmonic substrate. It is worth noting that, for this specific system, only one of the linear light polarizations is capable of exciting the plasmonic resonance.

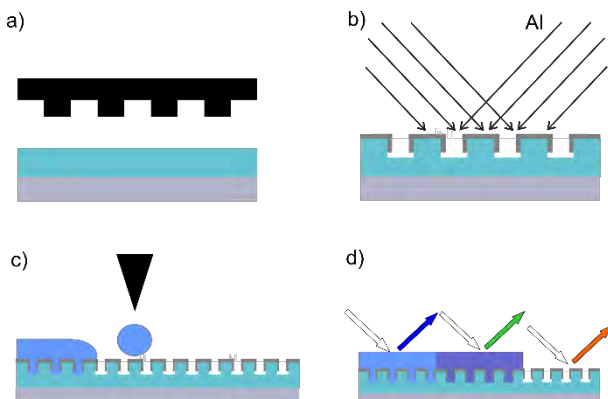


Figure 1: Schematic showing the experimental procedure.

The plasmonic substrate can be obtained by replicating a binary grating either by UV casting or hot embossing into a polymer substrate (Figure 1a) and subsequently evaporating it with aluminum from both sides (Figure 1b). Through self-shadowing of adjacent ridges, disconnected wires are formed. Finally, an inkjet printer is used to dispense a transparent high

refractive index material onto the plasmonic substrate and hence form a colored picture (Figure 1c and d).



Figure 2: A plasmonic structure, bearing a volleyball player inkjet printed with high refractive index material, photographed in two different linear polarizations of light in two orientations.

Figure 2 depicts a volleyball player printed in this manner. Note that due to the polarization sensitivity of the substrate, the coloration of the picture strongly changes when observed through a linear polarizer (compare top to bottom pictures). This is true for the air interfaced part as well as for the printed part. For the present 1D structure, orientation of the sample is also important for its appearance as clearly visible in Figure 2. This tunable appearance of pictures is essential for visual applications like anti-counterfeiting and clearly not achievable with conventional inks and substrates. It is finally worth noting that large areas of homogeneous plasmonic nanostructures can be fabricated with high-throughput processes as they are roll-to-roll compatible. The printing technique could also be incorporated into such industrial fabrication lines, but is even exploitable by private customers with commercial desktop inkjet printers (as the one used in this report).

In summary, it was demonstrated that inkjet printing of dielectrics can be used to locally control the refractive index on a plasmonic substrate and thereby the resulting structural color. Since homogeneous plasmonic substrates can be fabricated with large-area, cost-efficient roll-to-roll manufacturing, customizing such structures with an established process like inkjet printing has a high potential for private, but also industrial applications and could even find its way into mass production of everyday products for decorative or anti-counterfeiting purposes.

Aerosol-jet Printing, an enabling Technology for printing Electrodes, Interconnects, Sensors or Antennas on 2-or 3-D Parts

G. Voirin, S. Lani, A. Bionaz, R. Smajda, R. Pugin

Aerosol-jet printing technology uses an additive manufacturing process that prints with high resolution different materials including conductive nanoparticles, dielectric pastes, semiconductor and other functional materials on 2D and 3D substrates. This flexible and cost effective printing technique is ideal to develop and prototype devices for the consumer electronics, sensors, MEMS, medtech and life science industries.

CSEM acquired recently the aerosol-jet printer AJ300 from OPTOMECH. The system consists of an ultrasonic atomizer for materials with a viscosity from 1 to 5 cP and a pneumatic atomizer for materials with a viscosity from 1 to 1000 cP that first create a dense mist of material droplets. The generated aerosol mist is then delivered to the printing head where a sheath gas accelerates, focuses and deposits it on the surface. During travel from the nozzle to the substrate (up to 10 mm) the particle stream remains focused. Therefore linewidth down to 10 microns can be written depending on the nozzle aperture and nature of the printed material. The AJ300 aerosol jet printer has a displacement capacity over 300×300 mm with an accuracy $\pm 6 \mu\text{m}$ and a repeatability of $\pm 1 \mu\text{m}$ which is compatible with microsystem fabrication.

Several conductive materials like inks based on gold or silver nanoparticles have been printed on different substrates. After thermal curing the resulting tracks showed good conductivity typically 2 to 3 times the value of bulk materials. Curing temperature is usually ranging from 150°C to 200°C depending on the nature of both the ink and the substrate. On nanoporous paper specifically designed for flexible electronics application, a curing temperature down to 80°C was demonstrated. Thus different features have been printed like connections for flexible photovoltaic cells (Figure 1), electrodes and antennas on plastic rods (Figure 2), or electronic circuits on nanoporous paper (Figure 3).

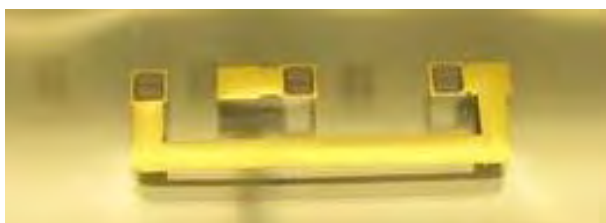


Figure 1: Printed interconnection for flexible PV cell.

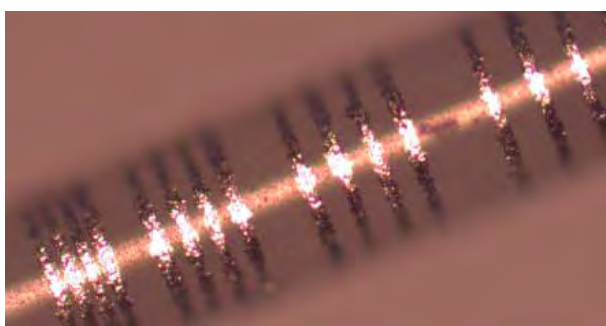


Figure 2: Printed electrodes or antennas on plastic rods.

Thanks to the large working distance (more than 5 mm) it is also possible to write on complex shapes substrates, as an example Figure 4 shows electrodes printed in the cavities of a complex 3D plastic part.



Figure 3: Printed electronic features on nanoporous paper.

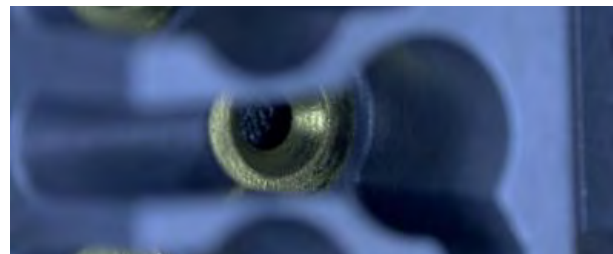


Figure 4: Printed conductive tracks on complex 3D shape plastic part.

In addition to conductive inks, UV curable polymers with a viscosity from 7 to 500 cP could also be printed. Such features allow us to isolate conductive tracks, to deposit tiny amount of glue for high precision assembly and also to fabricate directly in place gasket preventing gas or liquid leakage in microsystem assemblies.

Finally, the displacement table with high accuracy and repeatability combined with the alignment camera could be used to perfectly align printed patterns. Optical apertures can be printed and aligned directly on packaged light source or photodetectors to avoid tedious optical alignment.

Aerosol-jet printing is a versatile system able to print functional materials with different viscosities on structured substrates (plastic, ceramic, or metallic). Interconnections, electrodes, antennas and optical structures were printed to build several industrial prototypes and accelerate the development of microsystems. We should also notice here that this printing technology is scalable to support high-volume production requirements.

CSEM gratefully acknowledges the Wilsdorf foundation for financial support.

PV-CENTER & ENERGY MANAGEMENT

Christophe Ballif

The signing of a global protocol at COP21, now ratified by China and the USA, certainly makes the case that the years 2015 and 2016 will be remembered as special years, and indicates that—in the mid-to-long term—decisive action will have to be taken internationally.

Interestingly, however, so far most countries/entities are continuing not to take decisive action and are electing individuals who deny the scientific facts regarding the climate and the environment, or, even worse, sometimes claim to be taking action, but rather are engaged in mere greenwashing. Such an example is the “Terawatt initiative” announced by several countries and major energy companies, which supports “one terawatt” of worldwide PV installation by 2030. Even though that seems impressive, 1 TW of PV corresponds, in fact, to zero growth of annual PV module production (or even a regression when considering production levels in 2016), and is certainly not enough to create a decisive impact on global CO₂ emissions. To be serious, a factor of 3 to 10 times higher should be considered. In other words, we can still expect that—for a few years—stronger measures to curb CO₂ levels will come at a reduced speed. The factors prevailing in this (too) slow transition include traditional conservatism on the part of politicians and populations, lobbying employed by companies that wish to avoid a rapid depreciation of their assets (e.g., coal burning power plants or other assets in the fossil fuel field), and the difficult financial situation of many states, for which higher initial investments in energy efficiency, electricity management, and renewable electricity generation are perceived as a risk to the economy, rather than these states seeing the multiple long-term benefits of such moves.

Another example of inefficiency is the current situation with regard to the EU electricity market, which has reached the summit of absurdity. The failing mechanism of CO₂ emission certificates (linked to reduced demand and production overcapacity since 2008) means that the EU wholesale electricity price is now essentially dictated by the marginal price of electricity produced by the most polluting power plants—that is to say, coal burning plants. At a wholesale price below 3 cts/kWh, coal is banishing from the market gas power plants, which only pollute half as much and are much more flexible, and is endangering all production with clean resources (including hydro), unless such production benefits from support schemes. This situation calls for a modification of the CO₂ certificates systems, the rapid introduction of a bottom price for such emissions, and/or the prohibition of polluting power plants. However, at a time of “Brexit”, immigration questions, terrorism, and difficult economic situations in many EU countries, finding remedies to this situation is not a top priority. Because of an inability or absence of will to tax CO₂ properly, or to prohibit it in some applications, more and more forms of cleaner electricity need to be supported—including, for example, hydropower in Switzerland—giving them a chance to survive on the market.

At the same time, however, the pressure for change will continue to grow, thanks to some unique factors.

- Many municipalities and cities are more proactive at introducing change than countries are (see Switzerland, for example, and “les cités de l’énergie”). Bottom-up rather than top-down pressure will accelerate the transition process.
- Climate change skeptics could possibly become an endangered species given that 195 countries have signed the treaty issuing from the 2015 Paris Conference, thereby making more probable healthy debates on how to act rather than discussions that doubt the seriousness of the problem. The election of Donald Trump is certainly a setback, and an additional danger with regard to the climate and to affected populations, but at least the US will not be able to formally escape the treaty for the next four years, and a reaction to post-truth politics might emerge as well.
- Renewables continue to improve, in particular solar electricity, reaching ultra-low prices with power-purchase agreements down to 4.5 cts/kWh and even in some cases down to 3 cts/kWh for large parks in sunny countries, when low capital costs are available. In many places solar is becoming the electricity source with the lowest generation cost, opening further opportunities for storage in various forms, short- or long-term. The value of solar electricity still depends significantly, however, on local regulation, unless one can consume it all oneself.
- Emerging economies such as China continue to invest massively in renewables, creating a market-pull situation for many products and helping to make them more affordable.
- Finally, more and more business models and electricity/energy management solutions are being proposed and developed, creating a fertile ground upon which to prepare for the future. This is also the case for Switzerland, with a remarkable network of both start-ups and established player in the field of energy.

More generally, for Switzerland, the vision of the PV-center & Energy Management (PV&E) program at CSEM targets the following objectives:

- To provide cutting-edge innovation in the field of photovoltaic devices, realizing the best devices with a high potential for industrialization, and providing modules with the highest potential for adoption by the public in the built environment.
- To support the development of next-generation equipment and metrology systems, all along the value chain of photovoltaics, creating a sustainable cleantech value for existing and future CSEM customers.
- To provide new solutions for specialized devices, coatings, or materials with higher added value, and for PV components with enhanced functionalities.
- To bring solutions to the energy/electricity management field as we transition toward a society essentially powered by renewables, in which energy efficiency and management will be realized through intelligent hardware and algorithms.

General situation

In 2016, final infrastructure upgrades took place and are now fully operational:

Batteries and cells are now being tested at the ESREC BFH-CSEM storage research center in Biel and the center is being used for various demonstration projects.

At Innoparc, the 600 m² CSEM technology lab for module fabrication, measurement and test facilities are being used intensively. CSEM and SUPSI are now also collaborating to offer measurements and services in Neuchâtel. The testing facilities for the development of new products have been upgraded with several climatic chambers. In addition the facilities now include a separated room for the compounding and extrusion of larger polymer foils, an R&D line for the copper-plating of c-Si cells, a firing furnace for high-temperature c-Si cells, and a partially automated line for ultra-lightweight PV foils for airplane applications.

At Maladière 83, the cleanroom infrastructure is also running efficiently. High-T processes (e.g., POCl₃ and oxidation) are now in operation. Laser platforms have been adapted, with the installation of a high-productivity picosecond laser processing unit. All solar cell lines and coating tools are delivering state-of-the-art devices, and thanks to the support of a private foundation, additional equipment for the processing of next-generation passivated contact devices has been acquired.

In 2016, CSEM was able to further develop and extend its activities related to the PV&E program. The project portfolio gained in strength, with project revenues (industrial and competitive grants) significantly higher than in 2015. Staffing levels also grew, with over 50 persons (FTE) now involved in the various activities.

CSEM is involved in most major publicly funded programs in Switzerland (Nano-Tera, PNR70...) where it collaborates with the Swiss universities of applied science, EPFL, and EMPA. Finally, all activities continue to be connected to industry through direct mandates and CTI and EU projects/instruments. Around 40 external parties (industries and some collectivities or RTOs requiring services) are currently working directly with CSEM, benefitting from the program.

Activities and topics	Emerging and thin-film PV	PV cells and modules	Energy systems
Technology infrastructure platforms	Thin-film Si devices Thin-film coatings Perovskite PV Printable PV and OPV	High-efficiency c-Si cells Metallization & interconnections Polymers for high reliability PV module fabrication	Energy management services Micro-grid and storage
Metrology and characterization	Thin-film coating & laserling Cell pilot lines Module R&D lines Polymer compounding		Testing and reliability (with SUPSI) Storage R&D center (with BFH)

Figure 1: Schematic of the activities of the PV-center and Energy Management program. Top part—activities; bottom part—technology infrastructure platforms.

For 2017, the program's structure has been simplified and covers three general activities, which are divided into various topics. Typically, four to eight people are involved by topic.

A synopsis of the program is given in Figure 1. The bottom part of the figure illustrates the technology infrastructure platforms available, which is another way of looking at the program. This corresponds to hardware facilities platforms, which are complemented by additional software/hardware in laboratories (e.g., simulation platforms for electrical grids, for plasma modelling, micro-grid hardware...).

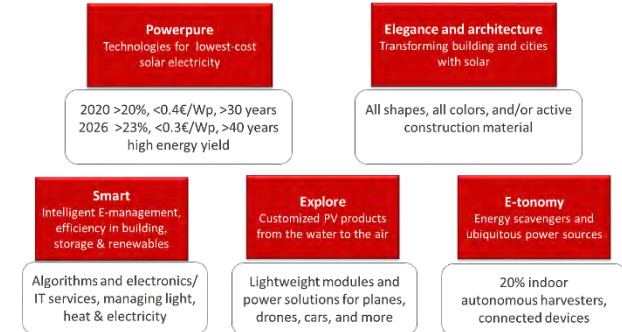


Figure 2: Representation of the program by field of application.

The activities are all strongly interlinked; the developments made in each activity can find applications in most other activities (e.g., solution processes oxides can be used for crystalline cells). Another, different, way of looking at the program is in terms of fields of application, as described in Figure 2, with the fields *Powerpure*, *Elegance and architecture*, *E-tonomy*, *Explore*, and *Smart*.

We give, below, some examples of the typical fields of application; more detailed reports on these examples can be found in the following pages.

Powerpure

The “Powerpure” field includes major improvements and innovations in cell processes and packaging, with the direct target of lowering solar electricity costs. For instance, multi-wire combined with SHJ bi-facial cells not only enters into this category, it also already quasi-attains the mid-term targets mentioned in Figure 2 (efficiency, reliability thanks to advanced polymer processing, and manufacturing costs), as was calculated in the xGW project.

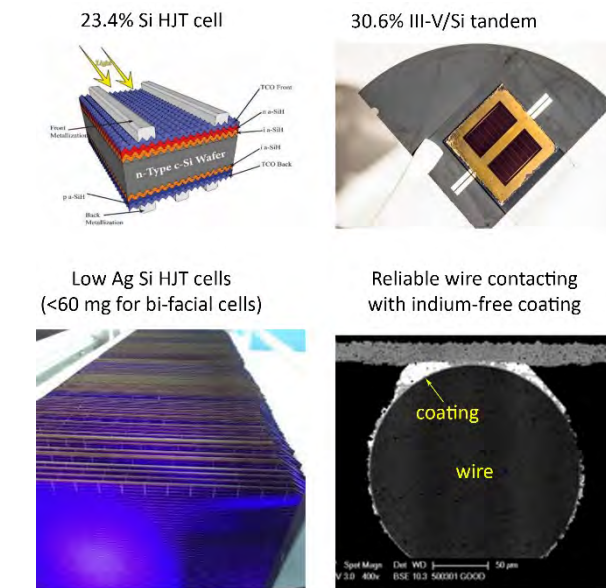


Figure 3: Example of Powerpure applications.

Powerpure also includes the demonstration of “next generation”, ultra-high efficiency tandem devices. A full Powerpure module integrates inputs from 5 to 8 topics (e.g., for a tandem PK/c-Si module) from the research program. In particular, SHJ cells with over 23.5% were manufactured with a simple process, tandem-certified III-V/Si cells with a world record efficiency of 30.6% were demonstrated together with NREL, and 4-terminal tandem perovskite/silicon cells were able to reach 25.6%.

Elegance

In the “Elegance” field, products and solutions are engineered and designed to make a novel generation of PV products that should change the way people see, and think about, solar. Transformative techniques are typically applied to modify the aspects of modules that can be mass-manufactured with standard processes. The reliability of products is at the heart of the field, and this involves assessing and producing advanced polymer foils. Examples of products under development include white photovoltaic building elements; crystalline, terra-cotta, large-area rooftop tiles; and lightweight, unbreakable modules for facades.



Figure 4: (Top left) terra-cotta, crystalline modules; (top right), simulation of a rooftop under construction; bottom, white modules undergoing outdoor test conditions assessment.

E-tonomy

The “E-tonomy” field relates to the potential of photovoltaics to scavenge (or collect) energy for a variety of applications. In a world where objects need to be interconnected, power sources—from a few micro- to a few tens of watts—will be increasingly required, as will energy management, and usage will need to be balanced at an appropriate level. Depending on the light spectrum (indoor or outdoor), typical intensity, and globally required energy, various technologies can be implemented (e.g., thin film Si, organic PV, III-V based devices, or c-Si). Several sets of prototypes and small series production runs were realized, achieving remarkable performance at low illumination. Over 100,000 devices were produced and tested.



Figure 4: Top—colored-PV coin (left); ultra-high efficiency low-illumination harvester (right). Bottom—cells in watches and on wristbands (MIP Wear-a-Watt) (left); indoor, printable/OPV design (right).

Smart

In a world of decentralized, interconnected energy/electricity sources, being “smart” means designing solutions that make possible enhanced flexibility/predictive capability, lower energy usage, and improved services to a specific community. Smart can apply to houses, to districts, and to cities, and to autonomous or mobile objects. Smart is here to manage not only electricity, but also heat, or light, or combinative forms of these three. This activity also targets cost reduction, increased reliability, and a higher acceptability of PV products in the built environment. It helps create new products by, for example, adapting existing mass-market technologies. Figure 5 illustrates some of the subjects treated in the field “Smart”.

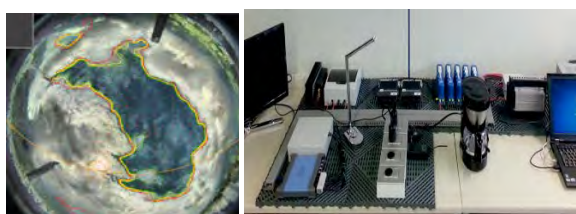


Figure 5: Being smart—using cloud pattern recognition to predict a PV plant’s short-term production output (left); laboratory “intelligent” micro-DC grid (right); optimizing consumption (bottom).

Platform for High-efficiency Silicon Heterojunction Solar Cells

M. Despeisse, A. Descoeuilles, C. Alleb  , N. Badel, L. Barraud, J. Champliaud, F. Debrot, A. Faes, A. Lachowicz, J. Levrat, B. Paviet-Salomon, L. Curvat, L. L. Senaud, J. Horzel, G. Christmann, D. Sacchetto, M. Benkhaira, S. Nicolay, C. Ballif

CSEM has set up a complete platform for the fabrication and the characterization of silicon heterojunction solar cells. Innovative and industry-relevant solutions are developed for the improvement of all cell processing steps, aiming for high conversion efficiencies at competitive costs. The technological topics covered at CSEM include wafer bulk quality improvements, wafer texturing and cleaning by wet-chemistry, PECVD depositions of ultra-thin passivating and contacting layers, PVD depositions of low-cost and/or high-mobility transparent conductive oxides, advanced cell metallization and interconnection processes and various characterization techniques. Efficiencies up to 23.44% have been demonstrated following the developments conducted in the frame of the FP7 European project HERCULES.

Silicon heterojunction (SHJ) solar cells present the decisive advantages to combine a high efficiency (potential for modules with >21% conversion efficiency) with limited number of production steps (pre-requisite for keeping reduced fabrication costs). The technology further exhibits a low temperature coefficient (<-0.3%/°C) as well as a high bifaciality (>90%), triggering high energy yield for bifacial SHJ modules in the field. Thanks to its symmetric structure and to the high level of surface passivation, the SHJ bifacial cell architecture is also the most suited for thin wafers integration. Calculations show that, with SHJ solar cells, the average leveled costs of energy could be below 4 ¢cts/kWh in sunny countries [1]. Since the PV-center creation in 2013, a strong emphasis is therefore set in CSEM on the development of a complete, performant and flexible platform covering all aspects of production and characterization of SHJ solar cells, from as-cut wafers to finished devices optimized for module integration. This technological platform allows CSEM conducting advanced R&D projects to develop new processes, materials, production and metrology equipment, as well as advanced concepts for improved performance and/or reduced production costs; and also to provide services and small batch production for its customers.

SHJ solar cells implement carrier-selective contacts with high surface passivation formed on crystalline silicon wafer with the deposition of hydrogenated amorphous silicon (a-Si:H) and transparent conductive oxide (TCO) layers. These hetero-contacts are demonstrations of so-called passivating contacts, enabling for its key advantage: increased operating voltages. The intrinsic a-Si:H layers deposited on the wafer surfaces provide excellent chemical passivation, yielding minority carrier lifetime approaching the theoretical limits: as a demonstration, carrier lifetime >50 ms could be achieved with a-Si:H layers deposited at CSEM on 500 µm thick wafers with a resistivity of 20 kOhm·cm. Such carrier lifetime is among the highest values ever reported to our knowledge for silicon with contactable passivation layers. Then, doped a-Si:H layers allow for the selective collection of one type of carriers while blocking the other type, with p-type doped layer acting as hole selective contact, and n-type doped layer as electron selective contact. In 2016, an advanced process for the intrinsic a-Si:H layer was developed on CSEM platform, to maximize passivation properties for complete in/ip SHJ cell precursor stacks while keeping a minimum thickness of about 4 nm for the intrinsic a-Si:H layer. This triggered an improvement of the electrical performance of the developed SHJ cells, with fill factor values up to 81.8% achieved for front emitter SHJ cells. Using Ag

printed metallization and indium tin oxide (ITO) and aluminum-doped zinc oxide (AZO) for the front and rear TCO layers, SHJ cells with an efficiency up to 23.44% were then demonstrated on CSEM SHJ solar cell platform.

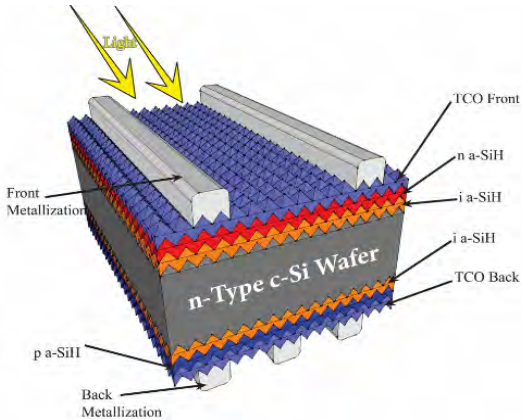


Figure 1: Schematic representation of the symmetrical structure of bifacial silicon heterojunction solar cell. Table detailing performance of the record SHJ devices fabricated in CSEM platform.

EFFICIENCY	VOC	JSC	FF
23.63 %	726.4 mV	40.15 mA/cm ²	81.03 %

At wafer level, special additives were developed to enable low reflectivity after texturing (<9% at 740 nm), while processes for the management of the silicon bulk and surface qualities were developed, yielding improved carrier lifetime of the produced SHJ precursors. Management of front and back optical losses were conducted, by minimizing the a-Si:H thickness, implementing high mobility TCO (with >100 cm²/V·s), using fine-line printing (<40 µm wide fingers) and adapting the cell with the integration of dielectric layers into advanced architectures at the front and at the rear of the solar cells. The conducted developments combined with the conducted investigations of advanced functional thin films produced by PECVD, PVD and ALD define the development roadmap towards >24% efficiency for such SHJ solar cells.

Some of the developments conducted on the CSEM SHJ cell platform are further presented in 2016 CSEM technological reports: implementation of AZO to replace ITO, integration of CSEM SHJ cells into world record tandem III-V/Si solar cells, implementation of silicon hetero-contacts in an all back-contacted cell structure, as well as developments of alternative metallization and interconnection technologies for SHJ solar cells.

[1] A. Descoeuilles, et al., Energy Procedia, 77, 508 (2015).

Back-contacted Silicon Heterojunction Solar Cells with a Simplified Photolithography-free Processing

B. Paviet-Salomon, A. Tomasi •, D. Lachenal ••, L. Barraud, A. Descoeuilles, G. Christmann, N. Badel, J. Geissbühler, A. Faes, B. Strahm ••, S. Nicolay, M. Despeisse, C. Ballif

In collaboration with EPFL and Meyer Burger Research, CSEM is developing the next generation of back-contacted silicon heterojunction solar cells, aiming at demonstrating top-level conversion efficiencies with a cost-effective process flow.

Crystalline silicon solar cells implementing passivating contacts based on hydrogenated amorphous silicon (a-Si:H) and transparent conductive oxide (TCO) layers demonstrate the key advantage of increased operating voltages, as demonstrated in CSEM silicon heterojunction solar cell (SHJ) platform. In addition, maximum optical performance can be achieved using an all back-contacted solar cell architecture, providing no metallization shadowing at the cell sunny-side. The back-contacted silicon heterojunction (BC-SHJ) architecture therefore represents one of the silicon solar cell approach with the highest efficiency potential, combining optimum electrical and optical performance. This was demonstrated in 2016 with the achievement by Kaneka, Japan, of a conversion efficiency up to 26.33% using such BC-SHJ architecture, establishing the world-record efficiency for single junction crystalline silicon solar cells. However, the successful industrial spread of BC-SHJ devices is impeded by their complex and delicate process flow, usually involving several costly photolithography steps, to realize the patterned rear contacts. In the frame of the CTI project "PUNCH", CSEM, in close collaboration with EPFL and Meyer Burger Research, is developing the next generation of BC-SHJ devices, targeting high conversion efficiency along with a cost effective process flow.

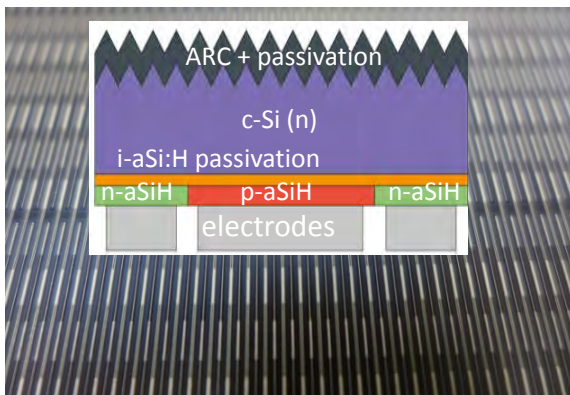


Figure 1: Schematic cross-section of the BC-SHJ devices developed, on top of a close-up view of the back side of a full 6-in BC-SHJ device.

CSEM developed and patented an innovative back side architecture^[1], based on shadow-masking and on advanced thin film layers stacks, enabling to accurately pattern the rear electrodes of BC-SHJ devices without the use of any photolithography step. The CSEM approach drastically reduces the number of process steps to only 8, compared to at least 14 steps for a photolithography-based process flow. This results in a potential cost-effective process flow for the mass production

of BC-SHJ devices. In addition, the developed rear side design features a lower contact resistance of the hetero-contact, hence yielding a reduced series resistance in the final device.

As a major achievement, CSEM together with EPFL and Meyer Burger Research fabricated in 2016 a 22.9%-efficient lab-scale BC-SHJ solar cell (9 cm^2), using the developed simplified fabrication steps and architecture. The current-voltage curve of this record device is plotted in Figure 2. This result demonstrates the high efficiency potential of the BC-SHJ technology developed at CSEM.

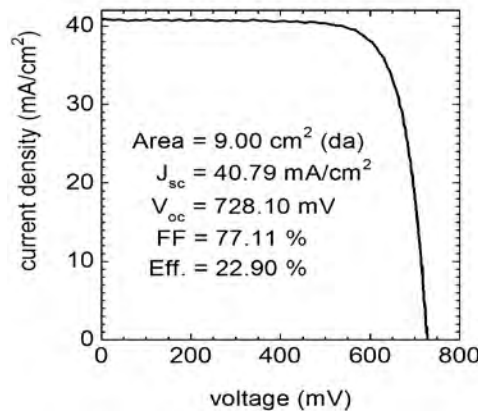


Figure 2: Current-voltage curve of the 22.9%-efficient record BC-HJT device jointly developed by CSEM, EPFL, and Meyer Burger Research.

The upscaling of this process flow was first conducted towards 25 cm^2 cells, with efficiency up to 22.8% demonstrated using the developed architecture. Then, upscaling to full 6-in wafers was initiated at the Meyer Burger Research facilities. The first large area BC-SHJ cells prototypes – obtained using mass production tools – demonstrated that the photolithography-free process flow developed has the potential for producing industrial BC-SHJ devices in a cost-effective way in the coming years. Strong focus is now set to achieve higher performance by further reducing series resistance of the devices.

Future work also focuses on the metrology and on the integration of the developed solar cells. Dedicated contacting units are being developed, while a module architecture specifically designed for BC-SHJ devices, based on the Meyer Burger SmartWire® technology, is being developed to efficiently integrate the cell developments into the final product.

This work is funded by the Commission for Technology and Innovation (CTI) under grant No 17705.1 PFNM-NM.

- EPFL, IMT, PV-Lab
- Meyer Burger Research

[1] B. Paviet-Salomon, A. Tomasi, M. Despeisse, C. Ballif, "Photovoltaic device and method for manufacturing the same", patent EP 15 19 2655 (2015).

Direct Interconnection of plated Silicon Heterojunction Solar Cells

J. Geissbühler, A. Lachowicz, A. Faes, J. Champliaud, J. Brossard, N. Badel, J. Horzel, M. Despeisse, C. Ballif

Copper electroplating is investigated as an alternative metallization technique for silicon heterojunction solar cells which suppresses entirely the use of silver and creates highly conductive metallic fingers. This process has been successfully implemented for bifacial solar cells in a R&D pilot line at CSEM. This metallization technique is particularly adapted for the direct cells interconnection method where conductive fingers are to maximize performance and minimize costs. This work was conducted in the frame of the SFOE pilot and demonstration Swiss-Inno-HJT project.

Copper electroplating is a promising next generation metallization technique for silicon solar cells, and in particular for silicon heterojunction solar cells (SHJ). Indeed, this method enables to suppress expensive silver in the SHJ cells manufacturing and furthermore allows the fabrication of more conductive and narrower finger geometries with respect to state-of-the-art printing of low temperature ($\sim 200^\circ\text{C}$) cured Ag pastes^[1]. In this prospect, a R&D plating pilot line was developed and ramped-up at CSEM for the production of copper plated SHJ solar cells. The established process starts with a low-cost hot-melt inkjet patterning technique in order to form an insulating mask with typically 30 μm -wide openings on a metallic seed-layer. Next, the seed-layer is locally thickened in those opened areas to form the metallic finger. This process takes place in vertical plating tools where both sides of the cells are plated simultaneously enabling a fast and simple manufacturing of bifacial cells metallization grids. Finally, both the insulating mask and the seed-layer are removed. Currently, these processes are further developed at CSEM to reduce the cost of patterning and of electrodeposition while increasing the conversion efficiency of SHJ devices.

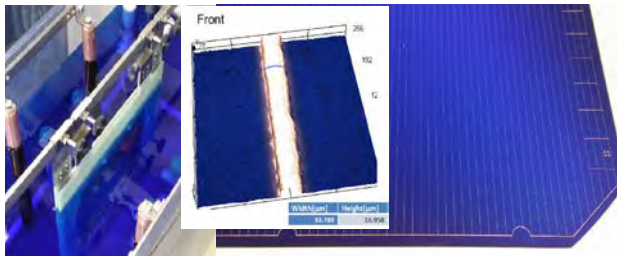


Figure 1: (left) Vertical plating bath for bifacial SHJ cells, (middle) 3-D reconstruction of a 35- μm -wide and $\sim 16\text{-}\mu\text{m}$ -thick electrodeposited copper finger; (right) plated metallization grid on SHJ solar cell.

With the developed materials and processes, highly conductive copper fingers typically $\sim 35\text{ }\mu\text{m}$ -wide and $\sim 16\text{ }\mu\text{m}$ -thick can be fabricated in CSEM R&D pilot line on full 6" bifacial cells, as shown in the 3-D reconstruction of Figure 1. This leads to line resistance of $0.3\ \Omega\text{ cm}^{-1}$, more than 3 times more conductive than a screen-printed silver counterpart, while significantly reducing the optical shadowing. The achieved performance is key for improving the performance of standard H-patterned silicon heterojunction solar cells interconnected by state-of-the-art ribbon soldering or gluing.

In parallel, alternative solar cell interconnection technologies and modules designs are being developed to improve performance, aesthetics and reliability. Among the developed approaches, CSEM focuses on the multi-wire technology,

relaxing the constraint on the metallization grid, and on the direct interconnection of segmented SHJ cells. The latter technique, also referred as "shingling", is presented in Figure 2, where the cells are cut in smaller sub-cells and stacked as roof-tiles with electrically conductive adhesive (ECA) to ensure a reliable electrical contact.

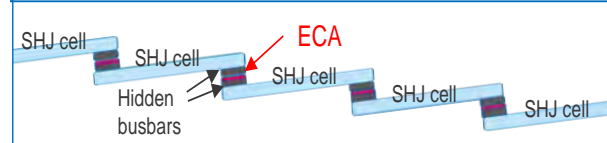


Figure 2: Schematic of the shingle cell interconnection approach.



Figure 3: Test module with 2 sub-cells featuring an electrodeposited copper metallization assembled with the shingle cell interconnection approach.

This direct interconnection method presents the advantages to suppress the optical and electrical losses related to the interconnecting ribbons present in state-of-the-art modules, to increase the power density and to yield improved aesthetics of the solar panel. This technique is currently investigated at CSEM with promising module efficiency of 20.6% achieved with screen-printed SHJ cells. In such advanced module configuration, the more resistive silver fingers implies to laser cut 4 to 6 sub-cells per 6" wafer cell, leading to damages potentially reducing electrical performance. These losses as well as the ECA consumption can significantly be mitigated by using copper plated SHJ cells where the highly conductive fingers enable to cut in only 3 or even 2 sub-cells reducing the area affected by the laser process, lowering the ECA amount required for the contact and the number of sub-cells to handle. An example of a test module with 2 copper plated cells is shown in Figure 3. With respect to state-of-the-art glued ribbon interconnection, the amount of ECA is reduced with such interconnection configuration, and power density increased. For the SHJ cells case, low damage segmentation must therefore be achieved to guarantee the high performance of such direct interconnected modules.

^[1] J. Geissbühler, et al. IEEE J. Photovoltaics 4, 4 (2014).

Multiple Metallization Schemes enabled by Multi-wire Interconnection.

A. Faes, C. Alleb  , N. Badel, C. Ballif, J. Champliaud, M. Dadras, M. Despeisse, J. Escarr  , J. Geissb  hler, J. Horzel, A. Lachowicz, J. Levrat

The SmartWire Contacting Technology provided by Meyer Burger consists in busbar-less cells interconnected using copper wires coated with a low melting point alloy, replacing the standard busbars and ribbons soldering. This multiple-wire approach permits using typically 18 wires instead of 3 to 5 ribbons, limiting the transport length in the cell metallization, therefore reducing the power losses in the metallization grid. This enables for the implementation of metallization lines with a line resistance up to $10 \Omega/cm$ without impacting the module electrical performance, providing opportunities for a great flexibility in the metallization techniques and materials for solar cells.

A variety of materials and techniques have been tested at CSEM for the fabrication of the metallization grids in silicon heterojunction solar cells. A first focus was set on fine-line screen-printing of low temperature cured Ag pastes. Following dedicated optimization, $\sim 30 \mu m$ large Ag fingers for $\sim 6 \Omega/cm$ line resistance and $\sim 60 \mu m$ large fingers for $1 \Omega/cm$ line resistance could be achieved. Pushing to the limits, ultra-fine-line printing of only $16 \mu m$ large fingers could be achieved through a mask opening of $12 \mu m$ and a mesh to opening orientation of 90° . In order to potentially lower metallization costs, not only a reduction of laydown material was studied, but also alternative materials such as copper-based low temperature cured pastes. First experiments demonstrated about $60 \mu m$ large printed fingers for a line resistance of $\sim 4.5 \Omega/cm$ using such material.

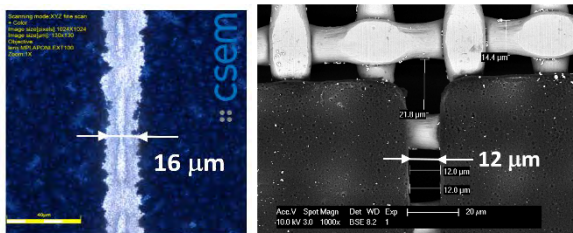


Figure 2: (left) Optical image of silver screen-printed finger, and (right) SEM image of the screen opening.

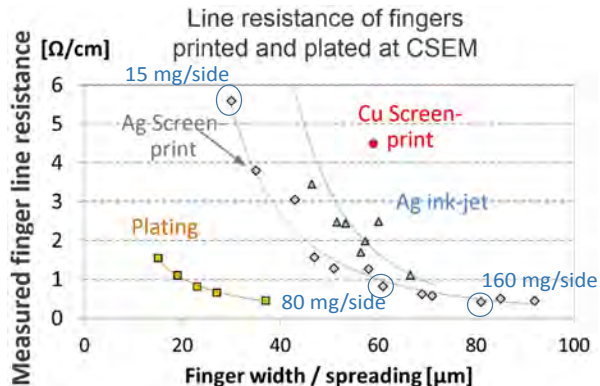


Figure 2: Measured finger line resistance vs. finger width for varying metallization techniques and materials.

A second focus was then set on alternative metallization techniques. Direct inkjet-printing of Ag was evaluated and different printing strategies were developed targeting either fine lines (minimum of $35 \mu m$ wide) or lines with high aspect ratio (up to 0.7, enabling for a line resistance of $1 \Omega/cm$ for $\sim 65 \mu m$ large fingers). Finally, the lowest line resistance for fine line metallization was achieved by copper electroplating, with down to $20 \mu m$ large fingers still with a line resistance of $1 \Omega/cm$, as produced in CSEM R&D plating pilot line.

In standard modules, cells are interconnected using 3 to 5 ribbons, imposing a line resistance below respectively 0.5 to

$1 \Omega/cm$ to ensure minimum electrical losses in the cell metal grid. Considering Figure 2, down to $20 \mu m$ large Copper plated fingers and down to $60 \mu m$ large printed Ag fingers can be implemented (the latter corresponding to a minimum laydown mass of about 80 mg of Ag per side without counting busbars). Alternatively, CSEM puts a strong focus in developing with Meyer Burger the SmartWire Contacting Technology (SWCT), which consists in interconnecting the cells via 18 wires instead of 3 to 5 ribbons: this strongly relaxes the constraint on the metallization grid to line resistances below $10 \Omega/cm$ still ensuring minimum electrical losses.

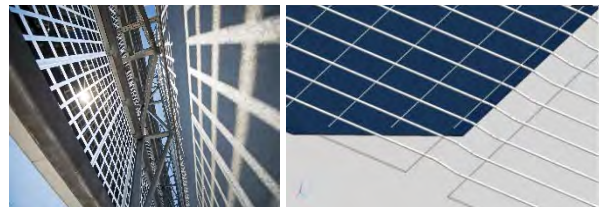


Figure 3: (left) Picture of the CSEM's facade from the backside of the solar modules (right) scheme of SmartWire interconnection of two busbar-less cells.

Considering Figure 2, all the developed metallization techniques and materials can now be employed: the multi-wire approach widens the possibilities offered for the metallization process and materials. Importantly, this first gives access to the implementation of fine-line printing even though line resistance of 2 to $6 \Omega/cm$ only are obtained. While this ensures enhanced performance via reduced shadowing ($\sim 0.5\text{--}1\%$ current generation increase), it can reduce Ag usage by up to a factor 5. Fine-line printing enabling for only 60 mg of Ag for both sides of bifacial SHJ cells (30 mg/side) was demonstrated at pilot level with 1000 cells processing, compatible with high performance multi-wire modules. Prototype modules were fabricated with silicon heterojunction busbarless cells produced with metallization grids based on fine-line screen printed Ag, screen-printed Cu based fingers, inkjet-printed Ag, as well as copper plated fingers. Each prototype module used 18 wires interconnection scheme, and was then tested for accelerated degradation under damp heat and thermo-cycling. All modules demonstrated $<5\%$ degradation after IEC testing standards, confirming the potential implementation of larger variety of metallization technologies and materials via the use of multiple-wire interconnection.

The new CSEM's solar powered facade implements such heterojunction cells interconnected by SWCT, further demonstrating improved aesthetics of this module concept for building integration.

Above 30% Efficiency Tandem Solar Cells using Silicon Heterojunction Bottom Cell

C. Alleb  , A. Tamboli •, D. Young •, S. Essig ••, B. Paviet-Salomon, A. Descoeuilles, L. Barraud, N. Badel, A . Faes, J. Levrat, M. Despeisse, C. Ballif

The CSEM PV-center and the National Renewable Energy Laboratory (NREL, USA) have jointly fabricated more than 30% efficient tandem solar cells using silicon bottom cells. This result sets a benchmark in the development of such silicon based tandem cells, approach followed by many groups worldwide to surpass the theoretical limit of silicon single-junction solar cells. The top cell was made of either GaInP or GaAs and fabricated by NREL, while the bottom cells were silicon heterojunction solar cells fully manufactured in CSEM fabrication platform. Special focus was set on optimizing the silicon cell for application in such tandem configuration. The top and bottom cells were mechanically stacked in 4-terminals tandem devices, and world record certified efficiencies of respectively 30.45% and 30.63% were achieved for GaInP/SiHJ and for GaAs/SiHJ tandem cells.

Within the next years the conversion efficiency of Silicon single-junction solar cells will converge towards its practical limit between 26% and 27% under one-sun operation. This performance limit can then be overcome by adding one or more cells with bandgap energy larger than 1.1 eV to the silicon cell. Thereby, short-wavelength photons are converted in the higher-bandgap top cells, reducing thermalisation losses in the solar cell and leading to the generation of an additional voltage. Simulations, based on the detailed balance limit, have shown that dual-junction cells with Si bottom cells can achieve theoretical efficiencies over 45%. The optimum top cell must feature a bandgap energy in the range of 1.6 to 1.8 eV and a high external radiative efficiency. In this context, large efforts are set worldwide in the development of such tandem solar cells using a silicon bottom cell, and in particular at CSEM to prepare the next generation solar cells.

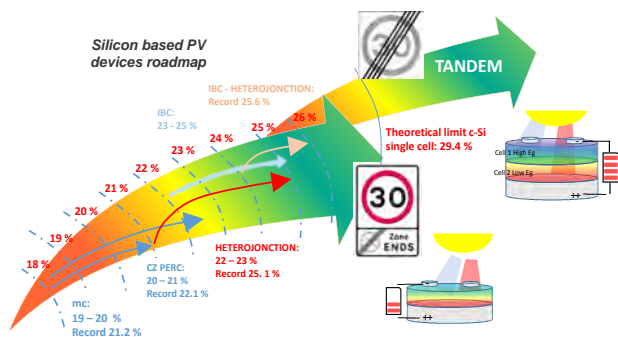


Figure 1: Schematic representation of silicon based PV devices roadmap for enhanced efficiency, with potential to overcome the 30% efficiency limit with tandem cells structures.

The Silicon heterojunction solar cells (SHJ) developed at CSEM are well suited for integration in tandem cells. SHJ cells have passivating contacts enabling for its key advantage of high operating voltages, and further provide excellent response in the long wavelength range, contributing to record 1-sun efficiencies (up to 23.44% achieved on CSEM fabrication platform). A challenge for SHJ cells remains the parasitic light absorption in the thin a-Si:H and TCO films especially for short wavelengths at the front side of the cell. The integration of a SHJ cell in a tandem device therefore cancels this intrinsic limitation of SHJ cells: excellent conversion of short-wavelength radiations up to typically about 700 nm is realized in the top cell and efficient conversion of the longer-wavelength radiations is achieved in the SHJ bottom cell. To demonstrate the potential of such tandem solar cells structures implementing a SHJ bottom cell, two different structures were tested in collaboration with NREL and EPFL. The CSEM SHJ bottom cells were

combined with top cells fabricated by NREL, either a rear-hetero-junction GaInP top cell or a GaAs top cell. The fabricated top and bottom cells were then mechanically stacked to form 4-terminals III-V/Si tandem cells, with each of the sub-cell being operated independently at its own maximum power point.

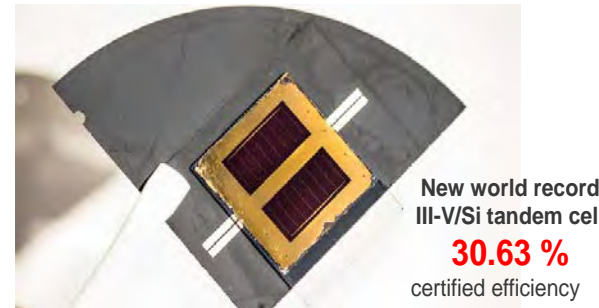


Figure 2: Picture of 1 cm² III-V/Si tandem cells mechanically stacked, demonstrating up to 30.63% record efficiency.

Main electrical characteristics of the devices are summarized in Table 1. The accurate analysis of the cumulative tandem cell efficiency requires the bottom cell JV-curve to be measured while the top cell is kept at its maximum power point. Under these conditions, resulting cumulative tandem cells efficiencies of 30.45% and of 30.63% are achieved.

Table 1: Characteristic parameters of the NREL certified JV-curves of the GaInP/SiHJ and GaAs/SiHJ tandem cells fabricated.

	V _{oc} [mV]	J _{sc} [mA/cm ²]	FF [%]	cell efficiency [%]	tandem cell efficiency [%]
GaInP/Si tandem, A= 1.005 cm²					
GaInP top cell	1448.3	15.30	85.1	18.83	30.45
Si bottom cell	691.9	21.49	78.2	11.62	
GaAs/Si tandem, A= 1.006 cm²					
GaAs top cell	1090.9	28.98	81.5	25.61	30.63
Si bottom cell	669.1	9.53	78.8	5.02	

To the best of our knowledge, these are the III-V/Si multi-junction solar cells with the highest one-sun efficiency ever reported. This efficiency exceeds the theoretical efficiency limit (29.4%) and the record experimental efficiency value (26.33%) of a Si single-junction, 1-sun solar cell and is also higher than the record efficiency 1-sun GaAs device (28.8%). It is also close to the record 1-sun efficiency for dual-junction solar cells of 31.1%, which was achieved with monolithic GaInP/GaAs devices. It therefore demonstrates the high potential of such tandem solar cells using SHJ bottom cell. This work opens the route for testing/developing new processes, materials and concepts enabling to further boost, establish PV as performant energy source.

Development of Indium-free TCOs for Silicon Heterojunction Solar Cells

G. Christmann, D. Sacchetto, L. Sansonnens, G. Wahli •, L. Barraud, A. Descœudres, B. Paviet-Salomon, A. Faes, J. Champliaud, N. Badel, B. Srahm •, M. Despeisse, S. Nicolay, C. Ballif

In the framework of the H2020 project INREP and the CTI project TACOS, CSEM develops in collaboration with the Meyer Burger Research (MBR) indium free transparent conducting oxides as a replacement for indium tin oxide.

High efficiency silicon heterojunction technology (HJT) solar cells are a very promising solution for the development of clean renewable energy sources. Indeed, this technology holds the highest record efficiency for single junction silicon solar cells (>26%). Furthermore, it is cost competitive thanks to a fabrication process involving a limited number of fabrication steps compared to other wafer based technologies. In this context, CSEM has developed a strong expertise in this technology, and in parallel, the Meyer Burger group is proposing a full platform for silicon HJT solar cell production. Despite its established advantages, it remains necessary to further increase the competitiveness of this technology to promote its adoption within a very conservative industry. With this in mind CSEM has been developing indium-free transparent conducting oxide (TCO) to replace the costly indium tin oxide (ITO) which is currently the standard material used in HJT as front and back electrodes (Figure 1).

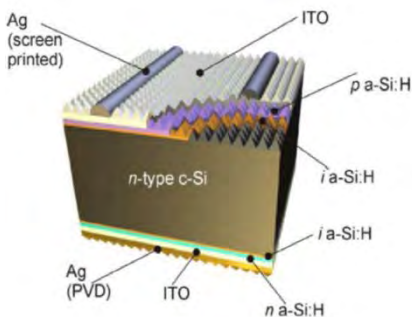


Figure 1: Typical semiconductor HJT solar cell structure.

The chosen alternative for ITO is aluminum-doped zinc oxide (AZO) as it has a high bandgap (3.3 eV), ensuring good transparency and can be doped to high carrier concentrations ($\sim 10^{21} \text{ cm}^{-3}$), allowing high conductivity. AZO can be sputtered, therefore targets can be installed into the existing ITO PVD tools. However, the properties of AZO are not on par with ITO: for typical layers used in solar cells the AZO mobility is $\sim 15 \text{ cm}^2/(\text{V.s})$ against $30 \text{ cm}^2/(\text{V.s})$ for ITO. Hence, to achieve the same sheet resistance a higher carrier concentration is required, thus increasing losses by free carrier absorption. AZO is also more sensitive to residual moisture, which raises concerns about process sensitivity and controllability but also about the reliability of finished devices incorporating these layers. Therefore, CSEM should demonstrate that it is possible to achieve similar cell efficiencies with AZO contacts than with ITO ones and that cells with AZO can be made in a production environment with good reliability.

The design of the solar cells was carefully considered in order to circumvent the intrinsic limitations of AZO with respect to ITO. For example a rear emitter design where the p a-Si is at the back and the n at the front has been chosen. This way wafer conduction helps current spreading thus relaxing conductivity

constraints on the AZO. Contacts were initially developed on CSEM cells, and then the process was tested on Meyer Burger 6 inch production cells. Figure 2 shows that replacing ITO by AZO can be done with minimal power conversion efficiency (PCE) losses (-0.2 point).

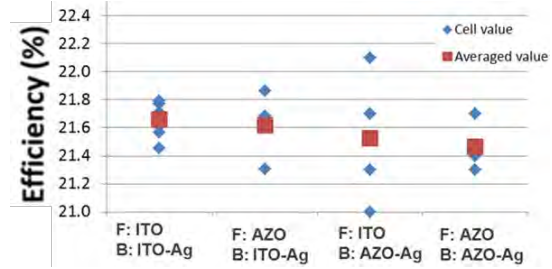


Figure 2: Comparison between AZO and ITO contacts on Meyer Burger HJT solar cells efficiency (F: front and back contact).

These very encouraging results were transferred on MBR tools with active support from CSEM, first on a semi-production scale tool and their full scale production scale allowing processing of 42 cells in one go. Initial runs on the large scale tool exhibited efficiencies 0.6 points below ITO reference but more recent results exhibited efficiencies 0.2-0.3 point below references, showing the results obtained at CSEM can be transferred on the production tools. Continuous process improvement is expected to further reduce the gap. Finally the reliability of cells using AZO was assessed and compared to ITO by testing 1 cell mini-modules for damp heat degradation (85°C; 85% humidity). It was observed that there is no significant difference between the two types of cells and the mini modules using AZO cells pass the IEC standard degradation test (<5% relative degradation for 1000 hours).



Figure 3: 16 indium-free cells demo module.

In summary AZO transparent electrodes as replacement for ITO is at a stage close to production with very similar PCEs and reliability and an industrial scale compatible process.

This work is supported by the Commission for Technology and Innovation (CTI) through the TACOS project and by the European Union's Horizon 2020 research and innovation program under grant agreement No 641864 (INREP).

• Meyer Burger Research

Upscaling of Perovskite-based PV Devices within Project CHEOPS

A. Walter, S.-J. Moon, D. Sacchetto, B. Niesen, S. Nicolay

By leading the European Horizon 2020 project CHEOPS (low Cost and Highly Efficient phOtovoltaic Perovskite Solar cells), CSEM is committed to bring the promising emerging PV material perovskite closer to the market. To do so, the project focuses on three main axes: development of perovskite/silicon tandem cells, encapsulation and stability, and upscaling.

Energy conversion efficiency of organo-halide perovskite based photovoltaic devices has rapidly advanced over the course of the past few years, reaching values in excess of 20%. However, most of the reported efficiencies are still on small lab-scale devices below 0.3 cm^2 . Therefore, an important effort to upscale such results is needed to demonstrate the commercial viability of this technology. In this sense, CSEM has demonstrated a minimodule with 11.5% efficiency on 12 cm^2 aperture area [1].

Moreover, perovskite possesses a wide bandgap that fills the requirements as a top absorber in tandem devices in combination with crystalline silicon, offering the potential for very high efficiencies, a route that is also explored by CSEM and its partners in the project.

In terms of scalability, efforts have been made recently at CSEM to go from 0.49 cm^2 cells to 1.015 cm^2 cells without a drop in efficiency. In fact, owing to a careful choice of materials and deposition processes, it has been possible to produce 1.015 cm^2 cells with an efficiency as high as 17% (measured with maximum power point tracking), a record for the simple $\text{CH}_3\text{NH}_3\text{PbI}_3$ absorber. In particular, CSEM's expertise in the deposition of TiO_x functional layers by magnetron sputtering has led to the synthesis of very efficient Electron selective contacts.

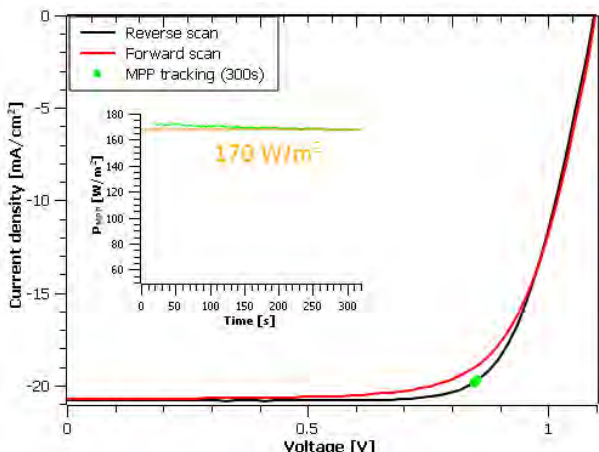


Figure 1: JV characteristics of a perovskite solar cell exhibiting a stabilized power output of 17%. The cell shows the typical hysteresis associated to perovskite solar cells.

These early results already set the necessary base for achieving the ambitious goal of the CHEOPS project, namely manufacturing high efficiency (above 14%) stable modules of at least $15 \times 15\text{ cm}^2$ in a pre-production environment.

As previously stated, one of the main interest of perovskite absorber is that it can provide a low-cost efficiency boost to existing crystalline silicon solar cells, such as the high efficiency silicon heterojunction cells developed at the CSEM PV-center. Within the frame of CHEOPS, CSEM and EPFL's PV-lab have already successfully demonstrated record breaking tandem cells. Two different tandem architecture are currently investigated: a monolithic integration, where the perovskite top absorber is directly grown on the silicon bottom cell, thus limiting the need for interconnections, and the so-called 4-terminal tandem, where two independently fabricated sub-cells are mechanically stacked together. Recent published results have shown a 20.5% efficiency for the monolithic tandem cell and a 4-terminal-like measurement demonstrating 25.2% [2].

Finally, on the material synthesis level, work is being conducted to implement a perovskite composition that would lead to cells both more stable and more efficient. Namely, a triple cations mixed-halide composition combining Pb, Cs and Br atoms is tested.

Table 1: Comparison between triple-cations mixed halide & "standard" cell.

	Eff. [%]	Voc [mV]	Jsc [mA/cm²]	FF [%]	MPP tracked P density [W/m²]
3-cations	18.74	1175.12	21.54	73.24	171.88
standard	16.88	1094.02	20.81	74.15	167.80

In the coming time, focus will be put on further upscaling these results while improving the stability of the cells. In that respect, specific encapsulation schemes are also under development at CSEM.

This work has received funding from the European Union's Horizon 2020 research and innovation program under Grant Agreement No. 653296.

[1] S.-J. Moon, J.-H. Yum, L. Löfgren, A. Walter, L. Sansonnens, M. Benkhaira, S. Nicolay, J. Bailat, C. Ballif, "Laser-Scribing Patterning for the Production of Organometallic Halide Perovskite Solar Modules", JPV, 5 (2015), 1087-1092

[2] J. Werner, L. Barraud, A. Walter, M. Bräuninger, F. Sahli, D. Sacchetto, N. Tétreault, B. Paviet-Salomon, S.-J. Moon, C. Allebé, M. Despeisse, S. Nicolay, S. De Wolf, B. Niesen, C. Ballif, "Efficient Near-Infrared Transparent Perovskite Solar Cells Enabling Direct Comparison of 4-Terminal and Monolithic Perovskite/Silicon Tandem Cells", ACS Energy Letters, 1 (2016), 474-480

Silicon Photovoltaics for Hydrogen Production

J.-W. Schüttauf, D. Dominé, A. Faes, M. Despeisse, C. Ballif, J. Bailat

The SHINE Nano-Tera.ch project aims at the realization of a fully integrated solar-to-hydrogen system using thin-film silicon solar cells. Compared to a standard approach with discrete elements – with separate solar panels and electrolyzer – an improved efficiency might be expected thanks to the recycling of the dissipated heat from the solar cell using the same components.

Due to the intermittent nature of renewable energy technologies such as wind and solar, their large-scale implementation requires solving current challenges related to energy storage.

A possible solution to elegantly store energy from sunlight in chemical bonds is the direct production of hydrogen using solar cells and water. Hydrogen can for instance be compressed, transported and stored; alternatively it can be injected in the gas distribution system as it is done, e.g., in a demonstration project in Germany.

The multidisciplinary Nano-Tera.ch project SHINE involves several research groups within the fields of optics for solar energy, optics and fluidics, semiconductor solar cells, electrochemical materials and system simulation^[1]. CSEM is in charge of developing the photovoltaic components of the system.

Thin-film silicon-based triple-junction devices have been developed to be integrated with electrolysis units. Such cells consist of a stack of two amorphous silicon subcells and one microcrystalline silicon subcell, and are optimized to achieve a sufficient voltage for water splitting when coupled to an electrolyzer.

At one sun illumination, an open-circuit voltage of 2.14 V and a power density produced at the maximum power point of 11.3 mW/cm² have been obtained, leading to a potential water splitting efficiency of 8.1%^[2]. This device has been successfully integrated in laboratory hydrogen production setups, so far leading to a stable solar-to-hydrogen conversion efficiency above 6% for over 20 hours.

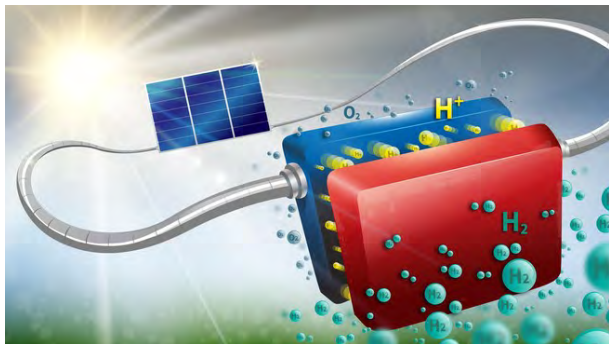


Figure 1: Artistic impression of our record solar-driven water splitting system^[3].

[1] <http://www.nano-tera.ch/projects/367.php>

[2] D. Dominé, et al., Proc. of WC PEC 6, Kyoto, Japan (2014).

[3] <https://actu.epfl.ch/news/an-effective-and-low-cost-solution-for-storing-solar/>

More straightforward solutions using silicon solar cells have also been studied, such as a serial interconnection of silicon heterojunction solar cells (see Figure 1). With this approach, we have obtained a stable (>100 h) solar-to-hydrogen conversion efficiency of 14.2% without DC/DC conversion, fully relying silicon-based solar cells and earth-abundant electrocatalysts^[4]. This value currently represents the highest reported efficiency worldwide for solar-driven water splitting based on silicon photovoltaics^[3-5].

The solar cells that have been applied in this study are of the same type and manufacturing procedure as the ones used in the façade covering the south side of the CSEM building in Neuchâtel (see Figure 2). Moreover, contrary to many other approaches presented in the literature, this solution provides an excellent stability. Efficiencies slightly above 16% should be practically possible on the short term following this approach.



Figure 2: Solar façade on the CSEM building in Neuchâtel.

As the components in the presented system are commercially viable, easily scalable and have long lifetimes, these devices have the potential to open a fast avenue towards the industrialization and deployment of cost effective solar-fuel production systems. As an example, a 12-14 m² system installed in Switzerland would allow the generation and storage of enough hydrogen to power a fuel cell car over 10'000 km every year.

CSEM thanks Nano-Tera.ch for its financial support received in the framework of the RTD project SHINE.

[4] J.-W. Schüttauf, M.A. Modestino, E. Chinello, D. Lambellet, A. Delfino, D. Dominé, A. Faes, M. Despeisse, J. Bailat, D. Psaltis, C. Moser and C. Ballif, J. Electrochem. Soc. 163, F1177 (2016).

[5] J. W. Ager, M. Shaner, K. Walczak, I. D. Sharp, S. Ardo, Energy Environ. Sci. 8, 2811 (2015).

Plastics Compounding Platform for Reliable and Dedicated Packaging Materials for PV Modules

H.-Y. Li, J. Escarré, G. Cattaneo, U. Fuerholz, C. Ballif, L.-E. Perret-Aebi

The compounding platform at CSEM has been expanded to better serve the needs for developing resistant and customized packaging materials for PV modules encapsulation. At the moment, cast film with width up to 20 cm can be extruded with capacity of 10 kg/h. Several ongoing projects have been benefitting from the platform and obtaining key R&D results. The expanded platform further strengthens the competitiveness of CSEM as a major R&D partner in the field of PV module technology.

The reliability of PV modules is critical for the further reduction of the levelized cost of PV electricity. A typical PV module mainly consists of front cover, stringed cells and back cover. For the structural integrity, those components are bonded with two layers of adhesive film, commonly referred as the encapsulant. These thin encapsulants, normally 0.4-0.5 mm thick, bare multiple important functionalities within the module, like the mechanical bonding, optical in-coupling, UV blocking, water/oxygen barrier, etc. Moreover, its stability under the combinational effects of light, heat and moisture has a significant impact on the reliability of the PV modules^[1]. The mostly used encapsulant in the past decades has been based on poly (ethylene-vinyl acetate) (EVA). It has been observed that EVA encapsulants of various grades from different manufacturers exhibit distinct outdoor reliability. The composition of the EVA base resins used therein is often similar with 26-32% of Vinyl Acetate. The key factor causing the different reliability is the formulation. This is also true for the polyolefin (PO)-based encapsulant, which is considered as a major alternative to EVA.



Figure 1: The compounding platform in CSEM. a) Extruder; b) Flat film line; c) Compounder; d) Pelletizer.

In the past year, CSEM has expanded the infrastructure available in the plastics compounding platform, to meet the growing needs of various projects on performing and customized PV packaging materials. Now the platform includes mainly the following facilities (see Figure 1):

- Dr.COLLIN TEACH-LINE twin-screw compounding ZK 25 x 24 L/D. Its max. throughput is 4.0 kg/h.
- Dr.COLLIN lab strand pelletizer

- Dr.COLLIN single-screw extruder 25 mm Φ x 25 D, Type E 25E. Its max. throughput is 10 kg/h.
- Dr. COLLIN flat film line consists of Chill roll with width of 350 mm, 2 flat-film die slot with width of 200 mm, winder and tempering unit.
- Chemical analysis facility (e.g. DMDR, DSC, FTIR, GC/LC-MS, Raman, GPC, NMR,...), partly in collaboration with external partners
- Extensive accelerating lifetime testing facilities: climate chambers for damp heat, thermal cycling, humidity freeze, UV+ damp heat; UV chamber; Ovens; highly accelerated damp heat testing setup (high-pressure cooker test).

With the expanded infrastructure, the platform can extrude packaging foil of 0.1 to 2.5 mm thick with the maximum width of 20 cm and maximum throughput of 10 kg/h. The platform has been supporting a few projects (internal, industrial and CTI). The highlights of the R&D results are listed here:

- EVA and TPO-based encapsulant with red-shifted UV absorption have been developed. The cut-off wavelength can be adjusted from 350 to 400 nm. The conventional approach with cut off at 400 nm results in slight yellowing. With the innovative approach, the yellowness is reduced.
- A technique has been developed and tested extensively to fine-tune the viscoelastic properties of the EVA or PO base material during the module lamination cycle. This approach is shown to be capable of producing EVA/PO-based packaging materials with customized processabilities to meet the specific needs of the novel module design or module lamination process.
- Conventional white EVA reflects rather uniformly in the UV, visible and near IR. By adjusting the formulation, a white EVA encapsulant with improved transmittance in the NIR range has been developed.
- For a specific project, a PO-based packaging material with improved adhesion to the surface of metal and Si solar cell is developed. The adhesion to the studied surface is enhanced by at least 3 times compared to the reference solution.

Besides the highlights above, progress has been made on developing EVA/PO-based PV encapsulant with superior environmental reliability to the commercial competitors. This will serve as the base for the further development of customized packaging materials.

^[1] H.-Y. Li, "Open the black box: understanding the encapsulation process of photovoltaic modules", Ph.D dissertation, EPFL (2013).

Solarstratos—a Solar Airplane to the Edge of Space

P. Duvoisin, J. Escarré, J. Levrat, R. Oleiwan, C. Ballif, L.-E. Perret-Aebi

CSEM, as technological partner of the Solarstratos project, has been responsible for the design, fabrication and integration of customized solar modules on an electrical airplane conceived to reach the stratosphere with the sole means of solar power. With a total weight of 700 g/m², the developed ultra-light weight solar panels can be integrated on to the Solarstratos airplane by means of an innovative fixation system. The project will move solar aviation one step closer to its use in close to space conditions what can open new possibilities in fields such as telecommunication, observation or earth monitoring.

Solarstratos project [1] primary goal is to further demonstrate the potential of renewable energies by reaching the stratosphere with a manned electrical airplane only powered by solar means, thus, establishing a new altitude world record for this flight mode. In this project, the role of CSEM has been the design, fabrication, testing and accurate integration of customized solar modules on the airplane structure with ideally no detrimental effect for its aerodynamics.

In order to maximize the overall energy density stored in the plane a key point was to minimize its weight. In order to achieve this target, CSEM has developed ultra-light weight solar modules by laminating at room temperature the solar cells in between a composite based back-sheet and a polymeric front cover by means of a pressure sensitive adhesive. The resulting modules have a total weight of 700 g/m² including the Sunpower silicon solar cells weight of 450 g/m².

These ultra-light weight PV panels are very fragile and easily damageable if mishandled. Thus, a manufacturing process has been designed and implemented allowing the modules to be kept over a rigid plate during all different fabrication steps until its final installation on the airplane structure. Thanks to this process, production yields close to 100% have been achieved, minimizing material waste.

CSEM has also proposed and delivered an innovative solution which ensures a secure fixing of the modules on the carbon/epoxy structure of the plane. This solution adds flexibility allowing for an easy replacement of the modules after installation. Thus, installed solar panels can be updated in the future or, in case of defaults such as solar cell breakage, replaced with no damage on the plane structure. This integration scheme can also be applied on existing electrical planes turning them into solar powered ones.

Solar modules will be subjected to harsh temperature conditions of around -70°C during the flight towards the stratosphere. These extreme temperatures could reduce adhesion between materials and create thermal stresses in welds able to deteriorate electrical connections between PV panels. Such conditions have been simulated on climatic chambers where test modules have been submitted to more than 200 cycles of temperature varying from -40°C to 85°C with no significant degradation. Additionally, adhesion at critical interfaces has also been measured for temperatures ranging from -70°C to 60°C. On the other hand, low temperatures present in the stratosphere are beneficial to increase the

energy yield of the PV panels, as their electrical output decreases with temperature at rates of 0.3-0.4% per degree Celsius. An experiment carried out by means of a helium-filled balloon has proven that the working temperature of a Sunpower solar cell can plunge from +40°C to -20°C when it reaches an altitude of 12 km in a sunny summer day. The data collected during this experiment is shown in Figure 1.

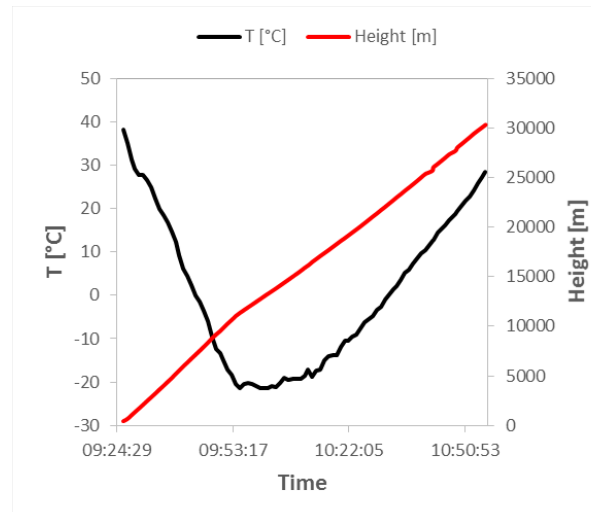


Figure 1: Solar cell operating temperature as a function of the height.

Solarstratos project represents a great opportunity for testing solar cells and materials, which are generally used in terrestrial applications, in close to space conditions gaining and accumulating an important amount of knowledge to be used in future prototypes.

The energy produced by the plane for different heights and positions relative to sun is estimated by means of a semi-empirical model developed by CSEM. This model is helping to select the most appropriate date, taking off location, flight height profile and overall plane path to optimize the solar energy generated during the flight. Moreover, data generated from this model are also used as input for the design of electronic components of the PV system such as the MPPT DC-DC converters.

Solarstratos paves the way to move solar and electric aviation one step closer to its use in space and opens new perspectives in different areas such as telecommunications, observation or earth monitoring.

[1] www.solarstratos.com

Embedded Light Management Films for All-season Energy-harvesting in Printed Photovoltaics

J. Mayer, T. Offermans, B. Gallinet, I. Zhurinsky, R. Ferrini

Applying light management on the device surface is a favorable method for efficiency enhancement, since it avoids complications with the delicate printing of the photovoltaic layers. Previously proposed structures, however, have their functional interface exposed to environmental impacts and stress. Here we demonstrate a photonic nanostructure that is able to increase the total yearly harvested energy by 13%. The nanostructure is embedded in a transparent film, providing a conformal light management device attachment that is protected from environmental exposure and dust.

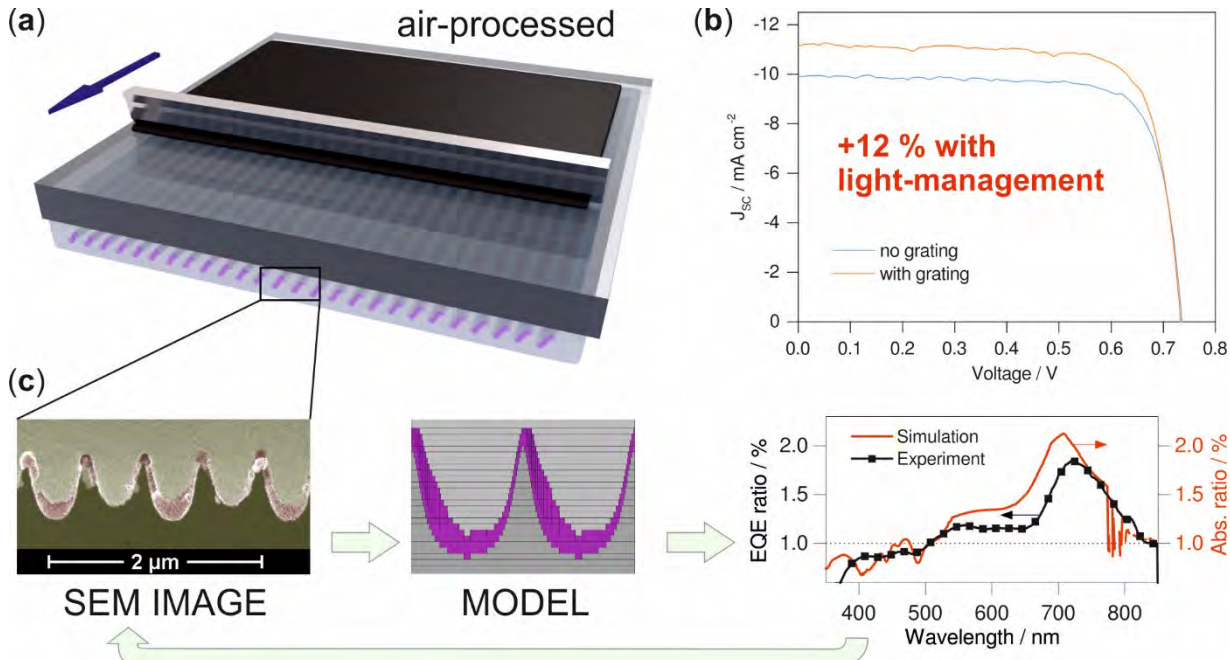


Figure 1: (a) Photovoltaic test cells are printed on a modified substrate with an attached light-management layer. Through light redirection via elaborated diffraction properties, the absorption in the absorber is enhanced and (b) a 12% increase in the efficiency is obtained. (c) A simulation platform was developed to predict, explain and design the impact of the photonic nanostructures for a given cell architecture and use case.

Organic photovoltaics (OPV) have recently reached over 11% power conversion efficiency (PCE) in single-junction and 13.2% in multi-junction cells, continuing their route towards commercialization. To further advance this progress, light management (LM) for organic photovoltaics has attracted increasing interest as an additional route besides material development and process and morphology engineering. It has been emphasized recently, however, that certain key aspects are crucial for a successful implementation of light management in printed thin film photovoltaics,^[1] namely i) avoiding electronic losses or parasitic absorption ii) developing structures that are cost effective in the integration and compatible both with mass-manufacturability and outdoor operation and iii) considering the integrated energy harvested throughout a full year, rather than only under standard test conditions (STC).

We therefore developed an elaborated diffractive nanostructure which provides a solution to these central points with an economically attractive enhancement-per-cost ratio. Figure 1a shows the printing of organic solar cells, which is independent from the LM layer that is attached on the light incident side of the substrate.^[2] Consequently, the morphology of the active layers, which is known to influence the electrical properties of

the device, is not affected and the absorption enhancement induced by the LM act directly on the efficiency (Figure 2b). Furthermore, the embedded LM films are protected against environmental influences and can be fabricated on large scales, for example integrated in a roll-2-roll production line.

A simulation platform was developed (Figure 1c), which is able to reproduce the absorption enhancement under STC in multiple devices (with an internal quantum efficiency assumed to be unaffected by the LM). It is observed that an overestimation of the enhancement arises from the limited geometrical extent of the charge collecting electrode. An even more effective collection of trapped light can thus be expected on larger scales.

Motivated by the good agreement of the spectral enhancement with the simulations under STC, an estimation of the full year current generation is given. Accounting for hourly spectrum, zenith and azimuth angle of a full year (clear sky), an increase in the harvested energy of up to 13% is predicted. Moreover, it is shown how the grating properties can be tailored by several parameters to take into account the illumination conditions of various application cases (automotive, facade, consumer electronics, shading) enabling the customization and optimization of the yearly energy harvesting capability.

^[1] Nat. Nanotechnol., 9, 19-32 (2014); Nat. Mater., 13, 451-460 (2014); Energy Environ. Sci., 7, 2123 (2014).

^[2] J. Mayer, et al., Opt. Express 24(2), A358-A373 (2016); submitted.

Results from Non-intrusive Load Monitoring

A. Hutter, S. Arberet, T.-H. Lee, R. Carrillo Rangel

Non-intrusive load monitoring (NILM) refers to the determination of the electrical load composition through a single point of measurement, e.g. at the main power feed. In this article we shortly review NILM techniques, position the CSEM approach and provide results from recent work.

NILM requires load curve data acquisition at an adequate rate so that distinctive load patterns can be identified. As the number of exploitable data features increases with the sampling frequency, the latter mainly determines the number of appliances that can be identified, see also Table 1 hereafter.

Data Frequency Analyzed	1 hr - 15 min	1 min - 1 s (1 Hz)	1-60 Hz	60 Hz-2 kHz	10-40 kHz	>1 MHz
Data Appearance						
Data Features Used by Algorithms	Visually observable patterns: duration and time of appliance use	Steady state steps/transitions of power	Steady state steps/transitions of power	Current and voltage, providing medium order harmonics to identify type & electrical circuitry in appliance	Current and voltage, providing very high order harmonics to identify both harmonic & the background noise of appliances	
Appliances Identified	Differentiates ~3 general categories: loads that correlate with outdoor temperature, loads that are continuous, and loads that are time-dependent	Top ~10 appliance types: Refrigerator, ACs, Heaters, Pool Pumps, Washers, Dryers, etc.	10-20 appliance types	Not known, see text for more details	20-100 specific appliances: e.g., differentiating between 2 lights requires separate power consumption data streams	

Table 1: Survey derived from approximately 40 studies^[1] showing exploitable data features and number of identifiable appliances as function of data acquisition frequency.

The disaggregation into individual appliances is based on statistical approaches, which try to identify known appliance signatures in the aggregated load curve. In general we can distinguish supervised and unsupervised approaches. Supervised approaches, which include optimization (sparse representation, dictionary learning, nonnegative matrix factorization, etc.) and pattern recognition (support vector machines, neuronal networks, hidden Markov models (HMM), Bayesian networks, etc.) techniques, require – often rather large – labelled data bases for training. Unsupervised approaches are based on parametric or probabilistic models that are used by feature detection models (e.g. on/off events) in combination with clustering approaches.

The NILM approach investigated at CSEM is unsupervised and exploits sparse signal decomposition based on the Orthogonal Matching Pursuit (OMP) algorithm with rectangular shaped boxcar atoms, see also Figure 1. The signal decomposition is based on active and reactive power on all three phases and has been mainly applied to 1 Hz signals.

A benchmarking study of the CSEM algorithm conducted last year was based on data from the publicly available data bases ECO (Switzerland) and DALE (UK), which both contain labelled data. The study revealed the following major points:

- In general, an average energy detection error of about 6.5% and event detection precisions above 95% have been observed.
- The currently used parametric models are not yet well suited for all encountered situation, such that the resulting energy estimation errors are then above 10%.

Concerning the second point, it is anticipated that tuning of the model parameters combined with some adaptations of the algorithm framework will allow to cope with such situations so that the performance observed in the first point can then be achieved in all situations.

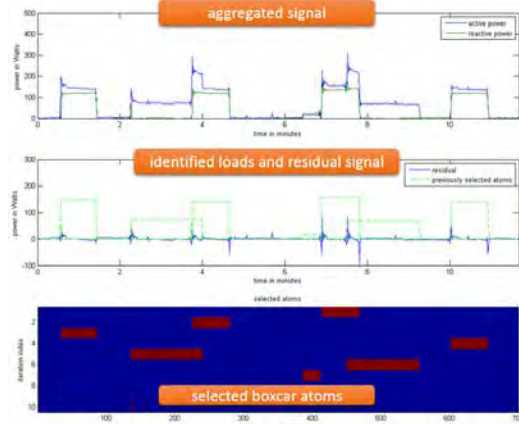


Figure 1: Illustration of CSEM's OMP-based disaggregation approach.

In early 2016 the CSEM NILM approach has also been applied to detect heat pumps at household level. Data sampled at 1 Hz from three households was analyzed for a duration of two weeks. The results from the benchmarking were confirmed with an average error of the daily energy consumption of 6.13%. For the activation events (e.g. turning an appliance ON) a recall^[2] of 96.4% and a precision of 99.1% were observed, whereas for the deactivation events (turning an appliance OFF) recall and precision were 96.4% and 98.8%, respectively. The study then investigated the effect of an increased sampling period (SP). For SPs of 30 seconds and 1 minute the average energy error decreased only slightly to 6.63 and 7.53%. A similar behavior was observed for the events statistics (see also Figure 2) which shows that reduced sampling frequencies down to about 1/60 Hz are possible.



Figure 2: Heat-pump activation event detection statistics.

The above example illustrates the performance of the patented CSEM approach, which is currently continuously extended to include new appliances.

[1] K. Carrie Armel, et al., "Is disaggregation the holy grail of Energy Efficiency?", Precourt Energy Efficiency Center PTP-2012-05-1.

[2] "Recall" is defined as the percentage of the number of all detected true positive events w.r.t. to all relevant positive events, whereas precision is the number of true positives w.r.t. all detected events.

TRIBUTE—Automatic Building Simulation Model Calibration and Diagnostics

E. Onillon, M. Boegli, E. Olivero

In the frame of the European FP7 project TRIBUTE, CSEM developed novel methods for the automatic calibration of Building Energy Performance Simulation models with the aim of reducing the gap between the building's predicted and measured energy consumption. Such a calibrated model allows real-time monitoring of the building's energetic evolution and the diagnosis of misbehaviors.

Buildings account for more than 40% of energy consumption and 36% of CO₂ emissions in the EU. The EU Energy Efficiency Directive^[1] establishes a set of binding measures to be implemented by EU members by the end of 2016 in order to reach a 20% energy-efficiency target by 2020. In order to reach this target, Building Energy Performance Simulation (BEPS) tools are widely used for modern mid-size to especially large buildings and thus throughout the full life cycle of such buildings. These models, if used throughout the building commissioning phase, might become a powerful means of helping building operators and facility managers to assess building energy performance, detect anomalies, and suggest management improvements. Nevertheless, today's BEPS models are largely insufficient, showing significant discrepancies between measured and computed building energy performances, limiting their applicability.

In the frame of the TRIBUTE project, based on a set of deployed sensors, methods that allow for automatic calibration of the underlying simulation model were developed. By continuously learning from operation, the results from TRIBUTE show a 15% reduction of the energy gap on test sites. The development of TRIBUTE relies on the IDA Indoor Climate and Energy (IDA-ICE) tool developed by EQUA Simulation AB, one of the TRIBUTE's partners. IDA-ICE is a whole-building simulation tool based on dynamic multi-zone calculations and provides results on thermal indoor climate and energy consumption. The proposed TRIBUTE method relies on three steps. First, the simulation model is established and a first simulation model calibration is performed. Second, a sensitivity study is performed, allowing determination of the simulation model parameter that has the largest influence on the building energy performance. Third, these parameters will be continuously learnt, while their evolution will indicate building ageing or faults. These developments are currently validated on a public building in La Rochelle France, namely the Vaucanson building, which is depicted in Figure 1. Figure 2 shows the results of the second step with the most critical parameters that need to be calibrated.



Figure 1: La Rochelle building, IDA-ICE 3D view.

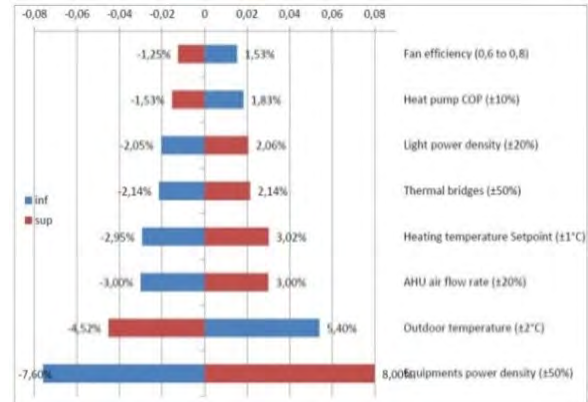


Figure 2: Impact of the most influential parameters on the total energy consumption of La Rochelle building model.

CSEM developed a calibration method based on a Support Vector Regression (SVR) method. A meta-model for the cost function is created by means of SVR. An example is shown in Figure 3 below, where the sensitivity of the cost function is illustrated in a 3D view for two parameters (on the left) and in 2D views for four parameters (on the right). As such, the SVR method offers a visual high-order sensitivity analysis tool. Based on such meta-models, the calibration procedure subsequently applies optimization, which is either gradient-based (such as the Levenberg-Marquardt algorithm) or gradient-free (such as the Nelder-Mead method). So far, the optimization aims at minimizing temperature error and total required power, both restricted to a certain zone. Two metrics were considered: the mean bias error and the Coefficient of Variation of the Root Mean Square Error (CVRMSE). For the La Rochelle building, a 15% error reduction has been achieved.

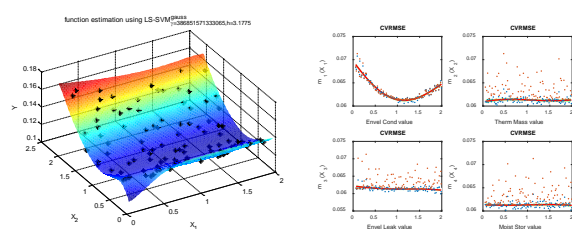


Figure 3: SVR meta-model cost function with two parameters (left) and four parameters (right).

The developed calibrated model lays the base for detecting building anomalies. The work has been carried out in the collaborative project TRIBUTE (<http://www.tribute-fp7.eu>) and is partly funded by the 7th Framework Program of the European Union (grant agreement no. 608790).

[1] Directive 2012/27/EU of the European parliament and of the council of 25 October 2012 on Energy Efficiency.

Electrical Energy Storage Optimization based on Predictive Control

M. Boegli, Y. Stauffer, S. Arberet, E. Onillon

In the framework of the European project AMBASSADOR, an online optimization aims at reducing the operational costs (i.e. global electricity bill) by taking into account all electric power generators and consumption elements of the districts and taking advantage of storage elements. The same framework can also be used to reduce the installation cost of batteries by performing an optimal sizing. To reach that goal, Model Predictive Control (MPC) is applied. MPC relies on adaptive models that predict the energetic behavior (production and/or consumption) of the various elements. Extensive simulations on experimental data were carried out under various real conditions and showed where significant savings can be achieved.

Increasing use of intermittent renewable energy sources, such as photovoltaics (PV) and wind turbines, as well as the availability of versatile storage equipment, offers the possibility of reducing costs by optimizing the energy flow between districts and electricity grid^[1].

The optimization is based on a Model Predictive Control (MPC) approach where the energy flow is optimized over a horizon of 24 h and updated every 15 min. In other words, the goal is to find the battery charge/discharge profile that minimizes costs over a 24-h horizon. The optimized control variable is the amount of charge or discharge of the battery. The main input variable is the aggregated energy, defined as the sum of renewable energy minus the sum of consumed energy, estimated over a 24-h horizon. The second input variable is the tariffs for buying from and selling to the grid, called TFG and TTG respectively. These tariffs can be variable (lower at night than in the daytime) or flat. Also, TTG can be equal to or different from (lower than) TFG. Third, the present state of charge of the battery storage is used as an input variable.

The optimization minimizes the resulting cost function, shown in Figure 1, taking into account efficiency factors and constraints. An extra constraint can also be added to avoid trading, that is, to prevent charging of the battery from the grid.

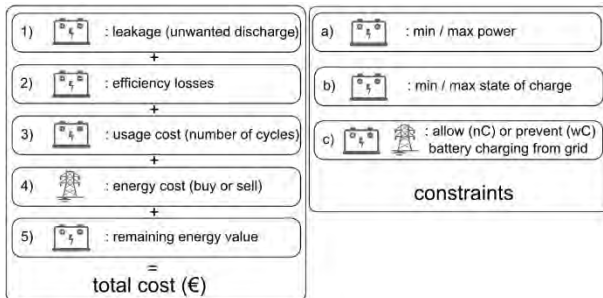


Figure 1: The different terms of the objective functions and constraints that are taken into account in the optimization problem.

Prediction models, based on Support Vector Regression (SVR) algorithms, estimate the production and consumption of the considered district elements. Prediction of renewable production, including PV and wind turbines, depends on the weather forecast (i.e. solar irradiance and wind speed) and time reference. Prediction of consumption elements, including houses, office buildings, and PMEs, depends on the weather forecast (i.e. temperature), working schedule, process planning, and time reference. Training of the SVR algorithm is done over the last 4–7 days with all available data.

This approach also makes it possible to optimize the battery size as early as the design stage, as illustrated in Figure 2.

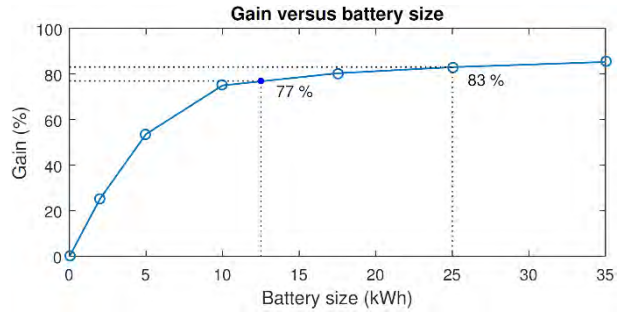


Figure 2: Optimization gain vs. battery size. When the battery size is halved from 25 to 12.5 kWh, the gain is reduced by only 6%.

In the following table, we qualitatively compare a solution without storage (NoSto) to two energy flow management strategies: simple storage (Sim Sto, acting as a buffer without optimization) and optimal storage based on MPC. For the latter we consider a version with no battery constraint (MPCnC), which allows trading, and a second version that prevents the battery from charging from the grid (MPCwC).

Table 1: Synthesis of various storage strategies and use cases.

	Variable Tariffs		Flat Tariffs		RoP
	Lo TTG	Hi TTG	Lo TTG	Hi TTG	
NoSto	😊	😊	😊	😊	😊
SimSto	😊	😊	😊	😊😊	😊
MPCwC	😊	😊	😊	😊😊	😊
MPCnC	😊😊	😊😊	😊	😊😊	😊

The results shown in Table 1 suggest the following conclusions:

- MPC shows significant advantages in the case of variable tariffs from and to the grid and is even better if trading is allowed.
- In the case of flat tariffs, MPC does not offer advantages compared to simple storage.
- Robustness towards Prediction errors (RoP) is average for MPCwC but rather good for MPCnC.

These conclusions were experimentally confirmed by the deployment of MPC strategies on a test site in Greece and with experimental data from the Swiss Energy Park.

[1] Y. Stauffer, S. Arberet, M. Boegli, E. Onillon, "Centralized energy optimization at district level", EnergyCon 2016.

Battery Performance Evaluation and Modelling for Stationary Applications

C. Brivio, V. Musolino, P.-J. Alet, L.-E. Perret-Aebi, C. Ballif

CSEM is developing battery models for stationary energy storage systems. These models are dynamic and aim at predicting battery performance based on operating conditions. They can be industrially implemented in energy management systems (EMS) or storage sizing tools for grid and off-grid applications.

Battery energy storage systems (BESS) are the ultimate flexibility resource in electricity networks. They are attractive both to grid operators — to reduce congestion and respond to imbalances between production and consumption — and to “prosumers” — to reduce their reliance on utilities. Despite a decrease in cell costs with a learning rate of 18% for lithium-ion batteries, BESS remain expensive. Optimizing the choice of technology and their size is therefore essential to financial viability. These design choices and the subsequent operation of the systems are difficult because the effective capacity, efficiency and lifetime of BESS strongly depend on operating conditions.

To support the design and operation of BESS, CSEM is developing a modular battery model based on the physical processes in electrochemical devices. The first step in this investigation consists in developing and running performance (cycling) tests and electrochemical impedance spectroscopy (EIS) measurements at the joint BFH-CSEM Energy Storage Research Center (ESReC) located in Nidau (BE).



Figure 1: Building and some laboratory equipment at BFH-CSEM Energy Storage Research Center (ESReC).

Six cell technologies are under investigation, four of them based on lithium-ion: lithium capacitor (LIC), lithium iron phosphate (LiFePO₄), nickel manganese cobalt oxide (NMC), and lithium titanate (LTO), as well as lead-acid and nickel metal hydride (NiMH).

EIS measurements provide the battery impedance as a function of the frequency, which reflects the main processes involved in the battery operation i.e., the charge transfer due to the redox reactions at the surface of the electrodes, diffusion of ions through the electrolytes, and changes to the crystalline structure of electrodes due to ion intercalation. Measurements are performed at different cell temperatures, states of charge and states of health in order to determine the influence of the operating conditions on the battery response.

For performance tests we use a combination of procedures from international standards e.g., IEC 62660-1 and our own. With these tests we can compare technologies with metrics such as the energy density, as shown on Figure 2 for seven electrochemical cells when fully discharged at different ambient temperatures.

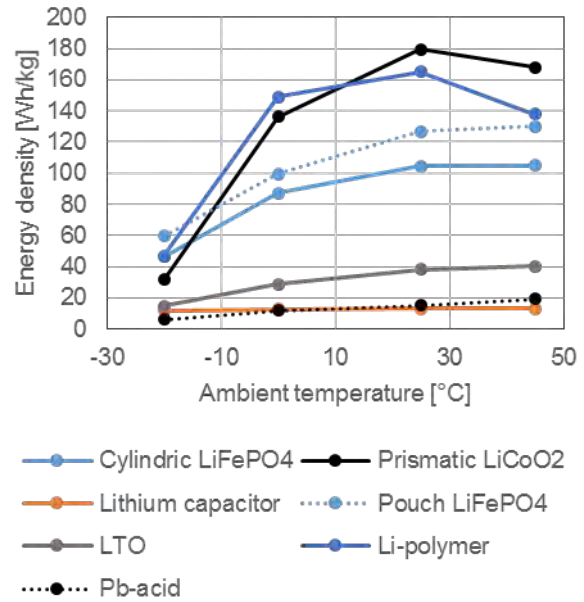


Figure 2: Battery cell energy density as function of ambient temperature.

The model is modular: each block represents a single physical phenomenon. Depending on the application, some dynamics can be neglected. In that case the complete model can be reduced to simplified, lower-order models.

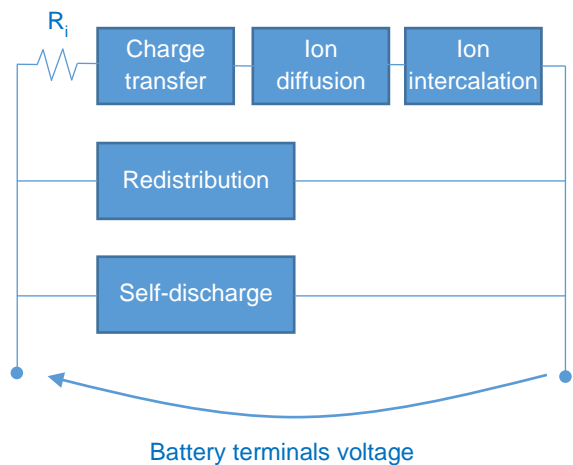


Figure 3: Structure of the dynamic battery model by CSEM.

Set-up and Operation of a Low-voltage DC Micro-grid Demonstrator

V. Musolino, P.-J. Alet, C. Rod, L.-E. Perret-Aebi, C. Ballif

CSEM is developing system architectures for isolated or grid-connected micro-grids. This project demonstrates how photovoltaic generation and electrical storage can be integrated with loads in a building. All components are interconnected in direct current (DC). A CSEM controller manages this micro-grid. It can be industrially implemented in applications ranging from commercial buildings to rural electrification.

Reduced costs of photovoltaic (PV) and storage systems make them attractive for individuals and companies to build micro-grids able to completely or partially satisfy their electrical energy needs. On the other hand a reliable and cost-effective system integration is required to guarantee the operation of such micro-grids and its possible interface with the public distribution grid. Distributing power in direct current (DC) instead of alternating current (AC) avoids multiple DC/AC converters and the associated losses, improves the power quality, and reduces the complexity of the whole system.

In this project a robust DC micro-grid control strategy, which requires no communication infrastructure, is being developed. A demonstrator has been realized (Figure 1); it consists in a DC micro-grid where a PV source, loads and a storage system are directly connected. The whole micro-grid is interfaced with the AC grid through a single power converter.

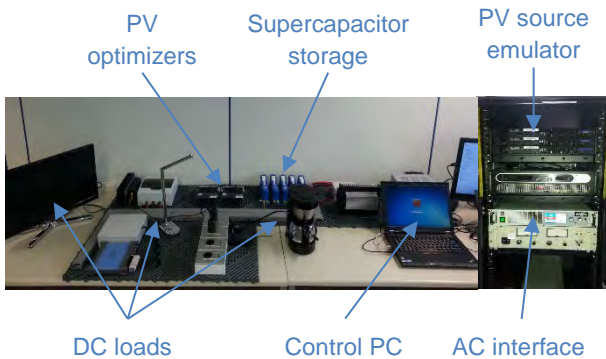


Figure 1: DC micro-grid demonstrator.

The selected storage technology is supercapacitors for two main reasons: first is the high performance in terms of efficiency and lifetime (up to one million full cycles) and, second is their state of charge (SoC) being simple to estimate.

The controller consists in a Python script running on a laptop, which sets and controls the power exchanged at the AC interface. The strategy consists of the following steps:

- Requesting power from the AC interface converter when the storage reaches its lower state-of-charge set point;
- Reinjecting back to the AC grid the excess of energy when the storage reaches its upper SoC set point;
- Setting a 0 power reference of the AC interface converter when the storage is between its lower and upper SoC set points.

The control strategy is implemented by a voltage controller which sets the current reference of the AC interface converter as a function of the storage SoC.

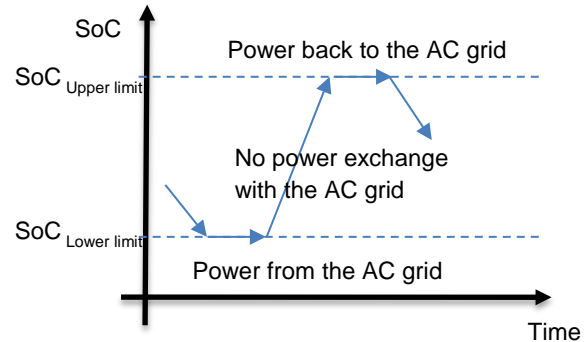


Figure 2: Control strategy of the interface converter.

Design rules for the controller have been developed to guarantee power quality on both the DC micro-grid and the AC grid. With the right bandwidth, the controller limits the power ramps towards the AC grid independently from the power oscillations in the DC micro-grid.

This ramp-rate functionality has been validated with a variable irradiance profile for the PV source derived from the EN 50530 standard for inverter testing. In Figure 3 the oscillations in PV power (due to irradiance variations), and in power exchanged with the AC grid are shown under different settings of the voltage controller. PV power ramps of 3.5 W/s (Figure 3 top) and 35 W/s (Figure 3 bottom) are mitigated down to 2.8 W/s and 10.5 W/s respectively with a fast dynamic control ("setting 1"), and down to 2.2 W/s and 5.9 W/s with a slow dynamic control ("setting 2").

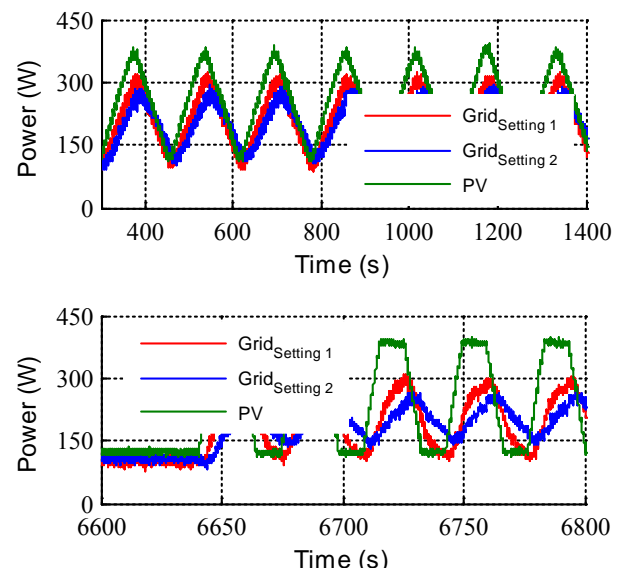


Figure 3: System response under a variable PV power profile.

This work was funded by the municipality of Neuchâtel. CSEM thanks them for their support.

Towards High Efficiency Flexible Printed Tandem Solar Modules

T. Offermans, M. Chrappa, J. Schleuniger, L. Mühlbach, R. Ferrini, G. Nisato

The Printable PV activity at CSEM addresses breakthrough, organic and inorganic printable materials and processing technologies that target applications with design added value and reduced environmental impact. The additive technologies developed are aimed at mass customizable manufacturing of PV products with high automation and reduced capital equipment cost. The objective is to provide Switzerland with know-how and technological options at the device design and process development level to support equipment developer, materials researchers and industrial suppliers as well as end users in the emerging field of printed PV.

From small hero cell to large area flexible demonstrator

During the past years, CSEM has developed their printing and device fabrication capability from lab-scale single cells made by spin-coating in an inert gas on small 2.5×2.5 cm glass substrates, through Doctor Blade coating in the ambient environment on increasingly larger substrates, to complete modules printed on flexible substrates. In parallel, CSEM developed efficient tandem cells by optimizing the optical stack, the charge transport and light in-coupling structure. Hero tandem cells were reproduced, blade coated in air from non-chlorinated solvents, with efficiencies ranging between 8 and 10%. A light management structure was designed and fabricated specifically for an already optically and electrically optimized homo-tandem cell, which increased the cell efficiency from an average of 9.2% to 10%.

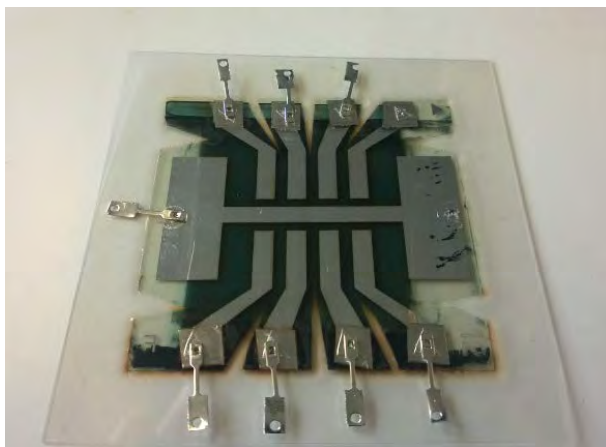


Figure 1: Photograph of the encapsulated flexible tandem solar cells.

These "hero" tandem cells were made on rigid ITO coated glass substrates, with an active area up to 1 cm^2 . In order to fabricate tandem cells on large area flexible substrates with the same high efficiency as on glass, in a first step a fabrication process was adapted for the flexible substrate, and in a second step the printing method was changed from blade coating to slot-die coating in order to obtain high uniformity coatings over a large area.

Tandem cells on flexible substrate

The change from rigid to flexible substrate is not trivial. The following two factors have a tremendous impact on the cell performance: 1) the optical properties of the substrate in the total stack, and 2) the roughness of the substrate. Optical simulations predict a 30% lower performance than the hero-tandem on glass. A major reduction in the photocurrent by 10-20% compared to ITO-glass is calculated due to a reduced transmission of the flexible substrate. In addition, a thick smoothening coating on the substrate is needed to ensure a good quality coating of the following six layers in the stack. As a result the maximum obtainable photocurrent drops further,

resulting in an efficiency of just over 7% using realistic, electrically non-limiting layer thicknesses. Tandem cells were fabricated accordingly on flexible substrates with a size of $5 \times 5\text{ cm}^2$. In order to demonstrate the robustness of the flexible tandem cells, the cells were encapsulated within ultra-barriers and electrical contacts were attached (photo in Figure 1). All cells, except one, remained functional with similar performance as measured before encapsulation. A slight drop in the V_{oc} is observed, and an improvement of the J_{sc} , resulting in a PCE of the encapsulated device of 6.5%, which is close to the 7% considered possible based on optical simulations.

Slot-die coated flexible tandem cells and modules

In order to demonstrate the upscalability of the tandem cell fabrication using an industrially relevant printing method, we set out to slot-die coat the cells on the flexible substrate. Note that in order to obtain high efficiency, control of layer thickness within 5-10 nm is needed, over the entire coating area. Thus one challenge to be addressed when coating a large area is the flatness of the substrate during coating. In a R2R setup, this is done by adjusting the tension on the web, in the table top S2S setup, used in this work, this required the use of a rigid, flat carrier substrate. Within project Sunflower, CSEM together with its partners could make significant progress in the development of the fabrication process to make large area flexible tandem cells, resulting in two functional $12 \times 17\text{ cm}^2$ homo-tandem modules, slot-die coated in air, using non-chlorinated solvents, encapsulated, with a voltage output of 4-5 V, current output of ~100 mA under solar illumination.

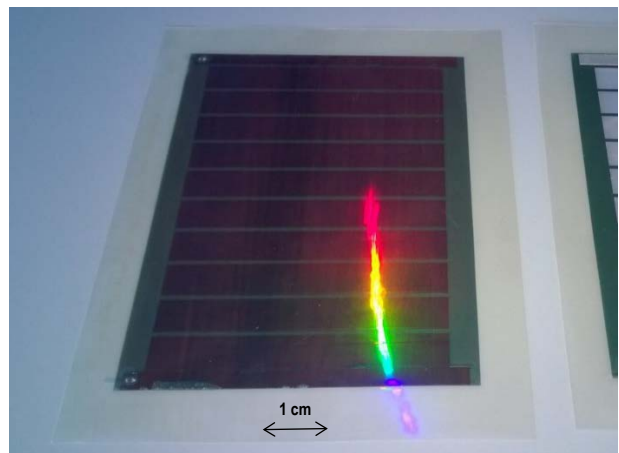


Figure 2: Photograph of one of the final flexible tandem demonstrator modules, encapsulated and laminated with a light management foil.

We gratefully acknowledge support from the EU project Sunflower (Nr. 287594), Interreg project Rhin-Solar and the Canton of Baselland.

SYSTEMS

Jens Krauss

The Systems research program is an interdisciplinary engineering endeavor that focuses on how to design, implement, manufacture, maintain, repair, and manage complex engineering systems over their life cycles. We place emphasis on innovations with system integration aspects of micro- and nano-subsystems as well as specific application demands such as resource limitations, miniaturization, precision, reliability, comfort, production cost, and environmental conditions. System integration requires significant coordination across disciplines and the development of new methods and modeling techniques as systems become smaller, interconnected, and more complex, approaching the physical limits. Issues such as engineering requirements, reliability, logistics, coordination, testing and evaluation, and maintainability, and many other disciplines necessary for successful system development, design, implementation, and ultimate decommissioning, become more difficult when dealing with large or complex projects. Therefore, system engineering also deals with work processes, optimization methods, and risk management and our teams strictly apply project management tools and processes—even in the design and early development phases—that adhere to the management standards of ISO-9001 and to the medical standards of the ISO-13485 quality system.

The Systems research program is application driven and strongly user-oriented. This is natural, given the fact that system objectives usually relate to overall performance, which is what interests the end user. Therefore, special consideration is given to such qualities as reliability, comfort, ease of maintenance, and convenience in operation. The final step of our application-driven research projects is typically an evaluation that attempts to find out how well the system works in the hands of the end user and/or as a subsystem in the operation of a global process. Our vision for the Systems research program is to promote innovative microtechnologies and new product concepts in the three application domains of (1) *Medical Device Technology*, (2) *Automation*, and (3) *Scientific Instrumentation*. In *Medical Device Technology* we innovate in the field of wearable human vital sign sensors and processing under ambulatory conditions and invest in the emerging domain of active medical devices, which includes (infusion) pumps and implants. Within the research activity *Automation*, we design and integrate new sensor and actuator concepts for (lab-) automation applications, in-process control, and in situ quality monitoring. Last but not least we design and implement innovative, complex, high-precision mechanisms for industrial applications and large science missions and continue development activities that focus on Si-based hybrid and compliant micro-mechanisms and miniature atomic clock building blocks, all within our *Scientific Instrumentation* research activity.

The research activities of the Systems research program aim at coordinating expertise across multiple CSEM research programs in the fields of sensing and actuating, signal processing and control engineering, high-precision mechanisms, additive manufacturing and instrumentation, low-

power electronics, wireless communication and software engineering, biomedical engineering, and automation. In order to strengthen further CSEM's position within the three application domains, the Systems research program today maintains an IP portfolio of roughly 50 granted patents. During the year 2016 four new patent applications have been submitted and more than 20 scientific papers have been published.

Long-term objectives

Medical Device Technology: The implementation of sensing and processing technologies in embedded, continuous on-body diagnostic systems will provide lifetime continuous access to clinical excellence. Such portable health systems have a wide range of applications in the domains of telemedicine, rehabilitation, security, homecare—in particular for the elderly, and health promotion, as well as sports, wellness, and fitness. Our medical device technology research activities range from innovative sensing technology for monitoring human vital signs to bio-signal processing and active medical device technologies. We aim to strengthen our know-how in biomedical engineering to encompass a broad range of areas, including the physics of environmental phenomena, sensor behavior, human motion, body size, ergonomics, manufacturability, and computer architecture, as well as wireless, low-power communication. The activity is ISO-13485 certified, stressing our strong commitment to developing high-quality medical devices.

Automation: The *Automation* research activity develops technologies for enhanced manufacturing and process flexibility, enabling high-quality, small-to-medium-volume products. The activity aims to drive the competitiveness of easy-to-use automated solutions with facilitated man-machine interaction and eco-friendly production processes with an attractive total cost of ownership compared to remote production sites abroad. We develop technologies designed around process and measurement solutions that lead to an optimum balance between flexibility, autonomy, and throughput. We put special emphasis on the system efficiencies that result from integrated, advanced sensory feedback.

Scientific Instrumentation: CSEM's cutting-edge microtechnologies in the areas of compliant and hybrid precision mechanisms, laser subsystems, and miniature atomic clocks have led to quantum leaps in the performance of scientific instrumentation for demanding applications such as space exploration, astrophysics, and medical and industrial instrumentation. The *Scientific Instrumentation* research activity focuses on the development of these key technologies and on their integration into fully operational hybrid systems. To prepare the future, our main goal is to continue to develop tomorrow's technologies, including flexure mechanisms in silicon (Macro-MEMS), laser sources and stabilization, and miniature atomic clocks, as well as LiDAR systems. Multi-physics simulations are a key asset in CSEM's expertise and are necessary for such complex, miniature, and fully integrated systems. The system complexity targeted is emphasized by significant miniaturization and limited available resources in terms of energy, computing power, and space.

Highlights

The System research program continues to be a pillar of CSEM's mission of technology transfer and has been interacting strongly with all other CSEM research programs over recent years. Special attention—in terms of strategic technology development, IP creation, and market analysis—is given to CSEM's Multidisciplinary Integrated Projects (MIPs) initiative, which promotes collaboration across all CSEM research programs. In the frame of this MIPs initiative, the System research program has further intensified its collaboration with the ULP Integrated System research program to strengthen CSEM's position in wearable technologies. The MIP "MiniNOB", which has been executed according the ISO-13485 medical standard, aims to demonstrate CSEM's novel, continuous, non-invasive blood pressure monitor, which is based on a dedicated, customized ASIC that helps to further reduce cost, dimensions, and power consumption. Another good example of multidisciplinary collaboration across CSEM's research programs is the MIP "HybSi", for which our experts in precision mechanisms joined forces with experts—in industrialization, packaging, and manufacturing capabilities—from our MEMS research program to position CSEM as the world's leading design house for compliant hybrid micro-mechanisms, so-called Macro-MEMS. The Genequand escapement, announced at the beginning of 2016 by the brand Parmigiani, is an outstanding result of CSEM's Macro-MEMS expertise. Last but not least, collaboration with the PV-center and Energy Management research program has been further intensified with a special focus on topics such as energy efficiency and storage, the power management of renewables, and the integration of PV cells into wearables. The MIP "Wear-a-Watt" aims at integrating PV cells that are highly efficient even under low illumination into dials and straps to power the necessary sensing, processing, and communication tasks of a smartwatch with solar cells alone.

Medical Device Technology: CSEM's medical-grade wearables are ready to revolutionize chronic disease management and will provide the caregiver and the patient with unprecedented insights, enabling precision medicine thanks to predictive personalized analytics. Smart wearables enriched with personalized coaching capacities will empower healthcare, moving people toward healthier lifestyles and the prevention of disease. Future monitoring systems will rely on higher miniaturization techniques in terms of sensor electronics, integrating customized, low-power components and innovative energy harvesting means. At CSEM, we have a track record of 20 years in building wearables and personal health solutions with leading customers and partners worldwide. We have grown, and are now a large and internationally recognized research team, and our ambition is to expand our wearable health solutions activities further. With this in mind, we would like to highlight the development of a novel, portable, and non-invasive continuous blood pressure monitoring device. This achievement is the result of the synergies we deploy with the activities of the ULP Integrated System research program, and a real-time demonstrator was presented on the occasion of the MEDICA fair in Düsseldorf this year. Moreover, during 2016 we were able to strengthen our position in the wearables domain by licensing our algorithm portfolio for human vital sign monitoring to half a dozen commercial partners.

Automation: The Automation research activity develops innovative technologies designed around process and measurement solutions that lead to an optimum balance between flexibility, autonomy, and throughput—that is to say, ease of use, including task programming and efficient processes. During 2016 major efforts have been deployed on the topic of Industry 4.0 and we would like to highlight the development of the so-called Work Place Companion. An intelligent, camera-based support system has been developed that monitors manual assembly process steps and interacts with the operator. It tracks the motions of the operator, work pieces, boxes, etc. in the working space in 4-D (position and orientation). The system learns correct assembly sequences in a teaching phase, can handle variances in individual execution, and reliably interprets assembly quality. CSEM, together with its industrial partner, will further enhance the Work Place Companion system concept, seeking an operational industrial solution.

Scientific Instrumentation: The major part of our scientific instrumentation research activities is framed within space projects, large science missions, and/or international astrophysics programs. Thanks to its track record of more than 30 years in the design, manufacturing, integration, and testing of active, high-precision opto-mechatronics systems, CSEM acts as a prime contractor for these large science mission projects, with Swiss SMEs, manufacturing entities, and local machine workshops benefiting through sub-contracts and purchase orders. For the reporting period, we would like to highlight the outcome of a CTI project accomplished with Witschi Electronics AG. Only six months after the termination of the project, and thanks to CSEM's expertise in opto-mechanical instrumentation, Witschi announced the launch of its product "WisiScope", a professional measurement system for the characterization of, and after-sales service for, mechanical watches. The scientific basis of this instrument was presented by Witschi on the occasion of the SSC conference 2016 in Montreux. Moreover, during the last year a special focus was given to laser development. Concerning laser sources, CSEM offers a very broad range of competencies allowing simulations and the realization of sources based on semiconductor lasers, on diode-pumped solid-state lasers, and on (fiber-based) amplifiers. These systems can be narrow-linewidth and continuous-wave or pulsed with pulse durations in the range of tens of femtoseconds to picoseconds, and an increased market demand for short-pulse high-power laser systems for micromachining applications can be observed today. Amplified systems using chirp-pulse amplification techniques have been realized to meet the requirements of bio-imaging and machining applications. During recent years, CSEM has placed an emphasis on stabilized lasers, and state-of-the-art cavity-stabilized continuous-wave lasers and optical frequency combs (stabilized, mode-locked femtosecond lasers) have been realized. The quintessence of these developments is the demonstration of a record-low phase-noise microwave generator. CSEM's advanced metrology and environmental testing capabilities have also proven to be a key asset, resulting in the launch of several space projects for the development of future telecommunication satellite hardware. In the near future, CSEM will orient its laser developments toward more environmentally robust systems; dedicated, high-performance, hands-free, low-power electronics; and fully integrated systems.

A Wearable Dietary Monitor using a PPG-based Chewing Sensor

L. Zhou, S. Pernecker, M. Crettaz, M. Frosio, A. De Sousa, M. Proen  a, P. Theurillat, G. Dudnik

CSEM has developed a novel wearable dietary monitoring system using a photo-plethysmography-based chewing sensor. Non-invasive, compact, and unobtrusive, it is dedicated to monitoring eating behavior and daily activity of teenagers and young adults with the aim of providing personalized guidance to tackle the ongoing obesity epidemic or eating disorders.

Obesity and eating disorders are a major health concern in the Western world: obesity has reached epidemic proportions globally, with 400 million obese adults worldwide and one billion who are overweight. Meanwhile, the prevalence of eating disorders, such as bulimia and anorexia, has essentially remained at about 3% across the population over the years.^[1] Most treatments are marginally effective, having minor clinical or sociological impact. Monitoring and modification of dietary behavior has been shown to be a significantly more promising approach for the treatment of obesity and eating disorders. Within the framework of the European project SPLENDID,^[2] CSEM has developed a novel wearable sensor for dietary monitoring, namely a photo-plethysmography (PPG)-based chewing sensor.

The system is composed of two parts: a PPG-based chewing sensor to detect chewing events and a dedicated data logger to store, process, and transmit the acquired optical data via Bluetooth. In addition, an activity sensor based on a triaxial accelerometer has been embedded in the data logger to monitor the movements and physical activity of the user. An associated smartphone application running specific algorithms allows personalized guidance to train users to improve their eating and activity behavior through the data transferred by the data logger. In order to have an unobtrusive and cost-efficient system as well as to promote its diffusion among teenagers and young adults accustomed to listening to music, the chewing sensor has been successfully embedded into a custom-designed in-ear headset. The chewing sensor is connected via a cable to the data logger ($45 \times 78 \times 14$ mm), as shown in Figure 1.

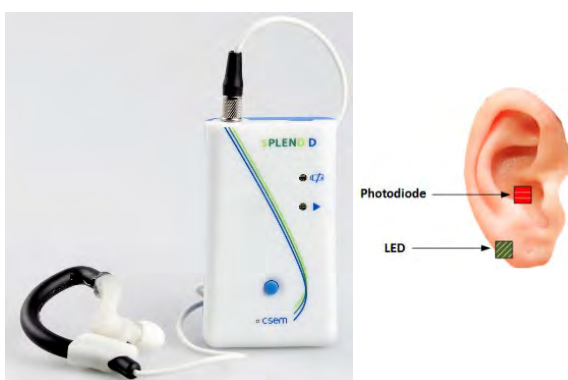


Figure 1: Wearable sensory eating tracker developed by CSEM. (Left) PPG chewing sensor connected to the data logger; (Right) PPG sensor placement.

Physiologically, the jaw and the ear are closely related. The mastication and the muscles which control the jaw are also

related to the ears. There is indeed strong experimental evidence that chewing activity significantly affects the PPG signal measured at the ear. The proposed PPG sensor is positioned in the ear concha with a Light-Emitting Diode (LED) placed behind the ear and a photo-diode inserted in the ear canal. Traditionally, measurement of heart rate or blood oxygen saturation by PPG is highly sensitive to movement artefacts; in our application, the signal of interest is in fact the signal captured due to movement caused by mastication.

The acquired optical signal is pre-amplified, filtered, and sampled at a fixed sampling frequency of 21.3 Hz. In order to avoid signal saturation due to high density of ambient light, a proprietary compensation technique is applied. Figure 2 depicts the signal-processing block diagram.

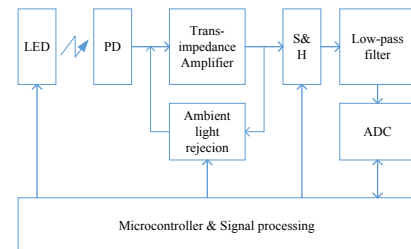


Figure 2: Signal-processing block diagram of the PPG sensor.

This in-ear PPG sensor is small and highly non-intrusive. As it does not capture sound, it is not affected by ambient noise, talking, or other types of parasitic signals.

The monitoring system has been evaluated on a dataset recorded at Wageningen University (the Netherlands). It contains recordings of 21 individuals wearing the PPG sensor. A segment of signal related to chewing events is shown in Figure 3. The sensor has yielded satisfactory results, especially for snack detection, where values of over 91% are achieved for both precision and recall.^[3] We thus believe that it can be used for robust, objective dietary monitoring in real-life conditions.

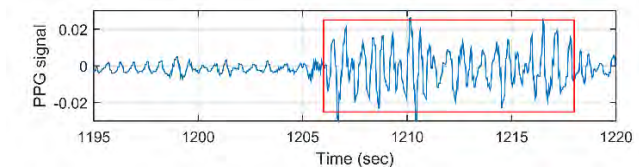


Figure 3: DC-free signal from the PPG chewing sensor. The red box indicates chewing activity.

This work has been supported by the European Community's ICT Program SPLENDID under grant agreement no. 610746, 01/10/2013–30/09/2016.

[1] <http://www.world-heart-federation.org/cardiovascular-health/cardiovascular-disease-risk-factors/obesity/>

[2] <http://splendid-program.eu/>

[3] V. Papapanagiotou, C. Diou, L. Zhou, et al., A novel approach for chewing detection based on a wearable PPG sensor, in Proc. EMBC 2016, 2016.

Wrist-located Optical Monitoring Device for Atrial Fibrillation Screening

M. Lemay, P. Renevey, M. Bertschi

Worldwide, there is a need to reduce healthcare costs. In this context, wearable technologies are being targeted as one of the major tools of value-based self-monitoring and large screening healthcare systems. Portable Holter monitoring systems, which represent a global market of more than 150 million U.S. dollars,^[1] are used to monitor patients suffering from cardiovascular diseases. The most common form of cardiac arrhythmia, affecting more than 10% of the population aged over 80 years,^[2] is Atrial Fibrillation (AF). Years of research in system design and signal processing have been necessary to bring wrist-located optical devices to a state able to accurately monitor cardiac activity.^[3] During the Nano-Tera project miniHOLTER, the feasibility of using such devices for the detection of AF was investigated. The present study constitutes the first clinical evidence of reliable AF detection using a wrist-located optical device.

Years of research on system design and on the enhancement of photoplethysmographic (PPG) signals have been necessary to bring PPG technology into wearable wrist-located devices able to accurately monitor cardiac activity during daily activities^[3]. Some questions remain unanswered: Is the monitoring of cardiac activity accurate enough for an ambulatory application? If so, to what extent can it substitute for ambulatory electrocardiographic (ECG) devices for large-scale screening of populations? This study aims at evaluating the performance of a wrist-located device based on PPG technology in terms of Atrial Fibrillation (AF) detection using features based on cardiac interbeat (RR) intervals.

In order to validate the detection of AF, signals were recorded at the University Hospital in Lausanne (CHUV) from patients admitted for AF or ventricular tachycardia ablation. Twenty PPG and 12-lead ECG signals were recorded simultaneously from patients in whom episodes of sinus rhythm (SR) and AF coexisted. From the PPG signals, RR intervals were estimated by detecting the systolic downstrokes. From the ECG signals, RR intervals were computed from detected R-waves provided by an electrophysiology system (Siemens Sensis). The resulting PPG- and ECG-based RR intervals were used to derive feature values in 10-s time windows. These features were the mean, median, minimum, and interquartile range. A total of 2213 (1927 of AF, 286 of SR) 10-s epochs were considered for AF versus SR classification using a support vector machine with a linear kernel trained using a leave-one-out procedure to avoid overfitting.

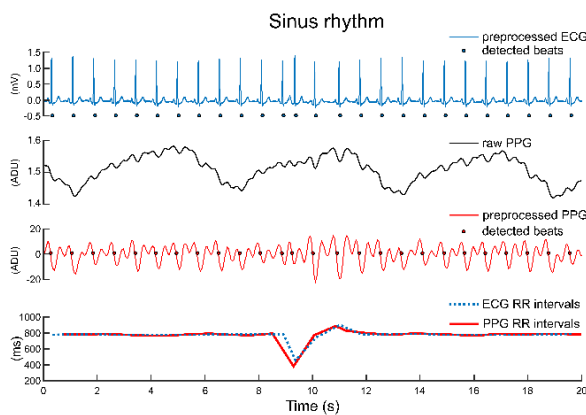


Figure 1: Example of ECG and PPG signals and post-processing results during SR.

- [1] Global Industry Analyst, Holter monitoring Systems – A Global Strategic Business Report, MCP-3334, 2012.
- [2] A.S. Go, et al., Prevalence of diagnosed atrial fibrillation in adults: National implications for rhythm management and stroke prevention: the AnTicoagulation and Risks Factors in Atrial Fibrillation (ATRIA) Study, JAMA, 285 (2001) 2370–2375.

Classification accuracies of 94 and 99% were obtained from PPG- and ECG-based features, respectively. It is interesting to compare this performance to a recently published study that compared AF detection performance between permanent pacemakers (accuracy of 99%) and implantable cardiac monitors (accuracy of 72%).^[4] The detection of AF embedded in these two implementable medical devices was also based on features extracted from the time series of RR intervals.

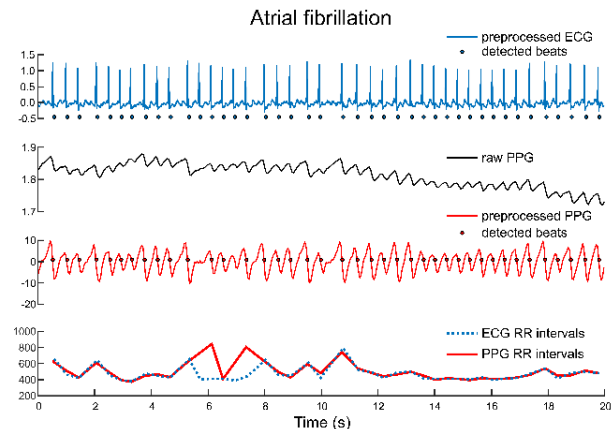


Figure 2: Example of post-processed ECG and PPG signals and post-processing results during AF.

Based on these encouraging results, the proposed wrist-located AF screening device challenges implantable cardiac monitors in controlled conditions. Several advantages over ECG-based devices must be mentioned, including the non-invasiveness, limited clumsiness, long-term monitoring, cost, and size. Furthermore, the possibility of integrating this technology in currently distributed smart watches and bracelets makes it very attractive for large population screening. To achieve a highly robust and accurate 24/7 AF screening device, further work is required regarding the improvement of cardiac beat detection during AF, the addition of a signal quality index in the classification procedure, and the investigation of additional features based on variation of PPG waveform morphology and magnitude.

- [3] J. Parak, et al., Evaluation of the beat-to-beat detection accuracy of PulseOn wearable optical heart rate monitor, Proc. IEEE Eng. Med. Biol. Soc., Milano, 2015, 8099-102.
- [4] S. Podd, et al., Are implantable cardiac monitors the "gold standard" for atrial fibrillation detection?, Europace, 18 (2016) 1000–1005.

Novel Ambient Light Rejection System for PPG-based Measurement Devices

P. Theurillat, E. Rincon-Gil, R. Gentsch, M. Correvon, P. Persechini, P.-F. Ruedi, J. Solà

Photoplethysmography (PPG) is becoming the standard technology for heart rate measurements in wearables because of its ease of use. Nowadays, numerous commercial off-the-shelf (COTS) analog front end (AFE) components dedicated to PPG are available. However, in everyday use cases, insufficient ambient light rejection (ALR) leads to poor AFE performances and subsequent inaccurate heart rate estimations. The results of a novel approach that solves ALR issues in daily life use cases are presented herein. CSEM has been active in the domain of PPG sensing and processing for more than 15 years, covering R&D activities ranging from optical design, AFE development, and embedded algorithms to application-specific integrated circuit (ASIC) implementation.

Current trends in photoplethysmography (PPG) measurement rely on the use of integrated analog front end (AFE) components. Advanced COTS AFEs have been designed to automatically cope with all known PPG variables and make them easy for the system architect to embed. Unfortunately, the performance of existing AFEs is not optimal in several real use cases, in particular when referring to ambient light rejection (ALR).

PPG is based on the use of light emitting diodes (LEDs) and photodiode (PD) sensors. The output signal modulation results from variations of light absorption of subcutaneous tissues due to the change of blood volumes originating from heart strokes and therefore enables heart rate (HR) assessment. The weak point of PPG is that the PD is actually mixed with two other components, [1] namely a motion artefact signal (which depends on body movements and system fixation) and an ambient light perturbation (which varies in intensity and pattern depending on indoor and outdoor environments, completely masking the signal of interest most of the time).

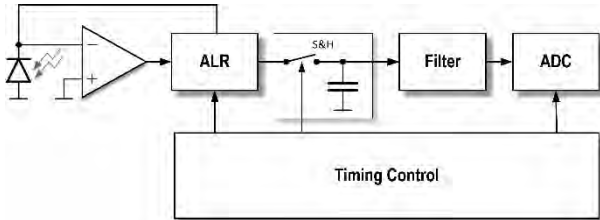


Figure 1: Simplified schematic of the novel ALR approach for PPG AFEs. Note that ambient light is directly removed at the first amplification stage, providing optimal PPG measurement performances in realistic indoor and outdoor scenarios.

The ALR state of the art for COTS AFEs is based on high-pass filtering of the output signal after a first amplification stage. More advanced implementations rely on sampling ambient light signals when the PPG-light source is switched off. A combination of both approaches is also known. Such implementations suffer from saturation of the first amplification stages when exposed to intense ambient light conditions.

CSEM has developed a new method that overcomes the aforementioned limitations by removing ambient light directly at the input of the first amplification stage, that is, on the PD itself. In addition to the advantages of 1) never saturating the analog chain and 2) avoiding the need for the microcontroller to sample ambient light, the major advantage is that the method allows for significantly higher analog signal gains. A simplified schematic of the implemented ALR is depicted in Figure 1. Additionally,

Figs. 2 and 3 illustrate the performance of the novel ALR approach in a realistic use scenario.

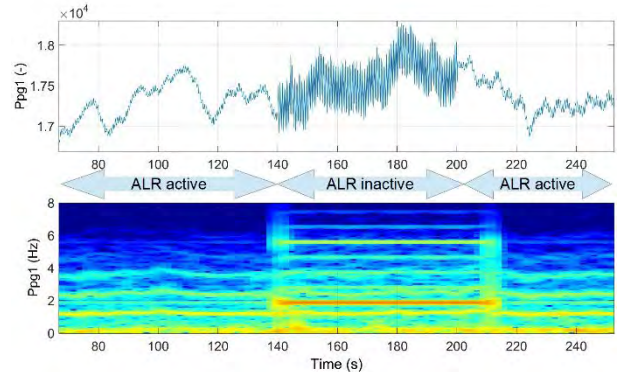


Figure 2: Performance of the novel ALR in a typical outdoor use case scenario; note the influence of ambient light on both the temporal and frequency signals during the 60-s disconnection of the ALR system. The user's pulse rate is 1 Hz and, during a walking exercise, the arm shadows the sun and produces a 2-Hz artefact.

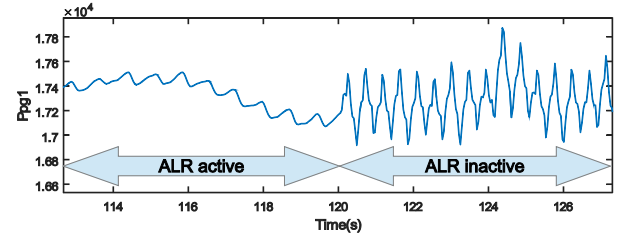


Figure 3: Detailed illustration of the performance of the novel ALR.

In order to set the novel ALR according to the benchmark of COTS AFEs, Table 1 provides a high-level benchmark comparison of performances, including: 1) the amount of saturation in the input stage, 2) the dynamic range accepted by the ALR, and 3) the power consumption.

Table 1: Performance of the novel ALR approach when compared to three competitor AFEs.

Feature	AFE 1	AFE 2	AFE 3	CSEM AFE
Saturation at input stage	GOOD	GOOD	MEDIUM	GOOD
Accepted light dynamic range	MEDIUM	BAD	GOOD	GOOD
Power consumption	GOOD	BAD	MEDIUM	GOOD

The novel ALR is now available at CSEM for demonstration purposes and is a main building block of the new generation of proprietary PPG-based wearables, measuring HR, SpO₂, NIBP, and other vital signs. The ALR described herein has been implemented into CSEM's proprietary PPG-dedicated ASIC (application-specific integrated circuit), called PulseMon, whose datasheet is available on request.

[1] M. Lemay, et al., Wearable Sensors, Elsevier, 2014, 105-129
ISBN 9780124186620.

Cuffless Blood Pressure Monitoring: CSEM's catalog of applications

J. Solà, M. Proença, F. Braun, A. Vybornova, C. Verjus, J.-M. Koller, A. Moreira De Sousa, M. Bertschi

The quest for sensors that can provide accurate beat-to-beat blood pressure measurements without inflating pneumatic cuffs has started around the globe. For more than 10 years, CSEM has been a pioneer in the development, implementation, and validation of novel solutions based on either pulse wave velocity or pulse wave analysis principles. CSEM's blood pressure technologies open the door to a catalogue of disruptive applications ranging from new paradigms in routine blood pressure measurement in the operating room to the first ever cuffless monitors for wearable 24/7 applications. Clinical validations of CSEM's technologies are ongoing in different Swiss university hospitals.

CSEM's strategy in the measurement of blood pressure (BP) is based on two measurement principles, depending on the targeted BP application (see Table 1):

a) Pulse wave velocity (PWV) principle: estimates of BP are obtained from measurements of the transit time of arterial pulses travelling from the ascending aorta towards the vasculature of the upper-thoracic skin;^[1]

b) Pulse wave analysis (PWA) principle: estimates of BP are obtained via a CSEM-proprietary analysis of arterial pulsatility patterns at body locations such as the wrist or the fingertip.^[2]

While both principles require a user-dependent calibration manoeuvre to provide absolute BP estimates, calibration-free estimates have been shown to provide an accurate indication of the BP trend over time, which is sufficient for most clinical scenarios.

Based on these principles, the results obtained from different ongoing clinical studies in Swiss university hospitals prove the feasibility of a catalogue of disruptive BP applications (Table 1).

Table 1: CSEM catalogue of cuffless BP applications.

BP application	CSEM cuffless solution
Continuous ambulatory BP monitoring 24/7	PWV measurements at the chest via CSEM's cooperative sensor technology (combined ECG, bioimpedance, and PPG sensors) ^[3]
Continuous BP trend monitoring during anaesthesia	PWA measurements at the fingertip via re-analysis of transmission PPG signals from routinely used PulseOx sensors. ^[4]
Continuous ambulatory BP monitoring during sleep	PWA measurements at the wrist via reflective PPG sensors integrated in a wrist watch device. ^[5]
Spot ambulatory BP monitoring	PWA measurements at the wrist via reflective PPG sensors integrated in a watch device.
Spot ambulatory BP monitoring	PWA measurements at the fingertip via reflective optical measurements from a smartphone camera.

Preliminary results of an ongoing clinical study (NCT02651558) at CHUV, Lausanne University Hospital, are illustrated in Figure 1. Ground-truth values of systolic, diastolic, and mean BP are obtained from an arterial line inserted at the radial artery. In this example, PWV measurements at the chest provide estimates of mean BP, and PWA measurements at the fingertip provide estimates of systolic BP.

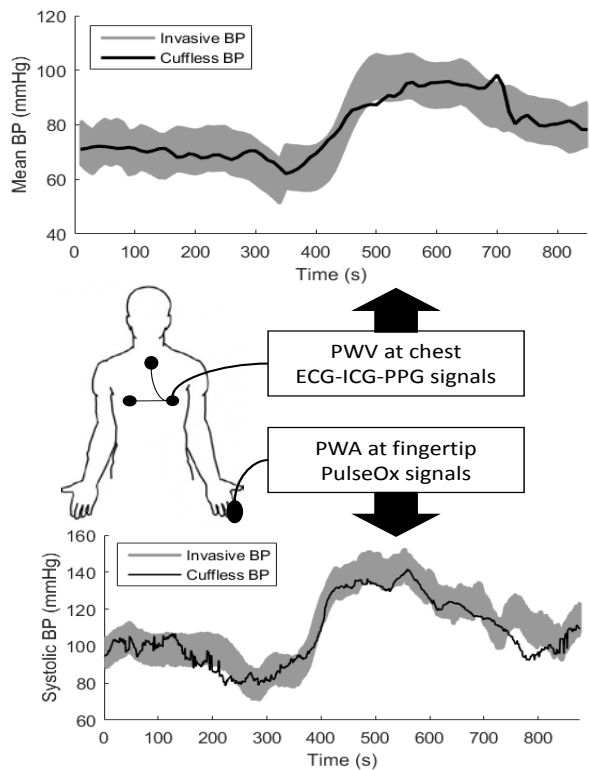


Figure 1: Example of good performance of CSEM cuffless technologies to estimate: a) mean BP via a chest sensor (upper panel), and b) systolic BP via a PulseOx sensor (lower panel), when compared to arterial line measurements on an anesthetized patient. Grey regions in plots depict reference BP ± 8 mmHg.

While CSEM technologies for cuffless BP are drawing the interest of numerous key players in the medical and wearable market, licensing of the dedicated patent portfolio for particular use cases is available upon request.

[1] J. Solà, Continuous non-invasive blood pressure estimation, ETHZ PhD dissertation No. 20093, Dr. Sc., 30 November 2011.

[2] M. Proença, et al., Method, apparatus and computer program for determining a blood pressure value, WO2016138965.

[3] J. Solà, et al., Non-invasive and non-occlusive blood pressure estimation via a chest sensor, IEEE TBME, 60(12), 2013.

[4] J. Solà, et al., Continuous non-invasive monitoring of blood pressure in the operating room: a cuffless optical technology at the fingertip, Proc. BMT2016, Basel, 2016.

[5] J. Solà, et al., Cuffless blood pressure monitoring: experimental evidences of a beat-to-beat PPG technique, Proc. EMBC2016, Orlando.

WELCOME—Wearable Sensors for Patients Suffering from Cardiopulmonary Diseases

J. Wacker, O. Chételat, M. Rapin, E. Haenni, J.-A. Porchet, A. Falhi, C. Meier, F. Braun, A. De Sousa, R. Rusconi

WELCOME is a project on a vest equipped with more than 20 sensors for measuring body signals with a high spatial resolution. Being fully wearable and intuitive to use, the vest makes home monitoring of patients suffering from, for instance, chronic obstructive pulmonary disease (COPD) with comorbidities such as chronic heart failure feasible.

An important area of progress in the modern treatment of chronic cardiopulmonary diseases is the personalization of therapy. Personalized therapy requires continuous monitoring of a patient's health status (e.g., to undertake preventive actions before an exacerbation). The most objective assessment of health status is done by measuring significant physiological signals and comparing them to a healthy population and/or by following them over time. Chronic diseases affecting multiple organs need parallel monitoring of several physiological parameters. Current devices for multi-signal recording are often bulky and do not allow the patients' state of health to be followed during their daily lives.

In the frame of the project WELCOME, CSEM has developed, together with a European consortium, a wearable system to continuously monitor a multitude of physiological parameters of patients suffering from chronic obstructive pulmonary disease (COPD) and comorbidities. The system consists of a vest with 21 so-called cooperative sensors based on a new technology patented by CSEM. The sensors are embedded in a vest (see Figure 1), where they measure and record multi-lead ECGs (electrocardiograms), heart rate and breath rate, arterial oxygen saturation (SpO_2), physical activity, chest sounds, and trans-thoracic impedance for electrical impedance tomography (EIT) of the lungs. The use of many sensors allows the acquisition of body signals with a high spatial density, paving the way to wearable imaging devices and giving access to enough information to process new secondary signals such as cuffless continuous arterial blood pressure^[1] or even pulmonary blood pressure^[2].

While existing multi-sensor systems usually require complex cabling between the sensors, the WELCOME vest contains only two simple wires, which facilitates production of the vest, allows a decrease in the size of the sensors, and increases the wearing comfort of the vest.^[3] Besides, the WELCOME sensor vest is standalone; that is, no external cabling is needed, and it can therefore be put on like a conventional undergarment, which makes it extremely simple to use in everyday life.

Figure 2 shows signals measured with the WELCOME vest in the first experiments. A multi-lead ECG is shown in Figure 2a. Moreover, SpO_2 and activity-related measurements are shown in Figure 2b and c. Figure 2d shows a time series of EIT images during one respiratory cycle, depicting the intra-thoracic impedance change mainly influenced by the ventilated lungs.



Figure 1: The WELCOME sensor vest (here shown half open) is equipped with 21 sensors (diameter: 38 mm; height: 10 mm), which are in direct contact with the skin and measure a wide spectrum of body signals with a high spatial and temporal resolution.

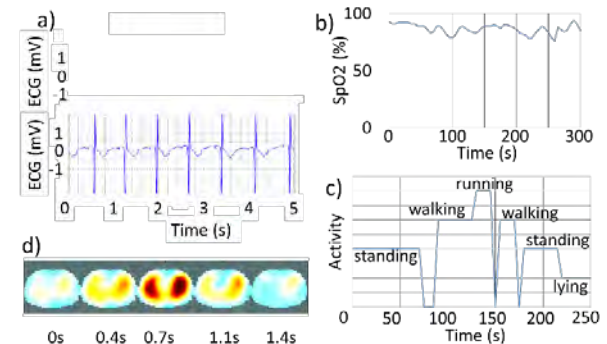


Figure 2: Some of the signals measured with the vest sensors: a) multi-lead ECG; b) SpO_2 ; c) activity; d) time series of some of the 80-Hz EIT images of the lungs during one respiration cycle (blue = low conductivity; red = high conductivity)

In conclusion, we have developed and presented a sensor system for measuring, in a continuous manner, multiple health-relevant physiological signals of patients suffering from cardiopulmonary diseases in their home environment. Thanks to patented CSEM technology, the vest is comfortable to wear and intuitive to use. All these factors together make the WELCOME vest a new device, unique in its kind yet competitive with respect to traditional non-wearable and wearable medical measuring devices in many applications.

The work has been carried out within the collaborative project WELCOME (www.welcome-project.eu) and is partly funded by the 7th Framework Program of the European Union (grant agreement no. 611223).

[1] J. Solà, et al., Non-invasive and non-occlusive blood pressure estimation via a chest sensor, *IEEE Trans. Biomed. Eng.*, 60 (2013) 3505.

[2] M. Proença, et al., "Non-invasive monitoring of pulmonary artery pressure from timing information by EIT: experimental evaluation

during induced hypoxia", IOP Publishing, *Physiol. Meas.* 37 (2016) 713–726.

[3] M. Rapin, et al., "Cooperative dry-electrode sensors for multi-lead biopotential and bioimpedance monitoring", IOP Publishing, *Physiol. Meas.* 36 (2015) 767–783.

Autonomous Medical Monitoring and Diagnostics

A. Lemkaddem, M. Lemay, M. Proen  a, P. Renevey, R. Delgado-Gonzalo, M. Bertschi

CSEM has developed a platform that evaluates how data mining and machine learning can pave the way towards autonomous medical monitoring and diagnostics. Even though the original conception was oriented towards space applications, CSEM's autonomous diagnosis platform can play an important role in many remote locations where telecommunications systems are not reliable.

Global plans for exploratory missions aim at extending the distances travelled by humans well beyond low-Earth orbit and establishing permanent bases on the surface of the Moon and Mars^[1]. This will inevitably lead to an increase of mission duration, radiation intensity, and degree of confinement and isolation to which the crews will be exposed. In this extended context, the astronauts should have the means to collect medical/physiological data in order to understand whether their health conditions are within nominal levels. The astronauts should be informed about possible diagnoses and should receive practical recommendations about treatment options in order to deal with medical issues with limited or no interaction with the Earth. The mentioned scenario is possible if and only if the astronauts and medical crewmembers have access to an autonomous medical monitoring system with embedded diagnostic algorithms.

The systems developed today very often target one type of arrhythmia detection.^[2] The results obtained from these studies are highly comparable with the outcome of the CSEM platform. In addition, the CSEM platform detects several types of cardiac arrhythmias simultaneously.

Figure 1 briefly describes the evaluation platform developed by CSEM. The general working principle of this pipeline can be explained as follows. It starts out with a selection of available medical databases, depending on the medical use case considered and the validation mode. All selected signals and associated annotated anomalies obtained from the databases (ground truth) are loaded into the algorithm pipeline. The "feature extraction & alignment" block is in charge of extracting generic and signal-specific features from the signals and thereafter aligning them with annotated anomalies used to train several "anomaly detection" models. These models (e.g. k-NN, SVM) aim at classifying the values of the features extracted as either "normal" or "abnormal". When at least one abnormal feature value is encountered, an anomaly is said to be detected. Being able to classify which type of anomaly has been detected based on which types of features have been classified as abnormal is the task of the "anomaly classification" models. Moreover, some models (anomaly detection and classification models) will perform both tasks jointly (anomaly detection and classification). The trained "anomaly detection", "anomaly classification", and "anomaly detection and classification" models are then applied to new data (validation dataset) during the validation phase of the algorithm pipeline (lower row of the block diagram) in the "apply trained models" block. Lastly, the performance of the models in terms of detection and

classification performance is assessed in the "performance evaluation" block.

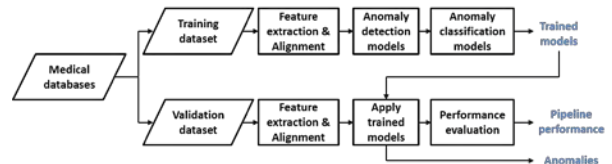


Figure 1: Overview of the developed evaluation platform.

Table 1 shows some of the results based on the MIT-BIH arrhythmia database (47 subjects). These results were obtained by using various models for the detection of a particular type of anomaly, in this case cardiac arrhythmias. Each individual heartbeat was classified by the anomaly detection models as either normal (sinus rhythms) or abnormal (cardiac arrhythmias). Comparing the detected anomalies to the ground truth (annotated anomalies from the databases), sensitivity and specificity scores were computed to assess their performance. The harmonic mean of sensitivity and specificity was also computed as a global performance measure.

Table 1: Performance scores from the normal (sinus rhythms) versus abnormal (cardiac arrhythmias) classification.

Classification Scores	k-NN	SVM Linear	SVM Nonlinear
Sensitivity	87%	89%	90%
Specificity	76%	95%	90%
Harmonic mean	81%	92%	90%

While Table 1 illustrates the results of the normal versus abnormal separation (anomaly detection), Table 2 shows the performance of the models for anomaly classification. The CSEM pipeline manages to classify the normal beats with an accuracy of 94% when using SVM Linear. The atrial fibrillation classification work best with k-NN (78%), while the highest classification score for premature ventricular contraction was obtained with SVM Nonlinear (78%).

Table 2: Classification scores of the different cardiac rhythms. PVC = Premature Ventricular Contraction, AF = Atrial Fibrillation.

Cardiac rhythms	k-NN	SVM Linear	SVM Nonlinear
Sinus rhythms	74%	94%	83%
PVC	66%	76%	78%
AF	78%	72%	71%

With the results obtained so far, the CSEM autonomous diagnosis platform demonstrates a promising capacity to be extended to other signals and pathologies.

[1] International Space Exploration Coordination Group, the Global Exploration Roadmap, 2013.

[2] P. Ziegler, J. Koehler, R. Mehra, Comparison of continuous versus intermittent monitoring of atrial arrhythmias, Heart Rhythm, 3(12) (2006) 1445–52.

Light Management for Treatment of Chronic Wounds

D. Kallweit, J. Mayer, O. Fernandez, N. Glaser, A. Luecke, A. Mustaccio, R. Ferrini

Chronic wounds represent a significant burden to patients, health care professionals, and health care systems, affecting over 40 million patients and creating costs of approximately 40 billion € annually. In the European project "MEDILIGHT" CSEM and its partners work on the development and fabrication of a medical device for professional wound care. The device will use recently proven therapeutic effects of visible light to enhance the self-healing process and monitor the status and history of the wound during therapy. Exposure of the chronic wound with certain colors and durations can induce the growth of keratinocytes and fibroblasts in deeper layers of the skin and is also known to have antibacterial effects predominantly at the surface layers of the skin. In order to be compliant with hygiene requirements the system consists of two main parts: 1) the wound dressing with the illumination system, and 2) the electronics for the controlling and the wireless communication. The disposable wound dressing hermetically seals the infectious wound whereas the illumination system can be reused during the treatment of one and the same patient. The illumination system is based on a LED foil and thin light management layers which makes it thin and mechanically flexible. It also comprises heat management structures and provides the required degree of breathability.

In the European project MEDILIGHT, CSEM developed an illumination system for the treatment of chronic wounds by means of elaborated illumination schemes. As shown in Figure 1, the MEDILIGHT systems consists of the wound dressing provided by the industrial partner Laboratoires URG0, the flexible illumination system, and the electronics for the controlling, the data acquisition and the wireless communication.

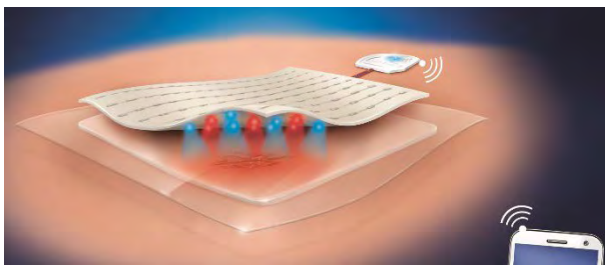


Figure 1: Illustration of the MEDILIGHT wound healing system. It consists of a disposable wound dressing, an exterior flexible illumination system with sensors and the controlling electronics.

The illumination system is positioned on top of the disposable wound dressing and consists of a flexible LED foil with homogenizing micro-optical layers on top, which provide a high level of illumination homogeneity in combination with high illumination efficiency; even when in direct contact with the flexible LED foil. The flexible LED foil is additionally fitted with a light harvesting layer collecting and redirecting misdirected light back to the wound.

The thin portable and mechanically flexible illumination system developed by CSEM provides an adjustable intensity density of up to 25 mW/cm^2 . It also provides enough breathability to allow the patient's exudates to be lead away as well as it provides integrated heat management structures to dissipate the heat generated by the LEDs.

Figure 2 shows the developed illumination system and the attained homogeneity.

Figure 2a shows the measurement of the homogeneity as well as the cross-section on the right. The tiny bright spots that can be seen (the peaks in the cross-section view) are not the LEDs but the tiny openings which belong to the URG0 wound dressing. A homogeneity (I_{\min} / I_{\max}) of 62% was achieved.

Figure 2b shows a photograph of the demonstration of the illumination system with one of the wound dressings developed at URG0 for best optical efficiency. The size of the demo is 16 cm^2 . Larger patches of up to 72 cm^2 based on flexible LED foils providing exactly the same power densities and homogeneity have also been built.

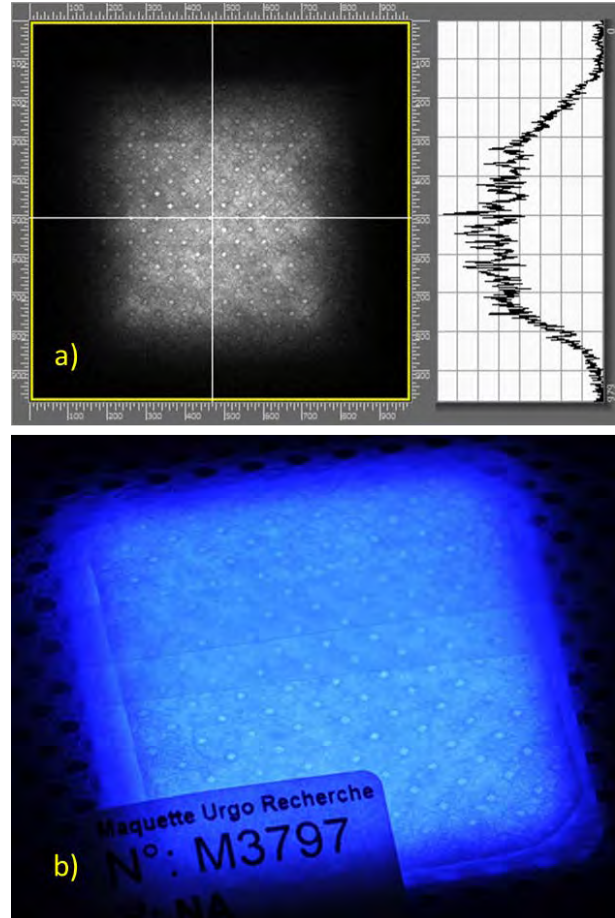


Figure 2: First demo of the thin 16 cm^2 MEDILIGHT illumination system. The demo consists of 32 LEDs, diverse light management elements for light redirecting and homogenization as well as the complete wound dressing from the industrial partner URG0 on top. The illumination system is able to provide high intensities up to 25 mW/cm^2 .

The project MEDILIGHT is funded by the European Commission (grant agreement no. 644267) and builds on the competencies of the following partners: Technical University of Berlin (Germany), Laboratoires URG0 (France), Ruprecht-Karls-University Heidelberg (Germany), CSEM (Switzerland), SignalGeneriX Ltd (Cyprus), Microsemi Semiconductor Limited (United Kingdom), and AMIRES s.r.o. (Czech Republic).

X-ray Phase Contrast Imaging: from High Resolution to High Speed

V. Revol, P. Schutz •, T. Stadelmann, I. Kastanis, E. Schaller

CSEM's X-ray phase contrast imaging (XPCI) facility was extended in 2016 and now covers non-destructive imaging from high resolution to high speed. Non-destructive inspection (NDI) is increasingly used in prototyping, manufacturing and repair of critical components such as aeronautical structures, automotive components, medical implants and opto-electronic packages. Beyond ensuring safety and reliability, the benefits of NDI include shorter development and validation cycles, improved production yield, reduced waste, lower part weight and better understanding of failure modes. CSEM's XPCI facility is accessible for external users; the technology is available for licensing to NDI equipment manufacturers.

Compared to conventional X-ray systems, X-ray phase contrast imaging (XPCI) brings the following advantages

- Higher contrast for lightweight materials
- Sensitive to micro and macrostructures

These advantages translate into better detectability of critical defects within the structure under inspection.

In the project ZEFIPACK—performed jointly with the Lucerne University of Applied Sciences and Arts—a new XPCI system was designed and realized at CSEM (see Figure 1). This system can achieve high resolution (down to 4 µm voxel size) by using a micro-focus X-ray source from Hamamatsu and a dedicated geometry.

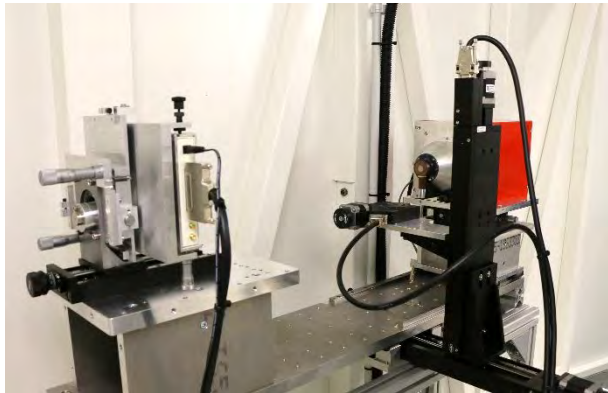


Figure 1: The high-resolution XPCI system.

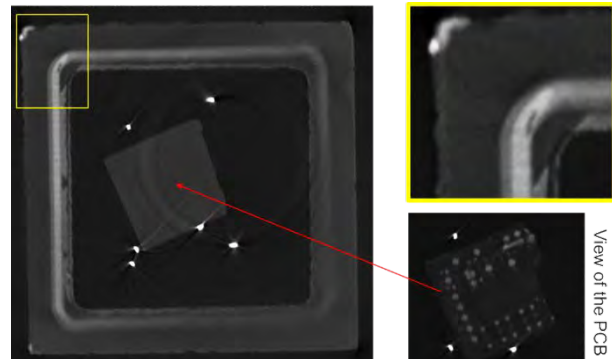
The system has been characterized on opto-electronic packages and polymer parts made by micro-injection. Figure 2 shows the results obtained on a hermetic sapphire package with embedded electronics. Defects can be observed in the bonding line (see yellow framed inset). This information allows optimizing the process parameters to maximize yield and hermetic sealing quality.

Typical XPCI applications are:

- Detection of defects in composites, polymers, aluminium and ceramic / CMC components (typical defects include porosity, cracks, fibre waviness, and moisture)^[1]
- Analysis of crack propagation
- In-situ monitoring of wetting in porous materials or textiles
- Characterization of precious stones and pearls^[2]
- Quality control of opto-electronic packages

• Lucerne University of Applied Sciences and Arts

^[1] C. Hannesschläger, V. Revol, B. Plank, D. Salaberger, J. Kastner, "Fibre structure characterisation of injection moulded short fibre-reinforced polymers by X-ray scatter dark field tomography", Case Studies in Nondestructive Testing & Evaluation 3 (2015) 34.



View of the PCB

Figure 2: Example of cross-section images obtained with the high-resolution XPCI system. Defects can be observed in the bonding line (yellow-framed inset).

The new system complements the existing XPCI systems listed in Table 1. With this addition, the XPCI facility can now provide solutions to industrial and academic partners for a broad range of applications in lightweight materials NDI.

Table 1: Summary of XPCI systems available at CSEM

Large-size radiography system	
Mode	XPCI Radiography (2D)
Sample size	Up to 100cm x 75cm
Energy range	40 - 70keV
Voxel size	Typ. 55 - 110µm
Versatile tomography system	
Mode	XPCI tomography (2D/3D)
Sample size	Up to 30x30cm
Energy range	20-70keV
Voxel size	Typ. 45 - 90µm
High-resolution tomography system	
Mode	XPCI tomography (2D/3D)
Sample size	Up to 3x3cm
Energy range	20-100keV
Voxel size	Typ. 5 - 25µm

We thank MCCS, the Cantons of Central Switzerland and the Swiss Confederation for supporting this work.

^[2] V. Revol, C. Hanser, M. Krzemnicki, "Characterization of pearls by X-ray phase contrast imaging with a grating interferometer", Case Studies in Nondestructive Testing & Evaluation 6 (2016) 1.

VISARD—Vision Automation Robotics Designer

M. Höchmer, I. Kastanis, P. Schmid

CSEM's VISARD offers a PC-based one-stop software solution for complex, special-purpose machines. Industrial automation faces many challenges: improving quality, increasing process reproducibility and lowering costs while fulfilling high customer expectations for flexibility and user friendliness. These demands are part of the Industry 4.0 trend, which aims at integrating traditional production with information and communication technologies. By applying state-of-the-art software design and introducing advanced control architectures VISARD enables efficient deployment of hardware-independent automation systems.

CSEM has created the Vision Automation Robotics Designer (VISARD) to drive special-purpose machines with minimum effort and maximum flexibility. The breakthrough was achieved by merging CSEM's industry-proven robotics and vision frameworks into a single tool. VISARD can be used in complex special-purpose machines as well as in simple measuring devices. It offers a smart PC-based solution for hybrid-control systems with heterogeneous hardware elements free of any Programmable Logic Controller (PLC).

VISARD uses a graphical, module-based approach that makes it flexible, extendable and easy to use by machine integrators, developers and end-users (Figure 1). Typical modules include cameras, robots, I/Os, logging, data management and algorithms for image or data processing (e.g. neural networks).

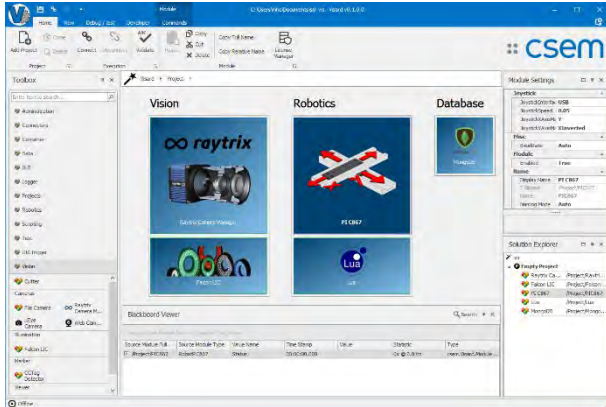


Figure 1: VISARD user interface.

The application's core is the control logic of a special purpose machine. Pure graphical descriptions of complex systems often result in confusing diagrams that are hard to maintain (e.g. LabVIEW). On the other hand, a framework that only offers low-level programming interfaces requires trained programmers and is not usable by machine integrators. VISARD provides multiple ways of linking modules. Simple and sequential processes can be connected graphically on the VISARD's user interface. More complex logic can be implemented using high-level scripting languages like Lua (similar to IEC 61131) also directly on the VISARD's user interface. Experts can write code in the underlying .NET framework (e.g. C# or Visual Basic).

The main challenge of a modern production system is to deal with slow, heavy data (e.g. images) and fast, light data (e.g. contact switch) in parallel. VISARD offers a novel data handling mechanism called the Blackboard (Figure 2).

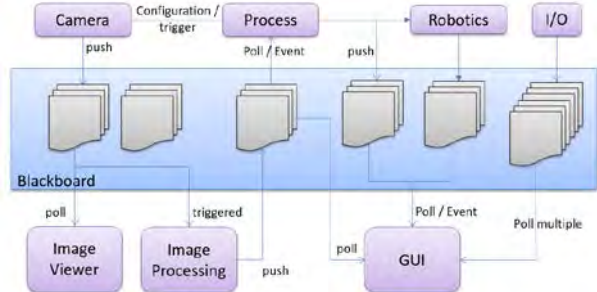


Figure 2: Blackboard data exchange mechanisms.

Source modules may push data to the Blackboard. Receiver modules may register to read this data by choosing whether to get the data by event, by polling or by a proprietary zero-miss polling that guarantees no data will be lost even when polled at low-frequencies. Memory is managed automatically by the Blackboard and the VISARD GUI allows monitoring its content live. The Blackboard implementation has been tested on a representative industrial PC and can handle more than 1.5 million transactions per second (Figure 3). A transaction may be an I/O change, an image or a measurement.

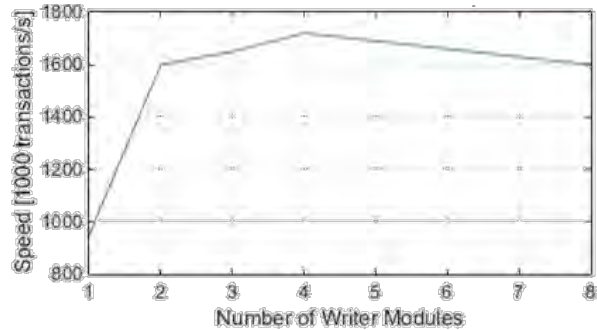


Figure 3: Blackboard transaction performance results.

SQL/NoSQL modules are available that store relevant system and process data. In combination with reporting modules, this allows VISARD's vertical integration into existing ERP systems and automatic generation of weekly management reports.

VISARD is a fast growing toolbox. The latest implementation provides full support for Raytrix^[1] 3D light-field cameras with multi-GPU support and load scheduling. The system can handle three 3D quality gates in a high-speed production line, processing 6 parts per second per gate.

We thank MCCS, the Cantons of Central Switzerland and the Swiss Confederation for supporting this work.

[1] www.raytrix.de

Visualization Tool to Understand the Learning of a Deep Network

J. Sun, I. Kastanis

Visualizing the learning process of a deep network is of great value to interpret this novel technique in industrial applications. The t-Stochastic Neighbor Embedding (t-SNE) technique is utilized to display graphically the learning data as well as the activity of the hidden layers of a trained deep network. The visualization shows how the deep network learns the natural cluster characteristics of the training data.

Deep learning has achieved success in various application domains, such as image classification and speech recognition. As a pioneer in applying deep learning algorithms in industrial automation, CSEM developed Tileye for image recognition and surface inspection tasks as well as Tilear for precision-machinery quality inspection. While these systems performed outstandingly, it remained challenging to explain their working principles concisely to new customers. A deep network assembles diverse non-linear functions with millions of parameters, which are difficult to interpret, remaining a “black box” for the customer. Visualization of the learning process and learned features are thus necessary to assist the interpretation of this new technique.

Tilear is a precision-machinery quality-inspection software system based on a deep auto-encoder. The acquired signals from product samples are always high-dimensional. t-Stochastic Neighbor Embedding (t-SNE) [1] was selected to create 2D visualization maps due to its ability to embed high-dimensional data into a low-dimensional space while preserving local relations between data points (i.e. data points close to each other in the original high-dimensional space remain close to each other in the embedded low-dimensional space). The algorithm can be summarized in two steps (refer to [1] for a thorough mathematical description):

- Model the neighborhood relations between data points by using joint probability distributions over pairs of data in both the original high-dimensional and the mapped low-dimensional space. Data points close to each other in the space have thus a high probability of being picked up as neighbors, whilst data points far away from each other have a low probability of being categorized as neighbors.
- Minimize the Kullback-Leibler divergence between the probabilities in high-dimensional and low-dimensional spaces with respect to the locations of the points.

In order to visualize the learning process of a well-trained deep auto-encoder, the following steps were performed:

- Retrieve the well-trained deep auto-encoder.
- Propagate samples in the test dataset through the well-trained auto-encoder, obtaining the hidden layer activity vectors of each sample.
- Apply t-SNE to these hidden layer activity vectors and the raw samples.
- Display the t-SNE mapped low-dimensional data in 2D.

Figure 1 shows an example visualization of the raw data and hidden activity vectors of different hidden layers of a well-trained Tilear network based on t-SNE. The blue circles represent good samples while the red crosses represent defective samples. Visualizations of raw data and hidden layer activities of a well-trained network are ordered from a to e.

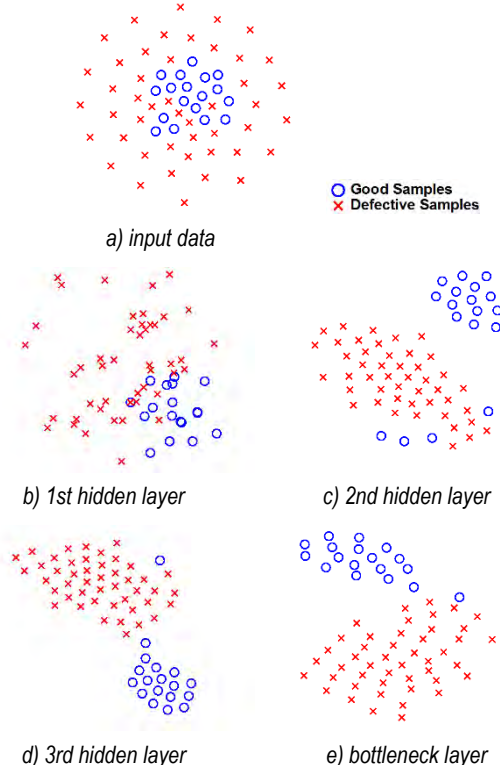


Figure 1: t-SNE 2D maps of layer activity vectors of a well-trained deep auto-encoder network based on raw audio signals.

Figure 1 shows how raw sample data in the dataset are mixed up and not separable. However, clusters of good and defective samples emerge as the learning progresses from low-level to high-level hidden layers (b to e). The learned clusters in the bottleneck layer form the basis to perform fault detection.

The visualization of the learning process clearly shows how the natural clusters buried in the raw high-dimensional space are learned by the network. This type of visualization is an invaluable tool to demonstrate the working principles of Tileye and Tilear to potential customers, facilitating the industrialization of the technique.

We thank MCCS, the Cantons of Central Switzerland and the Swiss Confederation for supporting this work.

[1] M.Laurens van der, G.Hinton, "Visualizing data using t-SNE", Journal of Machine Learning Research (2008) 2579.

Novel System for Pressure Measurements on Yacht Sails

T. Burch, H. Dong, S. Bitterli, K. Krasnopski, E. Schaller, I. Bayati •, S. Muggiasca •, M. Malandra ••

CSEM has developed a novel pressure-measurement system with Politecnico di Milano and North Sails based on MEMS sensors and pressure-strip technology. The system was developed for the Lecco Innovation Hub Sailing Yacht Lab^[1] and has been tested in an extensive wind tunnel campaign^[2].

Pressure measurements on thin shapes like sails are very challenging. Knowing the effective pressure distribution over the sail plan is of great interest for its aerodynamic and structural design. The system developed enables such measurements and is therefore a valuable tool for the selection and the optimal use of materials and sail production techniques.

The system is based on 9 pressure scanners (Figure 1) each providing 16 sensors connected to pressure strips distributed on different sections of the main sail and the jib of the test yacht. The MEMS pressure dies integrated in the scanner are a new generation of piezo-resistive differential low-pressure sensor membranes that reach very low full-scale ranges below 1000 Pa. The MEMS sensors are cost efficiently bonded to a FR4 substrate using innovative die bonding techniques based on elastic adhesives.



Figure 1: Pressure scanner with CAN cable (1) and strip adapter (2).

Scanner key specifications

FS pressure range	± 1000	Pa
Measurement resolution	0.01	% FS
Static accuracy after zeroing	0.25	% FS
Sample rate	1 - 100	Hz
CAN Interface	1	Mbit/s
Size	65x55x6	mm
Weight	50	g

The pressure strips are made of thin polymer films with integrated micro-channels, which enables pressure propagation from the tap to the respective sensor of the connected pressure scanner. The main advantage of the strips is their low weight and the flexibility of this foil, which allows fast and non-invasive application to the sails.

• Politecnico di Milano

•• North Sails

The performance of the measurement system was evaluated in static and dynamic tests as well as in wind tunnel tests in upwind configuration on a 1:10 scale model of a 48 foot cruiser-racer. A set of pressure strips with a total number of 144 pressure taps was mounted (Figure 2). The strips were attached on both sides of the main sail and the jib in order to measure differential pressure between the leeward and windward sides. The scanners were placed in the hull of the model. In addition, flying shape measurements based on time of flight (TOF) technology were performed.



Figure 2: Pressure-strips (in white) applied to the main sail of the 1:10 scale model during wind tunnel test.

The wind-tunnel test results gave relevant insight explaining the dependency of sail-plan trimming on sail pressure, driving forces and flying shape measurements (Figure 3). Further measurements on the full-scale sailing yacht lab on Lake Como are planned for the end of 2016.

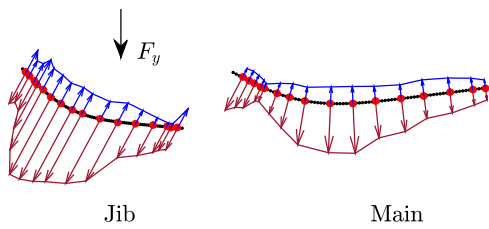


Figure 3: Visualization example of pressure distribution based on wind tunnel measurements at an apparent wind angle of 20°.

The system is a major improvement compared to state-of-the-art pressure measurements on flexible sails. It is expected that in the future such measurements on scale models and full-scale yachts will provide a reference database for validating CFD simulation models and further optimize the structural design and aerodynamics of sails.

We thank MCCS, the Cantons of Central Switzerland and the Swiss Confederation for supporting this work.

[1] Fossati, et al., "A Novel Full Scale Laboratory for Yacht Engineering Research", Ocean Engineering 104 (2015) 219-237.

[2] Fossati, et al., "Pressure Measurements on Yacht Sails: Development of a New System for Wind Tunnel and Full Scale Testing", 22nd CSYS (2016) 84-96.

Ultra-low Phase Noise Microwave Generated with Photonics

E. Portuondo-Campa, G. Buchs, S. Kundermann, L. Balet, S. Lecomte

A record-low phase noise floor for photonics-generated microwaves obtained from commercial PIN InGaAs photodiodes has been achieved. At a carrier frequency of 9.6 GHz, the microwaves were generated using optical frequency combs based on diode-pumped solid-state lasers emitting at telecom wavelength and referenced to a cavity-stabilized continuous-wave laser. Using a novel fibered polarization-maintaining pulse interleaver, a single-oscillator phase-noise floor of -171 dBc/Hz has been measured.

The generation of microwave signals with very low phase-noise and frequencies typically in the range of 10 GHz is essential in applications such as telecommunications, radar technologies, synchronization of scientific facilities, and time and frequency metrology. In recent years, photonics-based approaches have opened new routes towards the generation of ultra-low phase-noise microwave signals, in particular the approach described here, based on the use of optical frequency combs (OFC) [1]. Compared to other types of microwave sources, this method, illustrated in Figure 1, results in the lowest close-to-carrier phase noise and short term instability that can be achieved today, while reaching very low far-from-carrier noise floors.

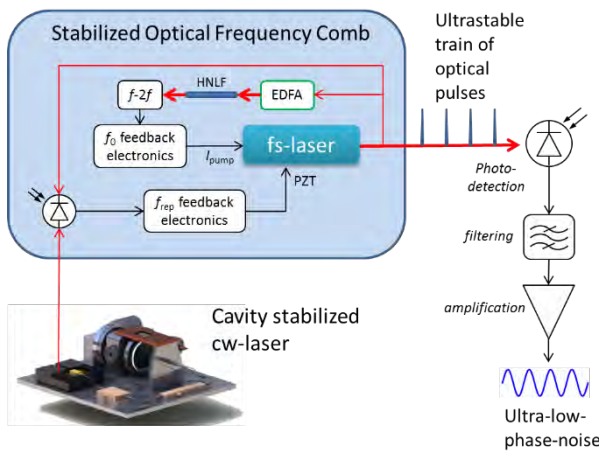


Figure 1: System diagram for photonics-based source of ultra-low phase-noise microwaves.

At the origin of the stability of this oscillator there is an optical frequency reference consisting in a continuous wave (cw) laser, stabilized on a high-finesse cavity. At CSEM, this type of optical frequency references have demonstrated Hz-level stability at 1s time-scale, corresponding to a fractional frequency stability in the order of 10^{-15} . To put it in perspective, this corresponds to the ratio of 1 s to 30 million years.

Using this type of laser as frequency reference it is possible to stabilize the whole spectrum of an optical frequency comb (OFC) by means of several feedback mechanisms. The OFC in our case consisted in a passively mode-locked diode-pumped solid state laser, emitting femtosecond pulses at 1550-1560

optical wavelength (eye-safe, telecom band). When the spectrum of the OFC is stabilized, the train of femtosecond optical pulses emitted by the laser exhibits ultra-low timing jitter, corresponding to the same relative stability of the cw frequency reference. The pulses can then be detected with a photodiode to produce a periodic electronic signal with ultralow-phase noise. Unfortunately, the pulse repetition rate of a femtosecond oscillator is typically in the range of tens of MHz to 1 GHz. In order to generate a signal with 10 GHz carrier frequency, a high harmonic of the electronic signal can be selected by filtering; but in general, due to the small amplitude of high harmonics, the quantum shot-noise effect will severely limit the relative phase noise floor of such microwave. To circumvent this problem, the pulse repetition rate of the laser can be multiplied by splitting, delaying and recombining the optical pulses in a pulse interleaver scheme [2] as shown in Figure 2.

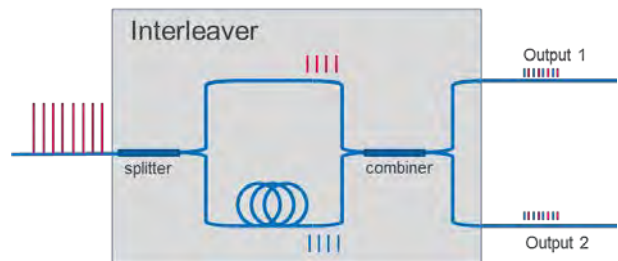


Figure 2: 1-stage optical pulse interleaver scheme resulting in duplication of pulse repetition rate.

A novel design of fiber pulse interleaver conceived and fabricated at CSEM allowed selectively enhancing the 9.6 GHz harmonic of the photo-detected signal from an original optical pulse train of 100 MHz rate. The protocol for fiber interleaver fabrication developed at CSEM, allows control of the inter-pulse delay to a precision of 1 ps, and permits recovering the whole input optical power at a single output channel, with only minor losses at the interface between the 6 implemented stages. This strategy, combined with the high performance of in-house developed control electronics for laser stabilization enabled the generation of ultra-low phase noise microwaves, demonstrating the lowest noise floor far-from-the-carrier obtained so far with commercial PIN InGaAs photodiodes, at a level of -171 dBc/Hz for a single oscillator [3].

- [1] A. Bartels, S. A. Diddams, C. W. Oates, G. Wilpers, J. C. Bergquist, W. H. Oskay, L. Hollberg, "Femtosecond-laser-based synthesis of ultrastable microwave signals from optical frequency references," Opt. Lett. 30(6), 667–669 (2005).
- [2] A. Haboucha, W. Zhang, T. Li, M. Lours, A. N. Luiten, Y. Le Coq, G. Santarelli, "Optical-fibre pulse rate multiplier for ultralow phase-noise signal generation," Opt. Lett. 36(18), 3654–3656 (2011).

- [3] E. Portuondo-Campa, G. Buchs, S. Kundermann, L. Balet, S. Lecomte, "Ultra-low phase-noise microwave generation using a diode-pumped solid-state laser based frequency comb and a polarization-maintaining pulse interleaver", Opt. Expr. 23(25), 32441-32451 (2015).

A Vision-based LiDAR Sensor Technology for Space Debris Removal

A. Pollini, C. Pache, S. Pernecker, M. Tomil, L. Giriens, G. Perruchoud, F. Droz, J.-L. Nagel, P.A. Beuchat, J. Bennes, A. de Souza.

The vision-based navigation (VBN) sensor is the most technically demanding payload of a 100-kg class satellite to be launched in May 2017 by the Nanoracks Kaber deployment system installed on the International Space Station. The VBN sensor has been developed in view of space rendezvous and active debris removal applications. The implemented sensor architecture can also be considered for future automotive, unmanned vehicle (e.g. drone), cattle, and forestry management applications.

The activities of human beings in space have progressively generated a huge amount of garbage, to such an extent that today it is a concern for spacefaring nations. Satellites and orbiting debris collisions happened on several occasions. The International Space Station (ISS) modifies its orbit almost daily to avoid threatening debris.



Figure 1: Launcher tank recovered in South Africa. (Argus/Enver Essop).

In 2014, around 600 pieces of debris totaling 100,000 kg re-entered the Earth's atmosphere. In a little more than half a century, more than 4800 launches have placed some 6000 satellites into orbit. Less than 1000 are still operational today. The US Space Surveillance Network tracks and maintains a catalogue of more than 12,000 orbiting items. Objects larger than approximately 5 to 10 cm in low Earth orbit and 30 cm to 1 m at geostationary altitudes are monitored. Only 6% of the catalogued objects are active!

The most effective means of stabilizing the amount of orbiting debris is by mass reduction within regions with high densities of space debris. A credible solution has emerged over the recent years, which is to actively remove inactive objects.

The EC FP7 RemoveDEBRIS project/mission aims at performing in-orbit Active Debris Removal (ADR). The scenario of this low-cost mission (€11.3M) involves a microsatellite of 100 Kg, called RemoveSAT. It will eject and then capture and deorbit two space debris targets, called DebrisATs. Various rendezvous, capture, and deorbiting key technologies such as net and harpoon and LiDAR-based vision sensors will be evaluated in-orbit. Vision-based sensors are paramount for the success of ADR missions. They allow identification of the debris' geometrical features and main tumbling axis. No proximity navigation and capture can be envisaged without this information.

RemoveDEBRIS is one of the world's first and perhaps the most important in-orbit ADR demonstration. It is a vital prerequisite to achieving the ultimate goal of a cleaner Earth orbital environment. CSEM is part of a consortium led by the space department of Surrey University, with SSTL and Airbus as the main space industries. CSEM is responsible for the vision-based navigation (VBN) sensor.

The VBN sensor is made of two main sub-systems: a flash imaging LiDAR and a color camera. The innovation stands in the LiDAR as the camera is an off-the-shelf product. As it is a low-cost mission, most of the components are not space-qualified components. The whole system has been designed and realized by CSEM.



Figure 2: VBN sensor with laser head, LiDAR receiver, and camera.

The sensor's mass is 2 kg and its size is 10×10×15 cm³. It is specified to take 3D images at a distance between 1 and 20–40 m.

Currently, the VBN sensor proto-flight model is functionally tested. Figure 3 shows the target used for these tests and Figure 4 shows a raw image generated by the LiDAR.

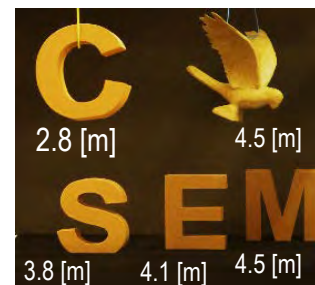


Figure 3: Target for the functional tests.

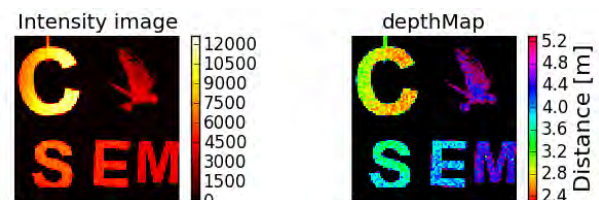


Figure 4: Images generated by the LiDAR (intensity on the left and distance on the right).

The LiDAR generates two images: one intensity image, like any camera, and a distance or depth-map image that provides the 3D information. Environmental tests and delivery to SSTL for integration on the satellite are planned for October and November 2016, respectively. The launch is planned for May 2017.

This work has been supported by the European Community's Space Research Program under grant agreement no. 607099.

Efficient Femtosecond Laser Stabilization via Stimulated Emission

G. Buchs, E. Portuondo-Campa, S. Lecomte

A novel scheme for intra-cavity control of the carrier-envelope offset frequency of a 100-MHz mode-locked Er:Yb:glass diode-pumped solid state laser based on the modulation of the laser gain via stimulated emission of the excited Er^{3+} ions is demonstrated. This method makes it possible to bypass the ytterbium-system few-kHz low-pass filter in the f_{CEO} stabilization loop and thus to push the phase lock bandwidth up to a limit close to the frequency of the relaxation oscillations of the erbium system. A phase lock bandwidth above 70 kHz has been achieved with the fully stabilized laser, leading to a low noise stabilized frequency comb.

Optical frequency combs (OFCs) constitute an essential tool for time and frequency metrology and optical spectroscopy applications today.^[1] This requires fully stabilized combs, implying that both the repetition rate (f_{rep}) and the Carrier-Envelope-Offset (CEO) frequency (f_{CEO}) are stabilized. f_{rep} stabilization is usually implemented by acting on the laser cavity length via different techniques, enabling large stabilization bandwidths. Feeding back the phase error signal from an f -to- $2f$ interferometer to the laser pump power is a standard way to stabilize f_{CEO} . However, here the phase lock bandwidth is limited by the stimulated lifetime of the gain medium. Achieving a large phase f_{CEO} lock bandwidth is of high importance for Er:Yb:glass diode-pumped solid state lasers (DPSSLs), since they have demonstrated very low timing jitter figures^[2], making them particularly interesting for reference frequency distribution through telecom fibers and ultra-low phase noise microwave generation^[3].

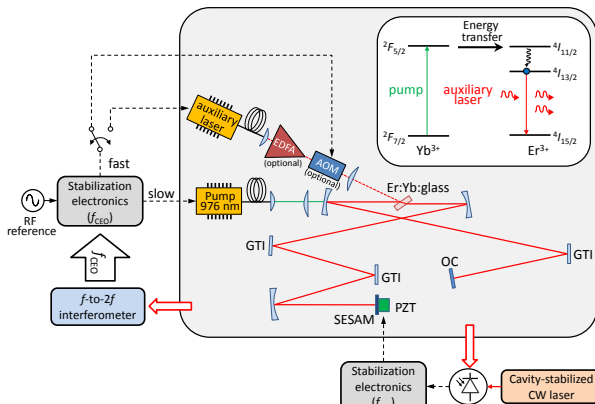


Figure 1: Schematics of the femtosecond DPSSL architecture with the external modulation laser source acting on the laser Er^{3+} transition of the Er:Yb:glass gain medium for stabilization of f_{CEO} . $\lambda_{\text{emission}} = 1554 \text{ nm}$, $f_{\text{rep}} = 100.05 \text{ MHz}$, pulse duration: 165 fs (transform-limited). (Inset) Energy diagram of the Er:Yb:glass system with stimulated emission modulation of the gain from the auxiliary laser.

Here,^[4] a new approach to intra-cavity CEO stabilization in an Er:Yb:glass DPSSL emitting at telecom wavelength (Figure 1) has been demonstrated. A direct action on the population inversion between the lower and upper states of the Er^{3+} ions (energy diagram in the inset of Figure 1) makes it possible to

extend the f_{CEO} feedback bandwidth via a bypass of the few-kHz cut-off frequency low-pass filter induced by the excited Yb^{3+} ion decay rate. This was achieved through stimulated emission induced by an external laser source emitting at a wavelength lying within the transition linewidth in order to depopulate the excited Er^{3+} state.

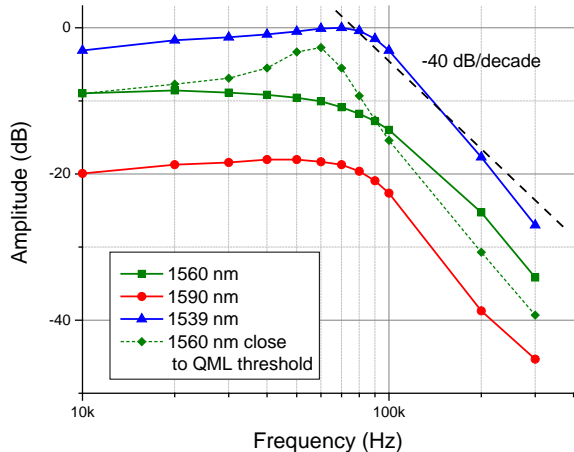


Figure 2: Transfer function of the auxiliary laser power to femtosecond laser output power with 100% modulation depth, rescaled. For 1560 nm, the transfer function (arbitrarily offset) close to the QML threshold shows a typical oscillation relaxation resonance at about 57 kHz.

This gain modulation principle was tested by measuring the transfer function of the auxiliary laser power to the femtosecond laser output power (f_{CEO} is directly linked to intra-cavity power fluctuations). The features of the results displayed in Figure 3 indicate that the energy transfer low pass filter has been suppressed and that the global transfer function is now reduced to a second-order low-pass filter corresponding to the three-level-laser transfer function of the Er^{3+} system.

Using the full stabilization scheme (f_{rep} and f_{CEO}) described in Figure 1 (elements outside the grey rectangle), a phase lock bandwidth above 70 kHz has been demonstrated, leading to a state-of-the-art in-loop integrated phase noise [1 Hz – 1 MHz] of 120 mrad.

[1] N. R. Newbury, "Searching for applications with a fine-tooth comb", Nat. Photonics 5 (2011) 186.

[2] E. Portuondo-Campa, R. Paschotta, S. Lecomte, "Sub-100 attosecond timing jitter from low-noise passively mode-locked solid-state laser at telecom wavelength", Opt. Lett. 38 (2013) 2650.

[3] E. Portuondo-Campa, G. Buchs, S. Kundermann, L. Balet, S. Lecomte, "Ultra-low phase-noise microwave generation using a diode-pumped solid-state laser based frequency comb and a polarization-maintaining pulse interleaver", Opt. Express 23 (2015) 32441.

[4] L. Karlen, G. Buchs, E. Portuondo-Campa, S. Lecomte, "Efficient carrier envelope offset frequency stabilization through gain modulation via stimulated emission", Opt. Lett. 41 (2016) 376.

Additive Manufactured Metallic Compliant Mechanisms and Flexible Structures

H. Saudan, L. Kiener, E. Dominé, K. Vaideeswaran, Y. Zangui, M. Dadras

With its highly promising technology, the application of additive manufacturing (AM) processes for space applications is a constantly growing topic of interest among the main actors in the space industry. While most of the research and development work performed presently is focused on reproducing and optimizing designs of what could be described as “structural or massive parts”, little work related to the manufacturing of thin, flexible structures has been published up to now. CSEM is developing a production method based on AM-SLM (selective laser melting) to be applied to the development of its FLEXTEC (flexure structure technology)-based precision mechanisms, a core competency of CSEM that has been widely used in the past 30 years in the framework of space, the watch industry, and scientific instrumentation projects.

FLEXTEC-based mechanisms, also known as compliant mechanisms, can achieve macroscopic linear or rotary motion without friction, wear, or backlash and with extremely high fatigue performances thanks to the elastic deformation of flexible structures arranged in a special manner. In spacecraft, they cover various functions such as launch locking, linear or rotary scanning for ultra-high precision optical instruments, pointing mechanisms for antennas, and more. A notable example is CSEM's corner cube mechanism flying onboard the MetOp satellites, with more than 700 million cycles to date.

Up to now, the complexity of compliant structures has required highly sophisticated and expensive manufacturing methods, with the gold standard being wire electro-discharge machining from a bulk material block with consecutive large material losses and very long and delicate machining procedures. Today, this paradigm is questioned due to the new possibilities offered by additive manufacturing (AM) technologies.

After showing, in 2014, the feasibility of building an elementary compliant structure made of 316L stainless steel (see Figure 1) with AM-SLM (Selective Laser Melting), CSEM successfully developed – in the framework of an internal research project carried out with the company 3D PRECISION – an end-to-end SLM-based manufacturing and post-processing production method for a high-strength stainless steel chemically comparable to the widely known and used 17-4PH.



Figure 1: 316L stainless steel AM-SLM built linear stage.

The optimization of the SLM process was carried out as an iterative task that consisted of producing test samples through a set of well-defined parameters and analyzing them with the aim of minimizing the porosity and optimizing the microstructure and surface roughness. A last optimization phase was carried out to determine the best thermal post-processing strategy, and the best variant was identified through experimental testing of the mechanical performances of several sample groups.

The tensile testing of the various groups of samples produced highlighted the tremendous improvement associated with the Hot Isostatic Pressing (HIP) treatment, with the conclusion that the SLM built material can offer tensile performances similar to those of a commercial grade 17-4 PH stainless steel. The micrograph fracture analysis confirmed the positive influence of the HIP treatment, as shown by Figure 2.

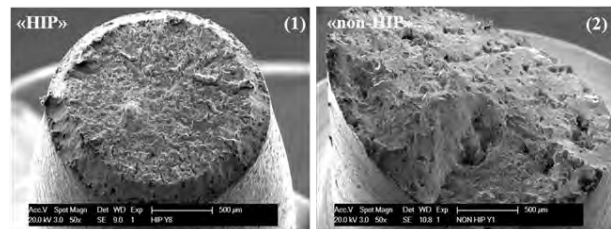


Figure 2: Alternate bending fatigue test results for AM-SLM samples.

The fatigue performances of flexure test samples were investigated in detail through an alternate bending fatigue test campaign covering four different sample groups (the test bench principle is illustrated in Figure 3). The fatigue test data collected helped understand the contribution of key material and surface defects to the final fatigue performances and highlighted the beneficial effect of the HIP treatment on the fatigue performances.

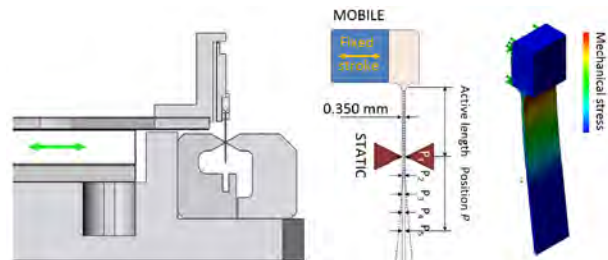


Figure 3: Alternate bending fatigue test principle.

A major conclusion is that despite a 23% loss in fatigue performances observed with respect to flexure elements built from commercial grade material, it is possible to design and produce – provided that a well-adapted sizing, in-depth SLM process mastering, and wise post-processing strategy are used – a compliant structure offering a lifetime of over 15 million cycles. This confirms the high enabling potential of AM-SLM in the domain of FLEXTEC-based precision mechanisms. This potential will be further assessed through a detailed study of the new flexure topologies enabled by SLM. The present work will be presented at the 14th European Conference on Spacecraft Structures, Materials and Environmental Testing.

Qualification Test Program for CCM and Prototype Flight Model

P. Spanoudakis, J. Bennes, M. Gumy, L. Kiener, I. Kjelberg, E. Onillon, G. Perruchoud, Y.-J. Regamey, H. Saudan, P. Schwab, V. Teodoridis

The corner cube mechanism (CCM) engineering qualification model has completed its test program. The flight models have been assembled and will commence their flight acceptance test campaign before their integration in the interferometer assembly for the Meteosat Third Generation satellites.

The corner cube mechanism (CCM) of the infrared sounder (IRS) for the Meteosat Third Generation (MTG) satellites completed an extensive qualification test campaign to show that the high-precision mechanism can meet stringent requirements for operation in the harsh environment of space in geostationary orbit.

The qualification test program was performed at both component/sub-system level and mechanism level. One of the critical components at sub-system level is the voice-coil actuator supplied by Cedrat Technologies (F). A lengthy qualification program was undertaken with the supplier to qualify the new magnets and coatings to meet specific MTG requirements for long-term storage conditions of 20 years. Typical tests included thermal vacuum cycling (100 cycles, -40°/+80°C), thermal humidity tests (95% RH, 1 bar, 45°C, 240 h), and epoxy resin adherence to validate the robustness of the various processes used.

The engineering qualification model (EQM), which is identical to the flight model (FM) version, is considered as a prototype. Performance level tests with this mechanism were performed, for example:

- trajectory generation and motion control,
- lateral deviation of the corner cube from a true straight line,
- dynamic exported forces.

The objective of the test campaign was to validate the design, manufacture, and assembly processes of a mechanism that is as representative as possible of the final flight version.

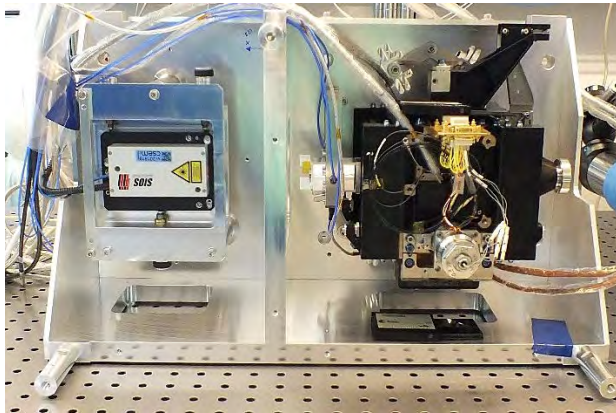


Figure 1: EQM mounted on performance test bench with interferometer in ISO5 (Class 100) cleanroom conditions.

The critical performance parameters measured during these tests were the mobile mirror lateral shifts and the speed stability. The maximum lateral deviation (parabolic shift) for a stroke of 18 mm (± 9 mm) was measured at 1.7 μm in Z and 1.2 μm in Y compared to the 2- μm specification (± 5 mm stroke).

Mechanical vibration tests simulate the extreme noise and vibration environment generated during the rocket launch. The delicate mechanism is in a launch locked configuration in order

to ensure that it will survive the vibration loads. The EQM survived the random profile vibration tests and shock tests in all three directions. Following the environmental tests, the performance tests were repeated and a close inspection of the launch locking device critical surfaces was made. No degradation was noticed.

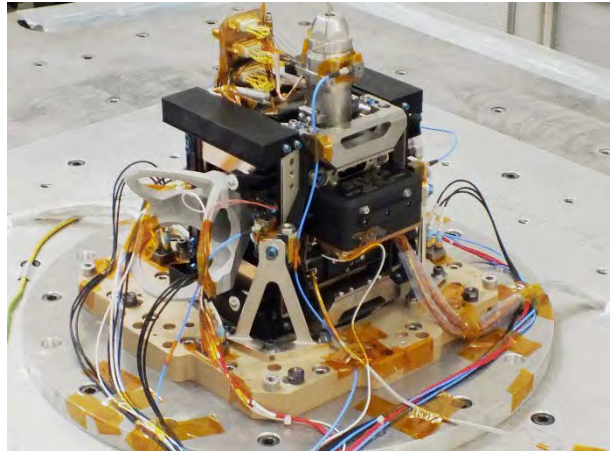


Figure 2: EQM instrumented and mounted on vibration shaker table.

The last series of tests were performed on a micro-vibration test bench that is used to measure the exported forces of the CCM while in operation and to inject a simulated spacecraft disturbance noise profile. While the mechanism was displacing the corner cube at a speed of 1 mm/s, during the reversal stroke, the forces exported to the instrument were measured as 7.2 mN.

With the injected micro-vibration disturbance profile, two speed stability parameters were measured:

- the absolute value of speed error during the dwell time measured at 0.73 mm/s (spec: 0.25 mm/s)
- the standard deviation of speed error during dwell time measured at 0.29 mm/s (spec: 0.06 mm/s)

Even though these values are out of specification, the results were expected since they are directly proportional to the injected disturbance levels. The injected disturbance is a sum of various satellite sub-system contributions, such as cryo-coolers, thrusters, and reaction wheels, which are being reviewed at satellite level to determine budgets and margins.

In parallel with the EQM qualification, the manufacture and assembly of the two FMs began and they are now at CSEM premises for the integration of sub-systems prior to the start of the FM acceptance test campaign.

This work is performed in partnership with Thales Alenia Space in Cannes (TAS-F) and is funded by the European Space Agency. CSEM thanks them for their support.

ULTRA-LOW-POWER INTEGRATED SYSTEMS

Alain-Serge Porret

The Ultra-Low-Power (ULP) Integrated Systems program addresses the key challenges faced and the technologies required when building very-low-power, (often) wirelessly interconnected, embedded smart systems or remote sensing nodes. The availability of such components is central to several global technological trends, such as the Internet of Things (IoT) revolution, the advent of wearable technologies for wellness and medical applications (in line with the needs of an aging population), or the generalization of machine-to-machine (M2M) communications required by Industry 4.0.

It is generally recognized that the number of interconnected devices will continue to increase exponentially (wearable items in our clothes or on our wrists, for implantable health monitors, at home in our appliances, to improve the security of our transport infrastructure, to track goods, etc.), to the point where they become essentially invisible to the end user (pervasive technology).

These trends are largely made possible by today's mature IC technologies, which allow the packing of an incredible number of interfaces and remarkable amounts of computational power in an ever-smaller volume, with constantly shrinking costs and lower power consumption. Therefore, the development of ASICs (application-specific ICs) is a significant element of the program's activities, although COTS (commercial, off-the-shelf) solutions are used when suitable devices are available.

The overall technological realm of the program encompasses mixed-signal devices, embedded processing, sensor interfaces, wireless systems, and vision technologies with a mixed hardware and software approach. It is clearly aligned with the "More than Moore" paradigm, which is in line with the general directions being taken by the Swiss economy, its inventiveness (doing more with less), and its capabilities (investment requirements within the scope of SMEs' available resources).

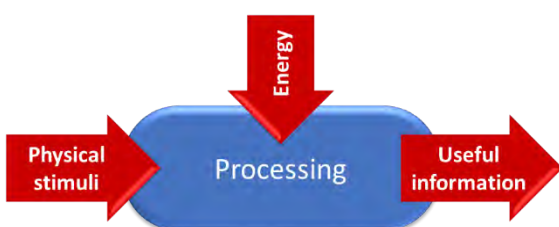


Figure 1: Basic structure and function of a remote sensor node.

Figure 1 shows the basic structure of a generic sensing node, which (1) collects and manages electrical energy to (2) acquire physical stimuli and (3) process them locally—in both the analog and digital domains—in order to extract the relevant information and (4) communicate this information to a central unit, often wirelessly. The focus of the program is to provide solutions to these four key technical challenges as follows—

- *Energy management:* this includes the smart management of batteries, but also energy harvesting from photovoltaic cells, from thermo-electric generators, or from wireless power transmission, moving devices toward maintenance-free, environmentally friendly, zero-battery operation.

- *Sensing interfaces:* a great many different types of physical quantities may need to be sensed by the broad range of applications covered by the program. These monitored quantities are getting more varied and include environmental parameters (such as the monitoring of harmful gases) and non-invasive vital sign monitoring (for instance, heart rate at the wrist or with the help of advanced vision systems). These measurements require sophisticated electronic interfaces and processing, which are even harder to design within the additional constraints of the ULP context.
- *Processing and extraction of relevant data:* in many cases, transmitting the raw information from the sensors is not efficient or secure. Local pre-processing, event classification, and the encoding of the data enable faster, much safer, and overall energy-efficient solutions that—moreover—will not generate unnecessary data “pollution” and will thus prevent the clogging of the precious, and shared, airwaves.
- *Transmission of extracted information, remote management, and coordination of distributed operations:* wireless communication requires a significant amount of energy. Optimized solutions need to be carefully devised, balancing various trade-offs for each specific application, at both the hardware and software levels. This also includes specific solutions for the integration and fusion of data from heterogeneous sensor networks, and the growing challenge of network security management.

The markets covered by the program are very diverse, as the generic nature of Figure 1 suggests, and are growing in scope with the development of the Internet of Things (IoT) paradigm, which is also aligned with the global trends of “wireless everywhere” and “smart everything”. Applications include:

- Consumer electronics (Bluetooth Smart devices, GPS-enabled devices, home automation and security systems, and image classification);
- Industrial systems (high-performance sensor interfaces, sensor networks for harsh environments, and optical quality control);
- Metrology (integrated measurement microsystems or optical encoders for various purposes);
- Medical and wellness (implants, vital sign monitoring, and electronic prostheses).

The long-term objective of the program is to provide the unique technologies required to build commercially successful, state-of-the-art sensing platforms and remote sensing nodes, with a focus on very-low-power (even battery-less), low-voltage, miniaturized devices.

This objective is pursued not only by the continuous improvement of component performance, but also by system-level optimizations. All relevant hardware and software aspects—from signal acquisition to signal processing, embedded software, and communication—are covered (in close conjunction with other CSEM programs).

A significant emphasis is placed on ensuring that the result is suitable for future industrialization without a major redesign or many compromises. Sometimes, ultimate performance is therefore less central than the stability and reproducibility of the results in a real environment.

Many of the applications concerned cannot benefit from wired power, either because the device must be mobile or worn or because it is implanted or is not located near a suitable power source, or simply because the wiring necessary to connect a large number of remote nodes is impractical. Therefore, reducing power consumption to increase battery life, ultimately to the point where energy harvesting enables zero-battery solutions, is paramount to the whole program.

The ULP Integrated Systems program is subdivided into three research activities, as follows:

- The *Vision* activity provides complete, embedded vision solutions that not only capture images, but also locally extract relevant features. It covers the complete acquisition chain from pixel sensing and electronics (components), via optics and processing hardware (system), to image processing and recognition tools (algorithms). In this area, better IC technologies also enable local processing and accurate pattern recognition, in an energy-efficient way, of the large amount of data generated. It is foreseen that imagers sensitive to much more than just visible light will eventually become mainstream—with applications in infrared, X-rays, or THz bands—and will be mixed with new multi-spectral capabilities and innovative optics.
- The *Wireless* activity similarly aims at providing complete solutions, which wirelessly transmit information through a network at a low energy cost for the remote nodes and are tailored to specific applications. It includes the development of narrow- and wideband ULP radios and antennas (components), of dedicated protocols taking advantage of the specifics of these components and applications (algorithms), and of complete wireless sensing nodes and network architectures (system). The main markets targeted are wireless sensor networks (WSN and IoT) and wireless body area networks (WBAN). Emerging technologies supported include robust, flexible, and software-defined radios, as well as RF sensing in the radar and sub-THz bands.
- Finally, the *System-on-Chip* activity provides the missing elements with which to complete a fully integrated solution. It includes ULP sensor interfaces; power management and energy-optimized digital processing (components); embedded, real-time control and processing software (algorithms); and power-efficient design methodologies and design flow (system). Notable novel directions include vital signs monitoring, brain/neural system interfaces, and sub-/near-threshold logic circuits.

Our efforts in the field of near- and sub-threshold digital circuit design have been stepped up in 2016. Lowering the supply voltage of a digital circuit to close to the value of the transistor threshold voltage has demonstrated the ability to provide a major energy-efficiency improvement over mainstream design techniques. In “Sub-threshold Latch-based icyflex2 32-Bit Processor with Wide Supply Range Operation” (page 125), a

processor was integrated into a $0.18\text{ }\mu\text{m}$ process and demonstrated full functionality for a supply voltage ranging from 0.37 V to 1.8 V, over process and temperature corners. This type of design opens the door to adaptive dynamic voltage frequency scaling (ADVFS) over multiple frequency decades and a wide range of operating conditions. CSEM has also designed a standard cell library using deeply depleted channel (DDC) 55 nm technology and operating at 0.5 V. The article “Library Design in a DDC technology optimized for sub-T” (page 127) shows how minimum speed degradation can be guaranteed through a technique that radically tightens the process corner spread.

These advances in the reduction of energy per operation enable new kinds of “zero-battery” devices that rely only on ambient energy. In “A Fully Integrated Adaptive Energy Harvesting System for Ultra-low Power Applications” (page 129), a fully integrated platform is presented where a photovoltaic cell is coupled with a sub-threshold microprocessor. It can harvest ambient light both indoors and outdoors, and manages power levels ranging from μW to mW with optimal efficiency.

Wireless communication is at the center of the Internet-of-Things but is still one of the most energy-intensive and challenging technologies. In “Secure Wireless Link for Ultra-low Power WSN” (page 118), the timely topics of data protection, entity authentication, and key management are discussed in relation to the specific constraints of embedded platforms. On a related topic, “Making Self-healing Wireless Networks Power Efficient” (page 115) explores ways to provide high reliability in multi-hop data collection applications, where the network requires adaptive routing, while limiting the energy and traffic overhead.

Bluetooth Smart is a pervasive communication standard, and CSEM has been, for many years, a leading provider of compatible silicon IPs. “Implementing Bluetooth Low-Energy 5 on icyTRX” (page 123) describes the latest improvement of our solution.

RF waves can not only be used to send information; they can also be a powerful way of probing the environment. For instance, the study “RF Sensing of Human Physical Condition in the mm-Wave / THz Frequency Range” (page 112) investigates the detection of mental and light physical stress via measurement of the skin’s reflectance. Inexpensive 3-D printing technology can be used to build antennas for such RF-sensing applications and are explored in “3D Printed Antennas for mmWave (100 GHz – 500 GHz) applications” (page 113).

Like RF-sensing, hyperspectral imaging allows the collection of radically new information from a simple camera snapshot, thus enabling a wealth of new applications. “Hyperspectral Imaging using a Commercial Light-field Camera” (page 111) proposes a solution to get up to 81 spectral channels (or fundamental “colors”) from a single exposure, using off-the-shelf components.

Finally, the Vision-in-Package (VIP) is a sugar-cube-sized camera with a low-power processor, a high dynamic range imager, optics, and a communication interface. In “Real-time Face Detection and Recognition on the VIP System” (page 106), an efficient algorithm has been built on this platform, requiring significantly less power and resources than existing solutions. It is envisioned that many other machine-vision applications could be similarly embedded in this tiny, low-cost, smart camera.

Illumination for a Laser Profilometry System Targeting Fast Moving Objects

C. Gimkiewicz, F. Kaess

Laser profilometry is suitable for *in-situ* measurements of fast moving objects as required by many applications of robotics and automation, mobile vehicles as well as in the field of transportation and autonomous circulation. Accurate measurements of items moving at very high speed are necessary for the observation and control of positioning tasks, abrasion processes, or pressure induced profile changes, for example to ensure safety and quality in a cost-effective way. The presented illumination method for a laser profilometry system allows the measurement of a profile precision in the order of 0.1 mm at speeds up to 100 km/h.

Laser profilometry is a contactless technique to measure the relief of a distant surface. It makes use of a projected laser pattern onto the target object. The deformation of the known laser pattern allows to evaluate the objects surface profile by triangulation. In order to capture object features within the pixel resolution of the camera, the time of image acquisition is short. For example, the desired resolution is in the order of 0.1 mm, meaning that an object detail of a size of 1 mm should be imaged onto 10 pixels. For a speed of 100 km/h (27778 mm/s), the sensor shutter speed and/or the illumination time has to be shorter than 3.6 μ s. The object reflectivity in most cases is very low, since the surface of interest is not a mirror but has scattering and absorbing properties. Experiments for a field of view of around 200 mm and an object distance of around 400 mm have shown that the laser power has to be in the order of several Watts and focused to a line width of less than 1 mm to achieve profile accuracies in the order of 0.1 mm in real world conditions (e.g. sunlight). However, increasing the laser power increases the minimum feature size of the laser pattern so that profile features are less resolved, since high-power lasers come with larger beam diameters. This is especially true when limitations on robustness, size and handling demand a connection of the laser light to the measurement set-up via an optical fiber: In this case, a small fiber core is not capable to endure high laser power on the long term. A laser beam coupled into a single mode fiber, for example, offers a maximum power of around 100 mW, a multimode laser however can offer up to 4 W when coupled into a multimode fiber with a 50 μ m core size, and up to 8 W for a 100 μ m multimode fiber.

Typical laser line-generating optics are based on a single lens design to be compatible with a compact and cost effective product. Typical line width is <1 mm and the line-generating optics are designed for single mode lasers or single mode fibers. Here, we present an optic that is designed for multimode lasers and generates one or multiple laser lines with off-the-shelf components. We have employed cylindrical lenses. As a consequence the beam shaping in the xz-plane (with the z coordinate as the beam direction) is nearly independent of the optical functions in the yz-plane. Only the length of these "line-spreading-beam-path" in the xz-plane (Figure 1) has to be adapted to the length of the "line-focusing-beam-path" in the yz-plane.

In order to generate multiple lines, a diffraction grating can be placed at the output surface of the laser line-generator.

The "line-spreading-beam-path" consists of a collimating cylindrical lens and a line-generating lens, i.e. a Powell like a sphere [1], which is in principle a combination of an axicon and a short focal length lens. Such line-generating lenses are designed to achieve a homogeneous power distribution along the laser line. However, in a profilometry system with a camera, a flat top power distribution might not be the optimum, since usually the imaging optics of the camera transfers less power from the edges of the field of view than from the center. (The effect is known as "Cosine Fourth" law and describes the falloff of the illuminance across a camera image.) A homogenous illuminated laser line would appear darker at the image edges on the camera's sensor. The advantage of our design is that it allows to counterbalance the falloff: By changing the position of the collimation lens, different power distributions can be achieved and the mentioned relative darkening of the image toward its borders can be compensated.

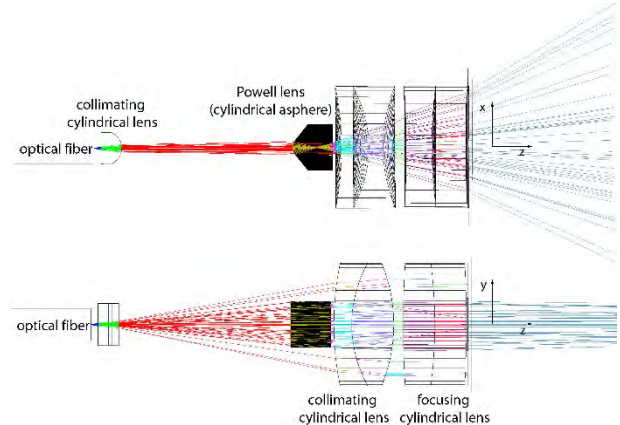


Figure 1: Scheme of the laser line-generator optics. The upper image illustrates the "line-spreading-beam-path" as a scheme in the xz-plane, the lower image shows the "line-focusing-beam-path" as a scheme in the yz-plane.

In our current design with an object distance of 400 mm, the size of the optics is 70 mm in length, excluding the fiber connector, and 25 mm in diameter; the large diameter is necessary to reduce the effect of the diffraction on the laser line width. We have calculated a total line focus size of FWHM = 0.35 mm for a 50 micron fiber output and FWHM = 0.75 mm for a 100 micron fiber. With this optical design, a profile resolution of less than 0.1 mm can be achieved with a 4 W laser coupled to a 50 micron fiber in real world conditions.

[1] I. Powell, "Linear diverging lens", Patent No. US4826299 A (1989).

Real-time Face Detection and Recognition on the Vision-In-Package System

E. Türetken, E. Franzi, P.-A. Beuchat

Automated facial analytics has a broad range of applications in many industries such as biometrics and market research. Existing solutions require significant hardware resources that consume substantial amounts of power and are costly. To address these limitations, we developed a complete real-time face detection and recognition system that is low-power, compact and inexpensive.

Facial analytics and recognition is a rapidly growing market expected to reach \$ 20 billion by 2025^[1]. From surveillance and access control systems in smart buildings to retail stores that automatically collect viewership and demographics, there is an ever growing need for compact and reliable solutions.

One of the major barriers to rapid adaptation of this technology, especially in applications with low-power, small-size and low-cost requirements, is the computationally demanding nature of the algorithms involved. As a result, existing solutions on the market rely on GHz-clocked multi-core processors that are neither power-efficient nor cost-effective.

The Vision-In-Package (VIP) system is designed to address these challenges. It is a compact camera system with a low-power processor (ARM Cortex M4/M7 with 8 MB RAM), a high-dynamic range imager, optics, and a communication interface. The system occupies only around 4 cm³ and weighs less than 20 g including a battery cell. It features a complete facial analysis pipeline running in real time and fully embedded within the VIP system.

The software is compact and stand-alone with no external dependencies. It is comprised of a minimal version of the uKOS operating system^[2] and a face analysis package running on it. Unlike existing systems that run on powerful hardware architectures, our system requires several orders of magnitude less CPU time and memory. The analysis pipeline runs at around 4-5 frames per second at QVGA resolution on the VIP and consists of the following steps, also depicted in Figure 1.

- Face detection: All the faces in an acquired frame are detected, which typically takes less than a hundred ms to run and requires only a few hundred KB of RAM memory;
- Facial landmark localization: Facial attributes, such as corners of the eyes and nose, are located within each detected face region;
- Normalization: Involves a rough geometric transformation that aligns the eyes horizontally and scales the face to a standard size, and a photometric normalization that removes non-linear intensity variations caused by shadows and non-uniform illumination;
- Face recognition: Descriptive features are extracted at landmark locations and used for uniquely identifying people in a database of registered faces. New individuals can be registered to this database instantly at any time with just a single click and without requiring any re-training.

These steps are made possible by using efficient machine learning algorithms including the Adaboost, ensemble of

regression trees and LBP algorithms, which we trained on millions of examples with ground truth annotations. The resulting classifiers typically take a few hundred kilobytes of space and are fast to run even on low-end mobile processors.

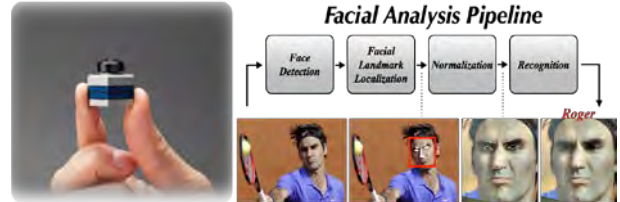


Figure 1: The VIP system (left). The facial analysis pipeline (right).

The combination of compact design offered by the VIP system and the efficiency of the face processing pipeline allows for applications with low-power consumption, small-size & weight, or low-cost requirements. We believe the following industries offer numerous opportunities for a widespread use of our technology:

- Wearables: Fast and compact facial analytics on smartwatches or eyewear can give users a secure and more personalized experience, and possibly provide new health screening tools for children and elderly;
- Marketing & advertisement industry: Collecting viewership and demographics data, such as age and gender that require prior facial analysis, allows advertisers to objectively assess the effectiveness of their campaigns. The data can be collected from cameras installed in digital advertising displays in retail outlets, or billboards on streets;
- Robotic/toy industry: Facial recognition and analysis can provide more personalized interactions for robotic pets allowing them to recognize their owners, play with them, read their moods and emotions;
- TV manufacturers: Combined with hand gesture recognition, facial analytics can provide a unique and personalized interaction experience with TV sets;
- Automotive industry: Facial expression analysis can be used to help improve driver safety by monitoring driver drowsiness and distraction. Furthermore, recognition of the driver allows driver customization such as automatically adjusting vehicle settings to his/her personal preferences;
- Security: Using low-power or solar-powered facial recognition systems opens up new possibilities in the security domain such as monitoring remote locations without electricity, or easing the deployment of camera networks in populated public areas such as airports.

^[1] Research and Markets, "Global facial recognition market analysis & trends - Industry forecast to 2025", (2016).

^[2] E. Franzi, "The µKernel project", www.ukos.ch (2016).

A Contactless Vision-based Technology for Heart and Respiration Rates Estimation

V. Moser, F. Braun, A. Lemkaddem, S. Dasen, O. Grossenbacher, A. Chebira

A contactless vision solution has been developed to estimate heart and respiratory rates. This solution is based on the real-time processing of a sequence of images taken with a camera at one meter from the subject. The face and chest are recorded at 20 frames/second. A region of interest is selected on the forehead or the cheek to estimate the heart rate while the chest is used to estimate the respiratory rate. This technology will be tested in the neonatal intensive care unit and its performance compared to current solutions, based on gel electrodes, which are sensitive to body movements and thus responsible for a high rate of false alarms.

An increasing number of parameters are monitored in the neonatal intensive care units. This results in additional sensors placed on the body of the babies generating discomfort and stress. Moreover these sensors are often sensitive to body movements. In view of reducing the sensitivity to such motion artefacts and increasing the patient's comfort, contactless solutions for vital signs monitoring are needed.

CSEM's technology uses two highly sensitive cameras:

- Day vision: UI-3240CP-C-HQ with e2v Sapphire 1.3 Mpixel sensor (color sensor)
- Night vision: UI-3240CP-NIR-GL with e2v Ruby 1.3 Mpixel sensor (monochrome sensor with enhanced sensitivity in near-infrared) combined with a near-infrared light source

Three algorithms have been developed to process the images taken with these two cameras and thus estimate the heart and respiratory rates (HR / RR). Each of them works as well in day condition as in night condition with near-infrared illumination.

The algorithm for the estimation of the RR is based on the detection of chest movements. The developed approach uses a simple projection-based motion estimation, allowing for a real-time implementation [1]. The HR estimation algorithm detects the fluctuations of the skin color in a region of interest (ROI), which are due to blood volume changes. On each frame, the mean value of pixels is computed over the ROI. A real-time adaptive band-pass filter [2] is applied on the fluctuation of this mean value to estimate the dominating frequency, corresponding to the HR. The aforementioned HR algorithm is very sensitive to movements. Therefore, CSEM had to develop a third algorithm, which allows to compensate the movements by tracking the skin region. This algorithm uses support vector machine to track the selected ROI.

CSEM acquired a database with ground truth synchronization to evaluate the developed algorithms. A total of 16 subjects (11 male / 5 female) underwent the protocol described hereafter. The protocol consists of the following three sequences which were performed twice, once with artificial light (using the color camera) and once in darkness (using a near-infrared light source and the monochrome camera):

- Respiration sequence, 4 minutes recording: to train and evaluate RR algorithm
- Handgrip sequences leading to changes in heart rate, 4 minutes recording: to train and evaluate HR algorithm

- Movement sequences, 2 minutes recording: to train and evaluate the tracking algorithm

Besides the video data (investigational device), various physiological parameters were synchronously recorded using the BIOPAC system (reference device): ECG, respiration, SpO₂ and accelerometer.

CSEM combined the three algorithms in an application that allows to acquire and analyze images in real-time or to load existing ones from the database (Figure 1). Our application plays the sequence and displays the estimated heart and respiratory rates. It can superpose the ground truth curves (BIOPAC) if available.

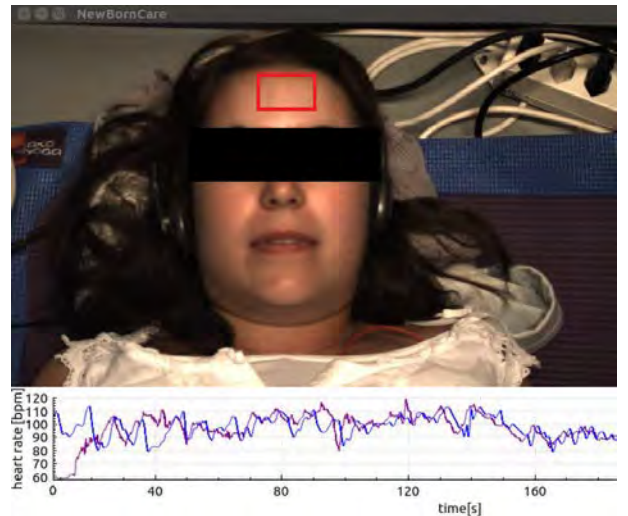


Figure 1: Application that estimates HR and RR in real-time or compares the estimated HR and RR from a video sequence with the corresponding ground truth. The tracked ROI for HR estimation is displayed in red. The mismatches that can be seen at the beginning of the sequence are due to the initialization time.

The performance of the algorithms was evaluated on the 16 adult subjects tested: The HR could be estimated with an average absolute error of 3.14/4.21 beat per minute on the visible/dark sequences, the RR could be estimated with an error of +/- 2.4 breathes per minute. These promising results - if confirmed in larger clinical datasets - could open the way for a new generation of contactless vital signs monitoring.

This work has been done in collaboration with STI-JMV and LTS2 laboratories from EPFL.

[1] F. Braun, A. Lemkaddem, V. Moser, S. Dasen, O. Grossenbacher, "Camera-based respiration monitoring", BMT (2016).

[2] S. Fallet, et al., "Real-time approaches for heart rate monitoring using imaging photoplethysmography", CinC Computing in Cardiology (2016).

Compact and Flexible Tracking System for Total Knee Replacement Surgery

P. Volet, D. Hasler, P. Nussbaum, F. Kaess, E. Grenet, E. Franzi, A. Chebira, S. Cloix, B. Perrin, C. Hennemann, Y. Brunet, P.-A. Beuchat, Y. Liechti, R. Jose James, M. Fretz, N. Schmid, T. Stadelmann, L. Beynon

In the context of total knee replacement surgery, a wireless and battery powered tracking system using shadow imaging technology has been developed for measuring the 6D position of a surgical tool relatively to the patient's bones.

The overall goal of the project is to develop a smart, patient customizable instrumentation to assist surgeons during a total knee replacement. To this end, CSEM developed a miniatureized tracking system based on shadow imaging technology [1, 2] that can be directly integrated with patient-specific templates and surgical instruments.

Before the surgery, the patient undergoes a scanning procedure (CT-scan), from which a 3D model of the patient's anatomy and landmarks are computed to form a preliminary plan for the implantation. During surgery, the patient's anatomy is registered using a specific template (negative form) that fits the bone, to match the 3D models and initial plan with the surgical situation. With the tracking system integrated into the surgical templates, the application can directly compute and render the exact position of a surgical tool relatively to the patient's bone. The system also allows to intra-operatively plan and adapt the implant position.

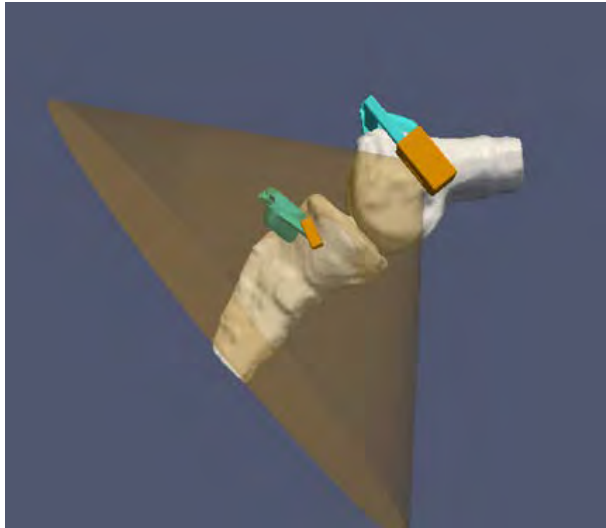


Figure 1: Simulation of the target and tracker devices (yellow) mounted with CAD-designed patient-specific tools (Medivation AG).

The tracking system is made of two separate devices. The tracker device includes an image sensor, a microcontroller running a micro kernel operating system and a Bluetooth low-energy communication system-on-chip. The target device includes an IR receiver and five LEDs that are fired sequentially under the control of a small microcontroller.

Shadow imaging is a technology that uses an image sensor with an optical mask placed on top of it. By synchronizing the LEDs and the image sensor, each LED casts a shadow on the

image sensor, from which one can compute the direction of the light source and then reconstruct the 6D position of the target. The use of an optical mask instead of traditional optics results in a very compact system in particular given the wide-angle constraint. Moreover, shadow imaging offers better precision and better depth of focus.



Figure 2: Sensor (left) and tracker (right) prototypes mounted on optical posts (front covers removed).

In the context of such a knee surgery application, the target device must be able to move up to a distance of a dozen of centimeters in front of the tracker device and to rotate with an angle of more than ± 45 degrees in all direction. The typical positioning accuracy is much less than ± 1.0 mm and the typical angular accuracy is less than ± 1.0 degrees. The operating temperature ranges from 10 to 30°C.

The target and tracker devices are both designed to be single use, battery powered and fully wireless. The size of the tracker prototype is $26 \times 44 \times 24$ mm including the space required by a CR123 battery. The overall size of the target prototype is $26 \times 32 \times 14$ mm. The tracking system can operate at more than ten 6D measurements per second with an autonomy of several hours. The addressing and synchronization of the LEDs is done by the tracker device using a dedicated IR link. The control and data communication between the tracking system and the surgical navigation system relies on Bluetooth Low-Energy services.

This project has been done in collaboration with Medivation AG in Brugg and has been funded by the Swiss Commission for Technology and Innovation (CTI project 17244.2 PFLS_LS). CSEM thanks them for their support.

[1] E. Grenet, et al., "spaceCoder: a nanometric 3D position sensing device", CSEM Scientific and Technical Report (2011) 89.

[2] E. Grenet, et al., "Embedded sun tracker with extreme precision", CSEM Scientific and Technical Report (2013) 100.

An Integrated Circuit for Future X-ray Imaging Detectors based on a Ge Pillars Absorption Layer

R. Quaglia, P.-F. Ruedi, Y. Zha, A. Bischof, M. Despont, P. Niedermann

We have developed an integrated circuit for single X-ray photon counting. The circuit will be coupled with a Ge layer which acts as an X-ray absorber material for a new generation of X-ray imaging detectors for applications in various fields from medical imaging to physics experiments. The proposed solution has potential advantages in terms of cost, reliability and modularity compared to the state of the art.

This work has been developed in the framework of the SNFS-NOVIPIX project. The goal of the project is the realization of a novel topology of X-ray imaging detector based on a germanium absorption layer intended to be readout by a single photon counting circuit. In the NOVIPIX concept, a hetero-junction diode (sensing element of the pixel) is formed between the wafer substrate (n-type) and a germanium layer (p-type) deposited on the backside of a thinned CMOS wafer. The germanium layer is deposited as structured pillars [1], taking also advantage of the CSEM MEMS capabilities. The diode formed in this way allows for the design of a monolithic detector with advantages in terms of cost, reliability and modularity compared to single photon detectors (e.g. HPD, Hybrid-Pixel Detectors) where a silicon detector has to be bump-bonded to the CMOS readout IC. Applying a sufficiently high negative voltage on this diode, a depletion region is formed between the Ge pillars and the wafer substrate. Figure 1 shows a lateral view of the pixel under development within this project. When an X-ray photon is absorbed, electron-hole pairs are created and, while holes are collected at the common cathode, electrons are collected by a pixel anode. Since the total charge collected at the anode is proportional to the energy released by the incident photon, a proper circuit can be placed inside each pixel in order to count (photon counting) the number of incoming photons exceeding one or more given thresholds.

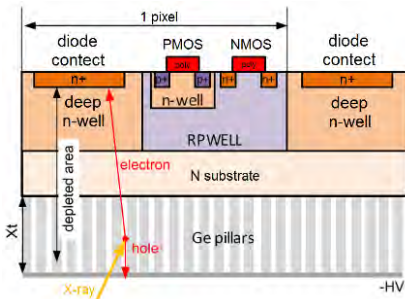


Figure 1: Lateral view of the NOVIPIX pixel.

As germanium has a higher absorption coefficient than silicon, a detector made of germanium has the great advantage of a wider energy range of applications (e.g. 20-80 keV) whereas traditional silicon detectors have very low efficiency. The higher efficiency of such a detector is also advantageous for low energy X-ray medical imaging (e.g. mammography) because a smaller total ionizing dose is required. However, the unconventional diode formation and smaller bandgap material (0.67 eV of Ge vs 1.12 eV of Si) result in a higher leakage current from the detector (expected in the mA/cm² range) that has to be compensated by the analog front end.

Recently, CSEM has developed a photon counting chip for a similar project [2]. Starting from that result, a new design has been carried out to reduce the pixel size (reducing the leakage current per pixel) while concurrently enhancing the functionalities by adding a second threshold discrimination capability (dual energy discrimination). The new circuit is implemented on a 16 × 16 pixels array (each pixel is 100 × 100 μm) and has been designed in a 0.15 μm CMOS technology. Figure 2 shows the structure of a single pixel.

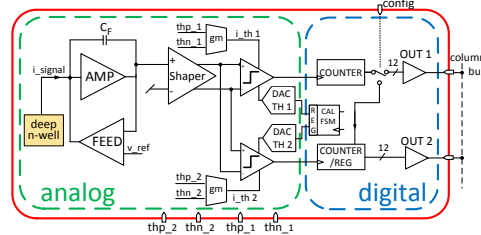


Figure 2. Building blocks of the single pixel.

The pixel architecture can be logically split in two parts: An analog front-end (green dashed box in Figure 2) and a digital back end (blue in Figure 2). The analog front-end is composed of a charge sensitive amplifier with a feedback circuit to compensate for the detector leakage current. This feedback block has been designed to guarantee stability with a leakage current up to 1 μA per pixel. After a shaping stage (bandpass CR-RC), the signal is converted into the digital domain by two continuous-time comparators designed to achieve good performances with a small area and low-power consumption. The thresholds are set by global references common to all pixels. Two 6-bits DACs (one per comparator) and a finite state machine are added to calibrate the thresholds mismatch. The outputs of the discriminators are then counted (each counter is incremented at every discriminator commutation) by two 12-bit ripple counters that store the number of photons exceeding each respective threshold during an acquisition. The output of the pixel is purely digital. An alternative configuration uses the second counter as a register and allows a simultaneous acquisition and reading (single threshold detection). The chip peripheral circuits include some bias generators and digital logic, providing row synchronization and serialization of the column outputs. The pixel power consumption is 18 μW.

The chip is currently under test and will be submitted soon for the final integration with the germanium layer.

The project partners are EMPA and ETH Zurich. This work was partly funded by the Swiss National Science Foundation (SNSF). CSEM thanks them for their support.

[1] C. V. Falub, et al., "Scaling hetero-epitaxy from layers to three dimensional crystals", Science 335 (2012) 1330.

[2] Y. Zha, et al., "Pulse counting energy-sensitive X-ray detector IC", CSEM Scientific and Technical Report (2013) 102.

Vision-based Monitoring of Manual Assembly Processes

I. Kastanis, M. Höchemer, S. Widmer, P. Schmid

A system was implemented for monitoring manual assembly processes using specially developed visual markers in conjunction with machine learning methods that recognize the actions of the assembly worker. The system learns by instruction and provides online information to the user about the assembly tasks within the process. In line with Industry 4.0 concepts, this monitoring system is highly configurable offering a great degree of flexibility that makes it an excellent tool for customized small-batch production runs.

Manual assembly processes are still very common in many industrial shop floors. The repetitive nature of these tasks makes them error prone, effectively reducing the overall quality of the manufactured parts. Current methods for quality control typically combine a human supervisor and an automated test station. The proposed system offers an automated solution for quality assurance, which is especially important for medical devices as well as other sensitive areas where manufacturing quality must be 100 %.

The goal of this project was to develop a machine vision and learning system that monitors the manual production of parts and offers assistance to the worker in order to recognize their gestures and avoid errors. This reduces the costs and the resources and guarantees consistency in production. The developed solution is based on a PC system with a connected camera that overlooks the work area.

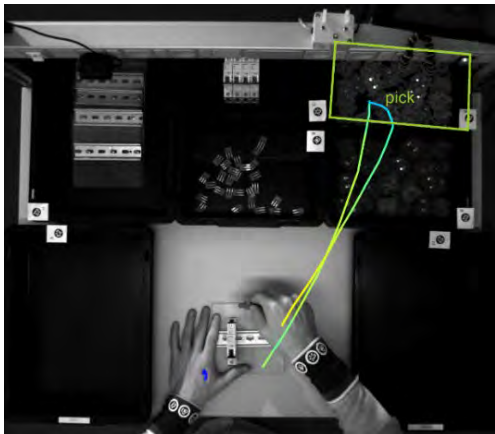


Figure 1: System-camera view. A picking action is recognized.

Tools, component boxes and both hands of the worker can be continuously detected and tracked by using visual markers developed specifically for this project. The system learns with the use of machine vision how the correct execution of the assembly is performed. This is achieved in the learning phase where the process steps from a human worker are observed, analyzed and recorded as "correct" steps. For the robustness of the training, the system must be capable of tolerating variations from different individuals, it is often the case that the positions of component boxes is not fixed. In most cases, a test device is used at the end of the assembly to verify different aspects of the finished product, for e.g. weighting, electrical tests, visual measurements. During these monotonous assembly tasks, it is frequent that after hundreds of correctly assembled products, the test device detects a defect but the worker places it out of habit in the box of "good" parts. The

developed solution offers for this case an additional level of quality assurance by having test and measurement devices connected to the system. In the learning phase, the system learns that a defective product goes in the reject box, and a non-defective goes in the "good" parts box.

Another important aspect for error reduction is the ability of the system to display live information to the worker during assembly. Since the system is aware at all times which steps of the process have been completed and which should follow, it can inform the worker about the next steps that need to be executed. Using past information, the system can dynamically assess which variation of the process the worker is currently performing, if a valid one exists. In the case of an error, the system notifies the user and can allow error correction and continuation of the process.



Figure 2: 6D-pose visual markers used for tracking (developed by CSEM).

The tracking of the visual markers was a challenging task due to the many markers that need to be detected and tracked simultaneously in high-resolution images. The required tracking speed for a trained worker makes standard marker technology ineffective. Further, complete pose is desired for analyzing the assembly motions. Appropriate markers were developed in conjunction with detection and tracking algorithms that are capable of complete 6D-pose detection with 60 fps in high-resolution images in a robust manner where short occlusions do not cause problems.

A complete solution for monitoring manual assembly processes was developed offering visual assistance to the worker. A short video can be found on the CSEM YouTube channel [1]. By using machine learning, the processes can be learned by instruction in an efficient manner without requiring expert personnel reducing therefore the ramp up time and the initial setup costs. The developed markers offer robust detection and tracking in high-frame rates, capable of capturing human-hand motion. The dynamic and configurable nature of the system has the potential to reduce the amount of errors in manual assembly lines and offer an automated tool for quality assurance.

The work has been supported by the Swiss Commission for Technology and Innovation CTI (project Nr. 16025.1 PFIW-IW) as a part of the Approbate project in collaboration with Credimex AG [2] and Maxon Motor AG [3].

[1] youtu.be/zBao3QunnGY

[2] Credimex AG, Switzerland

[3] Maxon Motor AG, Switzerland

Hyperspectral Imaging using a Commercial Light-field Camera

R. P. Stanley, A. Chebira, A. Ghasemi, L. A. Dunbar, E. Franzi

Snapshot hyperspectral imaging allows the collection of both spectral and spatial information in a single exposure. A common solution is to create a huge array of filters on the detector. We apply the approach of Levoy & Horstmeyer to build a hyperspectral camera based on a Lytro™ commercial light field camera. We show reconstructed hyperspectral images with 9 spectral channels and show how this can be increased to achieve 81 spectral channels in a single snapshot.

Hyperspectral imaging allows the collection of spectral information from across the EM spectrum while still retaining the spatial information. Typically, a hyperspectral camera will create a 3D cube of images, wherein the spectral information for each location or pixel on the image is depicted. This modality is naturally fitted for objects/materials identification or detection processes, and has encountered a large success in the agriculture and food industries to name a few.

In snapshot spectral imaging, the 3D cube of images is taken in one shot, with the advantage that dynamic scenes can be analyzed. The simplest way to make a hyperspectral camera is to put an array of wavelength filters on the detector and then integrate this detector with standard camera objectives [1]. The technical challenge is to make arrays of N wavelength filters and repeat this sequence up to 100'000 times across the detector array, where each individual filter is matched to the pixel size and can be as small as a few microns.

In this work, we generate the same effect with just one N wavelength filter array, which is then multiplied and imaged optically onto the detector to achieve the same effective filter array. This was first outlined by Levoy and Horstmeyer [2,3] using microlens arrays in a light-field camera (Plenoptics 1.0). Instead of building our own light-field camera, we used an existing commercial camera, Lytro™ [4].

There were three major challenges in this work. The first was to design an optical system that would be compatible with the Lytro camera. Second, to override the camera hardware and firmware to get access to the raw data, and third, to reorganise the information into different spectral channels.

The design we developed is based on a telecentric system. This is a system without parallax so that the size of an object does not depend on its distance (as long as it falls in the depth of field of the camera). Telecentric systems are well suited to the type of light-field system we want to build.

Our design was implemented in the lab, using a linear variable wavelength filter as the core wavelength selecting element. The wavelength transmitted by the filter depends on the position. The uniqueness of the light-field camera system is that it converts this spatial variation into angle information, which is then extracted at the detector using a microlens array.

Adapting the Lytro camera was not trivial and required a careful disassembly. The data was extracted using an open source Matlab toolbox [5] that was adapted for our needs.

The system was tested using a colour checker card and a white light source. The results of the data before and after analysis can be seen in Figures 1 & 2. Figure 1, is the raw data as read from the Lytro camera, processed with a demosaic filter. After using the Matlab toolbox the multispectral mosaic can be displayed (see Figure 2).

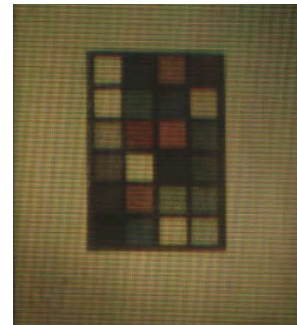


Figure 1: An image of a colour checker card, normally used for color calibration, in the hyperspectral imaging system. This shows the raw image extracted from the camera.

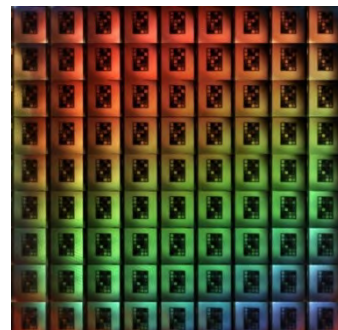


Figure 2: A multicolour image reconstructed from the raw data of Figure 1. The non-uniformity in the individual images is due to experimental artifact.

In conclusion we designed, built and tested a snapshot hyperspectral imaging system using a commercial light-field camera. The camera is polyvalent and can be adapted to many needs. The next step is to replace the Lytro camera with a CSEM module which can allow real-time spectral image extraction.

[1] <http://www2.imec.be/content/user/File/Brochures/cmos imagers brochure-april26.pdf>

[2] M. Levoy, et al., "Light field microscopy", ACM TOG Transactions on Graphics 25 (2006) 924.

[3] R. Horstmeyer, et al., "Flexible multimodal camera using a light field architecture", ICCP IEEE Int. Conf. on Comp. Phot. (2009) 1.

[4] Lytro, Inc., USA

[5] <https://ch.mathworks.com/matlabcentral/fileexchange/49683-light-field-toolbox-v0-4>

RF Sensing of Human Physical Condition in the mm-Wave / THz Frequency Range

O. Vorobyov, E. Daskalaki, C. Hennemann, J.-D. Decotignie

The objective of this study is to investigate the possibility of detecting mental and light physical stress via measurement of the reflectance of the skin in the mm-wave/sub-THz band. The combination of the spatial and temporal response of the reflectance offers the potential to enable a generic method for non-contact sensing of the physical and emotional state of human beings.

Various sources in literature have reported the possibility to detect stress based on changes in the galvanic skin response (GSR) [1]. It has also been shown that the GSR is correlated with the reflection coefficient of the skin and that it is possible to assess it via changes in the skin's reflectance at frequencies in the mm-wave / sub-THz band (e.g. 75-170 GHz).

Currently, these frequency bands can be reached with CMOS technology, which is capable of operation up to about 500 GHz. This, coupled with the fact that mm-wave / sub-THz radiation is non-ionizing, opens the door for realization of miniature, low-power, safe and low-cost solutions for potential applications in the domains of health (e.g. contactless scanner for stress sensing) and security (e.g. remote lie detector).

In the present study, the detection of physical and mental stress is investigated through measurements of the skin reflectance in two frequency bands: 75-110 GHz (Band-I) and 325-500 GHz (Band-II). The skin reflectance was measured during rest and after mental and physical stress. Physical stress was induced by grabbing a dynamometer with 15 N of force for 5 minutes. Mental stress was achieved with the use of the Stroop Test (online test(s) to test capacity to direct attention) for 15 minutes.

The measurement setup his shown in Figure 1 below.



Figure 1: Measurement setup.

Three measurement conditions were considered: (1) Rest; (2) Mental stress: After stroop test for 15 minutes and (3) Physical stress: After dynamometer under 15 N of force for 5 minutes.

Stress measurements were always preceded by a rest period of at least 15 minutes. Three locations on the hand were considered for the purposes of the measurements (Figure 2): arm, hand and finger.



Figure 2: Measurement locations.

Figure 3 depicts the averaged results of measurements performed between 440 GHz and 480 GHz in frequency band II for at least five persons. It can be seen that the shape of the measured amplitude (i.e. the shape of the spectrum) over this frequency range is effectively the same in the case of stress as it is in the case of rest. However, there is a clear difference between the results at rest and under stress. The measured amplitude response is stronger in the case of stress than at rest (i.e. about 7 dB across the frequency range for measurements performed on a hand (top) and 3.5 dB in the case of measurements performed on a finger (bottom)). Similar results were obtained in the case of frequency band I, but the differential between case of stress and rest was found to be much smaller (i.e. 1 dB).

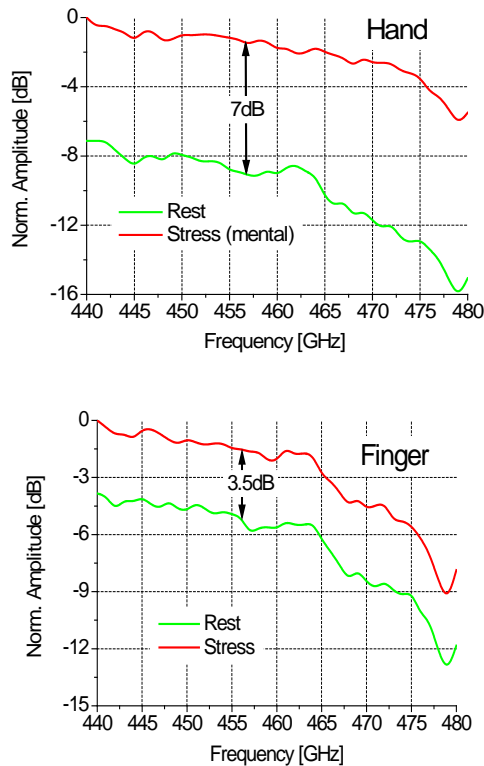


Figure 3: Mental stress based on measurement of the skin reflectance on a hand (top figure) and on a finger (bottom finger). The measurements were performed in frequency band II (440-480 GHz).

The results, in particular in frequency band II, demonstrate the potential for remote, non-contact sensing of stress [1]. This research has been supported by funding from an internal CSEM Grant and EU H2020 Framework program (M3TERA, grant no. 644039).

[1] M. V. Villarejo, et al., "A stress sensor based on galvanic skin response (GSR) controlled by ZigBee", Sensors 5 (2012) 6075.

3D Printed Antennas for mmW / Sub-THz (100GHz–500GHz) Applications

O. Vorobyov, A. Bischof, J. R. Farserotu

Inexpensive 3D printing technology can be used to build antennas for RF sensing solutions for food safety, health, security, industrial and many more applications. By using a 3D printer, we can rapidly prototype inexpensive plastic based antennas; providing the required radiation system performance.

Until recently, it remained difficult to realize low cost and miniature solutions in the mmW / sub-THz band; the lower end of this frequency band was difficult to reach with CMOS technology, while relatively large and expensive sources and detectors were required at the higher frequency end of the band. Today, though, given recent advances in integrated circuit technology (IC), the mmW / sub-THz band is at the forefront of sensing and imaging. At CSEM, the M3TERA [1] and TeraExplore [2] projects address the subject of THz sensing. They share a common objective: to develop heterogeneous integration platforms that enable manufacturing of compact, reliable and advanced-performance mmW and THz systems at reasonably low cost. Possible applications of the M3TERA and TeraExplore platforms include:

- Food safety – remote sensing of impurities in dry food: metal, plastic, glass
- Health / security – stress sensing via skin reflectance, remote sensing of respiration and heart rate
- Industrial – radar for level measurements
- 3D imaging

The focus of the discussion that follows is on the design and implementation of low-cost antennas implemented using 3D printing technology for the M3TERA and TeraExplore platforms.

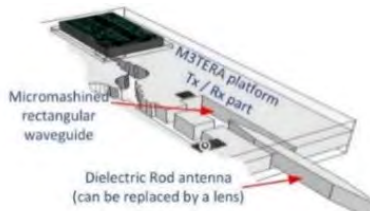


Figure 1: General drawing of the M3TERA miniature platform module.

A conceptual illustration of the miniature M3TERA platform is provided by Figure 1 (telecom and sensing applications). The M3TERA sensing prototype is focused on operation in the 122-123 GHz ISM band. The sensor relies on the use of either FMCW radar or RF signal reflectance techniques. In order to help meet the M3TERA target of miniature, low-cost solutions, and improve the manufacturability of the antennas, while maintaining acceptable performance, printed plastic (dielectric) antennas have been designed and developed (Figure 2). The size of the antenna is nominally around 8λ and the gain is about 20 dBi. The antenna is well matched to the target 122-123 GHz band, as well as to the 145 GHz M3TERA telecom band. New antennas, designed to meet the needs of

different applications (gain, directivity, frequency of operation) can be rapidly prototyped. In the future, such antennas are envisioned for use as part of a versatile RF sensing platform, where the antennas may be readily removed and changed for another suited the application in a manner analogous to the changing of the "head" on a probe, and where the sensing technique may be also be adapted and optimized as required for the application (as well as to control the antenna beam) via real-time algorithms running on a software defined radio (SDR).

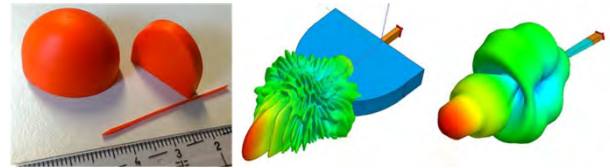


Figure 2: Prototyped 3D plastic antennas (left) and corresponding HFSS computational models with theoretical radiation patterns (right).

The TeraExplore active multi-color imaging THz detector operates in the 0.3 THz–0.5 THz frequency range and is used for inspection of composite materials and solar cells. The THz detector to be developed is based on the "direct detection method", i.e. it consists of a UWB antenna and a CMOS based RF receiver. An UWB antenna (0.3 THz–0.5 THz) is being prototyped at CSEM with resolution of about 80 μm (Figure 3). The antenna will be co-integrated with the IC to meet system requirements.



Figure 3: Helix antenna (from left to right): antenna model, realized 3D solution with helix inside and helix wire outside (TeraExplore project).

In summary, low-cost 3D printing technology is able to fulfil the needs of the RF sensing applications in the mmw / sub-THz frequency band. Through the use of 3D printing technology, we can rapidly prototype different, miniature, plastic antenna heads (e.g. lens antenna for an industrial application). The prototyped antenna "heads" can be readily attached to the test platform boards, providing the required radiation pattern needed in support of tailoring and optimization of the performance of the RF sensor to the target application.

[1] M3TERA (EU project under GA No 644039) www.m3tera.eu

[2] E. Le Roux, *et al.*, "TeraXplore—Single Detector for Multi color Terahertz (THz) Imaging", in this report, page 20.

WiseSkin for the Restoration of Natural Sense of Touch

E. Daskalaki, J. R. Farserotu, J.-D. Decotignie, D. C. Rojas Quiros, V. Kopta

Today, there is no solution for the restoration of a natural sense of touch to persons using prosthetic limbs. WiseSkin combines ultra-low power (ULP) wireless sensor networks, smart materials and sensory feedback to develop sensing skin that can be attached to artificial limbs. The solution has a high potential impact in the field of hand and arm prostheses, as well as rehabilitation of nerve injuries, stroke recovery and in the field of cognitive neuroscience. WiseSkin technology also has industrial applications in the domains of robotics (tactile robots), health and safety (e.g. Smart Gloves).

As the population of the world continues to grow and age, the number of people suffering amputations is expected to increase, placing a strong demand for solutions to improve their quality of life. The target of the WiseSkin project is to provide a non-invasive, ULP and scalable solution for the restoration of natural sense of touch to persons who have lost a limb and are using prosthetics [1].

The first functional WiseSkin prototype (prototype 1) has been developed and tested. The core elements of the system are:

- A miniature sensor-communication module (SCM) integrating an ST-Microelectronics pressure sensor, an IcyTRx radio [2] and a Planar Inverted-F Antenna matched at 2.45 GHz. Wireless communication is based on the Bluetooth Low Energy (BTLE) protocol. The SCM size is 12×17×1.73 mm³.
- A flexible and stretchable silicone scaffold substrate in which the SCMs are integrated to form the sensing artificial skin. The substrate is encapsulated on both sides with a thin and flexible metallized foil in order to provide power and shielding to the SCMs and additionally to function as a waveguide for data propagation (Figure 1).
- A non-invasive sensory feedback based on the stimulation of the patient's phantom map achieved through a vibro-electro-tactile actuation display attached to the patient's residual limb

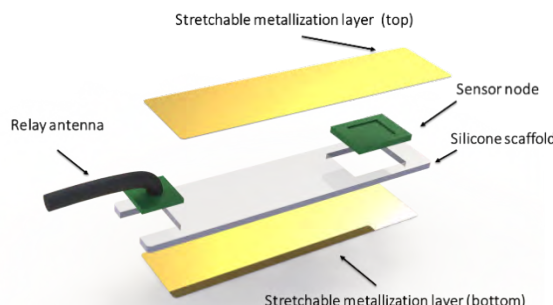


Figure 1: 3D rendering of WiseSkin prototype 1.

For the purposes of the WiseSkin prototype 1, five SCMs (one per fingertip) have been integrated in the silicone substrate, which covers the palm of the MyoHand prosthesis (Figure 2). The test configuration and communication flow are illustrated by Figure 3.

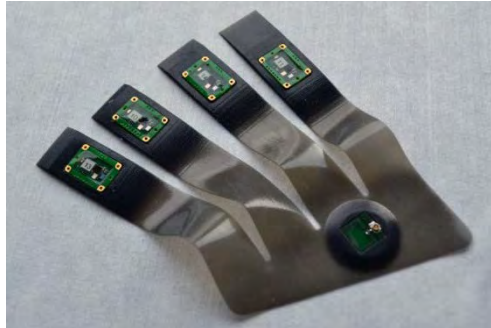


Figure 2: WiseSkin with sensor nodes integrated into the substrate.



Figure 3: WiseSkin prototype 1 test configuration.

The "skin" is nominally 2-3 mm thick, including the sensor nodes, but it is thinned down to 0.3 mm in regions without sensor nodes in order to improve the mechanical flexibility (i.e. where the fingers bend). The metallic layers are overlayed on the scaffold and connected to a 3V DC power supply (in the future, the power supply of the myoelectric prosthesis would be utilized).

The sensor data propagates between the metallization layers to a relay antenna on the palm and then to an iPad. The iPad functions as the master node to which the SCMs are connected via BTLE in a star topology. The sensor data is then transmitted via WiFi from the iPad to a PC, which drives the tactile feedback display attached to the patient's residual arm. In the future, it is envisioned to replace the antenna relay node by a bridge-gateway that is integrated into the skin, and the skin depicted in Figure 2 would be replaced by a new soft skin designed by EPFL with integrated metalization layer.

WiseSkin is a Swiss nano-teria funded project carried out by CSEM, EPFL and BFH. CSEM would like to thank all of the involved parties for their support. The first tests with real patients were performed in April-May 2016. Testing is ongoing and the building blocks for prototype 2 are in development.

[1] J. R. Farserotu, C. Anfolk, J.-D. Decotignie, D. C. Rojas Quiros, V. Kopta, "WiseSkin for tactile prosthetics", CSEM Scientific and Technical Report (2014) 135.

[2] V. Peiris, M. Kucera, N. Scolari, A. Vouilloz, E. Le Roux, "An ultra-low power bluetooth smart integrated solution", CSEM Scientific and Technical Report (2012) 97.

REP—Making Self-healing Wireless Networks Efficient

D. C. Rojas Quiros, D. Piguet, J.-D. Decotignie

Wireless Sensor Networks are a keystone of the Internet-of-Things. In order to recover from environmental disturbances and provide high reliability in multi-hop data collection applications, networks require adaptive routing (self-healing). However, the implementation of adaptive routing imposes a cost in terms of energy and traffic overhead and can result in packet losses while the network recovers. CSEM's answer to this challenge is REP, a method to significantly improve the speed and reduce the overhead required to implement self-healing. REP can also improve the performance of mobile networks, indoor localization and Radio Tomographic Imaging, among other fields of application.

Wireless sensor networks (WSNs) promise an Internet of Things with thousands of reliably connected low cost devices that can operate autonomously for years. However, real life deployments have shown that WSNs are subject to multiple perturbations (such as road traffic, weather, hardware malfunctions, etc.) that, if not handled correctly, can adversely impact their reliability and battery-life.

The state-of-the-art solution today is a protocol stack that combines a low-power listening medium access control (LPL-MAC) with a routing protocol. The LPL-MAC duty cycles the radio to prolong the battery-life, while the routing protocol autonomously repairs (self-heals) the topology. For example, Contiki OS (a dominant operating system for WSNs) has two default stacks that follow the previous scheme: RPL (a routing protocol proposed by the IETF) + ContikiMAC and Contiki-Collect (another routing protocol) + ContikiMAC.

Each self-healing procedure requires sending packet probes in order to estimate the quality of the neighboring links (Link Estimation, LE) and to evaluate alternative routes. This process presents a significant energy and traffic overhead. Moreover, a lengthy recovery impacts the reliability of the network, since the nodes might not have valid routes to convey the data until the healing is completed. These factors limit the application and effectiveness of network self-healing techniques by forcing protocol designers to reserve it only for disruptions deemed as critical.

At CSEM, we created REP, a novel mechanism that leverages LPL-MACs in order to significantly improve the utility of self-healing networks. REP does so by reducing the energy consumption and the traffic overhead associated with self-healing, making self-healing a more attractive solution for reducing packet losses in networks.

Operating principle

REP performs LE by exploiting a common resource in LPL-MACs: the packet repetitions used to wake up neighboring nodes during a transmission [1]. LPL-MACs achieve high-energy efficiency in the presence of low-traffic volume by keeping the radios in sleep mode, but require a transmitting node to send the same packet several times (i.e. the repetitions) in order to wake up the neighbors.

LE is a ubiquitous primitive in WSNs and typically requires broadcasting multiple beacons. Each beacon sent by the

routing layer necessitates the transmission of multiple repetitions of the same packet in the LPL-MAC (Figure 1 - Top). With REP, it is possible to send a single broadcast packet, but to overhear several repetitions, enabling us to extract the required LE information (Figure 1 - Bottom).

Results

An evaluation of REP was performed in a real WSN deployment. The evaluation system consisted of 10 TelosB nodes with ContikiMAC and ContikiOS (v. 2.7) arranged in a star topology, where a single node (N2, center of the star) broadcasted beacons and 9 other nodes independently estimated the quality of the link (N1 in Figure 1) [2]. The results show that the use of REP consistently reduces the overhead to perform a LE by two orders of magnitude (from 80 beacons to 1 beacon), while keeping an equivalent accuracy.

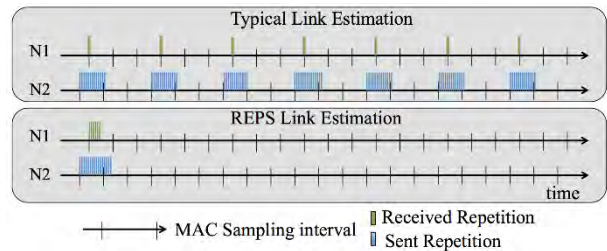


Figure 1: Typical LE schemes listen to 1 repetition per beacon, thus requiring multiple beacons in order to obtain several samples (top). REP overhears multiple repetitions enabling it to perform LE with a single beacon (bottom).

Application domains

Due to its ability to extend the battery-life, enable a more efficient use of the available bandwidth (less overhead) and reduce packet losses in the presence of channel perturbations, REP is convenient for large-scale deployments in general environments with hundreds of nodes, which may be difficult or expensive to access. Potential applications include environmental, industrial and infrastructure monitoring, as well as, home automation and body area networks.

The fast LE enabled by REP can also be exploited to improve the reliability of mobile networks by quickly adapting the topology to the displacement of the nodes. Moreover, REP increases the rate of information acquisition, which can improve the accuracy of radio tomographic imaging and indoor localization, among other applications.

[1] D. C. Rojas Quiros, D. Piguet, J.-D. Decotignie, "Poster: Single packet link estimation", EWSN Int. Conference on Embedded Wireless Systems and Networks (2016).

[2] D. C. Rojas Quiros, J.-D. Decotignie, "Poster abstract: Enabling a new resource for WSN radio tomographic imaging: LQI in transitional links", ACM SenSys Conference on Embedded Networked Sensor Systems (2016).

Publish-Subscribe Communication for Swarms of Unmanned Vehicles

P. Dallemande, D. Piguet, J.-D. Decotignie

CSEM has combined Publish-Subscribe communication, filtering techniques and time constraints in an ultra-low power wireless embedded platform to reduce data traffic and power consumption. This platform will be used in the context of swarms of unmanned flying vehicles.

The Publish-Subscribe communication model (P/S) is a powerful and power-efficient concept that allows for data-centric exchanges in an uncoordinated network of nodes. It is particularly well suited for the data communication across swarms of mobile unmanned vehicles (UxV). In the RAWFIE EC project [1], CSEM and other partners are using this concept for several purposes and in different environments (e.g. Apache Kafka over Internet protocols). CSEM is developing a "Proximity" component that provides P/S mechanisms in low-power, low-resource controllers present on UxVs participating to large-scale experiments.

The Proximity component aims at discovering the identity of neighboring UxV nodes in real-time and to possibly interact with them, without depending on any other external middleware, infrastructure or equipment. Each UxV uses the P/S services to exchange data that feeds its flight coordination controller, such as the identification of other UxV, speed, estimates of relative distances, perceived neighborhood (notification of UxV appearance and disappearance), status of the internal components of the UxV and, finally, sensor readings. It bears similarities to the transponders used on commercial airplanes.

The Proximity component is based on a dedicated, low-power, radio communication platform running the "Head" element of the Proximity component (Figure 1), which implements the P/S protocols and services as well as the interface with the other vehicle components. The "Delegate" element implements the interface running on the vehicle controller.

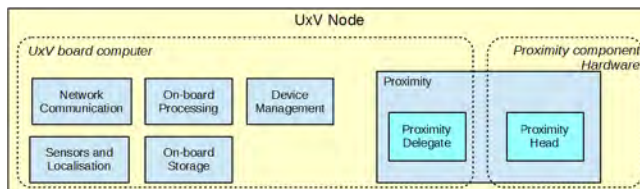


Figure 1: the RAWFIE UxV Node architecture including the Proximity component.

The Proximity component abstracts the mechanisms needed to store the acquired data waiting for subsequent transmission, either as a whole, or in parts. The Delegate allows the UxV to publish some of its attributes, which may be of interest for the other UxVs, such as identifier, status, etc. The Head transmits the corresponding data using the dedicated radio interface. Typically, the Delegate allows the UxV software for subscribing to Proximity component topics published by other UxVs. The Head forwards data received from the dedicated radio interface to the Delegate.

[1] The RAWFIE project is partly funded by the European Commission (FIRE+ challenge, Horizon 2020) under Contract Number 645220.

In order to reduce the traffic, the P/S services support filters on both content and context, as proposed in CCBR [2]. Filters on content data enable the publication of data only when the values are within a range of interest. Context filters are applied on some system properties for a fine selection of which UxVs can respond to a subscription. For instance, a content and context based subscription can request UxVs of type "aerial" to publish their battery level if it is below 20%. The way that content and context are filtered and the parties involved in that process are keys to the optimization of the P/S protocol.

The portion of the transmitted data that is not received by any legitimate subscriber, the protocol headers and the control messages, constitute the overhead. The Proximity component carries the filters in specific subscription messages, performs filtering primarily at the source on the out-going traffic to reduce bandwidth usage and energy consumption, and supports incoming traffic filtering in order to handle publications made from merged filters at the source.

The content and context filters proposed by CCBR are versatile enough for many applications because they allow subscriptions to specify the kind of data and source nodes as well as provide some in-network calculation that help reducing the amount of data carried. To further reduce the traffic, CSEM added the mechanisms for taking into account timing attributes, such as subscription validity (aka. lease time) and information life-time. Subscriptions include, for example, data validity and delivery timing information, so that data that has expired before reaching the destination can be discarded.

Combined with the ultra-low power communication protocol WiseMAC, the solution enables operation for days even after a UxV's main battery is depleted. It offers convenient bricks for increasing the safety of the RAWFIE elements and their environment by providing increased autonomy and a better means for reaction to single and multiple UxVs (e.g. collision avoidance). Typically, the UxVs communicate with the RAWFIE system through a primary communication interface, which the Proximity component can replace in case of failure, for transferring data and notifying the RAWFIE managers about the situation and the location of the UxV (useful e.g. for finding a UxV when it is lost). Further, the Proximity component can be used to relay topics published by UxVs, which are disconnected from the primary network, as well as, to gather data stored by sensors deployed on the ground, or in the water.

[2] G. Cugola, M. Migliavacca, "A context and content-based routing protocol for mobile sensor networks", Proc. EWSN European Conference Wireless Sensor Networks (2009) 69.

Autonomous Sensor Network for Smart Street Lighting

C. Hennemann, A. Restrepo Zea, P. Dallemande

CSEM has developed the Illumaction platform, a smart, autonomous and wirelessly networked platform for smart lighting applications. This platform forms the core of the demonstrator of an autonomous cooperative public-private lighting system, particularly well-suited to deal with complex urban environments.

Automatic light management in smart cities, or "smart lighting", is one of the most popular applications with respect to urban automation. Wireless communication, robustness, reactivity, and autonomy are key features of these applications, in particular for the sensors that are distributed in the surrounding environment to detect the various events. Partnering with the City of Neuchâtel, CSEM has developed a platform, based on the WiseMAC protocol, for interconnecting many such sensors and nodes dedicated to the control of the public and the private lighting elements in a wireless, robust, reactive, and autonomous network.

Artificial lighting is important for security, safety, comfort, etc. at night and may be during the day as well. Public and private lighting (e.g. commercial displays) are sometimes redundant. Usually, they are operated independently, which prevents them from cooperating. By fitting networked sensors (able to detect and report events and conditions) and bulb controllers into the lighting systems, it is possible to foster such cooperation, thus providing a better service, preserving security, safety and comfort. Although minimal in financial terms, energy savings are real and represent a great example and motivation to the public. As an added benefit, companion functions can be provided, such as energy metering, bulb failure detection, temperature and noise monitoring, crowd and traffic management, etc.

CSEM has developed in the past a number of smart wireless autonomous platforms (under the generic term of WiseNET) and devices, which are now used in various application domains, such as environmental monitoring, structural health monitoring, condition monitoring, home automation, health care, transportation, safety, etc. and more generally in the Internet of Things. WiseNET uses WiseMAC, which is one of the most power efficient wireless communication protocols, while offering mesh networking, self-healing, security and low end-to-end delays. WiseNET can operate in various environments, including, indoor, outdoor, urban or rural areas. In addition, it offers robustness with respect to partial communication failures or wireless link degradation by establishing alternative data transmission routes.

WiseNET forms the basis for the Illumaction system, which measures the light intensity and motion at several geographical points and sends the data to the local bulb controller, which embeds the logic for adjusting its intensity. As such, the system autonomously controls the lighting elements in complete autonomy (blue boxes shown on Figure 1). The mesh capability of the network allows for fully scalable collaboration over areas of any size, by conveying sensor data to any point in the network (Figure 1 shows one communication configuration, which can change over time). This allows, for example, for the extension of the lighted area around a person by involving remote bulbs, thus improving his/her comfort, security and safety.

The sensor data can optionally be reported to the central management process through an internet gateway (pink box shown on Figure 1), extending the system, e.g. to the entire city.

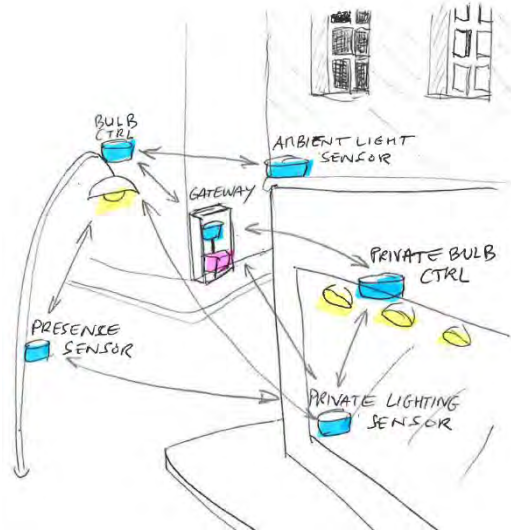


Figure 1: Example of CSEM smart lighting deployment.

The Illumaction demonstrator shown in Figure 2 is made of a bulb controller driving a LED panel through a 0-10 V D/A dimming interface (top right), an ambient light sensor (bottom right), and a relay between the sensor and the controller (middle right).



Figure 2: Example of CSEM smart lighting deployment.

The demonstration has proven the autonomous behavior of the system and its performance in terms of reliability and reactivity. The control loop, triggered by an induced change of the ambient light, followed by the transmission and the processing of the sensor value, ending with the modification of the D/A output takes less than a second. The power consumption of the sensors and the relays allows for several years of operations on a set of AA batteries. The mains power supply powers the LED panel and the bulb controller.

Secure Wireless Link for Ultra-low Power Wireless Sensor Networks

C. Kassapoglou Faist

CSEM provides solutions for secure communication in wireless sensor networks, addressing data protection (authentication, encryption, freshness, and confidentiality), entity authentication and key management. Implementations can be tailored to the needs of the application, to support various standards (IEEE 805.15.4 and 805.15.6, Bluetooth LE) and to run on a variety of embedded platforms.

As ultra-low power (ULP) smart wireless devices are becoming ubiquitous, the security of wireless communication links becomes vital. However, the wireless medium is open to anyone – or anything, making it easy to overhear and interfere with, thus requiring protective measures. In order to provide our customers with secure solutions, CSEM has been active in acquiring state-of-the-art know-how in wireless communication security for resource constrained devices and developing approaches to design adequate solutions, in particular in terms of key management. The solutions are tailored to the requirements of the application and cover the entire system lifecycle (installation, commissioning, replacement, etc.). The implementations run on various ULP embedded platforms and cover a variety of application domains ranging from environmental monitoring to safety in transportation.

The security services provided are: unilateral or mutual entity authentication for protection against man-in-the-middle (MITM) attacks; data authentication and integrity; confidentiality through end-to-end data encryption for privacy; data freshness, for protection against replay of old valid messages; access control and authorization. Most of these services rely on cryptography. As an example, Figure 1 shows CSEM's WiseMAC communication stack integrating security.

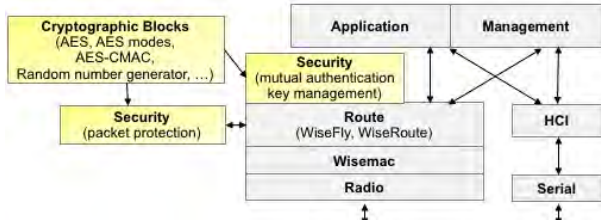


Figure 1: Security in WiseStack.

Due to limited resources (memory, computing power, energy consumption), the implementation of cryptography is based on symmetric cryptographic ciphers, which are less resource demanding. Specifically, we use the AES encryption algorithm (e.g. AES-128), which is a strong algorithm, with integrated hardware implementations available on a few platforms. AES is used for encryption (AES-CTR) and message authentication (AES-CBC) as well as in keyed hash functions involved in entity authentication and key agreement protocols (AES-CMAC), and in the incorporated strong random number generator [1].

The use of symmetric algorithms makes key establishment more complex and requires some form of initial trust. Using a network-wide key for all links in the network is not recommended, because of the lack of robustness in the event that a node is compromised. Instead, each node shares its own secret keys with the sink: a master key that is used exclusively

to derive session keys and the current time-limited session key used to protect the data. No other node is able to derive these keys. The session key is established using the master key and random data that the two parties exchange at session establishment, following a mutual authentication protocol. This approach may seem complex, but it is the best way to prevent key compromise: the master key is not exposed to attacks. Moreover, it provides a mechanism for session key refresh.

Distribution and management of the master keys depends on trust assumptions and configuration set-up. The difficulty is to install each master key on both the device and the sink (or base station) without a third party intercepting it. A simple solution is to have it installed on the node at the time of manufacturing and load it onto the sink manually. If the network set-up takes place in a controlled environment, the master key can be sent to the node by the sink over the air during an initialization phase where attacks are considered improbable. However, there are advantages in using a scheme where key distribution involves an operator device enabled with wired or close-range communication (serial, NFC): an out-of-band channel is available to load the key and proximity provides a guarantee on node identity. The operator device can either generate a master key for each node-sink pair (and later discard it) or read it on one device and copy it to the other. In case that the operator device is not trusted, the master key can be computed on each device based on a network-wide pre-programmed key (unknown to the operator) and on secret data loaded by the operator. As an alternative, a key transfer scheme can also be used: the two devices establish a temporary key during an authenticated pairing procedure - where, for example, they use the operator device to uniquely identify each other - and then have the master key transferred from one to the other, encrypted with the temporary key.

In addition to pairwise keys and in order to authenticate its broadcast messages, the sink can generate a group key and send it to each node individually, encrypted with the corresponding session key. Moreover, a mechanism allowing a node to establish pairwise keys with its neighbors in order to authenticate routing messages can also be provided.

CSEM has integrated security in small- and medium-size wireless sensor networks, in star or mesh topology. Platforms include a MSP430-CC1101 (AES hardware implementation), a MSP430-CC1125, as well as the in-house icyCOM SoC. Future work consists of proposing a Diffie-Hellman exchange based on elliptic curve cryptography, enabling the derivation of a secret key (the master key) over an authenticated channel without requiring a prior shared secret (but being more demanding on memory and computation resources).

[1] FIPS PUB 140-2, "Security requirements for cryptographic modules", (2001).

Long Range Low-power Localization

A. Restrepo Zea, M. Sénéclauze, J.-D. Decotignie

GPS has long been the reference for outdoor positioning; however, high power consumption and lengthy warm up time make it unsuitable for future low-power IoT applications. The advent of low power, Long Range (LoRa) localization technology, enabling relatively precise positioning of connected objects based on existing hardware, opens the door for future IoT applications, for example, in the domain of smart cities, facility management and supply chain, requiring low power outdoor positioning.

The introduction of a precise (<30 ns) time stamping of LoRa frames by Semtech opened the possibility of using a LoRaWAN infrastructure to permit the accurate localization of objects. Given the fact LoRa was developed for long-range and low-power IoT applications, this new feature is seen by some providers as a potential alternative to the energy-intensive GPS system.

The localization solver developed at CSEM as part of a CTI project with Semtech receives the data produced by the infrastructure (Localization data in Figure 1). This data is then used to generate a cloud of particles (intermediate potential positions) that is, in terms, used to generate a position [1].

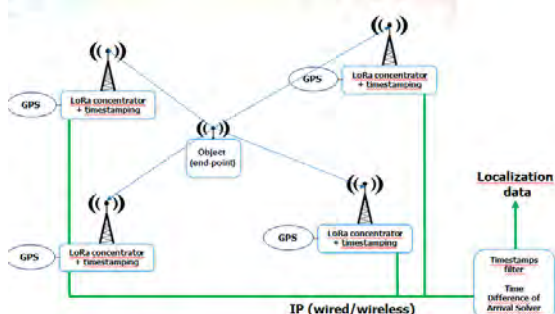


Figure 1: Typical LoRa infrastructure for localization.

Over the course of numerous measurement campaigns conducted both within the project (with Semtech) and outside the project (with potential customers), a large amount of data was collected and analyzed. This data enabled us to validate the algorithm as well as to assess its capabilities with respect to various use cases, ranging from open field to urban areas, with the aid of a set of custom tools that enable monitoring of the quality of the position estimation.

One tool, which is quite important for our solver, is called Variability of the Cumulated Distribution Function (VCDF). This function, depicted in Figure 2, allows for the representation of the performance of the algorithm used in terms of the error (i.e., cumulative error in % and error in meters). As particles are distributed and moved randomly, this graph illustrates the range of possible Cumulated Distribution Function calculated on different runs with the same data set.

The data from one of the measurement campaigns was selected in order to illustrate the algorithm. This data set is composed of about 100 measurements obtained from a single location in a typical urban area. The measurement setup is composed of 9 gateways spaced 800 m to 12 km apart (average >3 km). The gateways do not have antenna diversity and are communicating with a spreading factor of 12. The

positions of the gateways and the computed result are presented in Figure 3.

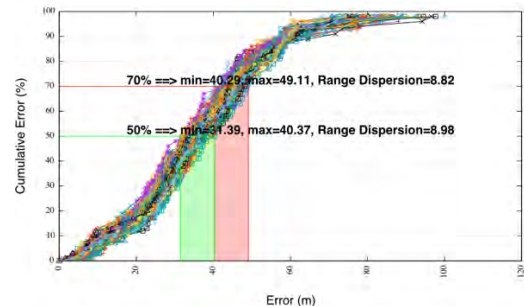


Figure 2: Variability of the cumulated distribution function.

Based on this setup and on the prior knowledge that the object was not moving, a set of estimated positions were computed using CSEM's solver. The solver was configured not to reinitialize its set of possible locations (belief) between each sequence sent by the object. The results show that the difference between the real position and the calculated position ranged from 30 m to 40 m 50 % of the time, and between 40 m and 50 m 70 % of the time (Figure 3). These results do not reach the accuracy that the GPS is able to achieve. However the goal of the project was not to compete in accuracy with the GPS, but to provide a solution that offers a good enough localization for some applications by benefitting from the regular communication with the object, thus without additional energy.

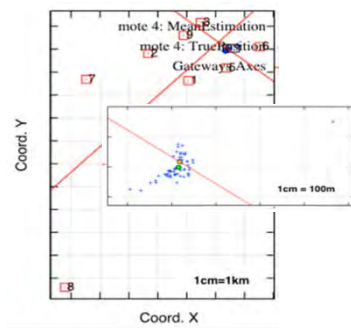


Figure 3: Geographic representation of the test site, CSEM IoTLoc, Mote position estimation (back figure), expanded view (insert).

The results presented above show that a reasonable accuracy can already be obtained without additional energy consumption in the context of communicating objects. The improvements yet to come in the time stamping and the solver, together with the lessons that will be learnt in big scale deployments to come will continue to improve the precision.

[1] A. Restrepo Zea, M. Sénéclauze, J.-D. Decotignie, "IoT objects localization based on time difference of arrival measurements", in this report, page 120.

IoT Objects Localization based on Time Difference of Arrival Measurements

A. Restrepo-Zea, M. Sénéclauze, J.-D. Decotignie

In the ecosystem of IoT applications, object localization and tracking play a predominant role. Although GPS is a possible solution to determine the position of “things”, its cost and power consumption are not compatible with most IoT applications. CSEM developed a GPS-free localization TDoA-based localization solver for IoT devices using long-range ultra-low power RF technology.

Over the past few years, CSEM has developed several localization solvers based on the radio Receive Signal Strength Indicator (RSSI), using both deterministic and probabilistic techniques. Experience has shown that probabilistic techniques, such as Particle Filtering, provide more accurate and robust location estimation than deterministic techniques.

Using RSSI is a very attractive because it does not require additional hardware components and (almost) all radios can measure the signal strength power of received packets. However, the RSSI distribution is not always symmetric and identical at all locations, it is also dominated by reflections and other sources of noise and it is sensitive to the relative orientation of the transmitting and receiving antennas. Additionally, for the same transmission conditions (transmission power, position and others), the RSSI measured on radios from various suppliers can be substantially different.

By comparison, when clock synchronization and time resolution/granularity are not a problem, time-based approaches, such as Time-of-Arrival (ToA) and Time-Difference-of-Arrival (TDoA), offer alternatives to RSSI techniques. Although sensitive to Non-Line-of-Sight (NLoS) conditions, these approaches have been shown to outperform RSSI techniques. TDoA only requires clock synchronization between anchors. This consideration, coupled with the availability of suitable radio technology for precisely determining the arrival times of the radio signals, drove the selection of a TDoA approach for the localization solver.

The basic idea behind the TDoA approach is to measure the arrival time of a signal transmitted by a target node. The difference of arrival times is calculated for each pair of anchor nodes and converted to a distance difference (Δ Distance). This Δ Distance together with the known positions of each pair of anchor nodes (behaving as foci), form a set of hyperbolas. Under ideal conditions, the intersection of the different hyperbolas yields the position of the target node.

The Particle Filtering algorithm implemented at CSEM is a particular case of Sequential Bayesian technique using a Monte-Carlo approach. The main objective is to determine the probability density function $p(x|z_0 \dots z_t)$ which means “What is the probability of being at position x at time t , given all previous measurements z , for all possible positions x ”. This probability density function is known as the *Belief* and it is represented by a set of N samples (particles). Each particle contains the coordinates of a possible position of the target node, and a weight which defines how near or far the position of the particle is from the position of the target node, given the TDoA measurements at time t . Particle Filtering is composed of 4 phases: Prediction, Updating, Resampling and Estimation.

At the beginning of the localization process, for the first execution of the *Prediction* phase, the particles are placed randomly in the deployment area. To accelerate the process of convergence, the particles are placed on points of higher

probability (i.e. on points over the locus of the nearest branch on the hyperbolas built based on the first measured TDoA/ Δ Distances; see Figure 1). In subsequent iterations, the particles are randomly moved from their previous positions to new positions, following a predefined model. Then, in the second (*Updating*) phase, the degree of validity of the predicted positions of the particles are determined based on the new TDoA measurements received for the signals transmitted by the target node. The hyperbola formed by each particle and each pair of anchor nodes is compared with those formed by the measured Δ Distances and each pair of anchor nodes and, depending on the similarity (or dissimilarity) a weight is assigned. The process is repeated, with the *Resampling* and *Estimation* phase, until convergence is achieved.

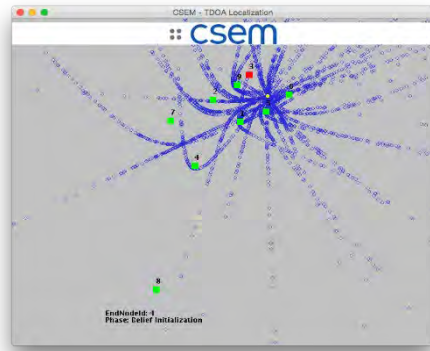


Figure 1: Particle initialization.

Figure 2 shows the Cumulative Distribution Function (CDF) obtained from a test in an urban environment using 9 anchor nodes spaced by 800 m to 12 km, and 4 static target nodes placed at different points. Each target node transmitted 60 beacons, one per second. 50 % of the beacons had a position estimation with an error less than 31.06 m and 70 % with an error less than 59.24 m. This reflects the propagation conditions and time stamp measurement variability. The results show that a good position estimation can be achieved using the Particle Filtering combined with TDoA measurements.

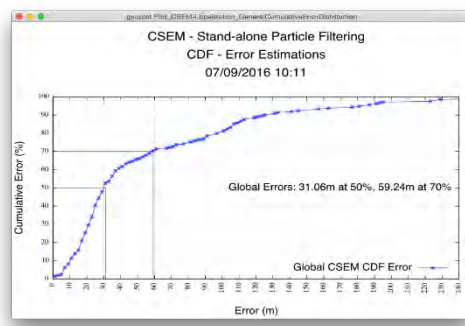


Figure 2: Cumulative error distribution.

Reactive Low-power Software Stack for BTLE Implementation

B. Perrin, A. Restrepo Zea

CSEM has combined its strengths in ultra-low power transceivers and optimized software protocol stacks to create one of the most power efficient Bluetooth Low Energy platforms. The slave protocol stack meets all of the BTLE timing constraints and is realized entirely in software. Updating to new versions of the protocol may then be performed by software updates without any need to redesign silicon.

CSEM has a long tradition of developing ultra-low power RF transceivers that are ahead of the competition in terms of their energy efficiency. The same applies to protocols. These two strengths have been combined to create a BTLE slave node that is entirely software upgradable. The platform complies with the Bluetooth Core Specification for a slave device. It can be upgraded to new versions of the standard via simple software updates.

Combined with the 2 Mbits/s analog front end, CSEM's IcyTRX-65 chip supports, among others, the Bluetooth LE and IEEE 802.15.4 (ZigBee) modulations. A customizable packet handler offers the ability to adapt the stack to support various protocols. The circuit also enables the platform to handle the hard BTLE timing constraint of the Inter Frame Space (TIFS), which must be precisely $150 \pm 2 \mu\text{s}$.

The transceiver is connected to a TI MSP430F5528 microcontroller on which the protocol stack operates. The developed stack includes all the BTLE slave features and functions: the link layer, L2CAP, GATT & GAP and a Security Manager for the "Just Works" scenario. This provides all of the necessary functionalities for a peripheral device to offer an easy interface to the most common smart phones and tablets.

Additionally, the software architecture is fully event-based, exploiting the rich pallet of interrupt sources generated by the transceiver. This results in a stack which is highly reactive while very power efficient. As an example, let us consider the case of advertising, which is likely to consume a large share of the energy budget in a typical sensor application. Figure 1 shows the current consumption during an advertising event. The microcontroller exchanges with the radio via SPI, captured by a logic analyzer, are superimposed in green on the picture.

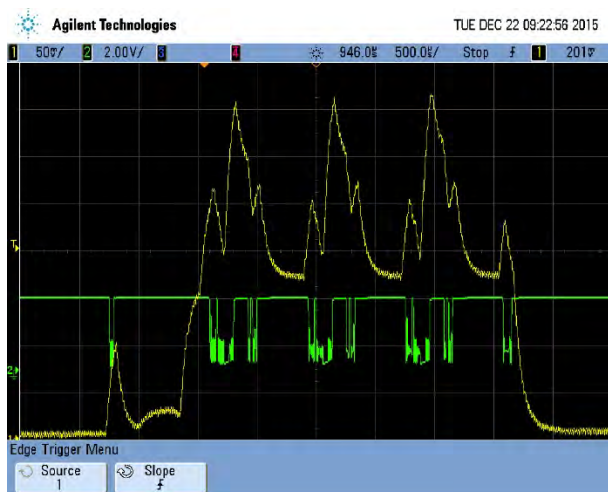


Figure 1: Advertisement current on the 3 channels.

The measurements reveal an energy consumption per advertisement of $28 \mu\text{J}$ on one channel and $65 \mu\text{J}$ on three channels. With an advertisement period of 100 ms, the average current is approximately $93 \mu\text{A}$ and $218 \mu\text{A}$ respectively (voltage over a 30Ω resistor serially connected).

A typical connection includes the discovery phase (0.8 s), the connection event (CE) and the transmission phase (in our example 20 bytes). Once the discovery has been completed, the average current is approximately $75 \mu\text{A}$ (empty PDU) and $90 \mu\text{A}$ (with the 20 byte payload) with a connection period of 100 ms. The energy cost of a CE is between 21 and $30 \mu\text{J}$. As such, the autonomy of the platform with a CR2032 battery (240 mA.h) is expected to be more than 1.5 years with an advertisement period of 1 second.

Our test board includes several sensors (accelerometer, magnetometer, barometers, temperature & humidity, etc.) and can be powered by a battery or an energy scavenging source. Its tiny size of 16 mm by 16 mm is suitable for applications where a small volume is required.



Figure 2: CSEM Memplant V2 test board.

The protocol software implementation provides for the coexistence, on the same processor, of the stack with the sensor application, measurement and pre-processing. This leads to an economy of silicon and space.

A such coexistence allows the application to be defined, designed and implemented so that it requests the use of resources only when needed. This enables further reduction in the overall power consumption.

The comparison with a TI CC2541 during a connection with a CE period of 1 s reveals a clear advantage: TI requires a consumption of $27 \mu\text{As}$ while the CSEM test board is around $18 \mu\text{As}$.

The results confirm that the optimized co-design approach followed by CSEM yields technical advantages and performance enhancements which ultimately translate into better products in various application domains, such as home automation, gaming, health, care, transportation, safety, etc.

Indoor Localization using IR-UWB

D. Barra

Ultra-wideband technology provides an excellent mean for wireless positioning due to its high resolution capability in the time domain. UWB is particularly well suited for localization indoors, where multipath environments make classical narrowband positioning unsuitable. Many commercial and industrial applications rely on positioning, such as retail, logistics and tool/robot/vehicle/people tracking, and could benefit from this technology.

The large bandwidth of ultra-wideband (UWB) radio (e.g. 500 MHz or more) offers high temporal and spatial resolution, which is beneficial for performance in strong multipath indoor propagation environments. More specifically, UWB enables centimeter accuracy in ranging. This feature is particularly interesting for many applications, from industrial (logistics, retail), consumer (home appliances), robotic, medical and sports (tool/vehicle/people tracking) to safety (access). When coupled with the Global Navigation System, UWB localization is seen as a means for augmenting the global navigation experience by enabling enhanced indoor accuracy.

Several techniques have been investigated in the past for indoor positioning, such as Wi-Fi-based or methods using received signal strength (RSS) and the "fusion" of inputs from multiple sensors. Recently, UWB has proven to be the most promising technique for improved indoor positioning, due to a combination of performance, affordable complexity and cost. During the last ISPN Localization Competition [1], 6 out of 10 of the winning localization technologies were based on UWB. Among them, the best were solely based on two-way time-of-flight (TWTOF) ranging and reached a 3D accuracy of 16 cm without calibration, whereas the best Wi-Fi based systems achieved not better than 1.2 m 2D accuracy with calibration.

CSEM has also been focused on TWTOF ranging with UWB for several years. This solution has been identified as offering the best trade-offs in terms of integration (small and low-power), cost and deployment (no calibration required). Other methods using angle-of-arrival (AOA) and time difference of arrival (TDOA) can also be used by TOF-based devices depending on the system and infrastructure requirements.

Recently, CSEM in cooperation with the startup 3db Access developed a highly integrated ASIC using Impulse Radio UWB (IR-UWB) for TWTOF ranging. The successful implementation of this circuit enabled the rapid development of a localization test setup. First experiments focused on 2D localization over a restricted indoor area as depicted in Figure 1 (top left).

For 2D localization, the minimum of three fixed UWB anchors were placed on the corners of a 2×4 m area on the floor (blue dots on the top right figure). Several points were accurately reported on a track representing a rectangle defined by the anchors (ground truth position, red crosses). TWTOF ranging measurements were taken between the unknown positions and the anchors. Trilateration using a least mean square (LMS) algorithm was used to extract positions (black dots). The latter points represent raw positions. For each of the 30 measured positions on the rectangular track, 10 ranging measurements

were performed with each of the three anchors. The median position is extracted out of these 10 positions. To improve LMS accuracy, the previous position has been used as first guess for the actual position.

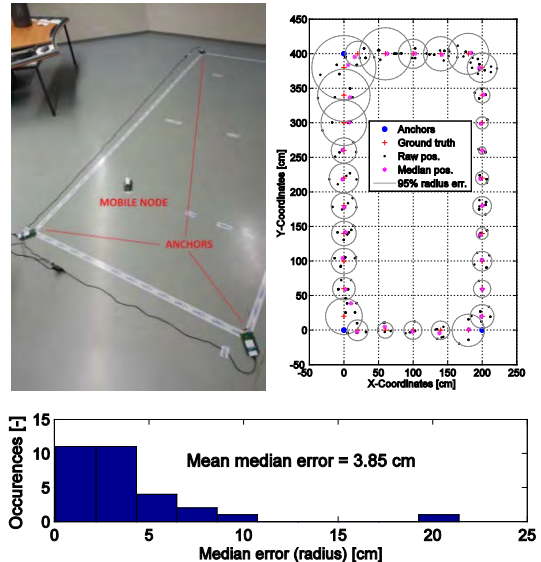


Figure 1: 2D indoor localization setup (left), raw results (right) and histogram of median position error for 10 measurements per position.

Results illustrated in the Figure 1 (top right) show non-optimum situations where the positions are close to anchors, the concrete wall and the floor. Individual measurements were found to have errors of up to 30 cm (grey circles); however, the median position (Figure 1, bottom histogram) over an average of 10 measurements displayed an outstanding performance, with a mean error of less than 4 cm, and a maximum error of 20 cm (due to first calculated position).

Initial experiments demonstrated the robustness and the accuracy of UWB for indoor localization. Future work will focus on three topics: 1) the addition of sensor information, such as accelerometers, gyros, RSS or GPS (sensor data fusion) in order to enhance accuracy; 2) the improvement of the localization using algorithms (such as Kalman or particle filter) and/or the diversity (channel frequency, antenna polarization); and 3) self-localization and self-configuration of the anchor nodes. The latter feature is particularly interesting with respect to the potential to reduce the complexity of network installation and therefore increase user acceptance, as manual measurements and configuration methods for obtaining anchor locations are tedious and error-prone. Deployment will be much easier using self-configuring methods where nodes cooperate with each other, estimate local distances to their neighbors, and converge to a consistent coordinate assignment.

[1] <https://www.microsoft.com/en-us/research/event/microsoft-indoor-localization-competition-ipsn-2016/>

Implementing Bluetooth Low-Energy 5 in icyTRX

N. Scolari

The Bluetooth Low-Energy 5 specification includes new features, notably a 2 Mbps mode and a Long-Range feature. The versatility of the icyTRX digital baseband, allowed us to implement the 2 Mbps mode without the need for changes. Implementation of the Long-Range feature required some modification of the baseband, but changes were minimized thanks to the modularity of icyTRX.

With the new Bluetooth 5 specification, the Bluetooth SIG intends to expand the number of use cases in which a Bluetooth radio can be deployed. In particular, the Low-Energy feature improves the data-rate and the range (distance). The first feature is realized by adding a 2 Mbps mode (the previous version of the Bluetooth Low-Energy (BTLE) supported only a 1 Mbps mode), while the second feature is implemented by adding a coding layer to the 1 Mbps mode. This coding layer enables us to keep the same analog radio front-end, and to add a simple coding/decoding layer to the digital baseband, extending the range. Two modes of operation are foreseen, one at 500 kbps and one at 125 kbps. Due to the convolutional codes, the gain in these modes is expected to be 4 dB and 12 dB respectively.

The icyTRX IP has a versatile digital baseband that already supports operation at a data rate of 1 Mbps, as well as other data-rates via different combinations of modulation and coding. Implementation of the BTLE 5 2 Mbps feature was straightforward: there was no need to modify the icyTRX radio, the analog or the digital parts.

As can be seen from Figure 1, bit-error rate (BER) sensitivity measurements performed at 2 Mbps demonstrate the excellent performance of icyTRX, which achieves a BER of 10⁻³ at about -95 dBm.

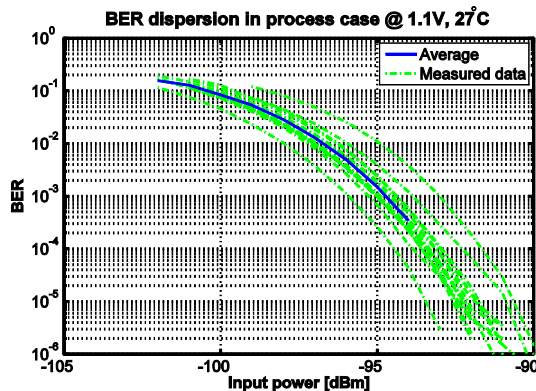


Figure 1: BER sensitivity at 2 Mbps measured over several samples.

The Long-Range feature is achieved by adding a coding layer to the 1 Mbps protocol. This coding layer is essentially composed of a rate 1/2 convolutional code combined with a coding pattern, similar to that of Manchester encoding. In the 500 kbps mode only the convolutional code is used, while the 125 kbps mode combines the two coding schemes. In either case, the access address of the packet is always coded at 125 kbps. Technically, both of these coding schemes were already implemented in icyTRX, so the change was straightforward and readily implemented.

On the other hand, this approach does not provide any major improvement in terms of sensitivity. In fact, the actual algorithms (e.g. the clock recovery algorithm) require a minimum SNR which is not compatible with the Long-Range feature. For this reason, it was necessary to implement

additional algorithms in the radio in order to assure the synchronization. These algorithms use the redundancy present in the preamble and the access address in order to add some processing gain and hence to be able to detect signals with a signal-to-noise ratio (SNR) lower than 0 dB. In particular, the Viterbi decoding algorithm for the access address requires a correct initialization, which can be achieved only by pre-synchronizing the demodulator with a rough access address detection. For these reasons, a series of correlators have been implemented in order to detect the different parts of a Bluetooth Long-Range packet.

Figure 2 shows some simulated results of this algorithm. The output of the first correlator looking for the access address of the packet is shown. Such algorithms improve the sensitivity of the radio; however, they can be very expensive in terms of gate count and thus power consumption. Nonetheless, the modular architecture of the icyTRX digital baseband enables us to readily add the additional blocks required to improve the sensitivity with a minimal effort.

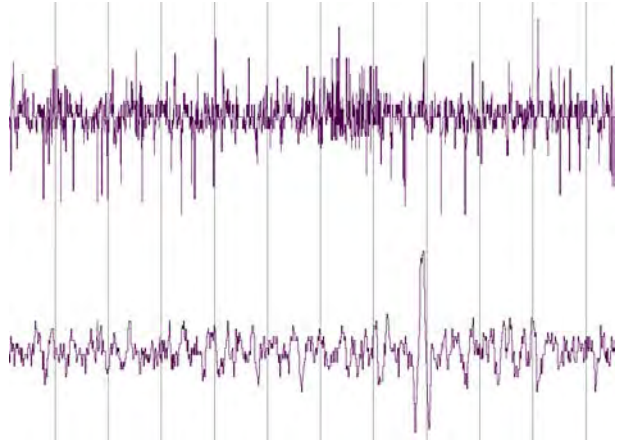


Figure 2: Simulation results of the correlation peaks obtained in the receiver: the first plot is the input signal, the second is the access address correlator output. The correlation peak is clearly visible.

The Long-Range feature has been tested on a setup composed by an icyTRX radio and an FPGA. In this configuration, the radio provides the output of the ADC to the FPGA, which performs the necessary demodulation steps. The preliminary results of this setup are promising; however a full silicon version is required to get rid of the limitations introduced by this setup.

The challenges introduced with the Bluetooth 5 specification have been easily met by the icyTRX platform, thanks to its flexible design.

Asynchronous Digital Design for Sub-threshold Regime Operation

S. Koumousi, M. Pons Solé, M.-N. Morgan, J.-L. Nagel, S. Emery

Reducing the supply voltage down to the sub-threshold regime allows a significant reduction of power consumption. However, synchronous sub-threshold designs are very sensitive to even small variations in process, voltage and temperature, which can either lead to incorrect functionality or degrade the performance due to huge design margins. On the other hand, asynchronous designs based on NULL Convention Logic (NCL) are self-timed designs that are insensitive to variations and thus require no design margins.

Asynchronous circuits can be classified into different categories depending on their degree of asynchronicity, from locally-synchronous to delay-insensitive. The latter category is extremely interesting for sub-threshold designs, which are very sensitive to both global and local variations, and also greatly simplifies design automation compared to other asynchronous approaches. However, designing delay-insensitive circuits usually comes at a cost, as they involve a large logic overhead e.g. due to completion detection.

In this work, NULL Convention Logic (NCL) was chosen among existing delay-insensitive asynchronous methodologies. Transforming a synchronous RTL design into its clockless NCL counterpart was done using UNCLE^[1], an academic set of scripts partly relying on conventional logic synthesizers to map synchronous RTL to a netlist of generic functions and, subsequently, into an NCL netlist. More information on the design flow can be found in^[2].

The TSMC 65 nm LP process was chosen for these experiments. An NCL sub-threshold standard cell library of 23 hysteresis state-holding gates was developed and used with UNCLE to generate an NCL-mapped netlist, which was subsequently placed-and-routed using standard tools. This step of the NCL flow required particular optimization, as an asynchronous design intrinsically contains many combinational loops when seen from a static timing engine, and prevent the tool from applying optimizations such as buffering and gate sizing. The focus was set on automatizing this loop breaking at specific locations and guaranteeing that all paths would get optimized. Finally, the netlist extracted from layout could be simulated at transistor level.

A 3-stage pipeline design was coded in synchronous RTL and used as a test case: the first stage consists of a 5-tap FIR filter; the second stage of a multiplication of the FIR output with an external control signal; the last stage of the addition of the upper and lower bits of the second stage output. The same functional verification was applied both to the synchronous RTL and to the NCL asynchronous transistor netlist to verify correct functionality of the layout.

The same RTL was physically implemented as a synchronous version (using an existing sub-threshold standard cell library) in order to compare the speed, power and sensitivity to variations of both synchronous and asynchronous versions.

Table 1 shows that the synchronous design was able to reach an operating frequency f_{CLK} of 81.3 kHz at 0.3 V in typical corner (TT), while the asynchronous design reaches 3x this

speed. The asynchronous speed degrades 30x in slow (SS) corner at -25°C, but improves 10x in fast corner (FF) at 75°C (the synchronous design is limited to 81.3 kHz for all corners in the absence of process sensing). However, the asynchronous NCL design typically has 1.7x the area of the synchronous version and, in nominal conditions (TT process corner, Vdd = 0.3 V, 25°C), the asynchronous version also exhibits 3x more energy consumption than its synchronous counterpart. Note that the asynchronous design functional validity was simulated down to 0.2 V.

Table 1: NCL vs. synchronous design performance.

Process corner	Temp	Voltage	Asynchronous		Synchronous	
			Average freq.	Power	Frequency	Power
SS	-25 C	0.3 V	6.25-8 kHz	4.15-4.33 nW	81.3 kHz	3-13 nW
TT	25 C	0.3 V	230-250 kHz	185-190 nW	81.3 kHz	20-38 nW
FF	75 C	0.3 V	2.38 MHz	3.8 uW	81.3 kHz	1.27-1.41 uW
Area			11.16 um ²			6.38 um ²

The asynchronous design automatically adapts to process, voltage and temperature variation and the computation delay is naturally data dependent. Table 2 summarizes the effect of operating condition variation on speed and power consumption with respect to nominal.

Table 2: Influence of operating conditions on speed and power.

Process corner	Temperature			Voltage			Data
	SS	TT	FF	-25C	25C	75C	0.2V 0.3V 1V
Frequency	-5x	1	5x	-5x	1	2.8x	-12x 1 100x ±18%
Power	-6x	1	6x	-4.9x	1	3.8x	-8.2x 1 1100x

Monte Carlo simulations at the worst case corner (SS, -25°C and 0.3 V) and at the maximal frequency of operation of 81.3 kHz showed that the synchronous design sometimes failed to operate correctly, whereas the NCL did not produce erroneous outputs. This demonstrates that additional costly design margins should be definitely added to the synchronous version to cope for the local variations and that they are not required for NCL design.

In conclusion, though the selected delay insensitive asynchronous design flow definitely proved to be robust to operating condition variations and to local mismatch, the logic overhead compared to a synchronous design mostly cancels the benefit of reducing design margins in terms of power consumption. Nevertheless this approach might still be interesting for systems running on very low-voltage and intermittent supplies (e.g. small solar cells), where a complex power management unit could be advantageously replaced by a self-timed, clockless digital approach.

[1] R. B. Reese, et al., "Uncle - An RTL approach to asynchronous design", Proc. ASYNC The Int. Symp. on Asynchronous Circuits and Systems (2012).

[2] S. Koumousi, "Asynchronous digital design for sub-vth operation", MSc thesis.

Sub-threshold Latch-based icyflex2 32-bit Processor with Wide Supply Range Operation

J.-L. Nagel, M. Pons Solé, T.-C. Le, C. Arm, D. Séverac, S. Emery

A 32-bit latch-based icyflex2 processor was integrated in EM Microelectronic Marin ALP CMOS 180 nm technology showing full functionality for supply voltage ranging from 0.37 V (i.e. subthreshold operation) to 1.8 V (i.e. super-threshold operation), over 5 process corners and for temperatures between -25 and 75°C. This possibility to maintain continuous full functionality by adapting the operation frequency and varying the supply voltage makes that design a perfect candidate for adaptive dynamic voltage frequency scaling (ADVFS).

The system micrograph is shown in Figure 1. It includes a latch-based 32-bit icyflex2 controller core [1], 2 kB of RAM, 8 kB of ROM, GPIO, JTAG, SPI and timer peripherals. It can either execute stand-alone functions from the ROM, or boot on an external non-volatile memory via SPI. On-chip debug is possible via JTAG interface.

A tailored standard cell library, as well as RAM and ROM memories were designed and optimized for subthreshold operation. The objective is to ensure a wide supply range operation (WSR), stretching from sub-threshold to super-threshold operation. High-threshold voltage (HVT) transistors were used to reduce leakage. The design was constrained for setup time at the minimum VDD of 0.54 V (corresponding to sub-threshold operation for the HVT transistors) in slow process and low temperature. The maximum VDD considered is 1.8 V. RAM and ROM memories were optimized to reach the same minimum VDD as standard cells to be able to use a single power domain. Optimized high-range level-shifters, allowing the up-conversion from sub-threshold to up to 3.3 V, were inserted in front of output pads of the JTAG and SPI peripherals.

The system performance was measured by running a software self-test (MBIST) of the RAM on the icyflex2 core, the code being stored in ROM. The March C algorithm was executed in around 37'000 cycles for the 2 kB of SRAM. The power consumption of this algorithm is relatively high, considering that the inner loop of the algorithm performs one ROM access, one RAM access and one arithmetic operation (add, sub, or) almost every cycle. The MBIST is also a comprehensive test for all system components as it tests the core as well as the RAM and ROM memories. The MBIST test was run for various temperatures, process corners and frequencies. The result of the MBIST (passed or failed test) is output on the GPIOs and was used to derive the maximum operating frequency.

Reducing the supply voltage logically leads to a reduction of the maximum operating frequency (see Figure 2). We computed the energy (per cycle) by normalizing the power by this maximum frequency. The Minimum Energy Point (MEP) corresponds to where the circuit operates at the highest energy efficiency (usually at a rather low operating frequency). For this circuit, MEP occurs below the threshold voltage, with energy per operation as low as 17.1 pJ/cycle at 19 kHz and 0.37 V. The energy per operation rises to 119.3 pJ/cycle at 1.1 V and 10 MHz, almost 7 times higher than at the MEP, demonstrating the clear advantage of sub-threshold operation in terms of energy as long as the system can cope with the reduced operating frequency.

The proposed icyflex2 processor's MEP was compared very favorably to other state-of art systems (see [2] detailed results).

We have demonstrated that combining latch-based design and sub-threshold allows a very wide supply range of operation. The next step will be to take advantage of these techniques in a fully adaptive system in order to automatically reach an optimal energy efficiency.

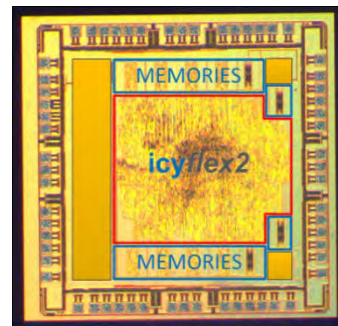


Figure 1: Die microphotograph of the subthreshold system.

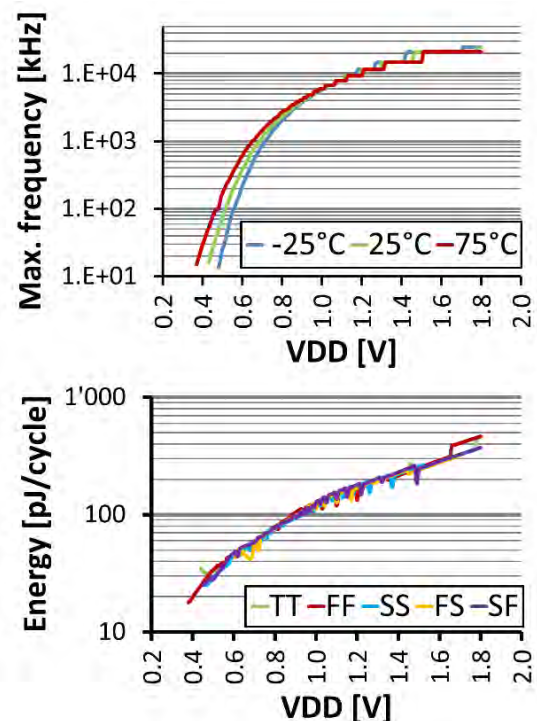


Figure 2: (top) Maximum operating frequency vs. supply voltage for a typical corner chip; (bottom) Energy per cycle measured at maximum operating frequency vs. supply voltage at 25°C for 5 process corners.

[1] J.-L. Nagel, et al., "The icyflex2 processor architecture", CSEM Scientific and Technical Report (2009).

[2] M. Pons Solé, et al., "Sub-threshold latch-based icyflex2 32-bit processor with wide supply range operation", ESSCIRC (2016).

Physical Unclonable Function (PUF) based on 0.18 um Sub-threshold SRAM

H.-R. Graf, M. Pons Solé, T.-C. Le, S. Emery

Physical unclonable functions (PUFs) have been proposed as central building blocks in a variety of cryptographic protocols and security architectures. In this study, the suitability to implement PUFs with existing sub-threshold 0.18 um SRAMs was evaluated. Operating PUFs in the sub-threshold region can enable adding security features in ultra-low power applications within a limited power budget.

Physical unclonable functions (PUFs) are increasingly proposed as central building blocks in cryptographic protocols and security architectures. Among other uses, PUFs enable device identification and authentication, binding software to hardware platforms and secure storage of cryptographic secrets.

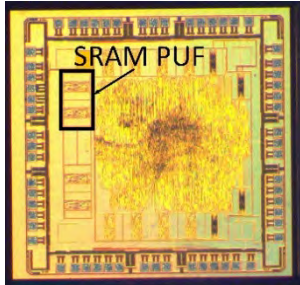


Figure 1: Chip photograph of sub-threshold 0.18 um SRAM PUF.

PUFs typically exhibit a challenge/response behavior: When queried with a challenge, the PUF generates an unpredictable but repeatable response that depends on the physical properties of the underlying PUF hardware. The most vital PUF properties are:

- Robustness
- Uniqueness
- Unpredictability

Robustness requires that, when queried with the same challenge multiple times, the PUF should generate similar responses that differ only by a small error that can be corrected by an appropriate error correction mechanism.

Uniqueness means that the responses for the same challenge on different PUF instances are uncorrelated, based on intrinsically unique and random physical variations of the implementing device.

Unpredictability guarantees that the adversary cannot efficiently compute the response of a PUF to an unknown challenge, even if he can adaptively obtain a certain number of other challenge/response pairs from the same and other PUF instances.

PUFs using intrinsic randomness of ASIC processes are highly attractive because they can be implemented with very small hardware costs, or even be built from existing hardware having the right properties. The most popular electronic PUF types are either delay-based (arbiter and ring oscillator PUFs) or memory-based (SRAM, flip-flop and latch PUFs).

For this study, the suitability of sub-threshold 0.18 um SRAM [1] (Figure 1) to implement PUFs was evaluated. Measurements on a total of 10 devices integrated in EM Microelectronic Marin ALP CMOS 180 nm technology with 2 SRAMs of 256 bytes each were conducted. At 17 different supply voltages (between 0.43 V to 1.2 V), the memory content after power-off-and-on cycles was read-out. The measurements were repeated 100 times for every challenge.

To evaluate robustness and uniqueness, the Hamming distance (in bits) was calculated and analyzed (Figure 2). Good robustness is shown with the intra Hamming distance of 0 bits at 70 % probability. The smooth Gaussian distribution of the inter Hamming distance indicates a good uniqueness as well by having 3-5 bits distance at a probability of 70 %. Further analysis shows that identification is possible and attests a good potential for unpredictability.

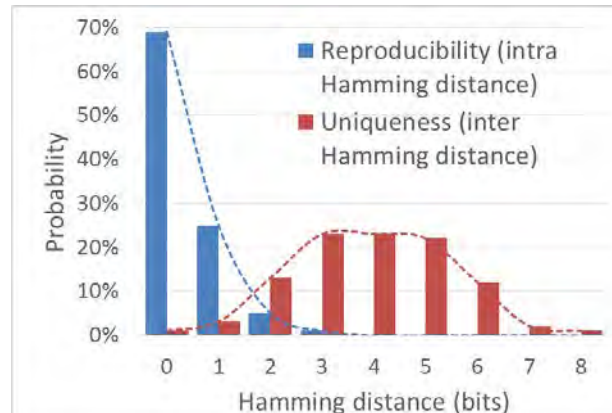


Figure 2: Robustness and uniqueness of SRAM based PUF.

For ultra-low power applications like IoT nodes, adding security features within the limited power budget is key. The presented sub-threshold SRAM PUF, that reaches static consumption in the order of a nW at 0.43 V, is therefore perfectly suitable for this kind of applications.

Next steps will require more measurements with more variations (e.g. impact of temperature and ageing), deeper analysis of the measurements and study of the entropy source (e.g. health check). With digital post-processing, the entropy could get improved. Finally, a system-level design would be required to implement the challenge-response behavior directly on the ASIC, not off-line as in this study.

This research has been funded by a CSEM Creativity Grant.

[1] M. Pons Solé, et al., "Sub-threshold latch-based icyflex2 32-bit processor with wide supply range operation", ESSCIRC (2016).

Library Design in a DDC Technology Optimized for Sub-threshold Regime

M. Pons Solé, J.-L. Nagel, P. Persechini, C. A. Salazar Gutierrez, D. Séverac, D. Ruffieux, S. Emery, K. Hashiba •, H. Kurata •

In collaboration with Mie Fujitsu Semiconductor Limited (MIFS), CSEM has designed a standard cell library using MIFS Deeply Depleted Channel (DDC) 55 nm technology operating at sub-threshold voltage. Lowering the circuit supply voltage reduces the power consumption, while body bias tuning guarantees minimum speed degradation and allows a drastic reduction of the spread of performance across the different corners.

DDC technology

DDC transistors use a standard bulk silicon structure with a few additional processing steps improving their performance (Figure 1). The main advantages are the reduction of the local variation of threshold voltage (V_{th}) of transistors and the improved control of V_{th} by body biasing techniques^[1]. Both features make the DDC transistor a perfect candidate for sub-threshold design where V_{th} variability implies a degradation and spread of performance that can reach up to 3 orders of magnitude when considering process, voltage and temperature variations (PVT).

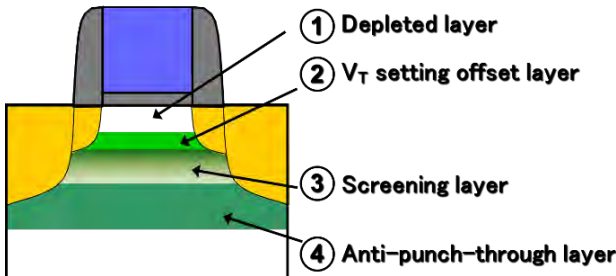


Figure 1: DDC transistor cross section layers.

Sub-threshold library with body bias control

A standard cell library optimized for 0.5 V operation was designed using DDC 55 nm Ultra-Low Leakage (ULL) transistors. The ULL option was chosen to reduce leakage (i.e. static consumption) in addition to achieving dynamic consumption reduction thanks to sub-threshold supply.

The library contains a reduced set of standard cells^[2], including power management cells (i.e. level shifters, power switches, isolation cells, always-on-buffers). Transistor sizing was optimized so that the effect of body bias control is maximized allowing to compensate the full range of PVT variations (e.g. slow corner at 0.45 V and -40°C can achieve the same speed performance as fast corner at 0.55 V and 125°C by tuning the bias). All transistors in the library were therefore designed with a unique width and length; the channel length was slightly increased as compared to a nominal voltage library and transistor fingers were used for different drive strengths.

An adaptive body bias control circuit generates P and N well bias voltages depending on PVT conditions and on a given circuit operation mode (e.g. fast, medium or slow modes). Alternatively, maximum reverse body bias (increasing V_{th} of transistors) can be applied in sleep mode to minimize leakage.

• Mie Fujitsu Semiconductor Limited

^[1] K. Fujita, et al., "Advanced channel engineering achieving aggressive reduction of VT variation for ultra-low-power applications", IEDM IEEE International Electron Devices Meeting (2011) 32.3.1.

Test vehicle circuit simulations

An 8 bit multiplier was used as a test vehicle for the standard cell library evaluation. The placed-and-routed layout was simulated at SPICE-level under different biases and PVT conditions. The simulation results are illustrated in Figure 2.

Performance at 0.9 V without bias control exhibits a spread of 3.2x and a maximum speed of the circuit of 74.5 MHz (the worst case determines the actual speed). At 0.5 V without bias control, the performance spread is 109x which results in unacceptable variation and also in very poor performance (0.7 MHz). Taking advantage of DDC bias control capability, the performance spread is reduced to 1.4x, 1.3x and 1.5x for fast, medium and slow modes (determined by the bias) respectively, which are smaller than the 3.2x spread observed at 0.9 V. At 0.5 V and fast mode, the maximum speed reaches 60.8 MHz, i.e. only 20 % less than the speed achieved at 0.9 V.

Regarding power consumption under typical conditions, the leakage power in sleep mode at 0.5 V is as little as 1.8 nW. Dynamic consumption is reduced by a factor of 3.4x (93.3 fJ/cycle versus 319.5 fJ/cycle) for 0.5 V in fast mode compared to 0.9 V operation.

Conclusion

Combining MIFS DDC technology and CSEM sub-threshold experience, we have developed a digital library allowing minimum degradation and spread of performance when operating at low supply voltage thanks to body bias control. Circuit consumption is also reduced by a factor better than 3x.

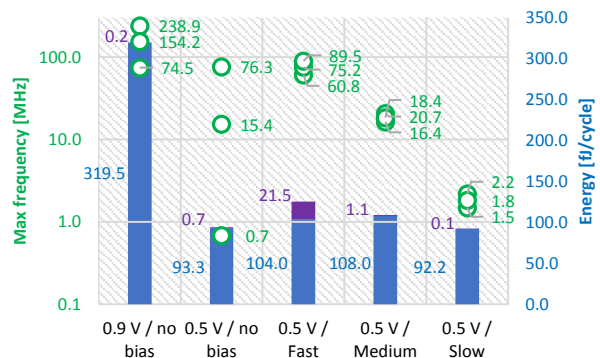


Figure 2: Multiplier maximum frequency and energy using sub-threshold DDC library. Best, typical and worst frequencies in the full range of PVT (green circles) show the performance spread. The bars indicate the dynamic (blue) and the static energy (violet).

^[2] M. Pons Solé, et al., "Ultra low power standard cell design using planar bulk CMOS in subthreshold operation," PATMOS International Workshop on Power and Timing Modeling, Optimization and Simulation (2013) 9.

Sensor Interface for a Resonator-type Mass Spectrometer

M. Augustyniak, J. Deng, C. Monneron, Y. Zha, P. Persechini, D. Schmid, P.-F. Ruedi

A highly sensitive sensor interface has been developed for application in ion mobility spectrometers or mass spectrometers based on ion oscillation, such as linear electrostatic ion traps, to sense the ions flying back and forth through ring electrodes. The detection principle has been validated with a discrete implementation, before the realization of a dedicated ASIC.

The electronic interface described here is an ion detector for a mass spectrometer, where focused ion bunches, accelerated to 4 kV, oscillate between two electrostatic mirrors. The oscillation frequency is mass-dependent: it is inversely proportional to the square root of molecular mass. For ion sensing, a metal, ring-formed sensing electrode is used. The ring electrode is electrically biased at a constant potential versus the system ground and is supposed not to disturb the trajectories of flying ions. Keeping the ring electrode at constant potential requires that, when charged particles pass through the ring, a mirror charge is induced electrostatically at the ring electrode. That charge is converted to voltage by an amplifier as a differential, continuous-time signal for off-chip analog-to-digital conversion. The gain of the sensor can be expressed in equivalent inverse capacitance, or in microvolt per electron. After analog to digital conversion, the data is post-processed to extract the information about ions flying through the ring electrode: peak amplitude corresponds to the amount of particles in each bunch and the frequency of the peaks is related to the molecular mass.

In a first step a discrete amplification chain embedded on a PCB has been used to test the principle under real conditions. Figure 1 shows measurement results where a bunch of Xe⁺ ions crosses two electrodes flying first in one direction (white trace first, then red) and then the same electrodes flying in the opposite direction (first red, than white).

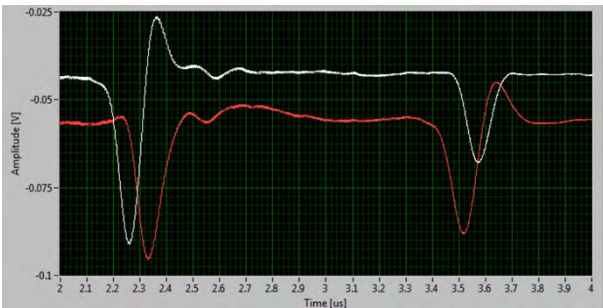


Figure 1: Measurements with a bunch of ions.

To further increase both sensitivity and bandwidth, a dedicated ASIC has been designed.

The most relevant parameters of the ASIC are: noise level, dynamic range and bandwidth. The noise floor limits the minimum number of particles that can be resolved. Since the detection noise – in terms of electron charges – is a product of the input-referred noise of the front-end amplifier by the input capacitance of the front-end amplifier, both have to be minimized for optimum performance. In order to minimize the input capacitance down to 900 fF, the ring electrode is directly manufactured on top of the ASIC through a special pad. The bandwidth of the detector needs to be large enough to correctly amplify even the shortest pulses of 1.3 ns duration, caused by highly-focused hydrogen ions.

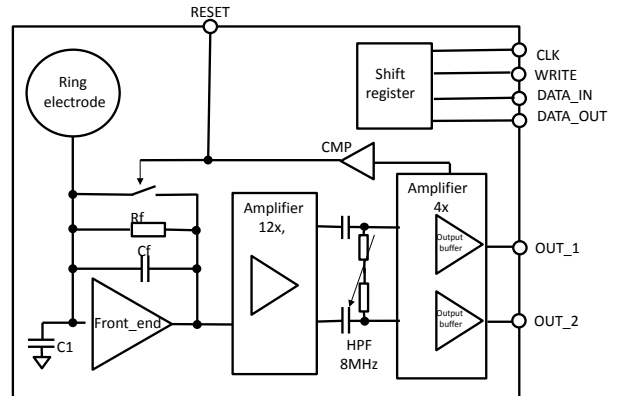


Figure 2: ASIC architecture.

Figure 2 presents the architecture of the ASIC. The first stage of the amplification channel is realized by the front-end amplifier, where the charge-to-voltage gain is determined by a feedback capacitor Cf. In parallel there is also a feedback resistor Rf to DC-bias the amplifier input. Since the effective gain of the whole ASIC is 29 μ V/e-, the remaining amplification and single-ended to differential conversion, is performed by a cascade of two amplifiers with a respective gain of 12x and 4x. Those amplifiers are separated by a high pass filter. The last stage is the output buffer designed to drive 50 Ohm / 20 pF output to the external analog to digital converter. The reset can be activated externally, or when the comparator CMP detects an output stack in case the ring electrode acquired too much charge because of a large ion bunch. The configuration of the sensor is controlled by a shift register.

Figure 3 shows the layout of the ASIC, realized in a 65 nm process. Area is 2.85 mm². Noise floor is 117 e- rms. The signal bandwidth spans from 8.5 MHz to 350 MHz.

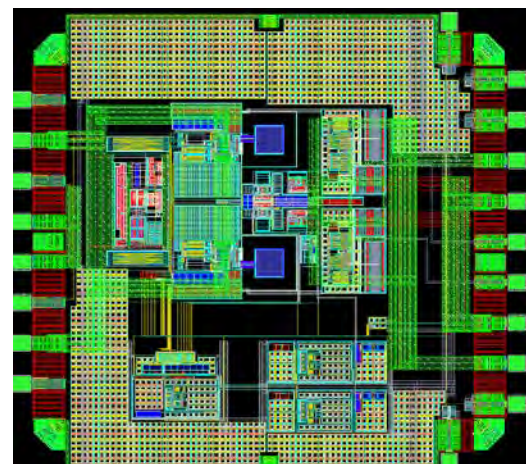


Figure 3: ASIC layout.

A Fully Integrated Adaptive Energy Harvesting System for Ultra-low Power Applications

J. Deng, Y. Zha, J.-L. Nagel, D. Ruffieux, P. Persechini, P.-F. Rüedi

The goal of this project is to implement a fully integrated platform with minimum external components for a PV cell energy harvester and a sub-threshold voltage microprocessor for ultra-low power applications. It can harvest the light energy in both indoor and outdoor environments with the input power ranging from μW to mW level with optimal efficiency.

Nowadays, for many systems, the power source is a bottleneck that limits the system lifetime and performance, adds manufacturing cost, and increases the system bulk and maintenance costs. A smart solution that could tackle this problem is using energy harvesting technology. To reduce system cost and volume it is desirable to integrate energy harvesting circuits with data acquisition, data processing, and communication circuits on the same chip for ultra-low power applications. This work focuses on a fully integrated photovoltaic (PV) energy harvester design optimized for both indoor and outdoor light intensity. As PV cells exhibit a strong non-linear electrical characteristic and must work in a variety of environments, they require the development of an adaptive solution to transfer the energy generated by the PV cells into a storage medium, such as a capacitor or a battery, while maintaining the working point of the cell around the optimal region (for which the transferred power is maximized) under changing illumination conditions. The design exhibits three main features:

- It minimizes the external components for cost-effectiveness and compactness
- It minimizes the power consumed by the power management unit (PMU) by using advanced nano-power circuits and a sub-threshold digital controller
- It maximizes the converting efficiency and automatically adapts to the environment changes for an optimized operation of the whole energy transfer path

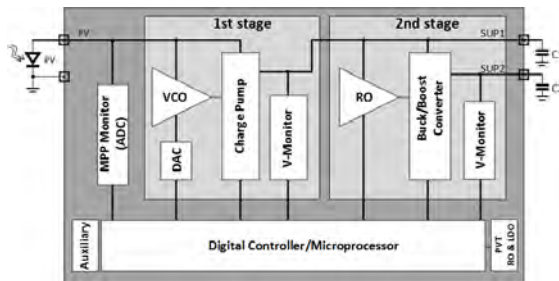


Figure 1: System block diagram.

The architecture of the system is illustrated in Figure 1. Only 2 external capacitors are needed. They act as the energy storage medium connected to the output of each DC-DC converter stage. The power converting efficiency is optimized for both the PV cell and the 2 stage DC-DC circuits (Efficiency simulation results are shown in Figure 2 and Figure 3 for 1st and 2nd stages, respectively). This is achieved by combining:

- A maximum power point tracker (MPPT) based on fractional open circuit voltage with self-adjustment to the input light and linearized PV cell voltage controlling algorithm

- A 2-stage switched-capacitor DC-DC converter with on-chip MIM capacitor placed on top of the digital core
- An advanced self-oscillating charge pump structure [1] for the 1st stage, working with PV cell voltages down to 0.35 V
- A combination of staircase and PWM control schemes for the DC-DC converter

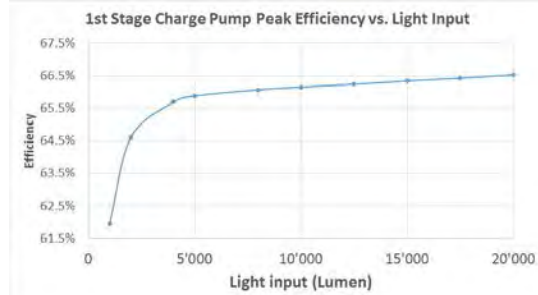


Figure 2: The simulated peak efficiency of the 1st stage as a function of illumination.

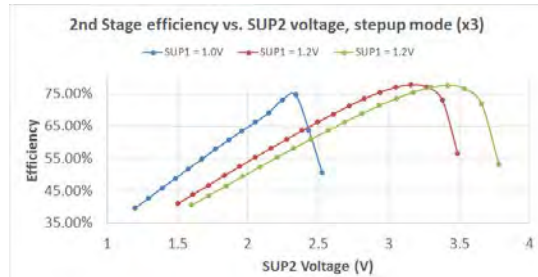


Figure 3: Simulated efficiency of the 2nd stage.

The energy transfer paths of the system with the voltage and peak efficiency is indicated in Figure 4.

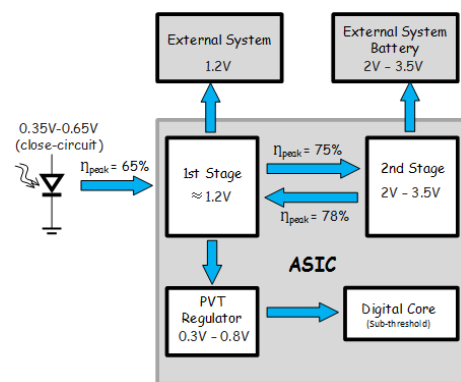


Figure 4: Energy conversion paths of the system.

[1] W. Jung, et al., "A 3 nW fully integrated energy harvester based on self-oscillating switched-capacitor DC-DC converter", ISSCC (2014) 398.

CMOS Embedded NEMS Resonator with Acoustic Confinement

S. Yandrapalli, D. Ruffieux, L. G. Villanueva •

The integration of CMOS electronic circuits and electromechanical resonators has been pursued for a long time to improve the overall performance of electromechanical oscillators. However, the post processing on the CMOS substrates that is necessary to attain this integration increases the production cost. This project presents a method of embedding a nano electromechanical resonator within a CMOS substrate with simulated resonator quality factor of more than 3000 at a frequency of 3.3 GHz.

The integration of additional electromechanical components on a CMOS chip has been subject to extensive research as it would allow for footprint and cost reduction. One of the main challenges in integrating MEMS resonators is the definition and release of the structure. The goal of this project is to embed a bulk acoustic resonator in the CMOS BEOL (interconnecting metal) layers that avoids the release step while still maintaining a high quality factor and electromechanical coupling of the device.

The release step is circumvented by placing the resonator in an acoustic bandgap created using a phononic crystal (PnC) structure that is made of the BEOL metals and dielectrics, as shown in Figure 1. The bulk acoustic resonator is a rectangular copper slab placed in the M5 layer which is designed to operate at its first fundamental mode of resonance. The resonator is actuated and sensed with neighboring electrodes placed on either side of the resonator and separated by 100 nm dielectric gaps.

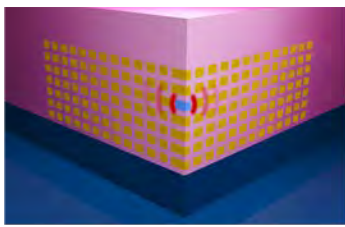


Figure 1: Schematic of one quarter model of the 3D acoustic cage with the mechanical resonator.

This particular implementation was designed using parameters of the TSMC 65 nm node technology with 7+2 metals. Phononic crystals are periodic structures designed such that the ensemble (metamaterial) shows a collective acoustic behavior that is different from either of the individual materials. Acoustic bandgaps were created due to the difference in densities and elastic properties (acoustic impedances) of the materials, namely Cu as a metal and low- κ porous oxide (SiOC) as the inter-metal dielectric [1]. The PnC is formed by repeating a unit cell consisting of a metal region surrounded by a dielectric (Figure 2). The band structure was computed by simulating the unit cell using finite element method and applying appropriate boundary conditions to emulate an infinitely repeating structure. The optimal effective acoustic length of each layer forming the reflector pair was matched to $\lambda/4$ of the required wavelength, in order to be confined for maximum efficiency. However, since heights of the metal and dielectric layers are fixed within a given

node, it is not possible to match the $\lambda/4$ condition. Instead, the effective path length of the reflector pair to $\lambda/2$ was matched. Taking n as the ratio of the longitudinal speed of sound in the inter metal dielectric (IMD) to that in the metal, the relation between heights and wavelength is given by $h_{Cu} + \frac{h_K}{n} = \frac{\lambda}{2}$.

A bandgap between 2.5 GHz to 4.3 GHz was simulated using such a simple 2D model as shown in Figure 2. The resonator was designed so that its frequency lies in the center of the bandgap and a high-Q bulk acoustic resonator was achieved.

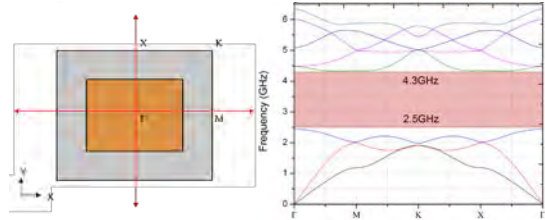


Figure 2: Unit cell and band structure indicating bandgap: frequency vs reduced wave vector path Γ -M-K-X- Γ .

The finite reflectors simulation was performed starting with a 2D model, followed by 3D extension to account for the appearance of new modes. Figure 3 shows the contour plot of displacement to visually demonstrate the effectiveness of the acoustic confinement.

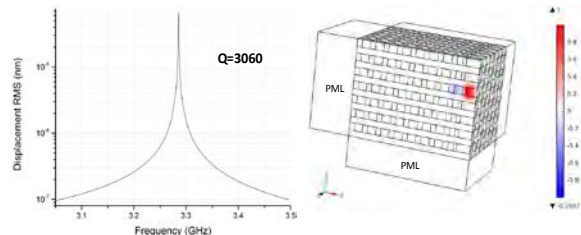


Figure 3: 3D quarter symmetric model.

A 3.3 GHz embedded CMOS NEMS resonator reaching a quality factor slightly above 3000 was designed and simulated. A Figure of Merit (FOM) $Q \cdot f = 10^{13}$ Hz could hence be obtained for an unreleased resonator that would come out of the foundry. Evaluated electromechanical coupling of these devices was 0.015 % thereby achieving a total FOM $Q \cdot k_t^2 = 0.46$. Provided those promising results are confirmed by the measurements of test structures, further work will address the design of a complete oscillator. This project was carried out in collaboration with the ANEMS group, EPFL.

• Advanced NEMS Group, EPFL, Switzerland

[1] K. W. Lee, et al., "Highly manufacturable Cu/low- κ dual damascene process integration for 65 nm technology node," IITC Int. Interconnect Technology Conference (2004) 55.

ANNEXES

Publications

- [1] J. Ansó, C. Dür, K. Gavaghan, H. Rohrbach, N. Gerber, T. Williamson, E. Calvo, T. Balmer, C. Precht, D. Ferrario, M. Dettmer, K. Rösler, M. Caversaccio, B. Bell, S. Weber, "A Neuromonitoring Approach to Facial Nerve Preservation During Image-guided Robotic Cochlear Implantation", *Otology & Neurotology*, 37 (1), January 2016, 89-98
- [2] L. Barbe, M. Alini, S. Verrier, M. Herrmann, "In Vitro Models to Mimic the Endothelial Barrier", *Alternatives to laboratory animals : ATLA*, 43 (3), December 2015, 34-36
- [3] T. Binninger, E. Fabbri, A. Patru, M. Garganourakis, J. Han, D.-F. Abbott, O. Sereda, R. Kötz, A. Menzel, M. Nachtegaal, T.-J. Schmidt, "Electrochemical Flow-Cell Setup for In Situ X-ray Investigations", *Journal of The Electrochemical Society*, August 2016, 906-912
- [4] L. Dümpelmann, D. Casari, A. Luu-Dinh, B. Gallinet, L. Novotny, "Fourfold Color Filter Based on Plasmonic Phase Retarder", *ACS Photonics*, 3, February 2016, 190-196
- [5] L. Dümpelmann, D. Casari, A. Luu-Dinh, B. Gallinet, L. Novotny, "Color rendering plasmonic aluminum substrates with angular symmetry breaking", *ACS Nano*, 9, November 2015, 12383-12391
- [6] S. Ehrbar, R. Perrin, M. Peroni, K. Bernatowicz, T. Parkel, I. Pytko, "Respiratory motion-management in stereotactic body radiation therapy", *Radiotherapy and Oncology*, 121, October 2016, 328-334
- [7] O. Fernández, R. Ferrini, "Modules LED à grande surface d'illumination (1re partie)", *Bulletin Electrosuisse*, 12/2016, December 2016
- [8] B. Gallinet, J. Butet, O.J.F. Martin, "Numerical methods for nanophotonics: standard problems and future challenges", *Laser and Photonics Reviews*, 9, November 2015, 577-603
- [9] I. Glowacki, Z. Szamel, G. Wiosna-Salyga, "Blue iridium complexes as electron trapping sites and efficient recombination centres in poly(N-vinylcarbazole) seen by spectrally resolved thermoluminescence", *Synthetic Metals*, 220, June 2016, 213-220
- [11] J. Gobet, P.-N. Volpe, M.-A. Dubois, "Friction coefficient of diamond under conditions compatible with microelectromechanical systems applications", *Applied Physics Letters*, 108 (12), March 2016, 1024103 1-4
- [12] D. Hengevoss, C. Baumgartner, G. Nisato, C. Hugi, "Life Cycle Assessment and eco-efficiency of prospective, flexible, tandem organic photovoltaic module", *Solar Energy*, 137, November 2016, 317-327
- [13] S. Heub, N. Tscharner, F. Kehl, P.S. Dittrich, S. Follonier, L. Barbe, "A Simple Method for Automated Solid Phase Extraction of Water Samples for Immunological Analysis of Small Pollutants", *Journal of Visualized Experiments*, January 2016
- [14] F. Isa, A. Jung, M. Salvalaglio, Y.-A Rojas Dasilva, I. Marozau, M. Meduna, M. Barget, A. Marzegalli, G. Isella, R. Erni, F. Pezzoli, E. Bonera, P. Niedermann, O. Sereda, P. Gröning, F. Montalenzi, H. von Känel, "Strain Engineering in Highly Mismatched SiGe/Si Heterostructures", *Material Science in Semiconductor Processing*, August 2016
- [16] F. Isa, M. Salvalaglio, Y. A. R. Dasilva, M. Meduña, M. Barget, A. Jung, T. Kreiliger, G. Isella, R. Erni, F. Pezzoli, E. Bonera, P. Niedermann, P. Gröning, F. Montalent, H. von Känel, "Highly Mismatched, Dislocation-Free SiGe/Si Heterostructures", *Advanced Materials*, 28, February 2016, 884-888
- [17] F. Isa, A. Jung, M. Salvalaglio, Y. Arroyo Rojas Dasilva, M. Meduna, M. Barget, T. Kreiliger, G. Isella, R. Erni, F. Pezzoli, E. Bonera, P. Niedermann, K. Zweiacker, A. Neels, A. Dommann, P. Gröning, F. Montalenti, H. von Känel, "Elastic and Plastic Stress Relaxation in Highly Mismatched SiGe/Si Crystals", *MRS Advances*, May 2016, 1-6
- [18] F. Isa, M. Salvalaglio, Y. Arroyo Rojas Dasilva, A. Jung, G. Isella, R. Erni, P. Niedermann, P. Gröning, F. Montalenti, H. von Känel, "From plastic to elastic stress relaxation in highly mismatched SiGe/Si heterostructures", *Acta Materialia*, (114), May 2016, 97-105
- [19] F. Isa, M. Salvalaglio, Y. Arroyo Rojas Dasilva, M. Meduna, M. Barget, A. Jung, T. Kreiliger, G. Isella, R. Erni, F. Pezzoli, E. Bonera, P. Niedermann, P. Gröning, F. Montalenti, H. von Känel, "Highly Mismatched, Dislocation-Free SiGe/Si Heterostructures", *Advanced Materials* (Deerfield Beach, Fla.), December 2015, 884-888

- [20] C. Jablonski, G. Grundler, U. Pieles, S. Stebler, R. Oehrlein, Z. Szamel, "Synthesis and Electrophoretic Properties of Novel Nanoparticles for Colored Electronic Ink and e-Paper Applications", CHIMIA, 70, May 2016, 366-368
- [21] B. Jost, A. Pommerol, O. Poch, B. Gundlach, M. Leboeuf, M. Dadras, J. Blum, N. Thomas, "Experimental characterization of the opposition surge in fine-grained water-ice and high albedo ice analogs", Ircus, 264, January 2016, 109-131
- [22] S. Karlen, J. Gobet, T. Overstolz, J. Haesler, "Non-destructive MEMS atomic vapor cells characterization by Raman spectroscopy and image analysis", April 2016
- [23] L. Karlen, G. Buchs, E. Portuondo-Campa, S. Lecomte, "Efficient carrier-envelope offset frequency stabilization through gain modulation via stimulated emission", Optics Express, 41 (2), January 2016, 376-379
- [24] J. B. la Cour, S. Generelli, L. Barbe, O. T. Guenat, "Low-cost disposable ALT electrochemical microsensors for in-vitro hepatotoxic assessment", Sensors and Actuators B: Chemical, January 2016
- [25] F. Lütfolf, D. Casari, B. Gallinet, "Low-cost and large-area strain sensors based on plasmonic fano resonances", Advanced Optical Materials, 4 (5), February 2016, 715-721
- [26] F. Lütfolf, O.J.F. Martin, B. Gallinet, "Fano-resonant aluminum and gold nanostructures created with a tunable, up-scalable process", Nanoscale, 7, November 2015, 18179-18187
- [27] M. Makha, S. L. Fernandes, S. Jenatsch, T. Offermans, J. Schleuniger, J.-N. Tisserant, A. C. Véron, R. Hany, "A transparent, solvent-free laminated top electrode for perovskite solar cells", Science and Technology of Advanced Materials, 17 (1), June 2016, 260-266
- [28] G. G. Mandayo, J. Gonzalez-Chavarri, E. Hammes, H. Newton, I. Castro-Hurtado, I. Ayerdi, H. Knapp, A. Sweetman, C. N. Hewitt, E. Castaño, "System to control indoor air quality in energy efficient buildings", Urban Climate, 14 (3), December 2015, 475-485
- [29] J. Mayer, B. Gallinet, T. Offermans, R. Ferrini, "Diffractive Nanostructures for Enhanced Light-Harvesting in Organic Photovoltaic Devices", Optics Express, 24, January 2016, A358-A373
- [30] K. Mondon, M. Dadras, J. Tillier, S. Gavard Molliard, "Influence of the Macro- and/or Microstructure of Cross-Linked Hyaluronic Acid Hydrogels on the Release of Two Model Drugs", Journal of Glycobiology, 5 (1), August 2016
- [31] G. Nisato, D. Lupo, S. Ganz (2016), "Introduction to Organic and Printed Electronics", G. Nisato, D. Lupo, S. Ganz (Eds.), Organic and Printed Electronics: Fundamentals and Applications, (pp. 1-9), CRC Press, 9789814669740
- [32] G. Nisato, D. Lupo, S. Ganz (2016), Organic and Printed Electronics: Fundamentals and Applications, G.i Nisato, D. Lupo, S. Ganz (Eds.), CRC press, 9789814669740
- [33] E. Oakton, D. Lebedev, A. Fedorov, F. Krumeich, J. Tillier, O. Sereda, T.J. Schmidt, C. Copéret, "A simple one-pot Adams method route to conductive high surface area IrO₂ -TiO₂ materials", New Journal of Chemistry, February 2016
- [34] E. Oakton, J. Tillier, G. Siddiqi, Z. Mickovic, O. Sereda, A. Fedorov, C. Copéret, "Structural differences between Sb- and Nb-doped tin oxides and consequences for electrical conductivity", New Journal of Chemistry, January 2016
- [35] L.-E. Perret-Aebi, J. Escarré Palou, G. Cattaneo, P. Heinstein, C. Ballif, "Les panneaux solaires blancs - Une révolution pour l'intégration architecturale", Bulletin, March 2016, 41-43
- [36] E. Portuondo-Campa, G. Buchs, S. Kundermann, L. Balet, S. Lecomte, "Ultra-low phase-noise microwave generation using a diode-pumped solid-state laser based frequency comb and a polarization-maintaining pulse interleaver", Optics Express, 23 (25), December 2015, 32441-32451
- [37] E. Portuondo-Campa, J. Bennès, L. Balet, S. Kundermann, F. Merenda, G. Boer, S. Lecomte, "Tunable dual-comb spectrometer based on commercial femtosecond lasers and reference cell for optical frequency calibration", Applied Physics B, 122 (7), June 2016, 1-9
- [38] M. Proença, F. Braun, J. Solà, A. Adler, M. Lemay, J.-P. Thiran, S. F. Rimoldi, "Non-invasive monitoring of pulmonary artery pressure from timing information by EIT: experimental evaluation during induced hypoxia", Physiological Measurement, 37 (6), May 2016, 713-726
- [39] V. Revol, A.-M. Madrigal, "Fast and reliable non-destructive of composites", JEC composites magazine, 106, July 2016, 53-54
- [40] V. Revol, C. Hanser, M. Krzemnicki, "Characterization of pearls by X-ray phase contrast imaging with a grating interferometer", Case Studies in Nondestructive Testing and Evaluation, 6, June 2016, 1-7

- [41] J.-W. Schüttauf, M.-A. Modestino, E. Chinello, D. Lambelet, A. Delfino, D. Dominé, A. Faes, M. Despeisse, J. Bailat, D. Psaltis, C. Moser, C. Ballif, "Solar-to-Hydrogen Production at 14.2% Efficiency with Silicon Photovoltaics and Earth-Abundant Electrocatalysts", *Journal of The Electrochemical Society*, 163 (10), August 2016, 1177-1181
- [42] E. Skobel, C. Knackstedt, A. Martinez-Romero, D. Salvi, C. Vera-Munoz, A. Napp, J. Luprano, R. Bover, S. Glöggler, B. Bjarnason-Wehrens, N. Marx, A. Rigby, J. Cleland, "Internet-based training of coronary artery patients: the Heart Cycle Trial", *Heart and Vessels*, October 2016,
- [43] Y. Stauffer, E. Olivero, S. Arberet, E. Onillon, L. Von Allmen, D. Lindelöf, C. Mahmed, "NeuroCool: an adaptive, model-predictive control algorithm for ventilation and air conditioning systems", May 2016,
- [44] Y. Stauffer, E. Olivero, S. Arberet, E. Onillon, L. Von Allmen, D. Lindelof, C. Mahmed, "NeuroCool: field tests of an HVAC control algorithm", May 2016
- [45] J. Tillier, T. Binninger, M. Garganourakis, A. Patru, E. Fabbri, T.-J. Schmidt, O. Sereda, "Electrochemical Flow-Cell Setup for In Situ and Operando X-ray Experiments", *Journal of The Electrochemical Society*, August 2016
- [46] E. Türetken, F. Benmansour, B. Andres, P. Glowacki, H. Pfister, P. Fua, "Reconstructing Curvilinear Networks using Path Classifiers and Integer Programming", *IEEE Transactions on Pattern Analysis and Machine Intelligence*, March 2016
- [47] N. Vukovic, J. Radovanovic, V. Milanovic, D. L. Boiko, "Analytical expression for Risken-Nummedal-Graham-Haken instability threshold in quantum cascade lasers", *Optics Express*, 24 (23), November 2016, 26911-26929
- [48] X. Wang, E. Türetken, F. Fleuret, P. Fua, "Tracking Interacting Objects Using Intertwined Flows", *IEEE Transactions on Pattern Analysis and Machine Intelligence*, December 2015

Proceedings

- [1] C. Allebé, A. Descoedres, L. Barraud, J. Levrat, M. Despeisse, C. Ballif, et al., "Hitting the symbolic 30% efficiency threshold of Si-based photovoltaics", PVSEC- Asia, Singapour (SG), 24-28 October 2016
- [2] S. Arberet, Y. Stauffer, M. Boegli, "Centralized energy optimization at district level", Energycon 2016, Leuven (BE), April 2016
- [3] L. Augel, I.-A. Fischera, L. A. Dunbar, S. Bechler, A. Berrier, D. Etezadi, F. Hornung, "Plasmonic nanohole arrays on Si-Ge heterostructures: An approach for integrated biosensors", Photonics West, San Francisco (US), January 2016
- [4] L. Barraud, M. Despeisse, S. DeWolf, B. Paviet, A. Descoedres, C. Ballif, "Implementation of intrinsic amorphous silicon layer into silicon heterojunction solar cells", Silicon PV 2016, Chambéry (FR), 07-09 March 2016
- [5] G. Basset, D. Marinov, C. Hofer, S. Cattaneo, P. Volet, B. Gallinet, M. Schnieper, R. Ferrini, "Extra flat, flexible and disposable endoscope for lateral imaging", Photonics West 2016, San Francisco (US), 13-18 February 2016
- [6] G. Basset, G. Quaranta, F. Lütolf, L. Davoine, M. Schnieper, "Subwavelength gratings for OVDs from local interactions to using light-transport", Optical Document Security (ODS) 2016, San Francisco (US), 10-12 February 2016
- [7] M.-C. Bay, R. Eckert, E. Grenet, R. P. Stanley, E. Franzl, H. Heinzelmann, C.-I. Ozdemir, H. Altug, L. A. Dunbar, "Integrated angular tracking and plasmonic membrane surfaces for a point of a care refractive index sensor", Photonics West, San Francisco (US), January 2016
- [8] N. Blondiaux, R. Pugin, G. Andreatta, L. Tenchine, S. Dessors, P. F. Chauvy, M. Diserens, P. Vuillermoz, "Fabrication of Functional Plastic Parts using Nanostructured Stainless Steel Mold Inserts", 4M/IWMF2016, The Global Conference on Micro Manufacture, Copenhagen (DK), 13-15 September 2016
- [9] M. Boegli, Y. Stauffer, K. Klobut, I. Hoyo, A. Samperio, "ICT-technologies for energy efficient buildings and districts", 41st IAHS World Congress, Sustainability and Innovation for the Future, Albufeira, Algarve (PO), 13-16 September 2016
- [10] E. Bozzo, T. Burch, A. Ciapponi, C. Heese, A. Hoogerwerf, N. Lan, A. Neronov, V. Revol, R. P. Stanley, "LIC and LID considerations in the design and implementation of the MEMS laser pointing mechanism for the EUSO UV laser altimeter", Pacific Rim Laser Damage 2016: Optical Materials for High-Power Lasers, Yokohama (JP), 18 May 2016
- [11] F. Braun, M. Proençā, J. Solà, M. Lemay, J.-P. Thiran, "EIT-Derived Stroke Volume is Impaired by Belt Displacement", ICEBI/EIT 2016, Stockholm (SE), June 2016

- [12] F. Braun, A. Lemkadem, V. Moser, S. Dasen, O. Grossenbacher, "Camera-Based Respiration Monitoring", BMT 2016, Basel (CH), October 2016
- [13] G. Bugnon, "White photovoltaic module technology development for building integration", CTI Micro-Nano Event 2016, Basel (CH), 30 June 2016
- [14] G. Cattaneo, P. Heinstein, K. Söderström, C. Ballif, L.-E. Perret-Aebi, "Integration of Photovoltaic Module into Building Facade", EUPVSEC 2016, Munich (DE), 20-24 June 2016
- [15] O. Chételat, J. Wacker, M. Rapin, J.-A. Porchet, C. Meier, A. Fahli, E. Haenni, L. Caldani, C. Mancuso, R. Paradiso, L. Arneth, "New biosensors and wearables for cardiorespiratory telemonitoring", Biomedical and Health Informatics (BHI), 24-27 February 2016
- [16] G. Christmann, D. Sacchetto, L. Sansonnens, L. A. A. Duval, M. Creatore, W. M. M. Kessels, G. Wahli, L. Barraud, A. Descoedres, B. Paviet-Salomon, N. Badel, B. Strahm, M. Despeisse, S. Nicolay, C. Ballif, "Silicon heterojunction solar cells using aluminum doped zinc oxide as back contact: sputtering and ALD", EUPVSEC 2016, Munich (DE), 20-24 June 2016
- [17] S. Cloix, T. Pun, D. Hasler, "Real-time Scale-invariant Object Recognition from Light Field Imaging", 11th Joint Conference on Computer Vision, Imaging and Computer Graphics Theory and Applications - VISAPP, Rome (IT), 27-29 February 2016, 336–344
- [18] F. Cosandier, F. Barrot, J. Kruis, L. Voruz, G. Musy, S. Droz, L. Giriens, W. Glettig, E. Dominé, "A three device silicon based platform for micro-assembly and characterization", EUSPEN, Nottingham (UK), 30 May-3 June 2016
- [19] A. Dan Tarniceriu, J. Parák, P. Renevey, M. Bertschi, R. Delgado-Gonzalo, I. Korhonen, "Towards 24/7 Continuous Heart Rate Monitoring", 38th Annual International Conference of the IEEE Engineering in Medicine and Biology Society (EMBC'16), Orlando (US), 16-20 August 2016, 186-189
- [20] R. Delgado-Gonzalo, A. Lemkadem, P. Renevey, E.M. Calvo, M. Lemay, K. Cox, D. Ashby, J. Willardson M. Bertschi, "Real-time Monitoring of Swimming Performance", 38th Annual International Conference of the IEEE Engineering in Medicine and Biology Society (EMBC'16), Orlando (US), 16-20 August 2016, 4743-4746
- [21] M. Despeisse, S. Essig, C. Allebe, M. A. Steiner, J. F. Geisz, B. Paviet-Salomon, S. Ward, A. Descoedres, L. Barraud, V. LaSalvia, N. Badel, J. Champliaud, A. Faes, J. Levrat, A. Tamboli, P. Stradins, D. L. Young, C. Ballif, "GaInP/Silicon dual junction solar cell with 29.8 % certified record efficiency", 14e Congrès Photovoltaïque National, Berne (CH), 22-23 February 2016
- [22] M. Despeisse, A. Faes, A. Lachowicz, N. Badel, J. Champliaud, J. Levrat, H. Watanabe, P. Papet, B. Strahm, Y. Yao, T. Soderstrom, C. Ballif, "Advanced Metallization and Interconnection Technologies for Silicon Heterojunction Solar Cells and Modules", 14e Congrès Photovoltaïque National, Berne (CH), 22-23 February 2016
- [23] M. Despeisse, L. Barraud, B. Paviet-Salomon, A. Descoedres, C. Allebé, J. Levrat, F. Debrot, A. Lachowicz, J. Geissbuhler, J. Champliaud, A. Faes, N. Badel, L.-L. Senaud, L. Curvat, J. Horzel, S. Nicolay, D. Sachetto, G. Christmann, L. Sansonnens, "Advances in Solar Cells implementing Silicon Heterojunction Passivating Contacts", Asian PVSEC 2016, Singapore, October 2016
- [24] M. Despeisse, A. Faes, N. Badel, A. Lachowicz, J. Geissbuhler, J. Champliaud, F. Debrot, B. Strahm, T. Söderström, C. Ballif, "Metallization and Interconnection Technologies for Silicon Heterojunction Solar Cells", Asian PVSEC 2016, Singapore, October 2016
- [25] L. Dümpelmann, A. Luu-Dinh, F. Lütolf, B. Gallinet, L. Novotny, "Plasmonic Color Filters for Industrial Applications", META'16 International Conferences on metamaterials, photonic crystals and plasmonics, July 2016
- [26] A. Faes, M. Despeisse, J. Levrat, J. Champliaud, A. Lachowicz, N. Badel, J. Geissbühler, H. Watanabe, T. Söderström, Y. Yao, J. Ufheil, P. Papet, B. Strahm, J. Hermans, A. Tomasi, J. Fleischer, P. V. Fleischer, C. Ballif, "Review on Metallization and Interconnection for Si Heterojunction Solar Cells", EUPVSEC 2016, Munich (DE), 20-24 June 2016
- [27] S. Fallet, L. Mirmohamadsadeghi, V. Moser, F. Braun, J.-M. Vesin, "Real-Time Approaches for Heart Rate Monitoring using Imaging Photoplethysmography", Computing in Cardiology 2016, Vancouver (CA), 11-14 September 2016
- [28] S. Fallet, V. Moser, F. Braun, J.-M. Vesin, "Imaging Photoplethysmography: What are the Best Locations on the Face to Estimate Heart Rate?", Computing in Cardiology 2016, Vancouver (CA), 11-14 September 2016

- [29] O. Fernandez, "Ultrathin direct-lit LED module with beam shaping thin-film optics", LED Symposium 2016, Bregenz (AT), 20-22 September 2016
- [30] R. Ferrini, O. Fernandez, S. Junger, K. Keränen, L. Barruetabéña, A. von Mühlenen, T. Dreyfus, "Large Area Intelligent Efficient High Quality Solid-state Lighting", OSA Light, Energy and the Environment Congress, Leipzig (DE), 14-17 November 2016
- [31] B. Gallinet, "Highly contrasted structural colors for industrial applications using the Fano lineshape", META'16 International COnference on Metamaterials, Photonic Crystals and Plasmonics, July 2016
- [32] J. Geissbühler, J. Werner, S. Martin de Nicolas, L. Barraud, A. Hessler-Wyser, A. Lachowicz, D. Sacchetto, M. Despeisse, S. Nicolay, A. Tomasi, B. Niesen, S. De Wolf, C. Ballif, "High-Efficiency Silicon Heterojunction Solar Cells with Molybdenum Oxide Hole Collector", Silicon PV Conference 2016, Chambéry (FR), 07-09 March 2016
- [33] M. Gresil, V. Revol, S. Consuelo Garcea, R. Chemama, G. Kanderakis, K. Kitsianos, I. Koulalis, M.-O. Sauer, H. Trétout, A.-M. Madrigal, "Comparison between Traditional Non-Destructive Techniques and Phase Contrast X-Ray Imaging applied to Aeronautical Carbon Fibre Reinforced Polymer", 19th World Conference on Non-Destructive Testing, Munich (DE), 13-17 June 2016
- [34] R. Jose James, G. Spinola Durante, M. Fretz, J. Gobet, C. Bosshard, "Miniature Long-Term Implantable Micro-packages", Biointerfaces International 2016, Zurich (CH), 23-25 August 2016
- [35] R. Jose James, J. Gobet, G. Spinola Durante, M. Fretz, "A novel packaging technology for miniaturization of active long-term implantable", ESTC 2016, Grenoble (FR), 13-16 September 2016
- [36] V. Kopta, D. Barras, C. Enz, "A 420 μ W, 4 GHz Approximate Zero IF FM-UWB Receiver for Short-Range Communications", 2016 IEEE Radio Frequency Integrated Circuits Symposium (RFIC 2016), San Francisco (US), 22-24 May 2016
- [37] Y. Lammen, A. Reinacher, I. Kjelberg, S. Droz, H. Jakob, F. Graf, Friederike, A. Alfred, "SOFIA Secondary Mirror Mechanism Heavy Maintenance and Improvements", SPIE Astronomical Telescopes + Instrumentation, Edinburgh (GB), 26 June 2016
- [38] S. Lani, Y-J. Regamey, D. Bayat, E. Onillon, "MEMS scanner integrating a position control system", Photonics West 2016, San Francisco (US), February 2016
- [39] L. Lombardo, S. Generelli, N. Tscharner, D. Migliorelli, N. Donato, "A compact electronic interface for electrochemical sensors", IEEE Sensors Applications Symposium 2016, Catania (IT), 20-22 April 2016, 429-432
- [40] A. Luu-Dinh, G. Basset, F. Zanella, C. Schneider, "Application of Photocurable Polymers for Casting of micro- and nastructures", PRN 2016, Brugg-Windisch (CH), 19-20 May 2016, 17
- [41] N. Marjanović, F. Zanella, J. Disser, A. Mustaccio, J. Schleuniger, G. Nisato, R. Ferrini, "Hybrid electronics systems by CSEM", LOPEC 2016, Munich (DE), 5-7 April 2016
- [42] N. Marjanović, J. Disser, F. Zanella, J. Schleuniger, A. Mustaccio, R. Ferrini, M. Schnieper, E. Assaf, "Sun sensor printed on flexible circuit board for picosatellites", 2nd Space Passive Component Days (SPCD), ESA/ESTEC, Noordwijk (NL), 12-14 October 2016
- [43] L. Mirmohamsadeghi, S. Fallet, V. Moser, F. Braun, J.-M. Vesin, "Real-Time Respiratory Rate Estimation using Imaging Photoplethysmography", Computing in Cardiology 2016, Vancouver (CA), 11-14 September 2016
- [44] V. Musolino, P.-J. Alet, L.-E. Perret-Aebi, C. Ballif, W. Martin, A. G. Azar, R. H. Jacobsen, V. Efthymiou, G. Graditi, N. Henze, M. Juel, D. Moser, F. Nemac, M. Pierro, E. Rikos, S. Tselepis, G. Yang, "Forecasting and observability: critical technologies for system operations with high PV penetration", EUPVSEC 2016, Munich (DE), 20-24 June 2016
- [45] V. Musolino, P.-J. Alet, L.-E. Perret-Aebi, C. Ballif, W. Martin, A. G. Azar, R. H. Jacobsen, V. Efthymiou, G. Graditi, N. Henze, M. Juel, D. Moser, F. Nemac, M. Pierro, E. Rikos, S. Tselepis, G. Yang, "Managing the quality of electricity supply under high penetration of photovoltaic generation with load shifting and inverter control", EUPVSEC 2016, Munich (DE), 20-24 June 2016
- [46] V. Musolino, P.-J. Alet, L.-E. Perret-Aebi, C. Ballif, W. Martin, A. G. Azar, R. H. Jacobsen, V. Efthymiou, G. Graditi, N. Henze, M. Juel, D. Moser, F. Nemac, M. Pierro, E. Rikos, S. Tselepis, G. Yang, "Effective Integration of PV source by means of DC microgrids", EUPVSEC 2016, Munich (DE), 20-24 June 2016
- [47] G. Nisato, "Towards next generations OPV: key results of the Sunflower EU project", International Conference on Flexible and Printed Electronics, Yonezawa City (JP), 6-8 September 2016

- [48] B. Paviet-Salomon, A. Tomasi, L. Barraud, D. Lachenal, A. Descoeuadres, N. Badel, H. Watanabe, A. Faes, G. Christmann, S. Nicolay, S. De Wolf, B. Strahm, M. Despeisse, C. Ballif, "Development of photolithography-free back-contacted silicon heterojunction solar cells with efficiency >22 %", 14e Congrès Photovoltaïque National, Berne (CH), 22-23 February 2016
- [49] B. Paviet-Salomon, J. Levrat, V. Fakhouri, Y. Pelet, N. Rebeaud, M. Despeisse, C. Ballif, "Accurate determination of PV cells and modules peak power from their I-V characteristics", EUPVSEC, Munich (DE), 20-24 June 2016
- [50] L.-E. Perret-Aebi, P. Duvoisin, J. Escarré, C. Ballif, "Solarstratos: pushing the solar technology to the edge of space", Asian PVSEC, Singapore (SG), 24-28 October 2016
- [51] L.-E. Perret-Aebi, "When PV modules are becoming real building elements: White solar module, a revolution for BIPV", Polymers in Photovoltaics 2016, Dusseldorf (DE), 02-03 February 2016
- [52] M. Pons, T-C. Le, C. Arm, D. Séverac, J-L. Nagel, M. Morgan, S. Emery, "Sub-threshold latch-based icyflex2 32-bit processor with wide supply range operation", 42nd European Solid-State Circuits Conference - ESSCIRC, Lausanne (CH), 12-15 September 2016, 41-44
- [53] M. Proença, F. Braun, E. Muntané, J. Solà, A. Adler, M. Lemay, J.-P. Thiran, S. F. Rimoldi, "Non-invasive Monitoring of Pulmonary Artery Pressure at the Bedside", IEEE EMBC 2016, Orlando (US), August 2016
- [54] M. Proença, F. Braun, J. Solà, A. Adler, M. Lemay, J.-P. Thiran, S. Rimoldi, "Pulmonary Artery Pressure by EIT: Experimental Evaluation", ICEBI/EIT 2016, Stockholm (SE), June 2016
- [55] V. Revol, K. Kitsianos, M. Gresil 3, H. Trétout, G. Kanderakis, M.-O. Sauer, I. Koulalis, T. Stadelmann, G. Tsamasphyros, A.-M. Madrigal, "Non-destructive evaluation, inspection and testing of primary aeronautical composite structures using grating-based phase contrast x-ray imaging", 7th International Symposium on NDT in Aerospace, Bremen (DE), 16-18 November 2015, We.5.A.3
- [56] C. Rojas, D. Piguet, J-D. Decotignie, "Poster: Single Packet Link Estimation", International Conference on Embedded Wireless Systems and Networks, Graz (AT), 15-17 February 2016, 263-264
- [57] E. Scolan, R. Smajda, G. Weder, G. Voirin, R. Pugin, Y. Michou, M.-C. Merienne, M. Lyonnet, A. Winzer, "Integration of New Sol-Gel Films Into Optical Chemical Sensors", Eurosensors 2016, Elsevier Ltd, Budapest (HU), 5-7 September 2016
- [58] K. Söderström, "Colored laminates for architectural building integration", PV Days 2016, Halle (DE), 27-28 September 2016
- [59] K. Söderström, L.-E. Perret-Aebi, P. Heinstein, "White solar modules: colored laminates for architectural building integration ", Photovoltaic, colors and innovation, Copenhagen (DK), 08 December 2015
- [60] P. Spanoudakis, P. Schwab, E. Onillon, L. Lisowski, P. Theurillat, O. Chételelat, C. Meier, "Operational Performance of MOSFIRE with Its Cryogenic Configurable Slitmask Unit at the W. M. Keck Observatory", SPIE 2016 Astronomical Telescopes & Instrumentation, Edinburgh (UK), 26 June 2016
- [61] Y. Stauffer, D. Ferrario, E. Onillon, A. Hutter, "Power monitoring based photovoltaic installation fault detection", ICRERA, Palermo (IT), 22-25 November 2015
- [62] A. Vorobyov, E. Daskalaki, C. Hennemann, J.-D. Decotignie, "Human Physical Condition RF Sensing at THz range", EMBS 2016, Orlando (US), August 2016, 4
- [63] A. Vorobyov, C. Henemann, P. Dallemagne, "Liquid Metal Based Antenna for Wearable Electronic", EuCAP 2016, Davos (CH), May 2016, 4
- [64] A. Walter, J. Werner, J. P. Seif, M. Bräuninger, S.-J. Moon, D. Sacchetto, C. Allebé, M. Despeisse, S. De Wolf, S. Nicolay, B. Niesen, C. Ballif, "High efficiency perovskite/crystalline silicon tandem solar cells with active area >1cm²", International Conference on Hybrid and Organic Photovoltaics (HOPV), Swansea (UK), 28 - 01 June 2016

Conferences and Workshops

P.-J. Alet, L. Bally, E. Olivero, F. Schmidhalter, C. S. Ellefsen, L.-E. Perret-Aebi, A. Hutter, C. Ballif, "Low-voltage grid assessment for demand-response systems", 2015 SCCER-FURIES Annual Conference, Lausanne (CH), 25 November 2015

G. Basset, "Extra flat, flexible and disposable endoscope for lateral imaging ", Photonics West 2016, San Francisco (US), February 2016

C. Bosshard, "Sensoroberflächen: von der Technologie zum Markt", Annual Event 2016: Oberflächen: Differenzierungsfaktor & Innovationsträger, Zug (CH), 22 November 2016

C. Bosshard, G. Basset, D. Marinov, C. Hofer, S. Cattaneo, P. Volet, B. Gallinet, R. Ferrini, M. Schnieper, "Extra-flat, flexible and disposable endoscope for lateral imaging", Microphotonics 2016, Berlin (DE), 11-13 October 2016

C. Bosshard, "Innovative solutions for light management and imaging for medical applications", EPIC Photonics Tech Watch, Berlin (DE), 11-13 October 2016

M. Dadras, "MEMS reliability for harsh environment & failure analysis", CMI Day, Lausanne (CH), 3 May 2016

M. Dadras, "Application de l'AFM pour assurer la fiabilité en microtechnique", AFM meeting, Bordeaux (FR), 17-19 November 2016

L. Duempelmann, D. Casari, A. Luu-Dinh, G. Basset, B. Gallinet, M. Schnieper, "Plasmonic Color Filters for Industrial Applications", Gordon Conference Plasmonics & Nanophotonics, Sunday River, Maine (US), 8-15 July 2016

A. Faes, M. Despeisse, J. Levrat, J. Champliaud, A. Lachowicz, N. Badel, J. Geissbühler, H. Watanabe, T. Söderström, Y. Yao, J. Ufheil, P. Papet, B. Strahm, J. Hermans, A. Tomasi, J. Fleischer, P.V. Fleischer, T. Takahashi, C. Ballif, "Advanced metallization enabled by multi-wire interconnection for silicon heterojunction cells and modules", 6th Metallization Workshop, Konstanz (DE), 02-03 May 2016

A. Faes, M. Despeisse, J. Levrat, J. Champliaud, A. Lachowicz, J. Geissbühler, N. Badel, J. Horzel, J.-W. Schüttauf, C. Ballif, "Silicon heterojunction metallization and modules approaches", Hercules Workshop, Berlin (DE), 10-12 October 2016

J. Farserotu, "From BAN to SmartBAN in the future IoT", SmartCOM 2016, Oulu (Fi), 17 May 2016

O. Fernandez, "Efficient high quality light management", Intelligent efficient solid-state lighting, Muttenz (CH), December 2016

R. Ferrini, "(O)LEDs: Innovative solutions for high quality large area solid state lighting", Forum LED Europe, Lyon (FR), December 2015

R. Ferrini, "LASSIE-FP7 Highlights", Intelligent efficient solid-state lighting, Muttenz (CH), December 2016

R. Ferrini, "Wearable light management system for light stimulated healing of large area chronic wounds", Photonics West 2016, San Francisco (US), February 2016

R. Ferrini, "Large Area Solid State Intelligent Efficient Luminaires", LASSIE-FP7 Workshop, L'Aquila (IT), July 2016

R. Ferrini, "Light Management at CSEM", SNI Workshop, Basel (CH), March 2016

R. Ferrini, "Large Area Intelligent Efficient High Quality Solid-state Lighting ", OSA Light, Energy and the Environment Congress, Leipzig (DE), November 2016

B. Gallinet, "Plasmonics for optical security and filters", Swiss Nano Convention, June 2016

J. Geissbühler, J. Werner, S. Martin de Nicolas, L. Barraud, A. Hessler-Wyser, A. Lachowicz, D. Sacchetto, G. Christmann, M. Despeisse, S. Nicolay, A. Tomasi, B. Niesen, S. De Wolf, C. Ballif, "High-Efficiency Silicon Heterojunction Solar Cells with Molybdenum Oxide Hole Collector", Silicon PV 2016, Chambéry (FR), 7-9 March 2016

M. Höchemer, "Neuronale Netze in der Praxis: Einführung und Anwendung in der Qualitätskontrolle", Swiss Mechatronics Day 2016, Winterthur (CH), 09 June 2016

R. J. James, G. Spinola Durante, M. Fretz, J. Gobet, C. Bosshard, S. Mohrdiek, A. Steinecker, "A novel packaging technology for miniature long-term active implants", EPoSS Annual Forum 2016, Lecce (IT), 13-14 January 2016

J. Kaufmann, "Using industrial ps-pulsed laser for micro-machining", Posalux Symposium on Glass Micro Machining, Biel (CH), 23 November 2015

L. Kiener, "Additive Manufacturing at CSEM", Swissmem Swiss Space Industries Group (SSIG) Mid-Year Assembly, Delémont (CH), 23 June 2016

I. Kjelberg, "Thermo-Mechanical Design For Space Optics", Space Optics Instruments Technology, Poltu Quatu (IT), 12 May 2016

G. Kotrotsios, "in Katalysatoren der Gesundheitsregion", Erster Plattform Gesundheit der Hauptstadtregion Schweiz, Fribourg (CH), 17 November 2015

J. B. La Cour, D. Migliorelli, S. Prill, S. Generelli, L. Barbe, C. Duschl, O. Guenat, "Electrochemical sensors for hepatotoxic assessment in a modular microfluidic system", Hemibio Symposium, Leuven (BE), 2-3 December 2015

N. Marjanović, J. Disser, F. Zanella, J. Schleuniger, A. Mustaccio, R. Ferrini, M. Schnieper, E. Assaf, "Hybrid integration approach; case study with sun sensor for picosatellites ", 10th ESA Round Table on Micro and Nano Technologies for Space Applications, ESA/ESTEC, Noordwijk (NL), 8-11 November 2016

C. Martin Olmos, J. K. Gimzewski, "Self Organization and Emergence of Dynamical Structures in Atomic Switch Networks", UCSB 2016, Santa Barbara (US), 16-17 May 2016

V. Musolino, C. Brivio, "Electrochemical Storage Systems: Characterization and Applications", Politecnico di Milano, Milano (IT), June 2016

G. Nisato, "CSEM submicron printable technologies", Micronarn alpine Meeting, Villars-sur-Ollon (CH), 1-2 February 2016

G. Nisato, et al., "Towards solutions processable, tandem, OPV: key results of the Sunflower EU project", ISFOE, Thessaloniki (GR), 4-7 July 2016

G. Nisato, "Building blocks for Printed, Flexible Sensors", Sensors, San Jose (US), 27-29 June 2016

G. Nisato, "Towards high performance OPV and related technologies: experiences from the Sunflower FP7 project.", European Photovoltaic Cluster General Assembly, Barcelona (ES), 25-26 May 2016

B. Paviet-Salomon, A. Tomasi, D. Lachenal, A. Descoedres, L. Barraud, G. Christmann, N. Badel, S. Nicolay, M. Despeisse, S. De Wolf, B. Strahm, C. Ballif, "Development of photolithography-free, large-area, back-contacted silicon heterojunction solar cells", IBC Workshop Freiburg, Freiburg-im-Breisgau (DE), 04-05 November 2015

B. Paviet-Salomon, "PUNCH: ProdUction-ready, Next generation back-Contacted silicon Heterojunction solar cells and modules", CTI Micro-Nano Event 2016, Basel (CH), 30 June 2016

C. Piguet, "Some Notes about the History of Low-Power", International Workshop on Power and Timing Modeling, Optimization and Simulation - PATMOS, Bremen (DE), 21-23 September 2016

P. A. Schmid, "Neuronale Netzwerke: Revolution im Alltag", TecNight by satw, Wohlen (CH), 1 December 2016

P. A. Schmid, "Industrial Approach: Automated Fault Detection with 1-Dimensional Sensory Signals for Quality Inspection", Swissphotonics - Machine Learning Workshop, Neuchâtel (CH), 1 February 2016

J.-W. Schüttauf, J. Bailat, C. Ballif, et al., "Device development from industry perspective: Photovoltaics", Pathways to Solar-Hydrogen Technologies, Leiden (NL), 13-17 June 2016

A. Steinecker, P. Schmid, "Monitoring vital signs with implantable pressure sensors", COMPAMED High-tech Forum by IVAM, Düsseldorf (DE), 17 November 2015

A. Steinecker, S. Widmer, M. Lützelschwab, P. Schmid, "Integration of Electronics into Textiles", Smart Systems Integration 2016, Munich (DE), 09-10 March 2016

A. Steinecker, S. Widmer, M. Lützelschwab, P. Schmid, "Integration of Electronics in Textiles", COMPAMED Hightech Forum 2016, Düsseldorf (DE), 14-17 November 2016

R. Vanta, S. Abolhassani, M. Dadras, "Examination of semiconducting properties of oxides in the vicinity of metal-oxide interfaces for selected alloys", EMC2016, Lyon (FR), 2 September 2016

K. Veideeswaran, Y. Zangui, O. Sereda, H. Saudan, L. Kiener, M. Dadras, "Effect of processing history on properties of additively manufactured 17-4PH steel", EMC2016, Lyon (FR), 2 September 2016

A. Walter, "Production technology to achieve low Cost High Efficiency photovoltaic Perovskite Solar cells", European Photovoltaic Cluster Workshop, Barcelone (ES), 25-27 May 2016

A. Walter, "Development of functional layers for Perovskite solar cells within PLIANT", European Photovoltaic Cluster Workshop, Barcelone (ES), 25-27 May 2016

Publicly Funded Projects

3R Research Foundation Switzerland	EndothelialChip – In vitro micro-vascular model mimicking the endothelial barrier
Canton of Neuchâtel	NECAN – Développement de solutions PV pour le bâtiment
CCEM – Electricity	CONNECT-PV – Conductive transparent electrodes: a competence cluster for highly efficient thin film photovoltaics
Eurostars	ALBIREO – Low-power impulse-radio ultra-wideband module for remote control and keyless access
Eurostars	CIT-MSA – Disposable sensor array for bioprocess monitoring in disposable bioreactors
Eurostars	DEBORAH – Optimization of design and control of district level thermal energy systems
Eurostars	HICOLA – Highly coherent laser for coherent communication and sensing
Eurostars	LAMMIC – Production of laminin-521™ coated microcarriers for stem cell expansion
Eurostars	PERISCOPE – NILM for Industrial and Public Buildings

Eurostars	POLYOMINO – All-in-one platform for the design and the production of customized free-form OPV modules
Eurostars	SWIRSENSE – Short-wavelength infrared tunable laser for sensing applications
Eurostars	WBPS – Wearable blood pressure system
Forschung Aargau	SECTEX – Development of hidden, shape and colour encoded micro flakes for robust textile authentication
Forschung Aargau	SENSORSURFACE – Colorimetric sensor structures on COP polymer foils for bioassays
Hasler Fondation	EYEWALK – Mobile ultra-light vision system for the handicapped
Nano-Tera	3D-SENSTEX – 3D Large scale Integration of sensors into smart textile
Nano-Tera	BREATHE – High throughput transducers to measure in-vitro muscle contraction
Nano-Tera	FLUSITEX – Developing a wound dressing with an integrated sensing layer for non-invasive wound monitoring using fluorescence lifetime detection
Nano-Tera	HEARRESTORE – Image-guided micro surgery for hearing aid implantation
Nano-Tera	ICYSOC – Inexact sub-near-threshold systems for ultra-low power devices
Nano-Tera	MINIHOLTER – Photoplethysmography-based ambulatory heart rate monitor device embedded into a smart watch
Nano-Tera	NAMBP – Night ambulatory monitoring of blood pressure
Nano-Tera	NEWBORNCARE – Reducing the false alarms of neonate vital sign monitoring via a computer vision-based approach to accurately measure heart and respiratory rates in a contactless way
Nano-Tera	OBESENSE – Monitoring the consequences of obesity
Nano-Tera	PARATEX – Novel smart textile to non-invasively monitor pressure, oxygenation and perfusion of tissue to prevent pressure ulcers in paraplegics
Nano-Tera	RASECAN – A new tool for rapid sensing of cancer by parallel AFM
Nano-Tera	SHINE – Solar to hydrogen integrated nano-electrolysis
Nano-Tera	SPINEREPAIR – Hybrid CMOS-polymer neural interfaces for restoration of sensorimotor function after spinal cord injury
Nano-Tera	SYNERGY – Realizing photovoltaic energy harvesting systems based on tandem solar cells with efficiency beyond that achievable with state-of-the-art industrial single-junction cells
Nano-Tera	SYNERGY – Systems for ultra-high performance photovoltaic energy harvesting
Nano-Tera	WISESKIN – Wise Skin for tactile prosthetics
NCCR – PlanetS	ASTROCAL – CALibration source for ASTROnometrical spectrometers
SATW	IMMOCOATING – Sensor coating for immobilisation of colorimetric bioassays on absorbance enhancing nano-gratings
SATW	META-SURFACES – Meta-surfaces—large-area metasurfaces for planar light management
SNI – Nanoargovia	NFOPTICS – Uniaxially oriented anisotropic electrospun nano-fibrous layers for optical applications
SNI – Nanoargovia	SICSTRUCT – Physical studies of SiC nano-trench-MOSFETs
SNSF	ACTIVE INTERFACES – Holistic strategy to simplify standards, assessments and certifications for building integrated photovoltaics
SNSF	CELLSTRATES – Smart engineered substrates for high throughput mechanobiology

SNSF	EOCOMB – Broadband optical frequency comb source based on electro-optic modulation for resolved comb line precision spectroscopy
SNSF	FASTIQ – Ultrafast infrared emitter on a quantum cascade
SNSF	HEMODYNAMEIT – Subject-adapted 3D dynamic bio-impedance models: application to blood pressure monitoring
SNSF	MAXIN – Hybrid PVT collector
SNSF	MUSCLELAB – Silicon elastomer structures to measure mechanical properties of muscle models
SNSF	NOVIPIX – Novel integrated pixel X-ray detectors
SNSF / program NRP 70	PV2050 – Novel generation perovskite devices
SNSF / program NRP 70	PV2050 – Photovoltaics into the built environment: from semi-transparent PV glazing to high efficiency roof integrated solutions
Swiss Federal Office of Energy (SFOE)	DCSMART – Distribution en courant continu dans les réseaux intelligents
Swiss Federal Office of Energy (SFOE)	PROSUMER-LAB – Einfluss neuartiger Strategien und Komponenten des Energiemanagements von netzintegrierten, intelligenten Gebäuden auf die Stabilität und Qualität des Haus- und Verteilnetzes
Swiss Federal Office of Energy (SFOE)	Swiss-Inno-HJT – Pilot production and demonstration of innovative high performance silicon hetero-junction PV cells, modules and systems
Swiss Federal Office of Energy SFOE	BRUTTEN – PV-Gebäudehülle mit warmem Erscheinungsbild im Wohnquartier
Swiss Federal Office of Energy SFOE	PVLIFE – Neuchâtel, musée suisse de l'architecture solaire à ciel ouvert
Swiss Space Center	E-GRIP – Einstein gravitational red-shift probe mission study

Swiss Commission for Technology and Innovation (CTI)

18101.1 PFNM-NM	3D NANOMET	Surface micro-nanostructuring of metallic surfaces for improved tribological performances
16429.1 INNO-IW	ADFEAS	Faisabilité du concept DTI-Communications du point de vue énergétique
18616.1	ALSCN	High volume process for AlScN thin film deposition
16025.1 PFIW-IW	APPROBATE	Automatisierte approbierte Qualität für manuelle Montage von kleinen Stückzahlen auf der Basis von selbstlernenden Bildverarbeitungsalgorithmen zur Arbeitsschrittkontrolle
17486.1 PFNM-NM	ATIPS	Advanced aircraft tire pressure sensing
18623.1 PFNM-NM	BIOWAVE	Realisation of the BIOWAVE pre-product, a BIometric Watch Activated by VEins
18473.2 PFNM-NM	BUBBLES	Fluid sensor with acoustical pattern analysis of physical properties and IoT integration
17623.1 PFNM-NM	CNT-SENSE	Surface enhanced Raman scattering sensor for airborne carbon nanotubes in workplaces
17863.2 PFLS-LS	COCO	Sustainable intensification of agricultural cropping systems supported by smart swiss ICT-AGRI solutions
18445.1	COMET	Contacting and metrology for advanced photovoltaic cells and modules technologies

18894.1 PFNM-NM	CORIBO	MEMS-based micro-Coriolis density and flow sensor bonding
25171.1 INNO-NM	COSTO	Feasibility study: Fingerprint of gemstones
18314.1	COTM	KU-KA frontend: Additive-manufactured Satcom user terminal front-end for connectivity on the move applications in Ku and Ka band
18888.1 PFES-ES	CUBIC 2	The world's lowest-power platform to wirelessly exchange information peer-to-peer
16692.2 PFIW-IW	CUMAPRO	Massenproduktion von kundenspezifischen PV-Modulen für die Gebäudeintegration, Customised Mass Production
17507.1 PFEN-NM	DAYGLAZING	Daylight and heat management foil for high quality illumination in buildings
17266.2 PFIW-IW	DEFIA	Development of novel electrode foil solution for solar cells interconnected with smartwire connection technology applied in the glass-glass module configuration
18421.1	DLC ABB	Improved DLC electrically active layer for high power bipolar silicon semiconductor
17324.1 PFLS-LS	DRDO	Device to reliably detect ovulation
17490.1 PFIW-IW	DSC-FAB	Production technology of durable dye-sensitive glass-modules for building integrated photovoltaic power generation
18633.1 PFNM-NM	DUALCOMB	Dual comb mid IR source technology
17708.1 PFNM-NM	ELECTROLUMINATI	Electro-illumination of dive watches through mechanical power generation
18003.1 PFNM-NM	FASTOBS	Dynamic nanoindentation enabling fast observation
17288.1 PFNM-NM	FELCOLAP	Fabric-based electrodes for large-area commercial OLED-based products for lighting applications
18481.1 PFNM-NM	FEMTOPOWER	Femtopower will develop ultrahigh power ultrashort pulse femtosecond laser source for highspeed industrial micromachining
19288.1	HIFILL	Industrial fabrication of ultra-high fill factor microlenses
16862.2 PFNM-NM	HIFLOW	High sensitivity flow sensor for extended flow range
25138.1	HI-MU-LENS	Wafer-scale integration of high-refractive index microlenses on III-IV semiconductor photodiodes
18099.1 PFNM-NM	HIPERSTEER	High performance beam steering unit
18307.1	HOT-WINDOWS	Heated aircraft windshields- development of a transparent and more reliable heating for the production of aircraft windshiled series
18611.1 PFNM-NM	HySurf	Microstructured hybrid surface with improved friction properties
10894.1 PFNM-NM	ICYAMR 2	Development of an automatic meter reader (AMR) for retrofit applications on existing meters
25137.1 PFNM-NM	INDIFUSEHOLDER	Ultra-low energy voltage indicator for new type of fuses
17142.2 PFEN-NM	IOTLOC	Development of a network for advanced low power localization using LoRa technology
18737.1	LAOSS	Large Area Organic Semiconductor Software for photovoltaic and light emitting devices (LAOSS)

16188.1 PFNM-NM	LASGRAT	High contrast gratings in vertical external cavity surface emitting lasers for gas sensing
18062.1 PFIW-IW	LETOP	Feasability study: Lever topologies for load cell
17508.1 PFNM-NM	LICOFO	Large-area light collecting foils for solar light concentration in photovoltaic devices
16871.1 PFNM-NM	LIDTDOS	LIDT und Degradations Prüftechnik für industrielle Anwendungen
18458.1 PFNM-NM	LIGHT HARV FOILS FEASIBILITY	Foils for transparent and colour-free solar energy harvesting
16044.2 PFNM-NM	LORNOFOX	A high performance time bounded fire hydrant network
18959.1 PFIW-IW	MAXIMAL	Modular radial and axial active magnetic bearing for maxon motors
18559.1 PFLS-LS	MEMO-MAB	Banking of human antibody repertoires for therapeutic use
16711.1 PFNM-NM	MICRO-FAS	Integrated fiber optics acceleration sensor
17728.1 INNO13-16-NM	MICROGRAVITY-TEST	Testing and validation of miniaturized fluid handling system for microgravity research
18325.1 PFNM-NM	MULTISENSOR	Development of a module integrating an optical temperature sensor and two optical accelerometer
18088.1 PFNM-NM	NANOWHITE	Process development and reliability of white solar module for BIPV
159541.1 PFEN/IW	NCOOL2	Development of a self-commissioning, predictive controller for central air conditionning
18760.1 PFNM-NM	NEURUG	Multi-well biosensor for drug screening applications
17372.2 PFNM-NM	NOVACAMERA	An infrared multispectral camera for gas detection and quantification
18808.2 PFIW-IW	OCTOPLUS	Advanced manufacturing cluster platform for thin films deposition
17896.1 PFIW-IW	OILGUARD	Oil in water monitoring
18646.2	OPTINCLINO	Optical inclinometer: Development of a fully packaged MEMS inclinometer with remote optical readout for structural health monitoring
18755.1PFNM-NM	OPTOGAS	CO ₂ /O ₂ gas mixing and sensing for life sciences
18327.1 PFNM-NM	OPTOREC	Development of high-end optical reference cavities for laser stabilization
18267.1 PFNM-NM	ORCA	On-reed camera array
18419.1 PFIW-IW	PEARLSCAN	Automatic assessment and measurement of pearl necklaces
18352.1 PFNM-NM	PIFPAF II	Pipetting system with flowsensor and microelement for passive flow control
17625.1 PFNM-NM	POMICLED	Powerful micronic light emitting diode for next generation micro-projectors
17244.1 PFLS-LS	POSBONE	Compact and flexible system for total knee replacement surgery
18926.2	PRINT-BAT	Feasibility study: Flexible printed batteries
18748.1 PFNM-NM	PRISM	High resolution multi-color detection system with adaptive algorithms for parallelized gene sequencing systems
18082.1 PFNM-NM	PROMISES	Perovskite photovoltaic material screening for enhanced stability

17705.1 PFNM-NM	PUNCH	Production-ready, next generation back-contacted silicon heterojunction solar cells and modules
11290.1 PFNM-NM	QUADLINE	A novel micro mark register head camera based on ultra-high-speed multi-linear image sensor
16108.1 PFNM-NM	SAIGA	Small antenna integrated in hearing aids
14782.1 PFLS-LS	SARENAPATCH	Micro patch portable pour l'injection en continu d'insuline
18465.1 PFNM-NM	SECUREFLIM	Fluorescence lifetime imaging microscopy (FLIM) for the product and brand protection market
18462.1 PFNM-NM	SILICON EYE	Design of a vision for positioning systems
16584.1 PFEN-IW	SILVERLINE 2	Next generation production processes and quality controls for watch batteries
16050.2-PFNM-NM	SPINBEAT-II	Leistungsmessgerät mit integrierter Trittanalyse und Effizienzfeedback für Radfahrer
16694.2 PFIW-IW	STABILITY	Dynamische Lageregelung für Hydraulikmodule demonstriert an einem Stelzentraktor im Rebberg
16853.1 PFNM-NM	SUNTRACKER	An accurate sun sensor for earth geographical north detection
17518.1 PFEN-NM	SUPERTC	SuPeRTC, a super high performance temperature compensated miniature real time clock module
18679.2	SWISSHOLO	Security 1st and 2nd level features provide (hidden) unique identifying structures for trademark protection of titanium implants
1799.1 PFNM-NM	SWW	OEM module and new algorithms (speed, sleep)
16637.2 PFNM-NM	TACOS	Development and integration of alternative transparent conductive oxides for silicon heterojunction solar cells
18939.1PFNM-NM	TEXAS	New casting tool for textured hydrogel surfaces for 3D cell culture
18130.1 PFIW-IW	TORS	Tribological optimization of spinning traveler and ring for spinning and twisting
18539.1 PFLS-LS	TRACTEUR	Development of an automated seed drill for the site-specific reseeding of grassland
18741.1 PFNM-NM	TRUEAIRSPEED	Pressure measurement system for paragliders
17324.1 PFLS-LS	U4P	Using physiological parameters measured with a wrist-worn device to predict ovulation, detect pregnancy, and monitor gestation
16185.1 PFNM-NM	VALIPLATE	Calorimetric tool for validating the liquid volume dispensed by liquid handling instruments
18621.1 PFEN-NM	WATT.CH	Smart wristband powered by PV cells
18091.1 PFEN-NM	WISEROCK	Low-cost WSN with GNSS capability for long-term landslide monitoring
18394.1 PFLS-LS	ZEPTOTRACK	Real-time surgical instruments positioning with reference integrated in surgical lamp

European Commission Projects

FP7 – ICT	ACTION	Active implant for optoacoustic natural sound enhancement
FP7 – TRANSPORT	AEROMUCO-COMPLEMENT	Aerodynamic surfaces by advanced multifunctional coatings
FP7 – NMP	AMBASSADOR	Autonomous management system developed for building and district
H2020 – ICT 2016	BIOCDX	A miniature bio-photonics companion diagnostics platform for reliable cancer diagnosis and treatment monitoring
FP7 – ICT	BIOFOS	Microring resonator-based biophotonic platform for food analysis
H2020 – LCE 2015	CHEOPS	Production technology to achieve low cost and highly efficient photovoltaic perovskite solar cells
FP7 – ICT	COLAE-COMPLEMENT	Commercialization clusters of OLAE (flexible, organic and large area electronics and photonics)
H2020 – ICT 2015	DETOP	Dexterous transradial osseointegrated prosthesis with neural control and sensory feedback
H2020 – LCE 2016	DISC	Double-side contacted cells with innovative carrier-selective contacts
FP7 – ICT	D-LIVER	Monitoring of patients with liver diseases
FP7 – SPACE	ELSA-COMPLEMENT	European levitated spherical actuator
FP7 – TRANSPORT	EVITA	Non-destructive evaluation, inspection and testing of primary aeronautical composite structures using phase contrast X-ray imaging
FP7 – ICT	FLEX-O-FAB	Pilot-scale hybrid roll to roll/sheet to sheet manufacturing chain for flexible OLEDs
FP7 – SPACE	FOSTERNAV-COMPLEMENT	Flash optical sensor for terrain relative robotic navigation
H2020 – MG 2014	FUTURESKY	Smart, green and integrated transport
H2020 – ICT 2014	GATEONE	Innovation service for European smartization by SMEs
FP7 – ICT	GO4TIME	Global, flexible, on-demand and resourceful timing IC & MEMS encapsulated system
FP7 – NMP	GREENANOFILMS	Development and application of ultra-high resolution nano-organized films by self-assembly of plant-based materials for next generation opto- and bio-electronics
FP7 – HEALTH	HEMIBIO	Hepatic microfluidic bioreactor
FP7 – ENERGY	HERCULES	High efficiency rear contact solar cells and ultra-powerful modules
FP7 – NMP	IMPRESS-COMPLEMENT	Flexible compression injection moulding platform for multi-scale surface structures
H2020 – EE 2015	INDIGO-2	New generation of intelligent efficient district cooling systems
FP7 – SECURITY	INGRESS	Innovative technology for fingerprint live scanners
FP7 – NMP	INNOVABONE	Novel biomimetic strategy for bone regeneration
H2020 – SC5 2014	INREP	Towards indium free TCOs
FP7 – ENVIRONMENT	INTASENSE-COMPLEMENT	Integrated air quality sensor for energy efficient environment control

H2020 – FOF 2016	KRAKEN	Hybrid automated machine integrating concurrent manufacturing processes, increasing the production volume of functional on-demand using high multi-material deposition rates
FP7 – ICT	LASSIE-FP7	Large area solid state intelligent efficient luminaires
H2020 – MG 2014	LYNCEUS2MARKET	Safer and more efficient waterborne operations through new technologies and smarter traffic management
H2020 – ICT 2014	M3TERA	Micromachined terahertz systems -a new heterogeneous integration platform enabling the commercialization of the THz frequency spectrum
H2020 – ICT 2014	MEDILIGHT	Miniaturized smart system for light stimulation and monitoring of wound healing
FP7 – NMP	MEGAROB	Development of flexible, sustainable and automated platform for high accuracy manufacturing operations in medium and large complex components using spherical robot and laser tracker on overhead crane
H2020 – ICT 2015	MIRPHAB	MidInfraRed PHotonics devices fABrication for chemical sensing and spectroscopic applications
FP7 – NMP	NANODIARA-COMPLEMENT	Development of novel nanotechnology based diagnostic systems for rheumatoid arthritis and osteoarthritis
H202 – SESAR 2015	NAVISAS	Navigation of Airborne Vehicle with Integrated Space and Atomic Signals
H2020 – LCE 2016	NEXTBASE	Next-generation interdigitated back-contacted silicon heterojunction solar cells and modules by design and process innovations
FP7 – ICT	PASTA-COMPLEMENT	Integrating platform for advanced smart textile applications
FP7 – ICT	PEGASO	Personalised guidance services for optimising lifestyle management in teen-agers through awareness, motivation and engagement
FP7 – SPACE	PHASER	High speed, high frequency electro-photonic ADC for space enabled routers
FP7 – NMP	PLIANT	Process line implementation for applied surface nanotechnologies
FP7 – ICT	POSITIVE-COMPLEMENT	A highly integrated and sensitive porous silicon based lab on a chip for multiple quantitative monitoring of food allergies at point of care
FP7 – NMP	PRIME	Plug and produce intelligent multi agent environment based on standard technology
H2020 – ICT 2014	RAWFIE	Road-, air- and water-based future internet experimentation
FP7 – ENVIRONMENT	RECONCILE-COMPLEMENT	Reconciliation of essential process parameters for an enhanced predictability of arctic stratospheric ozone loss and its climate interactions
FP7 – SPACE	REMOVE-DEBRIS	A low-cost active debris removal demonstration mission
FP7 – SECURITY	SAVE-MED	Tackling counterfeit medicines and related criminal networks
FP7 – ICT	SEMAIH	Scalable multi-criteria energy management infrastructure for aggregation of households
H2020 – ICT 2014	SMARTER-SI	Smart access to manufacturing for systems integration
FP7 – NMP	SMART-NANO	Sensitive measurement, detection, and identification of engineered nanoparticles in complex matrices

FP7 – NMP	SMARTRONICS	Development of smart machines, tools and processes for the precision synthesis of nanomaterials with tailored properties for organic electronics
FP7 – SECURITY	SNIFFER	Sensory devices network for food supply chain security
FP7 – SPACE	SOC-2	Towards neutral-atom space optical clocks: Development of high-performance transportable and breadboard optical clocks and advanced subsystems
FP7 – ICT	SPLENDID	Personalized guide for eating and activity behavior for the prevention of obesity and eating disorders
FP7 – ENVIRONMENT	STRATOCLIM	Stratospheric and upper tropospheric processes for better climate predictions
FP7 – ICT	SUNFLOWER	Sustainable novel flexible organic watts efficiently reliable
H2020 – FETOPEN 2014-2015	SUPERTWIN	All solid-state super-twinning photon microscope
FP7 – ICT	SWAN-iCare	Smart wearable and autonomous negative pressure device for wound monitoring and therapy
H2020 – EEB 2016	THERMOSS	Integration of advanced technologies for heating and cooling at building and district level
FP7 – NMP	TRIBUTE	Take the energy bill back to the promised building performance
FP7 – ICT	VIAMOS	Vertically integrated array-type Mirau-based OCT system for early detection of skin pathologies—Small or medium-scale focused research project (STREP)
FP7 – ICT	WELCOME	Wearable sensing and smart cloud computing for integrated care to COPD patients with comorbidities
FP7 – ICT	WISERBAN-COMPLEMENT	Smart miniature low-power wireless microsystem for Body Area Networks

European Space Agency (ESA), Swiss Space Office, Austrian Space Applications Programme (ASAP), and CNES Projects

ESA Projects

AMIGO	Autonomous medical monitoring and diagnostics
CCM-MTG	Development and manufacture of corner cube mechanisms for MTG satellite
CECILE	LiDAR integrating compressive sensing
CLUPO	CLUPI instrument for Exomars
C-MAC	Ceramic miniature atomic clock physics package – C-MAC PP
CS4SPACE	Compressive sensing
DANOE	High-dynamic absolute nanometric optical encoder technology assessment for space
DELIAN	Detrous lightweight arm for exploration
ENRUM	Space and energy resources utilisation mapping (EnRUM)
EUSO-B2	Extreme universe space observatory – Phase B2
FGU	Micro-optoelectronic frequency generation unit (FGU)
HOPP	Photodiode development
HOPWELL	Space validation of glass lid soldering techniques to hermetically seal small size optoelectronic parts

IHMDS-2	Integrated vehicle health management system demonstrator – Phase 2
ITI-SiC	Silicon carbide sensors for harsh space environments
MCC-X	Miniaturised motion controller customisation for exploration
MEMS GC-MS	MEMS-based gas chromatograph and mass spectrometer
MEMS-QUAL	Validation and experimental verification of ESA MEMS qualification methodology
MEMS-REAL	MEMS reliability assessment
MHIPIS	Miniature high performance imaging spectrometer for remote sensing
MILA	Miniaturised imaging laser altimeter (Miniature imaging LIDAR system, phase 1)
MLSCL	Sub-picosecond model-locked semiconductor laser for space missions
MTS	Miniature timing source (mTS): miniature atomic clock, MEMS vapor cells, ASIC specifications
NIRS	NIR immersed grating in transmission for high resolution spectroscopy
NPI-CELL	PhD on fabrication of miniature atomic cells
NPI-EIT	Wearable physiological sensor network–non-invasive and non-occlusive blood pressure (BP) measurement based on electrical impedance tomography (EIT)
OEO	Ultra-low phase noise reference oscillator
SAMTWO_6	Space active maser – six
STAR	Lidar for wavefront distortion
SWIRS	New generation SWIR immersed grating (phase1)
WALES-PLUS	Wafer level encapsulation for microsystems-PLUS
WATERLENS	Water availability–Improved monitoring, forecasting and control of water availability, quality and distribution

Swiss Space Office Projects

3D-EEE	EEE components produced by additive manufacturing
HYBSAT	Hybrid lightweight and flexible circuit boards (FCBs) for satellites and space

Austrian Space Applications Programme (ASAP) Projects

SPACEXCT	X-ray techniques for NDT and damage characterization for space materials and components
----------	---

CNES Projects

IASI-FM3PHASE 1B	IASI-FM3 Travaux préparatoires complémentaires à la réparation du mécanisme CCM
IASI-FM3REFUB	Perform refurbishment of actuator on IASI-EM at CSEM and IASI-FM3 at TAS

Industrial Property

In 2016, 20 invention reports were submitted internally for examination which have led to 15 patent applications filed in 2016 (12 regular applications and 3 provisional applications). The patent portfolio has been further enhanced by the extension of different countries of 9 patent files based on prior patent applications.

Collaboration with Research Institutes and Universities

University	Institute	Professor	Field of collaboration
Aristotle University of Thessaloniki	Laboratory of medical informatics	N. Maglaveras	Collection of large set of physiological signals
Berner Fachhochschule (BFH)	Institute for energy and mobility research	A. Vezzini	BFH-CSEM Energy Storage Research Center (ESReC): electrochemical storage
Brown University	School of engineering	A. V. Nurmikko	Integrated circuits for brain implants

<i>University</i>	<i>Institute</i>	<i>Professor</i>	<i>Field of collaboration</i>
Carleton University	Systems and computer engineering	A. Adler	Electrical-impedance tomography
CEA-LETI	Capteurs et actionneurs	M. Le Prado	Atomic gyroscopes
Christian-Albrechts-Universität zu Kiel	Klinik für Anästhesiologie und Operative Intensivmedizin	I. Frerichs	Electrical-impedance tomography
CHUV	Service de cardiologie	E. Pruvot	Cardiac arrhythmias
CHUV	Département anesthésiologie	P. Schoettker	Blood pressure
Croydon Healthcare NHS Trust	Trust R&D	J. Chang	Clinical validation
EMPA	Department of advanced materials and surfaces	P. Görning	X-ray read out circuits
EMPA	Swiss federal laboratories for materials science and technology	P. Hoffmann	Solid state lighting
EMPA	Laboratory for functional polymers	F. Nüesch	Organic PV
EPF Lausanne	Embedded systems laboratory	D. Atienza	ECG monitoring
EPF Lausanne	IMT/PVLAB	C. Ballif	Photovoltaics
EPF Lausanne	Galatea laboratory	Y. Bellouard	Femtolaser micro-structuring
EPF Lausanne	SAMLAB	N. de Rooij	Microstructural investigation
EPF Lausanne	ICLAB integrated circuits laboratory	C. C. Enz	Approximate arithmetic, ULP Radio and protocol for WiseSkin
EPF Lausanne	Laboratory of advanced semiconductors for photonics and electronics	N. Grandjean	GaN-based semiconductor lasers; Solid state lighting
EPF Lausanne	CIME	C. Hebert	Microscopy
EPF Lausanne	Instant-Lab	S. Henein	Precision mechanics
EPF Lausanne	LAP processor architecture laboratory	P. lenne	Embedded systems
EPF Lausanne	Laboratory of photonics and quantum measurements	T. J. Kippenberg	Optical microresonators and frequency combs
EPF Lausanne	LSBI Foundation Bertarelli Chair in neuroprosthetic technology	S. Lacour	Artificial skin, restore spinal connections
EPF Lausanne	Nanophotonics and metrology laboratory	O. Martin	Development of plasmonic sensors
EPF Lausanne	TCL Telecommunications Circuits Laboratory	A. P. Burg	Good enough circuits, ultra-low power and sub-threshold design
EPF Lausanne	eSpace	M. Richard	Space missions
EPF Lausanne	Laboratoire de production microtechnique	P. Ryser	1) Compact 3D force sensor 2) Indoor air quality sensor system
EPF Lausanne	Institute of microtechnology	H. Shea	Microtechnology/ Microscopy
EPF Lausanne	Hemodynamics and cardiovascular technology laboratory	N. Stergiopoulos	Cardiac output monitoring

<i>University</i>	<i>Institute</i>	<i>Professor</i>	<i>Field of collaboration</i>
EPF Lausanne	LTS2 signal processing laboratory 5	J.-P. Thiran	Electrical-impedance tomography
EPF Lausanne	LTS2 signal processing laboratory 2	P. Vandergheynst	Newborn vital signs monitoring based on multiple vision sensors; Signal processing
EPF Lausanne	SCI STI JMV Group	J-M. Vesin	Newborn vital signs monitoring based on multiple vision sensors; Signal processing
ETH Zurich	Integrated systems laboratory	L. Benini	Sub-near-threshold multicore
ETH Zurich	Institute for chemical and bioengineering (ICB)	A. deMello	Cell sorting/classification; Nanoparticle analysis
ETH Zurich	Photonics laboratory	L. Novotny	Development of plasmonic antennas
ETH Zurich	SCOP	R. Schüblin	Microscopy
ETH Zurich	Laboratory for solid state physics	H. von Känel	X-ray read out circuits
Fraunhofer Society	Group for automation in medicine and biotechnology	B. Grychtol	Electrical-impedance tomography
Hamburg University Hospital (UKE)	Klinik und Poliklinik für Anästhesiologie	D. Reuter	Electrical-impedance tomography
Hôpital Neuchâtelois, HNE	Département de médecine	C. Pellaton	Multiple collaboration including a clinical investigation on non-invasive blood pressure
Hôpitaux Universitaire de Genève	Département d'urgences pédiatriques	A. Gervaix	Monitoring de pneumonie
National Institute of Standards and Technology, NIST	Optical frequency measurements group	S. A. Diddams	Optical frequency combs and their applications
National Renewable Energy Laboratory, NREL	Photovoltaics	A. Tamboli	Multi-junction solar cells
Paul Scherrer Institute (PSI)	LNM	S. Abpöhassani	Microstructure
Politecnico di Milano	Department of energy	M. Merlo, A. Casalegno	Battery modelling
Technical University of Kaiserslautern	Chair of real-time systems	G. Fohler	Real-time networking
University Hospital of Bern (Inselspital)	Department ENT surgery	M. Caversaccio	Image-guided micro surgery for hearing aid implantation
University Hospital of Bern (Inselspital)	Cardiovascular department	S. F. Rimoldi	Blood pressure
University Hospital of Bern (Inselspital)	Department of pulmonary disease	T. Geiser	Oxygen therapy
University Hospital of Bern (Inselspital)	Department of sleep	S. Ott	Sleep analysis
University Hospital of Zurich	Clinic of neonatology	J.-C. Fauchère	Newborn vital signs monitoring based on multiple vision sensors

<i>University</i>	<i>Institute</i>	<i>Professor</i>	<i>Field of collaboration</i>
University Hospital of Zurich	Biomedical optics research laboratory, Division of neonatology	M. Wolf	Newborn vital signs monitoring based on multiple vision sensors; Neonate monitoring
University of Applied Sciences and Arts (FHNW)	School of life sciences	M. de Wild	Institute of medical and life sciences
University of Applied Sciences and Arts (FHNW)	School of life sciences	C. Hugi	Life cycle analysis of OPV
University of Applied Sciences and Arts (FHNW)	School of life sciences	U. Pieles	Biology and sensing
University of Applied Sciences and Arts, Lucerne (HSLU)	CC Mechanische Systeme	U. Lang	Nanofoils
University of Applied Sciences and Arts, Lucerne (HSLU)	CC Aerospace biomedical science & technology / CC Mechanische Systeme / CC Electronics	M. Egli, C. Haack, O. Schälli	Micro gravity incubator
University of Applied Sciences and Arts, Lucerne (HSLU)	CC Electronics	E. Niederberger	Solid state lighting
University of Applied Sciences and Arts, SUPSI	IDSIA Dalle Molle Institute for artificial intelligence	L. M. Gambardella	Machine learning
University of Applied Sciences and Arts, SUPSI	Department for environment constructions and design	R. Rudel	Testing and accreditation of modules
University of Applied Sciences, Bern	MSE	V. Koch	Sensory processing prosthetics
University of Applied Sciences, Zurich (ZHAW)	Institute of computational physics	B. Ruhstaller	Solid state lighting
University of Basel	Dept. of physics	E. Meyer	Nano Argovia project
University of Basel	Dept. of physics	C. Schöneberger	Development of light management optics for solar cells
University of Bern	ARTORG Center for biomedical engineering	S. Weber	Guided surgery; Image-guided micro surgery for hearing aid implantation
University of Fribourg	Faculté des sciences économiques et sociales	E. Davoine	Gestion des ressources humaines
University of Geneva	Exoplanetary systems	F. Pepe	Instrument for exoplanetary search
University of Geneva	Computer vision and multimedia laboratory	T. Pun	Obstacle detection for the elderly based on stereo vision
University of Lausanne	Institute of Geology	E. Verrecchia	Microstructural study
University of Lund	Department of biomedical engineering	C. Antfolk	Prosthetics

<i>University</i>	<i>Institute</i>	<i>Professor</i>	<i>Field of collaboration</i>
University of Neuchatel	Institute of biology	P. Junior	Microstructural investigation
University of Neuchatel	Institute of biology	F. Kessler	Microstructural investigation
University of Neuchatel	Laboratoire Temps-Fréquence	G. Miletí	Cell-based atomic clocks
University of Neuchatel	Institute of biology	J-M. Neuhaus	Microstructural investigation
Wyss Center	Bio and neuro engineering	C. Clément	Integrated circuits for brain implants

Teaching

	<i>Title of lecture</i>	<i>Context</i>	<i>Location</i>
F. Cosandier	Watt balance	Conception de mécanismes II	EPF Lausanne
M. Dadras	AFM/TEM/SEM	Doctoral Scholl EPFL	EPF Lausanne
	AFM/TEM	Master	HE-ARC
	Microscopy	Master	University of Neuchatel
J.-D. Decotignie	Informatique du temps réel	Bachelor informatique	EPF Lausanne
	Real time networks	Master computer and communication systems	EPF Lausanne
M. Despont	Packaging and hybridization, the valorization of MEMS technologies	Micro- 534 Advanced MEMS 2016 (D. Briand)	EPF Lausanne
J. R. Farserotu	Satellite communication systems and networks	Master degree course under Communication systems and space technology	EPF Lausanne
P. Feroleto	Cours gestion des ressources humaines	Bachelor 3rd year	University of Fribourg
I. Kjelberg	Thermo-mechanical design for space optics	Space optics instruments technology	Poltu Quatu (IT)
G. Nisato	Organic thin-film transistors (OTFTs): basics, applications, sustainability	Module sustainable production and clean technologies – Printed organic electronics	FHNW, School for Life Sciences, Basel
G. Nisato, O. Fernández, T. Offermans, N. Marjanović	Introduction to printed electronics	Training FSRM	CSEM Muttenz
C. Piguet	Microelectronics for systems-on-chips	Master, EPFL, Autumn semester	EPF Lausanne
	Green electronics	Invited course	ISEP Paris
	ICT for sustainable development	Invited course	ISEP Paris
	Microelectronic technology	ALaRI course on embedded systems	University of Lugano
D. Schmid	Smart body sensors: Lebensqualität oder Überwachung?	SATW TecDay	Kantonsschule Chur, CH
E. Scolan	Nano-/micro-structuration de revêtements élaborés par voie sol-gel: design, fabrication, intégration et application industrielles	Maîtriser le procédé Sol-Gel et ses applications industrielles aux matériaux multifonctionnels	Ecole Polytechnique, Paris

	<i>Title of lecture</i>	<i>Context</i>	<i>Location</i>
F. Zanella	Introduction to organic/printed electronics and Applications	Additive manufacturing of polymers Summer School	EPF Lausanne

Theses

PhD Degrees Awarded in 2016

<i>Name</i>	<i>University</i>	<i>Title</i>
E. A. Hammes	EPF Lausanne	Gas sampling using convection and humidity stabilization to improve point gas sensor responses
J. Kruis	EPF Lausanne	Design, analysis, testing and applications of two-body and three-body kinematic mounts
F. Lütfolf	EPF Lausanne	Optical properties of asymmetric, partially metallic gratings
R. Thirunarayanan	EPF Lausanne	Ultra-low power frequency synthesizers for duty cycled iot radios

CSEM Employees carrying out a PhD

<i>Name</i>	<i>Professor / University</i>	<i>Theme / CSEM Unit</i>	<i>Start year</i>
F. Braun	J.-P. Thiran / EPF Lausanne	Estimation of hemodynamics via electrical impedance / Systems	2013
S. Cloix	T. Pun, D. Hasler / University of Geneva	Stereoscopic computer vision / Integrated & Wireless Systems	2012
L. Dümpelmann	L. Novotny / ETH Zurich	Deep-subwavelength plasmonic nanostructures for light harvesting / Center Muttenz	2013
S. Karlen	G. Miletí / University of Neuchâtel	MEMS cells for atomic clocks / Systems	2014
V. Kopta	C. C. Enz / EPF Lausanne	FM-UWB radio for high-density wireless sensor networks / Integrated & Wireless Systems	2013
J. Mayer	C. Schönenberger / University of Basel	Light management and harvesting for photovoltaic and sensing applications / Center Muttenz	2014
T. C. Müller	A. P. Brug / EPF Lausanne	Variation-aware digital design / Integrated & Wireless Systems	2016
D. Müller	A. deMello / ETH Zurich	Miniaturization of asymmetrical flow field-flow fractionation / Center Landquart	2013
M. Proenca	J.-P. Thiran / EPF Lausanne	Estimation of hemodynamics via electrical impedance tomography / Systems	2012
G. Quaranta	O. Martin / EPF Lausanne	Color-selective and versatile light steering structures compatible with roll-to-roll technology and up-scalable fabrication / Center Muttenz	2015
M. Rapin	J. Snedeker / ETH Zurich	Wearable EIT system / Systems	2013
D. C. Rojas Quiros	J.-D. Decotignie / EPF Lausanne	Development of MAC and routing protocols for dense wireless sensor networks / Integrated & Wireless Systems	2014
F. Sorba	H. Shea / EPF Lausanne	Development of an integrated device for cell stiffness measurement / Micro&Nano Systems	2015

Name	Professor / University	Theme / CSEM Unit	Start year
J. Sun	H. Lissek, X. Falourd / EPF Lausanne	Anomaly detection in time varying signals for the quality inspection of electromotors / Center Alpnach	2011
A. Tuomiranta	C. Ballif / EPF Lausanne	Optimal design and operations of photovoltaic power plants / Photovoltaics	2015

Commissions and Committees

P.-J. Alet	Advisory board of European project MIGRATE European Technology and Innovation Platform Photovoltaics: member of the steering committee, member of the executive committee, leader of the grid integration working group Jury member for Intersolar Photovoltaics Award
F. Amez-Droz	CSEM Representative, Swiss Association of Science Journalism
C. Ballif	Silicon PV conference, member of the steering committee
C. Bosshard	BaselArea.Swiss: Member of Advisory Board and Technology Field Leader Micro, Nano & Materials CSEM Representative, European Photonics Industry Consortium (EPIC) Managing Director of the Swissphotonics NTN Photonics21, Board of Stakeholders
P. Dallemande	Secretary and Swiss representative of Technical Committee 5 "Information Technology Applications", International Federation for Information Processing (IFIP)
J.-D. Decotignie	ISO TC 65 Swiss Committee ISO TC 65C, WG16 convenor, Wireless Industrial Communication Standardization Program Committee, Conf. on Embedded & Real-Time Computing Systems & Applications (RTCSA), Daegu, South Korea Program Committee, Design Automation in Europe (DATE), Desden, Germany Program Committee, Euromicro Conference of Real-Time Systems, Toulouse, France Program Committee, Real-Time Networks and Systems, Brest, France Program Committee, Workshop on Factory Communication Systems, Aveiro, Portugal Program Committee, Workshop on Real-Time Networks, Toulouse, France
M. Despeisse	n-PV international workshop: member of the steering committee

M. Despont	<p>Board member of the Swiss-MNT network</p> <p>Chairman of the IEEE International Conference on Micro ElectroMechanical Systems (MEMS), Belfast, UK, 2018</p> <p>CSEM and HTA representative at the Micro- and Nano- Technology Workgroup, European Spatial Agency (ESA)</p> <p>External Expert at PhD Thesis, EPFL</p> <p>Member of the editorial board of Microelectronic Engineering Journal (Elsevier)</p> <p>Member of the executive board of the Swiss research program NanoTera</p> <p>Member of the Executive Technical Program Committee of Transudcers 2017, June 18-22, 2017, Kaohsiung, Taiwan</p> <p>Member of the Industrial Advisory Board, Nanotechnology Program, Prof H. Bahaskaran, Oxford University, UK</p> <p>Member of the Int'l Steering Committee of the Micro- and NanoEngineering (MNE) conference</p> <p>Member of the Technical Program Committee of European Solid-State Device Conference, ESSDERC (Lausanne, 2016)</p> <p>Programme Committee of the 10th ESA round table on Micro and Nano Technologies, ESA-ESTEC, 8-11 November 2016</p> <p>Senior Member of the IEEE Society</p>
M. El-Khoury	<p>CNCI Chambre Neuchâteloise du Commerce et de l'Industrie, Neuchâtel</p> <p>Concours International de Chronométrie, Le Locle, Membre du Comité d'honneur</p> <p>Conseil de l'Université de Neuchâtel</p> <p>Emirati-Swiss Friendship Platform, Abu Dhabi</p> <p>Nano-Tera, Member of the Steering Committee</p>
J. R. Farserotu	<p>Chair and Research Co-ordinator The Hermes Partnership</p> <p>Chair of ETSI Technical Committee Smart Body Area Networks (TC SmartBAN)</p> <p>Member of the Steering Committee and Technical Committee, IEEE International Symposium on Medical Information and Communication Technology 2016 (ISMICIT 2016)</p>
R. Ferrini	<p>Chair of the Swissphotonics Solid State Lighting - (SSSL) Swiss National Laboratory for Solid State Lighting</p>
E. Györvary	<p>Extended Board Member CSEM Brasil</p> <p>Extended Board Member of the Heterogeneous Technology Alliance (alliance federating the Fraunhofer (microelectronics), VTT, CEA-Tech and CSEM)</p> <p>Member of the Finnish Chamber of Commerce</p> <p>Member of the Latin American Chamber of Commerce</p> <p>Member of EARTO Working Group on Emerging Technologies for Healthcare</p>
H. Heinzelmann	<p>Program Committee, MNE Micro Nano Engineering 2016, Vienna</p> <p>Program Committee, SSI Smart Systems Integration 2016, Munich</p> <p>Steering Committee, CCMX Competence Center for Materials Science and Technology</p> <p>VP Nanotechnology, Swiss Society for Optics and Microscopy SSOM</p>
C. Julia-Schmutz	<p>Communication Coordinator within the Heterogeneous Technology Alliance (HTA)</p> <p>CSEM Representative, BioAlps</p>

H. F. Knapp	Board Member of Swiss Life Sciences Inartis Network Association Delegate for cluster initiative Toolpoint for Lab Science Jury Member for Zinno-Ideenscheck Member of the Executive Board of biotechnet, Switzerland
G. Kotrotsios	Le Réseau, Advisory Board Member of the Board of Directors of CSEM Brasil IEEE Subcommittee on Human-Machine in Manufacturing Environment IEEE Subcommittee on Computer Vision and Human-Machine Interaction in Industrial and Factory Automation Member of the Board of the Heterogeneous Technology Alliance (alliance federating the Fraunhofer (microelectronics), VTT, CEA-Tech and CSEM) Member of the Executive Board of EARTO, the European Association of Research and Technology Organisations Member of the Executive Board of EREA (the European Association of Aeronautics Research Centers) Member of the Swiss Academy of Engineering Sciences Micronarc, member of the Group of Experts
M. Krieger	CSEM Representative Greater Zurich Area (GZA) CSEM Representative Manufuture.ch association CSEM Representative SEMI global semiconductor industry association CSEM Representative Zürcher Handelskammer (ZHK) CSEM Representative, Advanced Factory Automation workgroup of Swissmem (AFA)
S. Lecomte	European Time and Frequency Forum (EFTF) scientific committee member
A. Madrigal	Chair person of the Advisory Board of the new Space exhibition of the Museum of Transport of Lucerne CSEM Representative, General Forum Clean Sky CSEM Representative, Network of European Research Organisations on ESA Issues (NERO) CSEM Representative, Swiss Aeronautics Security and Defense Division of Swissmem (Swiss ASD) CSEM Representative, Swiss Space Industries Group of Swissmem (SSIG) Expert for the evaluation of proposals for the Comité Consultatif pour les Technologies Spatiales (CCTS) of the Swiss Space Office (SSO) Member of the General Assembly of EREA (Association of European Establishments in Aeronautics) and CSEM Delegate in the Aviation and Security Research Groups of the Association Member of the Steering Committee of the Swiss Space Centre (SSC)
S. Mohrdiek	Member of Phonotics21 Work Group 6 - Design and Manufacturing of Components and Systems Swissphotonics, Head of Swiss Photonic Packaging Laboratory
G. Nisato	Member of the Board of the Organic and Printed Electronic Association (OE-A)
L.-E. Perret-Aebi	CTI expert in the micro-nano commission
C. Piguet	Steering Committee of the ALaRI Master Course, University of Lugano

D. Ruffieux	Member of the International Technical Program Committee of the European Solid State Circuit Conference (ESSCIRC) in the RF and mmWave Building Blocks
	Member of the International Technical Program Committee of the International Solid State Circuit Conference (ISSCC) in the Technology Directions sub-committee
E. Schaller	Member of the Executive Board of sensors.ch, Switzerland
P. Steiert	Advisory Board Member for Institute für Chemistry and Biological Chemistry at the ZHAW Advisory Council for cluster initiative Toolpoint for Lab Science Member of the Executive Board for microPark Pilatus

Prizes and Awards

- January 2016 Franco-Swiss Chamber of Commerce and Industry's Innovation Prize 2016 to CSEM and ONERA for the excellence of their technical outcomes in the development of a pressure-sensitive paint for aerodynamic analyses in transonic wind tunnels (Montreux, CH).
- January 2016 Swiss Environmental Award 2016, presented to CSEM for the development of white and colored solar panels with no visible cells or connections (Basel, CH).
- March 2016 The Best Paper Award was presented to CSEM, EPFL, and Meyer Burger Research at the Swiss PV Symposium. The team was rewarded for its joint work, entitled, "Development of photolithography-free, back-contacted silicon heterojunction (SHJ) solar cells with efficiency >22 %", a paper presented by Bertrand Paviet-Salomon of CSEM (Bern, CH).
- March 2016 At the 2016 International Conference on Crystalline Silicon PV, two awards were presented to CSEM for its collaborative work, respectively with EPFL on "High-Efficiency silicon heterojunction solar cells with molybdenum oxide hole collector" and with NREL on "Si-based tandem solar cells with 29.8% record one-sun efficiency" (Chambéry, FR).
- April 2016 Sylvain Karlen took home the 2016 EFTF Student Poster Award at the 2016 European Frequency and Time Forum (EFTF) for his work on "Non-destructive MEMS atomic vapor cells characterization by Raman spectroscopy and image analysis" (York, UK).
- May 2016 During LOPE-C 2016, the world's leading exhibition for printed electronics, the Organic and Printed Electronics Association (OE-A) awarded the Sunflower project (coordinated by CSEM) the "best publicly funded project demonstrator" prize for the "OPV living room" (Munich, DE).
- May 2016 Giorgio Quaranta and co-workers received the Best Poster Award at the CCMX annual meeting for their work on "Fabrication of plasmonic nanostructures and metasurfaces with UV imprint and thin metallic and dielectric coatings" (Bern, CH).
- May 2016 Christophe Ballif received the Becquerel Prize for Outstanding Merits in Photovoltaics for his scientific merit in the development of silicon heterojunction solar cells (Munich, DE).
- September 2016 Nico de Rooij elected Micro and Nano Engineering (MNE) Fellow 2016—recognition of his pioneering contributions in the fields of MEMS and sensor technology (Vienna, AT).
- September 2016 Lukas Hofer was recognized by the Graduate School Graubünden, for the best work carried out in the natural sciences, at the 5th Graubünden Forscht—Young Scientists in Contest congress. Lukas won the award for his poster, "Development of a miniaturized Fourier transform time-of-flight mass spectrometer" (Davos, CH).
- October 2016 The Best Poster Award of the ESA Space Passive Component Days 2016 was presented to Nenad Marjanović and co-workers for their work on "Sun sensor printed on flexible circuit board for pico-satellites" (Noordwijk, NL).
- October 2016 Luc Dämpelman was awarded 3rd prize in the D-ITET Research Photo Competition for his photo of a color filtering substrate in front of a Morpho butterfly (Zurich, CH).

CSEM SA
Jaquet-Droz 1
CH-2002 Neuchâtel

CSEM Alpnach
Untere Gründlistrasse 1
CH-6055 Alpnach Dorf

CSEM Landquart
Bahnhofstrasse 1
CH-7302 Landquart

CSEM Muttenz
Tramstrasse 99
CH-4132 Muttenz

CSEM Zurich
Technoparkstrasse 1
CH-8005 Zurich



www.csem.ch
info@csem.ch
jobs@csem.ch
